2017

Rotationally Inelastic Collisions of Ground-State Helium or Argon with NaK ($A^{\,1}\Sigma^+$)

Teri Price
Lehigh University

Rotationally Inelastic Collisions of Ground-State Helium or Argon with NaK ($A\,^1\Sigma^+$)

by

Teri Jean Price

A Dissertation
Presented to the Graduate Committee
of Lehigh University
in Candidacy for the Degree of
Doctor of Philosophy
in
Physics

Lehigh University
May 22, 2017

Approved and recommended for acceptance as a dissertation in partial fulfillment of the requirements for the degree of Doctor of Philosophy.

Teri J. Price
Rotationally Inelastic Collisions of Ground-State Helium or Argon with NaK ($A\,^1\Sigma^+$)

Date

A. Peet Hickman, Dissertation Director, Co-Chair

Accepted Date

Committee Members

John Huennekens, Co-Chair

Gary DeLeo

Slava V. Rotkin

Heather Jaeger

Acknowledgements

I'd like to thank my advisor and mentor, Professor Hickman. Learning from you has been a tremendous opportunity, and I've appreciated your patience, time, and kindness. You have taught me a lot, from AMO physics to writing, negotiating, and programming. Your excitement about the research has been infectious, and I've loved working on this project. With your guidance and support I have grown more confident over time, and I can never thank you enough for all you've done for me.

I'd also like to thank Professor Huennekens: you have been like a second advisor to me. Thank you for teaching me about experimental techniques in AMO physics and for inviting me to participate in your reading group. I've appreciated your career advice and the opportunity to meet your collaborators at Temple. Thank you for helping me find the right attitude for different situations and for your encouragement.

Thank you to my committee members, Professors DeLeo, Rotkin, and Jaeger, for coming to my committee meetings and reading my dissertation. I've appreciated your comments and suggestions about the research, and thank you in particular for encouraging me to think more about the propensity for Δj even transitions, the significance of β, and for helping me find a better basis set for Ar+NaK. Professor DeLeo: thank you for mentoring me as a GAANN fellow, helping me to become a better teacher and making sure I was adjusting well to graduate school. It was a great experience to participate in outreach programs with you and to be a judge for Scholastic Scrimmage. I will miss your jokes and stories.

Thank you to Ruthie Malenda, whose work I have continued. Your thesis helped me a lot, and hopefully I have done your work justice. I enjoyed driving to DAMOP

together and sharing hotel rooms with you and Kara. To Kara Richter, Josh Jones, and Carl Faust: thank you for welcoming me into the group, answering my questions about the experiments, and providing the experimental data referenced in this work. Kara: Thanks for teaching me about roller derby and for drawing an awesome dragon on my window! Josh: Thanks for telling me about fun (and delicious) places to go in town. Carl: Thanks for always being excited to explain things, for showing me the lab, and for telling me about the game.

I'd like to thank Keith, who has been with me all throughout graduate school. We have so many happy memories together, camping and going to the beach and playing basketball. You've helped me through difficult times, supporting and listening to me, and I don't know if I would have gotten through graduate school without you. Besides me, you've helped a lot of people, and you're going to be a great teacher.

Last but not least, I'd like to thank my mom, my dad, and my brother Bobby. Thanks for inspiring me in my research and for always believing in me. It is so nice to come home and see you all. You are always listening, even when I am stressed out and rambling! Thanks for encouraging me to have a life full of fun and adventure and for teaching me to learn something new every day. You are my role models, and I hope that I am growing up to be just like you. Bobby: you've grown a lot as I've gone through school. You've blossomed from my playful little brother into a mature, compassionate, hardworking man with many talents. I'm proud of you, and I hope you're proud of me.

Finally, I'd like to dedicate this dissertation to my late Aunt Nancy and my Pop Pop, Jim Cuff.

Contents

List of Tables

List of Figures

Abstract

We have performed quantum mechanical scattering calculations that describe collisions between He or Ar and NaK ($A^1\Sigma^+$) that change the rotational and magnetic quantum numbers, j and m. These calculations involved determining *ab initio* potential energy surfaces by using the GAMESS electronic structure code. The coupled channel scattering formalism, developed by Arthurs and Dalgarno, was used with the potential surfaces to calculate j and m-changing cross sections, along with the transfer of moments of the m distribution. Our calculations show a propensity for transitions with even values of Δj; the strength of the propensity depends on the perturber. These results are in good agreement with experimental data measured by the Lehigh group. We identify a region of the potential that tends to diminish the propensity and develop a simple model to explain why such a region arises. We develop a semiclassical model that leads to closed form expressions for semiclassical m-changing cross sections (where m is a continuous variable) and the distribution of final polar angles $\theta' = m'/\sqrt{j'(j'+1)}$. We compare our calculated semiclassical and quantum mechanical cross sections, and we identify special cases which admit analytic approximations to the polar angle distribution. One special case leads to a near-Lorentzian distribution, peaked where $\theta' = \theta$. Many results for He+NaK and Ar+NaK are well described by this case.

Chapter 1

Introduction

1.1 Motivation

Lehigh's atomic, molecular, and optical physics group, led by Profs. Hickman and Huennekens, has for several years performed theoretical and experimental studies of the following thermal collision process:

$$\mathrm{NaK}\,(v,j,m) + \mathrm{X} \rightarrow \mathrm{NaK}\,(v',j',m') + \mathrm{X} \qquad \mathrm{X} = \mathrm{He\ or\ Ar}, \tag{1.1}$$

where v is the vibrational quantum number, and j and m are the quantum numbers that define the rotational state of the molecule. For the experiments of current interest, NaK is in the $A\,^1\Sigma^+$ electronic state. The potential energy curve for this state is shown by the solid curve in Fig. 1.1; the state dissociates into Na($3s$) + K($4p$).

Hickman and coworkers [1–3] have performed calculations to model these collisions when $v = v'$ in Eq. 1.1. Calculations are also underway to provide cross sections for v-changing collisions in collaboration with R. C. Forrey at Penn State Berks.

Experimental studies have been carried out by Huennekens and coworkers at Lehigh and in collaboration with the group of A. J. Ross at Université Lyon 1 [4–7]. The experiments at Lehigh have addressed j- and m-changing collisions, and those at Lyon have provided information about v- and j-changing collisions. In

Section 1.2, we will discuss the experimental methods used. Here we highlight some experimental results and discuss our work within the context of those results.

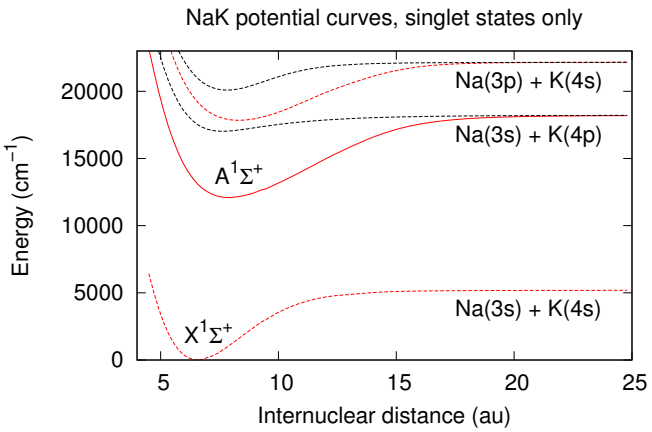

Figure 1.1: Some potential curves calculated by Magnier *et al.* [8] representing the first several electronic singlet states of NaK.

Wolfe *et al.* [4] and Jones [5] measured rates at which vibrationally elastic ($\Delta v = 0$) collisions with helium or argon change j by Δj. The rates are higher for transitions that change j by an even Δj than by an odd Δj. That is, they show a propensity for Δj even transitions. Moreover, the relative rates depend on the perturber. Jones [5] and Richter [6] extended this work and performed measurements for both vibrationally elastic and vibrationally inelastic collisions. In the former case they confirmed the previously observed propensity for Δj even transitions [5, 6]. They found no propensity for even Δj in vibrationally inelastic collisions.

In the case of a homonuclear diatomic molecule with no nuclear spin, there is a strict selection rule for Δj even transitions. When such a transition is induced by a collision with an atom, the selection rule is based on parity due to the inversion symmetry of the interaction with the atom and of the molecular states involved [9]. One might expect an approximate symmetry for a molecule like NaK consisting of

two similar atoms, leading to the propensity but not a strict selection rule. The selection rule for homonuclear diatomics involves the interaction of the molecule with the atom, and a semiclassical analysis by McCurdy and Miller [10] connects the propensity to that interaction as well. Their analysis suggests the propensity is sensitive to the degree to which the interaction potential deviates from inversion symmetry. The analysis, however, is semiclassical and assumes a specific form for the interaction potential. We were able to investigate the propensity quantum mechanically and with our calculated potentials.

The experiments performed by Wolfe *et al.* [4] and Jones [5] also provided information about vibrationally elastic m-changing collisions. The experiments involved preparing a rovibrational level (v, j) with a non-zero average m. Jones [5] measured the extent to which collisions with helium or argon changed the average value of m and found the change was greater for collisions involving argon.

In this dissertation we describe our calculations of v-, j-, and m-changing collisions and show how our results compare with the experimental data. We will also describe our investigation of the sensitivity of the propensity to changes in the interaction potential. Additionally, we address the discussion in the literature about whether the polar angle $\theta = \cos^{-1}\left(m/\sqrt{j(j+1)}\right)$ in the vector model for the rotational angular momentum is approximately conserved during inelastic collisions of atoms with small molecules [11, 12]. We develop a semiclassical model that predicts that θ is conserved in certain special cases and gives physical insight into this problem [3].

1.2 Overview of experimental methods

This section provides a brief overview of the experiments performed by Wolfe *et al.* [4] at Lehigh, by Jones [5] at Lehigh and at Université Lyon 1, and by Richter [6] at Université Lyon 1.

At the core of each experiment is a heat pipe oven where a cold buffer gas of argon or helium atoms can mix with NaK vapor at 600 K [13]. The oven may be

considered a cell environment because the NaK molecules experience collisions with buffer gas atoms coming from all possible directions.

1.2.1 Fluorescence spectroscopy

Wolfe *et al.* [4] and Jones [5] measured rates for vibrationally elastic j-changing collisions using laser-induced fluorescence (LIF) spectroscopy [14]. The experiment was performed at Lehigh using an optical-optical double resonance technique.

The experimental method is illustrated schematically in Fig. 1.2(a). First, a pump laser excites the NaK molecules from the ground state to a ro-vibrational level of the $A^1\Sigma^+$ excited state called the "directly pumped" level. Then a weak probe laser is scanned through the frequencies that correspond to excitation of the pumped level to another ro-vibrational level of a higher electronic state. The violet fluorescence from the decay of the higher electronic state is monitored as a function of the probe laser frequency (excitation scan). Strong signals (called direct lines) are observed at frequencies corresponding to specific transitions. Rotationally inelastic collisions may also occur while NaK is in the $A^1\Sigma^+$ state, as indicated by the curved arrows. The probe laser can also excite the collisionally populated levels, leading to weaker "satellite" or "collisional" lines in the spectra.

Figure 1.2(b) shows examples of the observed excitation scans. The top and bottom traces show total fluorescence versus probe laser frequency showing the effects of collisions of NaK with He and Ar, respectively. The large peaks (which actually go far off scale) at approximately 12446 cm^{-1} correspond to direct lines and the peaks labeled by $\pm 1, \pm 2, \ldots$ are the collisional lines corresponding to collisionally induced transitions with those values of Δj. The peaks associated with even values of Δj are generally larger than those associated with odd Δj. The spectra show a propensity for vibrationally elastic collisions with He or Ar to change j by an even Δj.

The measurements of Wolfe *et al.* [4] used argon as the buffer gas and initial state $A^1\Sigma^+(v = 16, j = 30)$. These were extended by Jones [5] to study helium collisions, other initial states, and also NaCs + He or Ar collisions. Jones [5] and

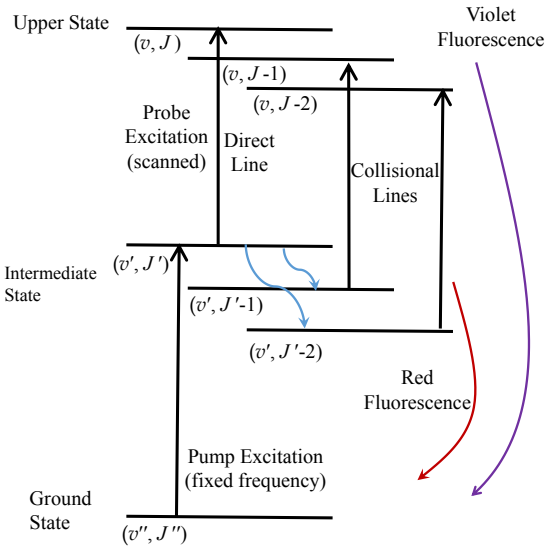

(a)

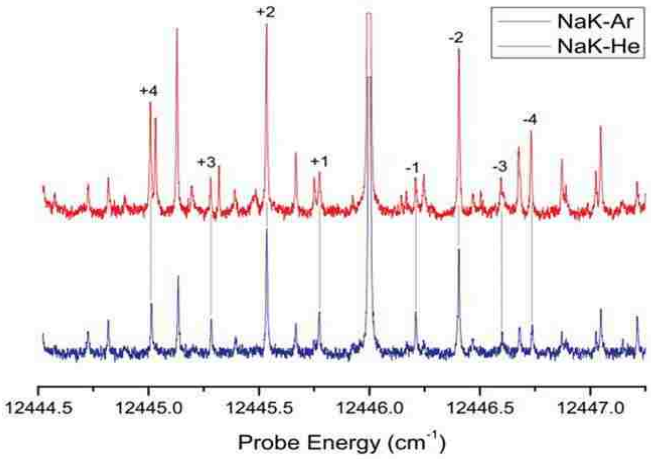

(b)

Figure 1.2: Panel (a) shows the optical-optical double resonance scheme used at Lehigh [5]. Panel (b) shows excitation scans for NaK $[A\,^1\Sigma^+(v = 16, j = 30)]$ with argon and helium perturbers [13].

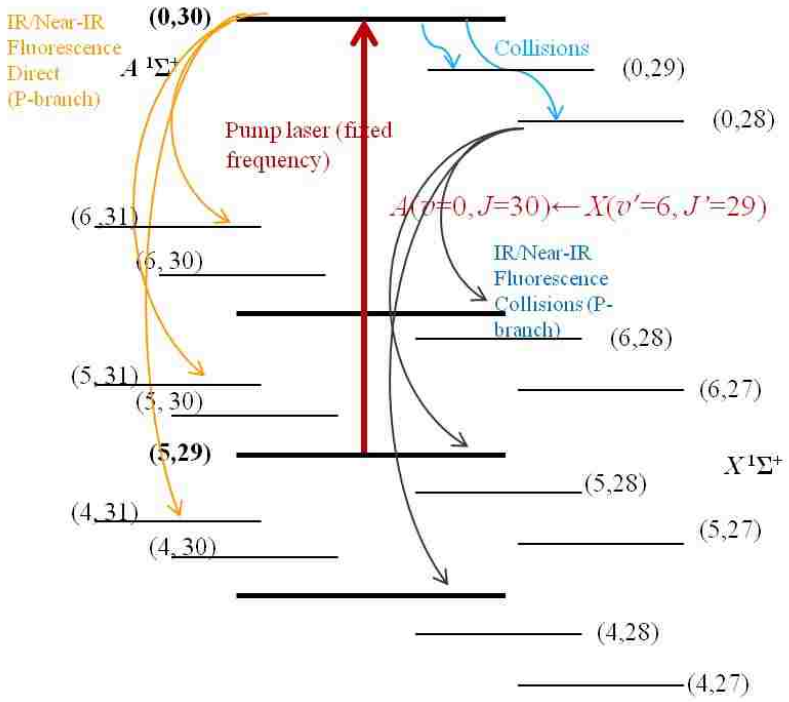

Figure 1.3: Fluorescence spectroscopy technique used in Lyon. The radiative transitions from the A state to the ground state satisfy the selection rule $\Delta j = \pm 1$. Only the transitions with $\Delta j = +1$ (P lines) are shown in the figure.

Richter [6] determined rates for j- and v-changing collisions at low initial v $(= 0, 1, 2)$ using Fourier transform spectroscopy [15]. This latter experiment was performed at Université Lyon 1 using a single-step excitation scheme.

The experimental method used in Lyon is illustrated in Fig. 1.3. A pump laser excites the NaK molecules to the directly pumped level (v, j) in the $A^1\Sigma^+$ state. Collisions with He or Ar can transfer population to neighboring levels (v', j') in the A state. A few such transitions are represented by blue arrows in Fig. 1.3. Radiative transitions from the directly pumped level and from the collisionally populated levels to the ground state are labelled "Fluorescence Direct" and "Fluorescence Collisions", respectively. The fluorescence from all levels of the A state to many different levels of the ground state is analyzed by a Fourier Transform Spectrometer (FTS), which provides the intensity of the fluorescence as a function of frequency.

The observed spectra are similar to those shown in Fig. 1.2(b) but exhibit weak lines not seen at Lehigh corresponding to much larger values of Δj and to vibrationally inelastic collisions. The weak lines imply that rates for v-changing collisions are an order of magnitude less than for j-changing collisions. The weaker lines can be resolved because the FTS collects fluorescence from all transitions simultaneously, eliminating issues related to the frequency drift of the laser. This feature allows for longer collection times than at Lehigh and therefore a higher signal-to-noise ratio.

Richter [6] used ratios of line intensities to extract rates for collisionally induced transitions within the A state. For vibrationally elastic collisions, the data show a propensity for collisions to change j by an even Δj. For vibrationally inelastic collisions, this propensity is absent.

1.2.2 Polarization labeling spectroscopy

Wolfe *et al.* [4] and Jones [5] also obtained information about m-changing collisions using polarization labeling (PL) spectroscopy [16] at Lehigh. First, they prepared an ensemble of molecules in the same rovibrational level such that the average value of m for the ensemble was not zero (as it would be if all m-values were equally populated). Then, they measured the average value of m' for those molecules that underwent a collisionally induced transition to the level (v, j'). The change in the average value of m provided information about the degree to which collisions mixed the values of m.

In the PL experiment they again used an OODR technique [14], but this time selection rules related to the polarization of the laser beams were exploited. Figs. 1.4(a) and 1.4(b) illustrate the method. Figure 1.4(a) shows the optical transitions involved. First, a circularly polarized pump laser excites NaK molecules from the ground state (also called the X state) to the directly pumped level (v, j) in the $A\,^1\Sigma^+$ state. For circularly polarized light, there is a selection rule for $\Delta m = \pm 1$, depending on the helicity. When the probe laser is on resonance, it creates a non-uniform distribution of m levels in the ground and A states, as illustrated in Fig. 1.4(b). The lower and upper horizontal lines represent the j levels of the initial (X) electronic

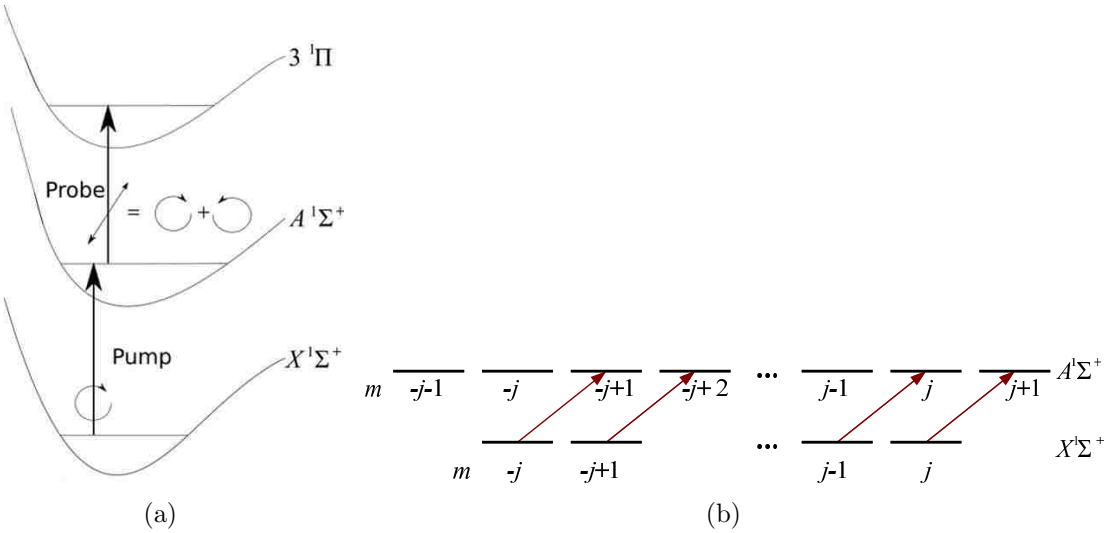

Figure 1.4: Panel (a) shows the polarization spectroscopy technique. Panel (b) shows a schematic of m-changing transitions caused by the pump laser.

state and the intermediate (A) state, respectively. The diagonal arrows represent transitions allowed by the selection rule for right circular polarization. One can see that the distribution of m levels in the A state will be weighted toward larger values of m. This distribution can be interpreted as an average "orientation" of the angular momentum vectors **j** of the molecules.

The second transition in Fig. 1.4(a) is driven by a weak linearly polarized probe laser. The linear polarization can be thought of as equal parts left and right circularly polarized light with respect to the propagation axis of the laser. When the scanned probe laser is tuned to an available transition to the upper $3\,^1\Pi$ electronic state, these two components will be unequally absorbed because of the non-uniform distribution of m levels created by the pump. The unequal absorption of the two components causes the transmitted probe beam to pick up a slight elliptical polarization. The uneven absorption can be detected by passing the probe beam through a polarizer oriented 90° to the probe's initial polarization. When the probe is off-resonance, it is completely blocked by the crossed polarizer. On resonance,

the strength of the light passing through the second polarizer is related to the orientation or average value of m of the ensemble. Comparing the strength of the transmitted probe for the direct lines (no collisions) and for satellite lines (for which a j-changing collision has taken place) provides information about the average value of m before and after collisions.

Wolfe *et al.* [4] performed measurements with argon perturbers and Jones [5] extended the experiments to include both helium and argon perturbers. Jones' [5] analysis incorporated the measurements made by Wolfe *et al.* [4] and he found argon was more likely to destroy orientation than helium.

1.3 Overview of dissertation

In this dissertation we will describe a series of calculations designed to model the collisions in Eq. 1.1. These calculations reproduce the main features of the experimental results and provide insight into these results. We also describe the semiclassical model we developed to investigate the approximate conservation of the polar angle θ in rotationally inelastic collisions.

Scattering calculations such as those performed here generally consist of two parts. First, one calculates a potential surface that determines the motion of the nuclei. Then one uses this surface in a dynamics calculation that provides the desired cross sections or rate constants.

Chapter 2 provides an overview of the theory behind the calculations. Our calculations were performed within the Born-Oppenheimer approximation, which is described in Section 2.1. We determined potential energy surfaces using techniques outlined in Section 2.2 and using the long-range analytic form of the potentials discussed in Section 2.3. We used these surfaces to carry out fully quantum mechanical scattering calculations using the Arthurs and Dalgarno formalism [17], which is summarized in Section 2.4. We discuss the theory related to m-changing collisions in Section 2.5.

In Chapter 3 we describe the calculation of our HeNaK and ArNaK potentials.

We show our potential surfaces in Section 3.1 and make some comparisons with experiment. In Section 3.3, we describe our fits to the analytic long-range potential.

Chapter 4 concerns the results of our scattering calculations. In Section 4.2, we report the results obtained with the calculated potentials and compare these results with experiment. Then in Section 4.4, we discuss how the propensity for Δj even transitions was affected by changes we made to the potentials, and we develop a model that provides insight into the origin of the propensity.

Chapter 5 reports the semiclassical model we developed for m-changing collisions. Sections 5.1–5.3 introduce the model and compare the results with quantum mechanical calculations. For both the semiclassical and quantum mechanical results, we predict a propensity to conserve the polar angle $\theta = \cos^{-1}\left(m/\sqrt{j(j+1)}\right)$ of the rotational angular momentum of NaK ($A\,^1\Sigma^+$) in collisions with He or Ar. In Section 5.4, we identify two special cases of our semiclassical model that allow analytic approximations. Collisions of He and Ar with NaK are often well described by one of those special cases.

Finally, in Chapter 6 we present concluding remarks and ideas for future projects.

Chapter 2

Theory

2.1 Born-Oppenheimer approximation

Our calculations are based on the Born-Oppenheimer approximation, which uncouples the electronic and nuclear motions of He-NaK or Ar-NaK [18]. All forces are determined by the potential for He or Ar plus NaK ($A\,^1\Sigma^+$), enabling us to perform what would otherwise be intractable dynamics calculations. In this section, we summarize the Born-Oppenheimer approximation and derive the equations for nuclear motion.

The He-NaK and Ar-NaK systems can be thought of as molecules. Like all molecules, they are composed of electrons and nuclei. Unless the nuclear kinetic energy of the molecule is extremely high, the electrons move much faster than the nuclei, because they are much lighter. Therefore the typical picture is that the wave function of the electrons in a molecule can adjust very quickly to the instantaneous position of the nuclei. The analysis leading to the Born-Oppenheimer approximation provides a framework for this physical picture. The result is that the electronic energy depends only on the nuclear positions, and the nuclei move in a potential determined by the electronic energy [18]. The Born-Oppenheimer approximation allows us to determine our potentials by calculating the electronic energies of the

HeNaK or ArNaK molecules as a function of the positions of fixed nuclei, as described in Section 2.2.

Here we'll follow the approach of Born [19] and Born and Huang [20] to derive the equations for nuclear motion and to indicate explicitly the terms that are often neglected. Although this approach is standard, and the approximation has been around a long time, some of the mathematical subtleties are still under investigation [21].

We start by defining the Hamiltonian for a molecule. Let the nuclei be labeled by Roman subscripts $(a, b, c, \ldots)$ and the electrons by Greek subscripts $(\alpha, \beta, \gamma \ldots)$. Additionally, let the nuclei and electrons have positions $\mathbf{R}_a$ and $\mathbf{r}_\alpha$, respectively, relative to some coordinate system. For simplicity, we assume there are no external fields and neglect magnetic interactions. Then the Hamiltonian for the molecule is

$$\hat{H} = -\frac{\hbar^2}{2}\sum_a \frac{\nabla_a^2}{M_a} - \frac{\hbar^2}{2m}\sum_\alpha \nabla_\alpha^2 - \sum_{a,\alpha}\frac{kZ_a e^2}{|\mathbf{R}_a - \mathbf{r}_\alpha|} + \sum_{\alpha<\beta}\frac{ke^2}{|\mathbf{r}_\beta - \mathbf{r}_\alpha|} + \sum_{a<b}\frac{kZ_b Z_a e^2}{|\mathbf{R}_b - \mathbf{R}_a|}, \tag{2.1}$$

where $k = 1/(4\pi\epsilon_0)$ is Coulomb's constant, M_a denotes the mass of nucleus a, and m is the electron's mass. The first two terms in the equation are the kinetic energy operators of the nuclei and electrons, respectively. The remaining three terms give the potential energy operator. These terms correspond to attraction between nuclei and electrons, repulsion between electrons, and repulsion between nuclei.

For our calculations, we solve the non-relativistic, time-independent Schrodinger equation,

$$\hat{H}\Psi = E\Psi. \tag{2.2}$$

The standard approach starts by expanding the wave function Ψ in a complete set of known states, which can in principle be obtained by solving the simpler problem in which the nuclei are stationary. The Hamiltonian for the simpler system, called the electronic Hamiltonian, is the full Hamiltonian in Eq. 2.1, except for the nuclear kinetic operator:

$$\hat{H}_\mathrm{e} = -\frac{\hbar^2}{2m}\sum_\alpha \nabla_\alpha^2 - \sum_{a,\alpha}\frac{kZ_a e^2}{|\mathbf{R}_a - \mathbf{r}_\alpha|} + \sum_{\alpha<\beta}\frac{ke^2}{|\mathbf{r}_\beta - \mathbf{r}_\alpha|} + \sum_{a<b}\frac{kZ_b Z_a e^2}{|\mathbf{R}_b - \mathbf{R}_a|}. \tag{2.3}$$

Section 2.2 outlines methods to find approximate solutions ψ_k and eigenvalues $E_{e,k}$ to the Schrodinger equation involving the electronic Hamiltonian,

$$\hat{H}_e \psi_k(\mathfrak{r};\mathfrak{R}) = E_{e,k}(\mathfrak{R})\psi_k(\mathfrak{r};\mathfrak{R}). \tag{2.4}$$

In this equation, $\mathfrak{R}$ is a set of fixed nuclear positions, $\mathfrak{r}$ is the set of electron positions, and $E_{e,k}$ and ψ_k depend parametrically on $\mathfrak{R}$. The ψ_k form a complete basis set. We assume they are normalized for each nuclear configuration $\mathfrak{R}$, and that each ψ_k is a continuous, differentiable function of $\mathfrak{R}$.

Since the ψ_k form a complete basis set for each $\mathfrak{R}$, the wave function for the system Ψ can be written exactly as a sum over the eigenfunctions ψ_k (or integral for continuum states):

$$\Psi(\mathfrak{r},\mathfrak{R}) = \sum_k F_k(\mathfrak{R})\psi_k(\mathfrak{r};\mathfrak{R}), \tag{2.5}$$

where $F_k(\mathfrak{R})$ is an expansion coefficient. Note that we are not actually assuming that the nuclei are stationary. We are simply expanding a wave function in a complete set of well-defined states.

By substituting Eq. 2.5 into Eq. 2.2, we can derive the following Schrodinger equation for the system:

$$-\frac{\hbar^2}{2}\sum_{a,k}\frac{1}{M_a}\left[\psi_k(\mathfrak{r};\mathfrak{R})\nabla_a^2 F_k(\mathfrak{R}) + F_k(\mathfrak{R})\nabla_a^2\psi_k(\mathfrak{r};\mathfrak{R}) + 2\nabla_a F_k(\mathfrak{R})\cdot\nabla_a\psi_k(\mathfrak{r};\mathfrak{R})\right] + \sum_k \left(E_{e,k}(\mathfrak{R}) - E\right)F_k(\mathfrak{R})\psi_k(\mathfrak{r};\mathfrak{R}) = 0, \tag{2.6}$$

By multiplying on the left by $\psi^*_{k'}$ and integrating over the electronic coordinates, we obtain a set of coupled differential equations for the nuclear functions F_k:

$$\left(-\frac{\hbar^2}{2}\sum_a\frac{\nabla_a^2}{M_a} + E_{e,k'}(\mathfrak{R}) - E\right)F_{k'}(\mathfrak{R}) - \frac{\hbar^2}{2}\sum_a\frac{1}{M_a}\int\psi^*_{k'}(\mathfrak{r};\mathfrak{R})\sum_k\left(F_k(\mathfrak{R})\nabla_a^2\psi_k(\mathfrak{r};\mathfrak{R}) + 2\nabla_a F_k(\mathfrak{R})\cdot\nabla_a\psi_k(\mathfrak{r};\mathfrak{R})\right)d\mathfrak{r} = 0. \tag{2.7}$$

The coupling terms on the second line of Eq. 2.7 indicate that the solution for any $F_{k'}$ depends on all the other F_k as well as on the derivatives of the electronic functions ψ_k with respect to the nuclear coordinates. If these terms could be dropped, the equations would become uncoupled and greatly simplified. The Born-Oppenheimer approximation amounts to neglecting these terms and is justified whenever the electronic functions ψ_k vary slowly with the nuclear coordinates. In fact, as will be discussed below, even when the coupling terms are not negligible, their influence is small when the electronic states are separated by a large gap [20], and this approximation can still be applied. When it applies, the Born-Oppenheimer approximation reduces Eq. 2.7 to a set of uncoupled equations for the nuclear wave functions $F_k(\mathfrak{R})$,

$$\left(-\frac{\hbar^2}{2}\sum_a \frac{\nabla_a^2}{M_a} + E_{\mathrm{e},k}(\mathfrak{R}) - E\right) F_k(\mathfrak{R}) = 0. \tag{2.8}$$

The electronic energies provide a potential in which the nuclei move, and the total wave function for the k^{th} electronic state is

$$\Psi_k(\mathfrak{r},\mathfrak{R}) = F_k(\mathfrak{R})\psi_k(\mathfrak{r};\mathfrak{R}), \tag{2.9}$$

so we can regard the expansion coefficient $F_k(\mathfrak{R})$ as a nuclear wave function.

The Born-Oppenheimer approximation is valid in many important cases, but it is not justified when the electronic state of interest is degenerate or quasi-degenerate. For example, two electronic states must often be included near an avoided crossing [22]. Conversely, when the energy gaps are large, the coupling terms have little influence even if they are not very small, extending the applicability of this approximation [20].

An alternative analysis of Morrison *et al.* [23] leads to the conclusions mentioned above. Rather than assuming that the coupled terms are small, as in perturbation theory, Morrison *et al.* started with a series expansion of Ψ and E. The leading term of the series expansion is $\Psi(\mathfrak{r},\mathfrak{R}) = F(\mathfrak{R})\psi(\mathfrak{r};\mathfrak{R})$, the result of the Born-Oppenheimer approximation. The first-order correction to the molecular wave function is a sum of terms directly proportional to the coupling terms and inversely proportional to the difference in total energy E between the state of interest Ψ_k and

another state $\Psi_{k'}$. If this first-order correction is small, we can assume the leading term (the Born-Oppenheimer approximation) is a good approximation. This analysis allows us to roughly say that the Born-Oppenheimer approximation is not valid when the electronic states are degenerate or quasi-degenerate, and that it is valid when the electronic states are very well separated.

For He-NaK and Ar-NaK, we expect the coupling terms to be negligible based on mass ratios and on the separation of our electronic state from the others. Let m be the electron mass and M be the total mass of the system. Then for He-NaK, $(m/M) \approx 8.3 \times 10^{-6}$, and for Ar-NaK it's even smaller. Furthermore, we are interested in the electronic state that corresponds asymptotically to He or Ar ($^1S_0$) + NaK ($A\,^1\Sigma^+$). The atomic states are well separated, and so are the singlet states of NaK for most internuclear separations, as can be seen in Fig. 1.1, so we expect that our electronic state is nondegenerate and that it is well separated from the other electronic states. (Note that our calculations neglect fine-structure effects [24].)

In the next two sections we will describe methods for calculating the intermolecular potential. Then in Section 2.4 we show how we use Eq. 2.8 to perform scattering calculations.

2.2 Electronic structure calculations

In this section we will summarize the methods used to calculate approximate solutions of the electronic Schrodinger equation (Eq. 2.4) and to provide potential energy surfaces (PESs) for our scattering calculations. The development of these methods is described in a historical context in [25], and additional details are provided in [26–32].

2.2.1 Formation of the molecular orbitals and Slater determinants

The starting point for calculating an approximate electronic wave function ψ^{approx} for a many-electron molecule is to define a set of single-electron wave functions called molecular orbitals (MOs). In analogy to the simple shell model of a many-electron atom, one assumes that up to two electrons may occupy each MO. Then one can construct an approximate many-electron wave function using a Slater determinant (or linear combinations of them).

For a molecule, a spin orbital is an MO that describes both an electron's spin and its spatial probability and amplitude distribution. It is defined to be a product of a spin function and a spatial orbital $\phi(\mathbf{r}_\alpha)$. The spin function, which depends on a spin coordinate ω, is either $\alpha(\omega)$ if the electron is spin up or $\beta(\omega)$ if the electron is spin down. We will let the variable $\mathbf{x}_\alpha$ denote the combined space and spin coordinates $(\mathbf{r}_\alpha, \omega)$. Then for a given spatial orbital ϕ_k, one can form two possible spin orbitals:

$$\chi_{2k-1}(\mathbf{x}_\alpha) = \phi_k(\mathbf{r}_\alpha)\alpha(\omega) \tag{2.10}$$

$$\chi_{2k}(\mathbf{x}_\alpha) = \phi_k(\mathbf{r}_\alpha)\beta(\omega). \tag{2.11}$$

The Slater determinant is defined in terms of the spin orbitals. We consider here the restricted closed-shell case in which N is even and $N/2$ spatial MOs are doubly occupied by electrons of opposite spin. Then the Slater determinant is

$$\mathcal{D}_0 = \frac{1}{\sqrt{N!}} \begin{vmatrix} \chi_1(1) & \chi_2(1) & \cdots & \chi_N(1) \\ \chi_1(2) & \chi_2(2) & \cdots & \chi_N(2) \\ \vdots & \vdots & & \vdots \\ \chi_1(N) & \chi_2(N) & \cdots & \chi_N(N) \end{vmatrix}, \tag{2.12}$$

where $\chi_k(m)$ is shorthand for $\chi_k(\mathbf{x}_m)$. The Slater determinant form of the electronic wave function maintains the indistinguishability of the electrons. It is also antisymmetric under exchange of the space and spin coordinates of two electrons, as a wave function for indistinguishible fermions must be. An antisymmetric wave function automatically satisfies the Pauli exclusion principle.

The Slater determinant will be used as an approximate electronic wave function in Section 2.2.3, and linear combinations of different Slater determinants will be used to construct approximate electronic wave functions in Sections 2.2.4 and 2.2.5.

For the remainder of this section we discuss how the spatial parts of the spin orbitals are determined. It is advantageous to expand the spatial orbitals in a known set of states, or basis. In principle, for a complete set of states a spatial orbital $\phi_k(\mathbf{r}_\alpha)$ can be written exactly as a linear combination of the basis functions, $\varphi_i(\mathbf{r}_\alpha)$,

$$\phi_k(\mathbf{r}_\alpha) = \sum_i C_{ki}\varphi_i(\mathbf{r}_\alpha). \tag{2.13}$$

In practice, one must truncate the infinite sum to a finite set of basis functions. Selecting the finite basis set requires judgement to balance the accuracy of the molecular orbitals and the computational resources the calculation will require. Once the basis set is selected, one can determine the optimal set of coefficients C_{ki} using methods described later in this chapter.

Each basis function is centered on a specific nucleus and has a simple analytic form. Here we summarize several forms that have been widely used. The first is the Slater-type orbital (STO), which has the form

$$s(\xi, \mathbf{r}_\alpha - \mathbf{R}_p) = P(x, y, z)e^{-\xi|\mathbf{r}_\alpha - \mathbf{R}_p|} \tag{2.14}$$

where x, y, and z are the cartesian coordinates of $\mathbf{r}_\alpha - \mathbf{R}_p$, $P(x, y, z)$ is a polynomial that depends on the angular momentum of the atomic orbital, and $\mathbf{R}_p$ is the position of nucleus p.

STOs are appealing because they can represent hydrogenic orbitals exactly and have the correct asymptotic behavior for any electron far from an ionic core. Most calculations, however, use an alternative form called the gaussian-type orbital (GTO):

$$g(\beta, \mathbf{r}_\alpha - \mathbf{R}_p) = P(x, y, z)e^{-\beta|\mathbf{r}_\alpha - \mathbf{R}_p|^2}. \tag{2.15}$$

The preference for GTOs arises because much of the computational effort to solve the electronic Schrodinger equation (Eq. 2.4) requires evaluating integrals. For large molecules, the integrals can involve as many as four basis functions centered on four

different atoms. These integrals can be done analytically with GTOs, but not with STOs.

The asymptotic behavior of GTOs is less satisfactory than that of STOs because the Gaussian exponential falls off very rapidly. This shortcoming can be offset, however, by writing each basis function as a linear combination of "primitive" GTOs called a contraction. A basis function φ that is a contraction of primitive Gaussian functions g centered on nucleus p is written as

$$\varphi(\mathbf{r}_\alpha) = \sum_{k=1}^{S} d_k g_k(\beta_k, \mathbf{r}_\alpha - \mathbf{R}_p). \tag{2.16}$$

The upper limit of the sum S is called the contraction length, the coefficients d_k are called contraction coefficients, and the Gaussian orbital exponents β_k are called contraction exponents. By optimizing S, the d_k, and the β_k, one can improve the asymptotic behavior of the basis function.

Many different types of basis sets have been developed. To illustrate the considerations involved in selecting one, we discuss several popular examples developed by Pople and collaborators [25].

In the minimal (the smallest) basis set, each basis function φ_i corresponds to an occupied atomic orbital of one of the atoms in the molecule. For example, in the STO-3G basis, each atomic orbital is represented by a contraction of three GTOs designed to approximate the best STO for that orbital. This basis set may also include contracted GTOs to represent orbitals occupied in excited states. Since each atomic orbital is described by one fixed basis function, this basis provides limited flexibility for the wave function of one atom to respond to the positions of the other atoms.

Larger basis sets provide greater flexibility. In double-zeta or triple-zeta basis sets, there are two or three basis functions per atomic orbital, respectively. Split-valence basis sets use one basis function per core atomic orbital and more for the valence orbitals. For example, the split-valence 6-31G basis [33–36] uses contractions of 6 GTOs for each core orbital, and each valence basis function consists of a contraction of 3 GTOs and an uncontracted GTO. With such a basis, the coefficients

in the linear combination of valence basis functions can change when other atoms are nearby.

Polarization basis functions allow the electron charge density within a molecule to deform in response to intramolecular or external electric fields. One basis set which includes these functions is the 6-31G** basis [37], where $(**)$ indicates the addition of a set of uncontracted p-functions to hydrogen atoms and a set of uncontracted d-functions to non-hydrogen atoms. The p-functions centered on hydrogen allow it to have an induced dipole moment within the molecule, and the d-functions centered on non-hydrogen atoms allow them to have induced quadrupole moments within the molecule.

Diffuse functions are used for electrons that can be found far from the nucleus. They are uncontracted Gaussians with small exponents. If they are included for non-hydrogen atoms in a Pople basis set, then a "+" is added to the name of the basis set, as in 6-31+G**. If they are also included for hydrogen atoms, then a "++" is added.

Chapter 3 gives more details of the specific calculations we performed for HeNaK and ArNaK, including the basis sets used.

2.2.2 Variational principle

The variational principle underlies many methods for finding approximate solutions to the electronic Schrodinger equation. The principle is that for any trial function ψ^{trial}, the expectation value of a system's Hamiltonian for ψ^{trial} is an upper bound to the exact ground-state energy. This principle can be proved in the following way.

The orthonormalized eigenfunctions ψ_k^{exact} of the Hamiltonian constitute a complete set of states, so any approximate wave function ψ^{trial} can be expanded as

$$\psi^{\text{trial}} = \sum_k a_k \psi_k^{\text{exact}}. \tag{2.17}$$

Then the approximate energy E^{trial} is

$$E^{\text{trial}} = \frac{\int \left(\psi^{\text{trial}}\right)^* \hat{H} \psi^{\text{trial}} \, d\tau}{\int \left(\psi^{\text{trial}}\right)^* \psi^{\text{trial}} \, d\tau} \tag{2.18}$$

$$= \frac{\sum_k E_k^{\text{exact}} \left|a_k\right|^2}{\sum_k \left|a_k\right|^2}, \tag{2.19}$$

where the integrals are carried out over the relevant coordinates τ. Subtracting the exact ground state energy from both sides of Eq. 2.19, one obtains

$$E^{\text{trial}} - E_0^{\text{exact}} = \frac{\sum_k \left(E_k^{\text{exact}} - E_0^{\text{exact}}\right) \left|a_k\right|^2}{\sum_k \left|a_k\right|^2}. \tag{2.20}$$

Since $\left(E_k^{\text{exact}} - E_0^{\text{exact}}\right)$ and $\left|a_k\right|^2$ are both greater than or equal to zero for all k,

$$E^{\text{trial}} \geq E_0^{\text{exact}}, \tag{2.21}$$

with equality if and only if $\psi^{\text{trial}} = \psi_0^{\text{exact}}$.

The variational method is implemented by specifying a form for the trial function that depends on a set of adjustable parameters and by varying the parameters to minimize E^{trial}. The minimum value of E^{trial} is the variational estimate for the exact energy. The parameters are intended to give the trial function the flexibility to represent a likely form for the wave function based on physical or chemical intuition, so that E^{trial} is as low as possible. E^{trial} is lowest when the trial function is the exact wave function. Although one does not know the exact wave function, the accuracy of the trial function can be assessed by using it to calculate known properties of the system.

The linear variational method is a special case of the variational method. It is used when ψ^{trial} is a linear combination of Q linearly independent, square integrable known functions f_i,

$$\psi_k^{\text{trial}} = \sum_{i=1}^{Q} c_{ki} f_i. \tag{2.22}$$

The linear variational method involves diagonalizing a matrix. When the f_i are orthonormal, this matrix is composed of elements H_{ij}, where:

$$H_{ij} = \int f_i^* \hat{H} f_j d\tau. \tag{2.23}$$

The lowest eigenvalue gives the upper bound to the ground state energy, and the corresponding eigenvector gives the expansion coefficients of the ground-state trial function. One also obtains the eigenvalues for the next $(Q-1)$ excited states, and these are upper limits to the exact excited state energies [38]. The corresponding eigenvectors are the excited-state trial functions.

When the trial function is the exact wave function, $E^{\text{trial}} - E^{\text{exact}}$ is zero. For this reason, we assume that the lower the minimum value of E^{trial}, the "better" the form of the trial function, even though a trial function with a lower minimum value of E^{trial} might actually give worse results for some molecular properties than a trial function of a different form with a higher minimum value of E^{trial} [39].

For electronic energies, the difference $E_k^{\text{trial}}(\mathfrak{R}) - E_k^{\text{exact}}(\mathfrak{R})$ may not be the same for each nuclear configuration $\mathfrak{R}$. This can introduce an error in the relative energies at two nuclear geometries $\mathfrak{R}_1$ and $\mathfrak{R}_2$. This error could increase even when the individual energies are lowered [39], so "better" trial functions do not always imply "better" relative energies. Of course, in the limit that the trial function is exact for all nuclear configurations $\mathfrak{R}$, the energy differences will be exact. Therefore it's important to choose a trial wave function that is appropriate for all $\mathfrak{R}$ involved in the calculation.

2.2.3 Hartree-Fock approximation

This section discusses the variational Hartree-Fock method and its application to closed-shell systems. In this special case, the number of electrons N is even, and each spatial orbital is doubly occupied by electrons with opposite spins. The trial function is a single Slater determinant:

$$\psi^{\text{HF}} = \mathcal{D}_0. \tag{2.24}$$

With this form of the wave function, one can variationally determine an approximate ground state energy for Eq. 2.4. To apply the method, one selects a basis set composed of $K \geq N/2$ basis functions. The variational parameters are the expansion coefficients C_{ki} of the spatial molecular orbitals (cf. Eq. 2.13). The optimal parameters (and therefore the optimal spatial MOs) are found by an iterative method [40]. The $N/2$ orbitals with the lowest energies are doubly occupied and are used in the final ground state wave function, Eq. 2.24. The other orbitals are unoccupied, and can be used to generate other Slater determinants that will be useful in the next sections. In the Hartree-Fock limit, the basis set is considered to be a complete set, and E_0^{HF} attains its lowest possible value for this form of the wave function.

The optimal MOs determine the trial function ψ^{HF} for which the expectation value of the electronic Hamiltonian, E_0^{HF}, is a minimum; this trial function is an approximate solution of the electronic Hamiltonian. It can be shown that the trial function ψ^{HF} is the exact solution to a simpler Hamiltonian, for which each electron experiences an average field due to the other electrons [26].

The iterative procedure for solving for the optimal MOs is called the Self-Consistent Field (SCF) method, and the nomenclature reflects the physical interpretation of the method. The SCF method starts with an initial guess for the MOs of the electrons. These MOs determine the charge density and average electrostatic field felt by the electrons. Then one calculates the MOs for electrons in that field. If the MOs are different from those specified in the initial guess, the process is repeated. The process ends when the results are self-consistent, and the effective field which produced the charge density is consistent with the field which would be calculated from the charge density.

2.2.4 Configuration Interaction methods

Often a wave function more accurate than ψ^{HF} is needed. The Hartree-Fock method neglects most electron correlation, which is the tendency for two electrons to avoid

each other. Moreover, when a closed shell molecule dissociates into open-shell fragments, the Hartree-Fock method leads to a trial function that is qualitatively incorrect for any $\mathfrak{R}$ near the dissociation limit. In order to treat such effects, the trial function is generalized to be a linear combination of Slater determinants $\mathcal{D}_i$:

$$\psi^{\text{trial}} = \sum_i c_i \mathcal{D}_i \tag{2.25}$$

In the Configuration Interaction (CI) method, the linear expansion coefficients c_i are obtained variationally and the orbitals contained in $\mathcal{D}_i$ are fixed. For example, the Single-Reference CI (SRCI) method starts with the Hartree-Fock (or an arbitrary) "reference" Slater determinant $\mathcal{D}_0$. Additional Slater determinants are constructed by promoting electrons from the occupied orbitals in the reference determinant to unoccupied orbitals.

If one promotes an electron from an occupied spin orbital χ_a to an unoccupied orbital χ_r, then χ_r appears in the Slater determinant rather than χ_a. We'll denote such a determinant as $\mathcal{D}_a^r$. Similarly, if one promotes two electrons from two occupied spin orbitals χ_a and χ_b to two unoccupied spin orbitals χ_r and χ_s, we obtain the determinant $\mathcal{D}_{ab}^{rs}$. Triple and higher excitations can be defined in a similar manner. The SRCI trial wave function ψ^{SRCI} is written as a linear combination of the reference and the additional determinants:

$$\psi^{\text{SRCI}} = c_0 \mathcal{D}_0 + \sum_{ar} c_a^r \mathcal{D}_a^r + \sum_{a<b,r<s} c_{ab}^{rs} \mathcal{D}_{ab}^{rs} + \ldots, \tag{2.26}$$

where the c's are the coefficients in the linear combination. The SRCI method constitutes a linear variational problem; the solution is determined by a matrix diagonalization.

Often one uses linear combinations of Slater determinants that are eigenfunctions of the total spin operator $\mathcal{S}^2$; these linear combinations are called spin-adapted Configuration State Functions (CSFs). In that case the trial function is a linear combination of CSFs rather than determinants, and the coefficients are still determined by the linear variational method.

In principle, the accuracy achievable for ground and excited state energies using the trial function in Eq. 2.26 is limited only by the amount of computer resources

available. In practice, one usually truncates the expansion in Eq. 2.26 and retains only certain excitations from the reference determinant. For example, only single and double (SD) excitations are included in the SR-CISD method. That method can provide excellent results for the ground state, but may be unreliable for excited states or for certain nuclear configurations $\mathfrak{R}$ of a closed-shell molecule that dissociates into open-shell fragments.

To amend the situation, one can perform a multiconfiguration SCF (MCSCF) calculation [29, 30] to determine MOs that give better results for excited state energies or energies for which the Hartree-Fock reference determinant is qualitatively incorrect. Like the CI method, the MCSCF method is variational and the MCSCF trial wave function ψ^{MCSCF} is a linear combination of determinants:

$$\psi^{\mathrm{MCSCF}} = \sum_i c_i \mathcal{D}_i. \tag{2.27}$$

The MCSCF trial function typically involves a smaller number of determinants than a CI trial function. This is because unlike a CI calculation an MCSCF calculation involves varying the coefficients of the orbitals contained in $\mathcal{D}_i$ and the linear expansion coefficients c_i simultaneously. One can choose a state averaging approach where the orbitals are optimized for multiple electronic states rather than one specific state. Energies and expansion coefficients c_i for different electronic states can be obtained.

One type of MCSCF calculation is the Complete Active Space SCF (CAS-SCF) method. This method involves selecting an "active" set of orbitals, usually those occupied by valence electrons and a few low-lying unoccupied orbitals. All possible determinants $\mathcal{D}_i$ (or CSFs) obtained from distributing electrons within the active space are used to construct the trial function ψ^{MCSCF}.

The MCSCF energies incorporate only some correlation and typically are not sufficiently accurate. The MCSCF trial function, however, provides multiple reference determinants with which one can perform a generalized Multireference CI (MRCI) calculation [29] to obtain more accurate energies.

In the MRCI procedure, each determinant (or CSF) obtained in the MCSCF calculation can be used as a reference determinant (or CSF). The computer time

(which is already quite large for SRCI) increases by more than a factor of the number of reference states. The number of terms in a Multireference CI calculation that only include single and double excitations (MR-CISD) can be quite large (millions or more) and so larger systems cannot be treated with this method.

2.2.5 Coupled-Cluster methods

When the MRCI method is too computationally expensive, an attractive alternative is the Equation-of-Motion Coupled-Cluster (EOM-CC) method [31]. In this section we introduce the method using the bra-ket notation.

The EOM-CCSD method is very similar to the SR-CISD method. In the SR-CISD method, one diagonalizes the electronic Hamiltonian in the space spanned by the relevant Slater determinants. In the EOM-CCSD method, one diagonalizes a similarity-transformed electronic Hamiltonian in the same space of Slater determinants. As will be shown below, the similarity-transformed Hamiltonian "folds in" the effect of excitations higher than just singles and doubles. It allows for excitations such as a quadruple excitation that is the product of two double excitations, incorporating the correlation (that is, coupling) between pairs (or clusters) of electrons.

As with the Single-Reference CI method, the Coupled-Cluster method starts with the Hartree-Fock (or an arbitrary) "reference" state $|\mathcal{D}_0\rangle$. Then additional states are constructed by promoting electrons from occupied spin orbitals to unoccupied spin orbitals. The cluster operator $\hat{T} = \sum_{i=1}^{N} \hat{T}_i$ operates on the reference state to promote electrons, with the $\hat{T}_i$ defined as

$$\hat{T}_1 |\mathcal{D}_0\rangle = \sum_{ar} t_a^r |\mathcal{D}_a^r\rangle , \qquad \hat{T}_2 |\mathcal{D}_0\rangle = \sum_{a<b,r<s} t_{ab}^{rs} |\mathcal{D}_{ab}^{rs}\rangle , \qquad \text{etc.} \tag{2.28}$$

The operator $\hat{T}_1$ promotes a single electron to an unoccupied orbital, $\hat{T}_2$ promotes two electrons to two unoccupied orbitals, and so on. The coefficients t will be determined in a manner described below and will be used to transform the electronic Hamiltonian.

To obtain the Coupled-Cluster ground state wave function, one operates on the

reference state with the wave operator $e^{\hat{T}}$:

$$\left|\psi_0^{\mathrm{CC}}\right\rangle = e^{\hat{T}}\left|\mathcal{D}_0\right\rangle = \left(1 + \hat{T} + \frac{\hat{T}^2}{2!} + \cdots\right)\left|\mathcal{D}_0\right\rangle . \tag{2.29}$$

The Taylor expansion of the wave operator shows that it includes such operators as $\hat{T}^2$, which for instance leads to quadruple excitations that are the product of two double excitations.

Now, denote the additional states constructed by promoting electrons from occupied to unoccupied spin orbitals as $\left|\mathcal{D}_{k>0}\right\rangle$, and define a transformed Hamiltonian $\bar{H}_{\mathrm{e}} = e^{-\hat{T}} H_{\mathrm{e}} e^{\hat{T}}$. Then one can derive the following Coupled-Cluster equations:

$$E_{\mathrm{e},0}^{\mathrm{CC}} = \left\langle\mathcal{D}_0\right| \bar{H}_{\mathrm{e}} \left|\mathcal{D}_0\right\rangle \tag{2.30}$$

$$0 = \left\langle\mathcal{D}_{k>0}\right| \bar{H}_{\mathrm{e}} \left|\mathcal{D}_0\right\rangle . \tag{2.31}$$

This nonlinear set of equations is solved iteratively for the parameters t and the ground state energy.

Excited state energies can be obtained starting with the Coupled-Cluster ground state wave function. In the Equation-of-Motion Coupled-Cluster method, one defines an excitation operator $\hat{R} = \sum_{i=0}^{N} \hat{R}_i$ that operates on the reference state (or the Coupled-Cluster ground state), where $\hat{R}_0$, $\hat{R}_1$, etc. are defined as

$$\hat{R}_0\left|\mathcal{D}_0\right\rangle = r_0\left|\mathcal{D}_0\right\rangle , \quad \hat{R}_1\left|\mathcal{D}_0\right\rangle = \sum_{ar} r_a^r \left|\mathcal{D}_a^r\right\rangle , \quad \hat{R}_2\left|\mathcal{D}_0\right\rangle = \sum_{a<b,r<s} r_{ab}^{rs}\left|\mathcal{D}_{ab}^{rs}\right\rangle , \text{ etc} \tag{2.32}$$

relative to the reference state $\mathcal{D}_0$.

To obtain excited states, one applies the excitation operator $\hat{R}$ to the Coupled-Cluster ground state $\left|\psi_0^{\mathrm{CC}}\right\rangle$:

$$\left|\psi_k^{\mathrm{CC}}\right\rangle = \hat{R}\left|\psi_0^{\mathrm{CC}}\right\rangle , \tag{2.33}$$

One can use Eqs. 2.29 and 2.33 and the fact that $\hat{R}$ commutes with $\hat{T}$ to derive the equation for the excited state energies in terms of the Hartree-Fock reference state $\left|\mathcal{D}_0\right\rangle$,

$$\begin{aligned} H_{\mathrm{e}}\left[\hat{R}e^{\hat{T}}\left|\mathcal{D}_0\right\rangle\right] &= E_{\mathrm{e}}^{\mathrm{CC}}\left[\hat{R}e^{\hat{T}}\left|\mathcal{D}_0\right\rangle\right] \\ \left(\bar{H}_{\mathrm{e}} - E_{\mathrm{e}}^{\mathrm{CC}}\right)\hat{R}\left|\mathcal{D}_0\right\rangle &= 0 \end{aligned}$$

The non-Hermitian operator $\bar{H}_{\rm e} = e^{-\hat{T}} H_{\rm e} e^{\hat{T}}$ is then diagonalized to obtain excitation energies. This differs from the SRCI method, for which $H_{\rm e}$ would be diagonalized for the same set of determinants.

EOM-CC is an exact method if one does not truncate $\hat{T}$ or $\hat{R}$, but this is often impractical. When $\hat{T}$ and $\hat{R}$ are truncated such that $\hat{T} \approx \hat{T}_1 + \hat{T}_2$ and $\hat{R} \approx \hat{R}_0 + \hat{R}_1 + \hat{R}_2$, this constitutes the EOM-CCSD approach. The nonlinearity of the wave operator is the reason that the EOM-CCSD results can be superior to the corresponding SR-CISD results; for EOM-CCSD the eigenvalues of $\bar{H}_{\rm e}$ are different from those of $H_{\rm e}$.

Since this is a single-reference technique, its results are not to be trusted in the dissociation limit for open-shell fragments. To obtain better results in that case, one can include noniterative triples corrections [32]. Work is also underway to optimize Multireference Coupled-Cluster calculations [41, 42].

Finally, we note that Coupled-Cluster methods are not variational but they are size consistent. In a size consistent method, the energy of a system of isolated fragments is the sum of the energies of each fragment. Truncated CI is not size consistent. One can make a correction to make the energies size consistent, but then the energies are no longer variational [29].

2.2.6 Counterpoise correction

Electronic structure calculations of a PES may exhibit what is called the Basis Set Superposition Error (BSSE) [43, 44]. This section describes a method for correcting for the BSSE called the Boys-Bernardi counterpoise correction [45]. The procedure assumes that the method used to obtain the PES is size consistent.

Scattering calculations involve the interaction energy between the target (fragment A) and the projectile (fragment B). This interaction energy is the energy of the molecule composed of fragments A and B minus the energy of each isolated fragment. The BSSE can arise when one performs a calculation for the energy of an isolated fragment that only includes the basis functions associated with that fragment.

When the fragments are well separated in the molecule, their basis functions overlap negligibly, and each fragment can only access its own basis functions. The interaction energy, however, is calculated for many $\mathfrak{R}$ for which the fragments are not well separated. Then, the basis functions overlap and one fragment can access the other fragment's basis functions.

If the basis set is not sufficiently complete, fragment B's basis functions provide extra flexibility for fragment A, and the energy of fragment A is different than it would have been if it could only access its own basis functions. The amount by which this energy is different from what it would be if fragment A could only access its own basis functions is the BSSE for fragment A, and it is different for every nuclear configuration $\mathfrak{R}$.

The counterpoise procedure involves calculating the energy of each isolated fragment differently. To calculate the energy of fragment A at a particular $\mathfrak{R}$, one leaves the basis functions for fragment B centered where fragment B would be, but one removes the fragment B. This gives the energy of the isolated fragment A for that $\mathfrak{R}$. Then one does the same thing for fragment B. These two energies are subtracted from the energy of the molecule at a given $\mathfrak{R}$ to correct for BSSE. The resulting interaction energy is the counterpoise corrected energy.

The size of the basis set influences whether this correction should be made or not, because the error due to basis set incompleteness can compensate for the BSSE [44]. For small basis sets, the results are better if one does not correct for BSSE. For medium-sized basis sets, some researchers advocate performing a half-half correction (that is, an average of the uncorrected and counterpoise corrected energies). The BSSE is negligible for larger basis sets and there is no BSSE for a complete basis set.

2.3 Long range potential theory

There are certain nuclear configurations $\mathfrak{R}$ for which one cannot obtain a reliable interaction potential using the methods described in Section 2.2. For large separations

between the target and the projectile, the accuracy of the electronic wave functions is limited by the Gaussian exponential form of the basis functions. Moreover, as mentioned previously, one obtains the interaction energy by subtracting the energies of the isolated fragments A and B from the energy of the molecule composed of A and B at a given $\mathfrak{R}$. These individual energies are reported by quantum chemistry codes with a certain precision, and eventually the interaction energy is within the noise level of the calculation.

Long range potential theory allows one to calculate very small interaction energies. Pack [46] gives a long range analytic form for a system composed of an S-state atom and a Σ-state linear molecule. In this section we will briefly summarize the physical contributions to the long range potential. Then we will introduce the long range analytic form provided by Pack.

2.3.1 Electrostatic, induction, and dispersion interactions

When fragments A and B are far apart, their electrostatic interaction can be considered a perturbation. The long range potential can be derived using perturbation theory as described in detail in [47]. To second order, and neglecting relativistic effects, one obtains the electrostatic, induction, and dispersion interactions summarized in this section.

Assume we have two neutral fragments A and B so far apart that they do not interact. For simplicity, assume they are both in nondegenerate ground electronic states ψ_0^A and ψ_0^B, with corresponding energies E_0^A and E_0^B. Then the electronic wave function is simply $\psi = \psi_0^A \psi_0^B$, and the total energy is $E_0 = E_0^A + E_0^B$.

As the fragments approach each other, one can represent their interaction by an operator $\hat{V}_{\text{int}}$ and obtain the following first and second order corrections to the energy using perturbation theory:

$$E_{\text{e}} = E_0 + \left\langle \psi_0^A \psi_0^B | \hat{V}_{\text{int}} | \psi_0^A \psi_0^B \right\rangle - \sum_{m \text{ or } n \neq 0} \frac{\left| \left\langle \psi_n^A \psi_m^B | \hat{V}_{\text{int}} | \psi_0^A \psi_0^B \right\rangle \right|^2}{(E_n^A - E_0^A) + (E_m^B - E_0^B)}. \tag{2.34}$$

The interaction energy operator $\hat{V}_{\text{int}}$ can be written in powers of $1/R$, where R

is the distance between the centers of masses of the two fragments. The interaction energy operator has the form:

$$\begin{aligned}\hat{V}_{\rm int} &= \frac{1}{R^3}\,(\text{dipole}-\text{dipole interaction}) \\ &+ \frac{1}{R^4}\,(\text{dipole}-\text{quadrupole interaction}) \\ &+ \frac{1}{R^5}\,(\text{quadrupole}-\text{quadrupole interaction}) \\ &+ \frac{1}{R^5}\,(\text{dipole}-\text{octopole interaction}) \\ &+ \cdots\end{aligned} \tag{2.35}$$

Although it has the form of the classical electrostatic interaction energy, $\hat{V}_{\rm int}$ is a quantum mechanical operator. Thus the multipole moments are the expectation values of multipole moment operators. For instance, the permanent dipole moment for fragment A in its ground state is

$$\mu = \left\langle \psi_0^A \left| \hat{\mu} \right| \psi_0^A \right\rangle . \tag{2.36}$$

One only needs an operational definition of the multipole moment operators to interpret the energy corrections.

The first order energy correction is the permanent-permanent multipole moment interaction:

$$W_{\rm el} = \left\langle \psi_0^A \psi_0^B | \hat{V}_{\rm int} | \psi_0^A \psi_0^B \right\rangle \tag{2.37}$$

This term is present when both fragments possess permanent multipole moments.

The induction interaction is the permanent-induced multipole moment interaction:

$$W_{\rm ind} = -\sum_{m\neq 0} \frac{\left| \left\langle \psi_0^A \psi_m^B | \hat{V}_{\rm int} | \psi_0^A \psi_0^B \right\rangle \right|^2}{E_m^B - E_0^B} - \sum_{n\neq 0} \frac{\left| \left\langle \psi_n^A \psi_0^B \left| \hat{V}_{\rm int} \right| \psi_0^A \psi_0^B \right\rangle \right|^2}{E_n^A - E_0^A} \tag{2.38}$$

The electrons of each fragment can reconfigure themselves in an electric field while the nuclei remain fixed at a given $\mathfrak{R}$. In the electric field created by the permanent multipole moments of fragment A, the electron cloud of fragment B distorts, and vice versa.

The dispersion interaction is the induced-induced multipole moment interaction:

$$W_{\rm disp} = -\sum_{m,n\neq 0} \frac{\left|\left\langle \psi_n^A \psi_m^B | \hat{V}_{\rm int} | \psi_0^A \psi_0^B \right\rangle\right|^2}{(E_n^A - E_0^A) + (E_m^B - E_0^B)} \tag{2.39}$$

The dispersion interaction does not have a simple classical interpretation. It is present even between two noble gas atoms (and causes deviations from the ideal gas law).

Evaluating the expressions given in Eqs. 2.37–2.39 leads to the following expansion for the total energy in inverse powers of R:

$$\begin{aligned} E &= E_0 + W_{\rm el} + W_{\rm ind} + W_{\rm disp} && (2.40)\\ &= E_0 - \sum_{n\geq 3} \frac{C_n}{R^n}. && (2.41) \end{aligned}$$

The coefficients C_n depend on the relative orientation of the fragments A and B.

2.3.2 Analytic form for the interaction between an S-state atom and a Σ-state linear molecule

Pack [46] gives the first three terms of the analytic form for the long-range potential between an S-state atom and a Σ-state linear molecule (excluding relativistic effects). He also provides a procedure for determining higher order terms. In this case, the C_n coefficients in Eq. 2.41 depend on the angle θ between the internuclear axis of the molecule and the vector associated with the distance R. Expanding these coefficients in Legendre polynomials, Pack [46] showed that:

$$\begin{aligned} C_6(\cos\theta) &= C_6^{(0)} P_0(\cos\theta) + C_6^{(2)} P_2(\cos\theta) \\ C_7(\cos\theta) &= C_7^{(1)} P_1(\cos\theta) + C_7^{(3)} P_3(\cos\theta) \\ C_8(\cos\theta) &= C_8^{(0)} P_0(\cos\theta) + C_8^{(2)} P_2(\cos\theta) + C_8^{(4)} P_4(\cos\theta) \end{aligned} \tag{2.42}$$

The coefficients depend on multipole moments of the molecule and the polarizabilities of both partners, and include the effects of both the induction and dispersion interactions.

2.4 Scattering theory

The methods of the last two sections can be used to calculate a PES that determines all of the forces between two molecules. Once these forces are obtained, a scattering calculation can be performed to determine solutions to the equation for nuclear motion, Eq. 2.8. In this section, we will discuss the formalism we use for scattering calculations.

2.4.1 Classical ideas

The classical scattering of structureless particles by a fixed central potential is illustrated in Fig. 2.1. In the figure, a particle approaches the potential parallel to the z-axis with some energy E. The particle's perpendicular distance from the z-axis is called the impact parameter b. When the particle is scattered by the potential, it is deflected by a polar angle θ called the scattering angle. If we assume that the deflection is a continuous, smooth function of the impact parameter, then all particles with impact parameter between b and $b+db$ scatter into a solid angle $d\Omega$. Classical scattering theory allows one to determine θ as a function of b and E.

The point of comparison between experiment and theory is typically the cross section. In the figure, an infinitesimal cross section $d\sigma(\theta, \phi)$ can be defined as the infinitesimal area $b\,db\,d\phi$ containing all the trajectories that result in scattering into the solid angle $d\Omega$:

$$d\sigma = \frac{\text{The number of particles deflected into d}\Omega\text{ per second}}{\text{Flux of incident particles}}. \tag{2.43}$$

Since the flux is the number of particles that pass through the infinitesimal area $b\,db\,d\phi$ in a given time, the infinitesimal cross section has units of area. The cross section is the integral of $d\sigma(\theta, \phi)$ over solid angle.

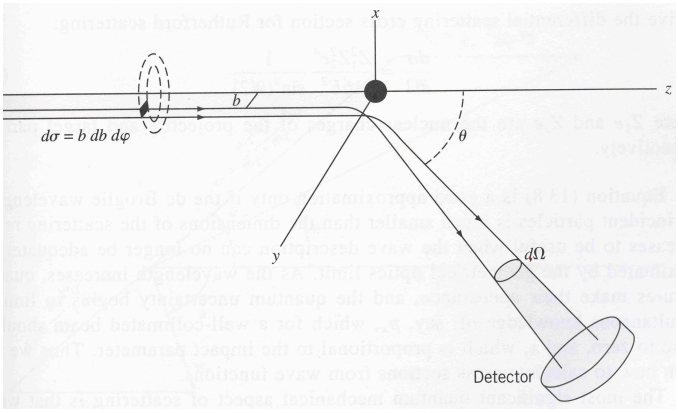

Figure 2.1: Classical scattering of a structureless particle by a fixed potential [48]. Reprinted with permission of John Wiley & Sons, Inc.

In the case of a two-particle collision, it is often convenient to perform scattering calculations in the center of mass system. In this system, the two-particle collision reduces to a one-particle problem. The effective particle has reduced mass $\mu = m_1 m_2/(m_1 + m_2)$, is moving with relative momentum $p = \mu v$ where v is the relative velocity, and is scattered by a fixed potential. The cross section is the same in the center of mass frame as it is in the laboratory frame.

2.4.2 Introduction to quantum mechanical scattering

There are many cases for which one would wish to determine quantum mechanical cross sections. Some examples include scattering events for which the particles have de Broglie wavelengths sufficiently large compared to the scattering region, or for which the collision partners are indistinguishable, or for events that involve tunneling or interference. In such calculations, one must find a solution to the Schrodinger equation of the system for a specified positive energy and then relate that solution to a cross section. Additional details are provided in texts on quantum mechanics, and some references are [49–53].

Just as in classical scattering, collisions between two particles can be reduced to one-particle problems by working in the center of mass frame. When the potential energy depends only on the relative coordinates of the particles, the Born-Oppenheimer nuclear wave function of Eq. 2.8 for the system can be expressed as the product of a function u describing the relative motion between the two particles and another function describing the motion of the center of mass.

In this section, we consider elastic collisions between structureless "particles", which could be elementary particles without spin or noble gas atoms. Letting V denote the interparticle potential, we can write the Schrodinger equation for the relative motion as

$$-\frac{\hbar^2}{2\mu}\nabla^2 u + Vu = Eu. \tag{2.44}$$

Cross sections can be found using the wave function u. The incident particle is represented by a plane wave with well-defined energy E, or momentum $\hbar k = \sqrt{2\mu E}$. In this section we will restrict ourselves to central potentials $V = V(r)$ that go to zero faster than $1/r^2$.

So that the problem will have azimuthal symmetry, one can define the z-axis parallel to the direction along which the incident plane wave approaches the potential. The incident plane wave is scattered by the potential, producing an outgoing spherical wave modulated by an angular amplitude $f(\theta)$. For a beam of incident particles, this model gives the steady-state, asymptotic wave function

$$u(r,\theta) \approx A\left\{e^{ikz} + f(\theta)\frac{e^{ikr}}{r}\right\} \qquad r \to \infty. \tag{2.45}$$

The quantity $f(\theta)$ is called the scattering amplitude and is related to the cross section by

$$\sigma = \int |f(\theta)|^2 \, d\Omega, \tag{2.46}$$

where $|f(\theta)|^2$ gives the intensity of the scattering at each angle. By finding a solution to the Schrodinger equation (Eq. 2.44) and matching its asymptotic form to Eq. 2.45, one can determine $f(\theta)$ and therefore σ.

For a central potential, angular momentum is conserved. If we use separation of

variables to solve Eq. 2.44 we expect to find solutions

$$u_{lm}(r,\theta) = \frac{y_{lm}(r)}{r} Y_{lm}(\theta,\phi) \tag{2.47}$$

Since the plane wave approaches from the z direction, the problem has azimuthal symmetry and $m = 0$. Thus we can find solutions of the form

$$u_l(r,\theta) = \frac{y_l(r)}{r}\sqrt{\frac{2l+1}{4\pi}} P_l(\cos\theta) \tag{2.48}$$

where $y_l(r)$ is a solution to the equation for radial motion,

$$\left(-\frac{d^2}{dr^2} + \frac{l(l+1)}{r^2} + \frac{2\mu}{\hbar^2}V(r) - k^2\right) y_l(r) = 0. \tag{2.49}$$

One can write a general solution to the Schrodinger equation as a linear combination of these solutions

$$u(r,\theta) = \sum_l \frac{y_l(r)}{r} P_l(\cos\theta) \tag{2.50}$$

where the expansion coefficients are contained in $y_l(r)$, as will be shown below.

One can determine the asymptotic form of $y_l(r)$ by looking at the form of the solution to Eq. 2.49 in the limit where r is large enough that $V(r) \ll 1/r^2$ can be neglected:

$$\left(-\frac{d^2}{dr^2} + \frac{l(l+1)}{r^2} - k^2\right) y_l(r) = 0. \tag{2.51}$$

The general solution to this equation is a linear combination of two linearly independent solutions, which may be chosen to be the real spherical Bessel functions of the first and second kinds, $j_l(kr)$ and $n_l(kr)$ [54], multiplied by r:

$$\frac{y_l(r)}{r} = A_l\left[j_l(kr) + R_l n_l(kr)\right] \tag{2.52}$$

The quantity R_l is the reactance $\mathbf{R}$ matrix, which is a 1×1 matrix in this case. Then the general solution Eq. 2.50 is, at large r where the potential is negligible,

$$u(r,\theta) = \sum_{l=0}^{\infty} A_l\left[j_l(kr) + R_l n_l(kr)\right] P_l(\cos\theta). \tag{2.53}$$

First, we will discuss how we relate A_l and R_l to the asymptotic form specified by Eq. 2.45 to determine $f(\theta)$ in terms of the R_l. Then, we will discuss determining the solution to Eq. 2.49 and matching it to the form specified by Eq. 2.52 at large r where the potential is negligible. This matching determines the numerical values of the R_l and leads to the value for the cross section.

The asymptotic forms of $j_l(kr)$ and $n_l(kr)$ are [54]:

$$j_l(kr) \approx \frac{\sin(kr - l\pi/2)}{kr} = \frac{e^{i(kr-l\pi/2)} - e^{-i(kr-l\pi/2)}}{2ikr} \tag{2.54}$$

$$n_l(kr) \approx \frac{\cos(kr - l\pi/2)}{kr} = i\left(\frac{e^{i(kr-l\pi/2)} + e^{-i(kr-l\pi/2)}}{2ikr}\right). \tag{2.55}$$

Using Eqs. 2.54 and 2.55, we see that as $r \to \infty$, Eq. 2.53 has the asymptotic form

$$u(r,\theta) \approx \frac{1}{kr}\sum_{l=0}^{\infty} A_l \left[\sin(kr - l\pi/2) + R_l \cos(kr - l\pi/2)\right] P_l(\cos\theta) \tag{2.56}$$

$$\approx \frac{1}{2ik}\sum_{l=0}^{\infty} A_l \left[(1 + iR_l)\frac{e^{i(kr-l\pi/2)}}{r} - (1 - iR_l)\frac{e^{-i(kr-l\pi/2)}}{r}\right] P_l(\cos\theta)$$

$$\approx \frac{1}{2ik}\sum_{l=0}^{\infty} A_l(1 - iR_l)\left[\left(\frac{1 + iR_l}{1 - iR_l}\right)\frac{e^{i(kr-l\pi/2)}}{r} - \frac{e^{-i(kr-l\pi/2)}}{r}\right] P_l(\cos\theta). \tag{2.57}$$

To determine $f(\theta)$ in terms of the R_l, we must write the model asymptotic wave function given in Eq. 2.45 as a sum over l. The incident plane wave can be written as a superposition of its angular momentum components using Rayleigh's formula,

$$e^{ikz} = \sum_{l=0}^{\infty} i^l(2l + 1)j_l(kr)P_l(\cos\theta), \tag{2.58}$$

and the scattering amplitude can be expanded in Legendre polynomials:

$$f(\theta) = \sum_{l=0}^{\infty}(2l + 1)f_l P_l(\cos\theta). \tag{2.59}$$

Each term in Eqs. 2.56–2.58 is called a partial wave. Since the angular momentum is conserved, each partial wave scatters independently, and the scattering amplitude is a sum over all partial wave contributions. By rewriting Eq. 2.45 using

Eqs. 2.58 and 2.59, the form of $j_l(kr)$ for large r, and the relationship $i^l = e^{il\pi/2}$, one finds that asymptotically:

$$u(r,\theta) \approx A\frac{1}{2ik}\sum_{l=0}^{\infty}(2l+1)i^l\left\{(1+2ikf_l)\,\frac{e^{i(kr-l\pi/2)}}{r} - \frac{e^{-i(kr-l\pi/2)}}{r}\right\}P_l(\cos\theta). \quad (2.60)$$

Equating the coefficients of the corresponding exponential terms for each l in Eqs. 2.57 and 2.60 leads to the equations

$$1+2ikf_l = \left(\frac{1+iR_l}{1-iR_l}\right) \quad (2.61)$$

$$A(2l+1)i^l = A_l(1-iR_l). \quad (2.62)$$

One can solve Eq. 2.61 to find f_l in terms of R_l:

$$f_l = \frac{1}{k}\left(\frac{R_l}{(1-iR_l)}\right). \quad (2.63)$$

Before we proceed to the determination of cross sections, we will identify three useful quantities related to R_l.

Equations 2.57 and 2.60 involve an incoming spherical wave $e^{-i(kr-l\pi/2)}/r$ and an outgoing spherical wave $e^{i(kr-l\pi/2)}/r$ multiplied by a factor $(1+iR_l)/(1-iR_l) = (1+2ikf_l)$. This factor is conventionally called S_l, the scattering **S** matrix:

$$S_l = 1+2ikf_l = \left(\frac{1+iR_l}{1-iR_l}\right), \quad (2.64)$$

When there is no scattering, $f_l = R_l = 0$ for all l, and $S_l = 1$. From S_l, one can define T_l, the transition **T** matrix, as

$$T_l = 1 - S_l = \frac{-2iR_l}{1-iR_l}, \quad (2.65)$$

which is zero for all l when there is no scattering. By rearranging Eq. 2.64, one finds that

$$f_l = \frac{S_l - 1}{2ik} = -\frac{T_l}{2ik}. \quad (2.66)$$

Equation 2.64 shows that S_l is unitary, so that one can write

$$S_l = e^{2i\delta_l}. \quad (2.67)$$

The real coefficient δ_l, which is called the phase shift, has a simple physical interpretation. The result of the scattering is a phase change $2\delta_l$ of the outgoing spherical wave in Eq. 2.60. When there is no scattering, $\delta_l = 0$; the outgoing wave is not phase shifted.

The f_l can be written in terms of the phase shift by using Eqs. 2.66 and 2.67:

$$f_l = \left(\frac{e^{2i\delta_l} - 1}{2ik}\right)\frac{e^{-i\delta_l}}{e^{-i\delta_l}} = \left(\frac{e^{i\delta_l} - e^{-i\delta_l}}{2ik}\right)\frac{1}{e^{-i\delta_l}} = \frac{e^{i\delta_l}}{k}\sin(\delta_l). \tag{2.68}$$

By inverting Eq. 2.64 to write R_l in terms of S_l, one can show that

$$R_l = i\left(\frac{1 - S_l}{1 + S_l}\right) = i\left(\frac{1 - e^{2i\delta_l}}{1 + e^{2i\delta_l}}\right)\frac{e^{-i\delta_l}}{e^{-i\delta_l}} = \frac{1}{i}\frac{e^{i\delta_l} - e^{-i\delta_l}}{e^{i\delta_l} + e^{-i\delta_l}} = \tan\delta_l. \tag{2.69}$$

We have defined four different quantities: the phase shift δ_l, and the **R**, **S**, and **T** matrices. As we have shown, they are all related, and the cross section can be expressed in terms of any one of them. We will show this by writing the cross section in terms of the f_l by using Eqs. 2.46 and 2.59 and the orthogonality of the Legendre polynomials,

$$\int_{-1}^{1} P_l(\cos\theta)P_{l'}(\cos\theta)\, d\cos\theta = \frac{2}{2l+1}\delta_{ll'}. \tag{2.70}$$

One finds that the cross section in terms of f_l is

$$\begin{aligned}
\sigma &= \int |f(\theta)|^2 \, \mathrm{d}\Omega = 2\pi \int_0^{\pi} f^*(\theta) f(\theta) \sin\theta \, d\theta && (2.71)\\
&= 2\pi \int_{-1}^{1} \left(\sum_{l=0}^{\infty} (2l+1) f_l^* P_l(\cos\theta)\right)\left(\sum_{l'=0}^{\infty} (2l'+1) f_{l'} P_{l'}(\cos\theta)\right) d\cos\theta && (2.72)\\
&= 2\pi \sum_{l=0}^{\infty}\sum_{l'=0}^{\infty} (2l+1)(2l'+1) f_l^* f_{l'} \int_{-1}^{1} P_l(\cos\theta)P_{l'}(\cos\theta)\, d\cos\theta && (2.73)\\
&= 4\pi \sum_{l=0}^{\infty} |f_l|^2 (2l+1). && (2.74)
\end{aligned}$$

The cross section contains no interference terms between the partial waves.

To determine the cross section, one uses Eq. 2.74 and the expression relating f_l to the appropriate quantity (Eq. 2.63, 2.66, or 2.68). The cross section can then be written in any of the following forms:

$$\sigma = \frac{4\pi}{k^2}\sum_{l=0}^{\infty}(2l+1)\sin^2(\delta_l) \tag{2.75}$$

$$\sigma = \frac{4\pi}{k^2}\sum_{l=0}^{\infty}(2l+1)\frac{R_l^2}{1+R_l^2} \tag{2.76}$$

$$\sigma = \frac{\pi}{k^2}\sum_{l=0}^{\infty}(2l+1)\left|1-S_l\right|^2 \tag{2.77}$$

$$\sigma = \frac{\pi}{k^2}\sum_{l=0}^{\infty}(2l+1)\left|T_l\right|^2. \tag{2.78}$$

The problem of determining the cross sections has been reduced to determining either δ_l, R_l, S_l, or T_l. To determine any of these quantities, one must solve

$$\left(-\frac{d^2}{dr^2}+\frac{l(l+1)}{r^2}+\frac{2\mu}{\hbar^2}V(r)-k^2\right)y_l(r)=0 \tag{2.79}$$

for each l with the boundary condition $y_l(0)=0$. One integrates this equation from $r=0$ to a radius $r_{\max}$ at which the potential V is negligible. One can match the asymptotic solution to the form specified by Eq. 2.52.

In principle, it's possible to determine S_l or T_l directly, but it is computationally advantageous first to determine one of the real quantities δ_l or R_l rather than the complex S_l or T_l. Then one doesn't need to calculate complex solutions to the real Schrodinger equation. Instead, one can determine real solutions, match to R_l, and then at the end use complex arithmetic to transform to S_l if necessary.

One can identify each partial wave with an impact parameter using the classical relation $\mathbf{l}=\mathbf{r}\times\mathbf{p}$. The magnitude of $\mathbf{l}$ is bp. By replacing the magnitude of $\mathbf{l}$ with $\hbar\sqrt{l(l+1)}$ and using $p=\hbar k$, one finds that $b\approx l/k$ or $l\approx bk$. The sum over l can be interpreted as a sum over the impact parameter. The maximum l needed to achieve convergence will be approximately related to the range of the potential.

The phase shift δ_l is the simplest way to describe elastic scattering, but the formulas cannot be generalized to the case where one of the collision partners has

internal structure and the potential is noncentral. In the next section, we will show how the **R**, **S**, and **T** matrices can be generalized to describe transitions among several quantum states.

2.4.3 Scattering by a rigid rotator

We use the quantum mechanical scattering formalism developed by Arthurs and Dalgarno [17] for the scattering of a structureless particle by a rigid rotator. This model is appropriate for a noble gas atom scattering from a diatomic molecule in a $^1\Sigma$ state with $v = 0$, in the case where vibrational excitation and nuclear spin can be neglected. The goal of the scattering calculations is to determine state-to-state cross sections for the rotational excitation of the molecule. Additional details are provided in [55, 56].

The scattering by a rigid rotator introduces some extra complications into the theory described in Section 2.4.2; the molecule has internal structure and the potential is noncentral. In this problem the total angular momentum **J** is conserved, where

$$\mathbf{J} = \mathbf{j} + \mathbf{l}, \tag{2.80}$$

the vector sum of the angular momenta **j** and **l** corresponding to the rotation of the molecule and the orbital angular momentum of the particle. The Arthurs and Dalgarno [17] formalism uses the total angular momentum representation, so the wave function for the system can be written as a sum of partial waves each with a definite J.

When a partial wave scatters from the potential, angular momentum can be transferred between j and l as long as J stays fixed. We will find that the wave function for a given J has contributions from basis functions for several different values of j and l.

One can generalize the quantum scattering theory outlined in Section 2.4.2 for systems with multiple internal states by introducing the notion of a "channel". Each channel represents a possible internal state. In the present case, for a given value of J, the channels can be labelled by the pairs (j, l). In a multichannel system,

there are several linearly independent solutions to the time-independent Schrodinger equation. Each solution corresponds to a collision with a different initial state, or entrance channel, and can be described using the same concepts that we discussed in Section 2.4.2. For each value of J, and for each possible initial state, we have one incoming spherical wave and several outgoing spherical waves, one for each possible final channel.

The potential is expressed using Jacobi coordinates, which are shown in Fig. 2.2 for the He+NaK system. The coordinate r is the bond length of the molecule, which

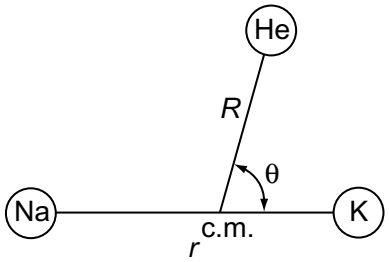

Figure 2.2: Coordinates for the He+NaK system. Reproduced from [2] with the permission of AIP publishing.

is considered fixed at $r = r_0$ for the present discussion; R is the distance between the atom and the center of mass of the molecule, and θ is the angle between the internuclear axis of the molecule and the atom. The unit vectors $\hat{r}$ and $\hat{R}$ define the orientations of the internuclear axis and the vector associated with the distance R.

The scattering is formulated in a space-fixed, center of mass frame. The Hamiltonian is similar to that defined by Eq. 2.44 in Section 2.4.2, except for an extra term $\hat{H}_{\rm rot}$ related to the internal structure of the molecule:

$$\hat{H} = \hat{H}_{\rm rot} - \frac{\hbar^2}{2\mu}\nabla_R^2 + V(R, r_0, \theta). \tag{2.81}$$

In this equation μ is the reduced mass of the atom-diatom system. The first term, $\hat{H}_{\rm rot}$, describes the rotational motion of the rigid rotator about its center of mass. Its eigenfunctions are the spherical harmonics $Y_{jm}(\hat{r})$, with eigenvalues $\hbar^2 j(j+1)/(2\mathcal{M}r_0^2)$. The quantity $\mathcal{M}$ is the reduced mass of the diatomic molecule; j is the rotational quantum number, and m is the corresponding magnetic quantum

number. The second term in Eq. 2.81 corresponds to the kinetic energy of the incident particle. Finally, the third term $V(R, r_0, \theta)$ represents the interaction potential of the system, which goes to zero as R goes to infinity.

At the beginning of this section, we mentioned that the incident plane wave is a superposition of partial waves with definite J. Since J is conserved, each partial wave scatters independently, so one can perform separate calculations for each J. In these separate calculations, one solves the equation for the relative motion

$$(\hat{H} - E)u_{jl}^{JM} = 0, \tag{2.82}$$

where J is fixed.

The eigenfunctions for the angular motion of the incident particle are $Y_{lm_l}(\hat{R})$, and combining them with the eigenfunctions of the rotator, one can define a set of coupled angular eigenfunctions

$$\mathcal{Y}_{Jjl}^{M}(\hat{r}, \hat{R}) = \sum_{m_l=-l}^{l} \sum_{m=-j}^{j} \langle jlmm_l | jlJM \rangle \, Y_{lm_l}(\hat{R}) Y_{jm}(\hat{r}), \tag{2.83}$$

where $\langle \cdots | \cdots \rangle$ is a Clebsch-Gordan coefficient. These $\mathcal{Y}_{Jjl}^{M}(\hat{r}, \hat{R})$ functions are eigenfunctions of the total angular momentum operator $\hat{J}^2$ and of $\hat{J}_z$. The system is symmetric with respect to rotation, and we will show that for a given J the results are independent of M.

The wavefunction for the system can be expanded in the $\mathcal{Y}_{Jj'l'}^{M}(\hat{r}, \hat{R})$:

$$u_{jl}^{J} = \sum_{j'l'} \left(\frac{1}{R} \right) X_{j'l'}^{Jjl}(R) \mathcal{Y}_{Jj'l'}^{M}(\hat{r}, \hat{R}). \tag{2.84}$$

This equation is analogous to Eq. 2.48 in Section 2.4.2.

By substituting the expansion Eq. 2.84 into Eq. 2.82, multiplying by $\left(\mathcal{Y}_{Jj''l''}^{M}(\hat{r}, \hat{R}) \right)^*$ and integrating over the angular coordinates, one obtains a set of coupled equations

$$\begin{aligned} &\frac{\hbar^2}{2\mu} \left(-\frac{d^2}{dR^2} + \frac{l''(l''+1)}{R^2} - k_{j''}^2 \right) X_{j''l''}^{Jjl}(R) \\ &\quad + \sum_{j'l'} \left[\int \int \left(\mathcal{Y}_{Jj''l''}^{M}(\hat{r}, \hat{R}) \right)^* V(R, r_0, \theta) \mathcal{Y}_{Jj'l'}^{M}(\hat{r}, \hat{R}) \, d\hat{r} \, d\hat{R} \right] X_{j'l'}^{Jjl}(R) = 0, \end{aligned} \tag{2.85}$$

where we have used the square of the channel wave number $k_{j''}$ given by rearranging the expression for the total energy of the system,

$$E = \frac{\hbar^2 k_{j''}^2}{2\mu} + \frac{\hbar^2 j''(j''+1)}{2\mathcal{M}r_0^2}. \tag{2.86}$$

Equation 2.86 shows that the total energy E is the sum of the initial kinetic energy of the incident particle and the initial rotational energy of the molecule.

The angular integral in Eq. 2.85 can be simplified by using a Legendre expansion of the interaction potential:

$$V(R, r_0, \theta) = \sum_n v_n(R, r_0) P_n(\cos\theta). \tag{2.87}$$

Substituting Eq. 2.87 into Eq. 2.85 leads to an expression for the integral in terms of the so-called Percival-Seaton coefficients [57], which are defined as

$$\begin{aligned} f_n(j''l'', j'l'; J) &= \int\int \left(\mathcal{Y}^M_{Jj''l''}(\hat{r}, \hat{R})\right)^* P_n(\cos\theta) \mathcal{Y}^M_{Jj'l'}(\hat{r}, \hat{R})\, d\hat{r}\, d\hat{R} \\ &= (-1)^{j''+j'-J} \sqrt{(2j''+1)(2j'+1)(2l''+1)(2l'+1)} \\ &\qquad \begin{pmatrix} l'' & l' & n \\ 0 & 0 & 0 \end{pmatrix} \begin{pmatrix} j'' & j' & n \\ 0 & 0 & 0 \end{pmatrix} \begin{Bmatrix} j'' & j' & n \\ l' & l'' & J \end{Bmatrix}, \end{aligned} \tag{2.88}$$

where $\begin{pmatrix} \cdots \\ \cdots \end{pmatrix}$ is a $3j$ coefficient and $\begin{Bmatrix} \cdots \\ \cdots \end{Bmatrix}$ is a $6j$ coefficient. The Percival-Seaton coefficients are independent of M.

The integrals in Eq. 2.85 become

$$\int\int \left(\mathcal{Y}^M_{Jj''l''}(\hat{r}, \hat{R})\right)^* V(R, r_0, \theta) \mathcal{Y}^M_{Jj'l'}(\hat{r}, \hat{R})\, d\hat{r}\, d\hat{R} = \sum_n f_n(j''l'', j'l'; J) v_n(R, r_0). \tag{2.89}$$

By inserting Eq. 2.89 into Eq. 2.85, one obtains the following set of coupled differential equations:

$$\begin{aligned} &\frac{\hbar^2}{2\mu}\left(-\frac{d^2}{dR^2} + \frac{l'(l'+1)}{R^2} - k_{j'}^2\right) X^{Jjl}_{j'l'}(R) \\ &\qquad + \sum_{j''l''} \sum_n f_n(j''l'', j'l'; J) v_n(R, r_0) X^{Jjl}_{j''l''}(R) = 0. \end{aligned} \tag{2.90}$$

In practice, the infinite sum over the channels (j'', l'') is truncated and one investigates convergence with respect to the number of channels. This is known as the close-coupling approximation.

The component $n = 0$ in Eq. 2.87 gives the central part of the potential, since $P_0(\cos\theta) = 1$. One can use the Percival-Seaton coefficient [57] for $n = 0$,

$$f_0(j''l'', j'l'; J) = \delta_{j''j'}\delta_{l''l'} \tag{2.91}$$

to split off the central part of the potential in the coupled equations:

$$\frac{\hbar^2}{2\mu}\left(-\frac{d^2}{dR^2} + \frac{l'(l'+1)}{R^2} - k_{j'}^2 + \frac{2\mu}{\hbar^2}v_0(R, r_0)\right) X^{Jjl}_{j'l'}(R) + \sum_{j''l''}\sum_{n=1} f_n(j''l'', j'l'; J)v_n(R, r_0)X^{Jjl}_{j''l''}(R) = 0. \tag{2.92}$$

If we only include the $j = 0$ state, the term on the second line of Eq. 2.92 vanishes, and we recover Eq. 2.79.

One can interpret Eq. 2.90 as an equation involving $N_{\text{chan}} \times N_{\text{chan}}$ matrices, where N_{chan} is the number of channels (j, l). Each column of the solution matrix $X^{Jjl}_{j''l''}(R)$ gives the expansion coefficients of the wave function for a different initial state jl, as shown in Eq. 2.84; these N_{chan} solutions are linearly independent. The term on the second line in Eq. 2.90 represents the coupling between various initial and final states; it is the matrix product of a coupling matrix $\sum_{n=1} f_n(j''l'', j'l'; J)v_n(R, r_0)$ and the solution matrix.

For a given J, linear combinations of the solutions $X^{Jjl}_{j''l''}(R)$ can be matched to a known asymptotic form, just as was done with solutions $y_l(r)$ in Section 2.4.2. The matching determines the cross sections for the rotational excitation of the molecule. The asymptotic form is:

$$X^{Jjl}_{j'l'}(R) = \delta_{jj'}\delta_{ll'}j_l(k_jR) + \sqrt{\frac{k_{j'}}{k_j}}R^J_{jl,j'l'}n_{l'}(k_{j'}R) \tag{2.93}$$

One can compare this equation to Eq. 2.52 in Section 2.4.2. The $\mathbf{R}$ matrix is now an $N_{\text{chan}} \times N_{\text{chan}}$ matrix, and there is a flux factor $\sqrt{k_{j'}/k_j}$ that accounts for the fact that each channel has its own wave number.

As in Eq. 2.65 of Section 2.4.2, we can relate the $\mathbf{R}$ matrix to the $\mathbf{T}$ matrix,

$$\mathbf{T} = -2i(1 - i\mathbf{R})^{-1}\mathbf{R}. \tag{2.94}$$

Partial cross sections for a fixed J can be given in terms of the T-matrix elements. By summing over the cross sections for each partial wave J, one obtains the total $j \to j'$ cross section

$$\sigma(j \to j') = \frac{\pi}{(2j+1)k_j^2} \sum_J \sum_{l,l'} (2J+1) \left| T^J_{jl,j'l'} \right|^2, \tag{2.95}$$

which one can compare with Eq. 2.78. The factor $1/(2j+1)$ arises because one averages over m and sums over the final m' to obtain the $j \to j'$ cross sections. Using the same reasoning as in Section 2.4.2, one still has $l \approx bk$. In order to relate the convergence of the sum over J to the range of the potential, however, it's more useful to use $J \approx bk$, although this relation is less accurate because a fixed J may have contributions from several values of l between $|J - j|$ and $|J + j|$.

It's useful to define the Grawert coefficients [58] when one needs cross sections for $jm \to j'm'$ transitions appropriate for a cell environment. The Grawert coefficients can be expressed in terms of the $\mathbf{T}$-matrix elements:

$$B_\lambda(j, j') = \sum_{l,l'} \left| \sum_J (2J+1)(-1)^J \begin{Bmatrix} j & j' & \lambda \\ l' & l & J \end{Bmatrix} T^J_{jl,j'l'} \right|^2 \tag{2.96}$$

where here they are defined to be symmetric with respect to j and j'; in the literature, sometimes a factor π/k_j^2 is included in the definition of the Grawert coefficients. The $jm \to j'm'$ cross sections are [11]

$$\sigma(jm \to j'm') = \frac{\pi}{k_j^2} \sum_{\lambda=|j-j'|}^{j+j'} (2\lambda+1) \begin{pmatrix} j & j' & \lambda \\ -m & m' & m-m' \end{pmatrix}^2 B_\lambda(j, j') \tag{2.97}$$

One can also express the $j \to j'$ cross sections in terms of the Grawert coefficients:

$$\sigma(j \to j') = \frac{\pi}{(2j+1)k_j^2} \sum_{\lambda=|j-j'|}^{j+j'} (2\lambda+1) B_\lambda(j, j'). \tag{2.98}$$

One can obtain this equation from Eq. 2.97, which is equivalent to Eq. 2.95, by averaging over m and summing over the final m'.

2.4.4 Vibrational dependence of the scattering

The Arthurs and Dalgarno [17] formalism was developed for a rigid rotator, where the internuclear separation r of the molecule is fixed at its equilibrium value r_0. One can generalize the formalism [59, 60] to incorporate the vibration of the molecule by modifying the Hamiltonian presented in Eq. 2.81. One must include the full kinetic energy operator for the motion of the target molecule, and one must extend the interaction potential $V(R, r, \theta)$ to include the dependence on the bond length r. This extended potential will include the interatomic potential for the target molecule, which we identify as

$$W(r) = \lim_{R\to\infty} V(R, r, \theta). \tag{2.99}$$

We can write the modified Hamiltonian in a form that isolates the term describing the molecular target:

$$\hat{H} = \left[\frac{-\hbar^2}{2\mathcal{M}}\nabla_r^2 + W(r)\right] - \frac{\hbar^2}{2\mu}\nabla_R^2 + [V(R, r, \theta) - W(r)] \tag{2.100}$$

$$= \hat{H}_{\mathrm{vib-rot}} - \frac{\hbar^2}{2\mu}\nabla_R^2 + [V(R, r, \theta) - W(r)] \tag{2.101}$$

The eigenfunctions of $\hat{H}_{\mathrm{vib-rot}}$ are products of a vibrational eigenfunction $\chi_{vj}(r)/r$ and $Y_{jm}(\hat{r})$. Therefore the total wavefunction for the system can be written in a form analogous to Eq. 2.84:

$$u^J_{vjl} = \left(\frac{1}{Rr}\right) \sum_{v'j'l'} X^{Jvjl}_{v'j'l'}(R)\mathcal{Y}^M_{Jj'l'}(\hat{R}, \hat{r})\chi_{v',j'}(r). \tag{2.102}$$

The vibrational wave functions $\chi_{vj}(r)$ are solutions of

$$\left[-\frac{\hbar^2}{2\mathcal{M}}\frac{d^2}{dr^2} + \frac{\hbar^2 j(j+1)}{2\mathcal{M}r^2} + W(r) - E_{vj}\right]\chi_{vj}(r) = 0, \tag{2.103}$$

where E_{vj} is the vibrational-rotational energy for a given v and j.

The total energy of the system is the sum of the initial kinetic energy of the incident particle and the initial energy of the vibrating rotator:

$$E = E_{vj} + \frac{\hbar^2 k^2_{vj}}{2\mu}. \tag{2.104}$$

By substituting Eq. 2.102 into the Schrodinger equation and following the derivation of Section 2.4.3, one finds the generalization of Eq. 2.90:

$$\frac{\hbar^2}{2\mu}\left(-\frac{d^2}{dR^2}+\frac{l''(l''+1)}{R^2}-k^2_{v''j''}\right)X^{Jvjl}_{v''j''l''}(R) + \sum_{v'j'l'}\sum_{n} f_n(j''l'',j'l';J)\mathcal{V}_n^{v''j''v'j'}(R)X^{Jvjl}_{v'j'l'}(R)=0, \quad (2.105)$$

where

$$\mathcal{V}_n^{v''j''v'j'}(R)=\int \chi_{v''j''}(r)\tilde{v}_n(R,r)\chi_{v'j'}(r)\,dr. \quad (2.106)$$

Equation 2.105 has the same form as Eq. 2.90, with the vibrationally averaged $\mathcal{V}_n^{v''j''v'j'}(R)$ replacing $v_n(R,r_0)$. The $\tilde{v}_n(R,r)$ are the Legendre components of the coupling function introduced in Eq. 2.101:

$$V(R,r,\theta)-W(r)=\tilde{V}(R,r,\theta)=\sum_n \tilde{v}_n(R,r)P_n(\cos\theta) \quad (2.107)$$

Subtracting $W(r)$ ensures that the Legendre components $\tilde{v}_n(R,r)$ all go to zero in the limit of large R. We note that $\tilde{v}_n(R,r_0)$ reduces to the $v_n(R,r_0)$ defined in Section 2.4.3.

2.5 Multipole expansion of m-changing collisions

The most straightforward way to analyze m changing collisions is in terms of $jm \to j'm'$ cross sections that describe the individual changes in m. An elegant alternative is to consider the distribution of m levels of an ensemble of molecules in a cell environment with the same j. This distribution can be expressed in terms of moments, which are defined below. The discussion follows previous work presented by ourselves [2] and others [11, 12, 61].

Let N^j_m be the number of molecules in the state $|jm\rangle$. For a fixed j the values of N^j_m define a distribution of m levels. One can transform the m distribution to a moment distribution [61] using the orthogonal transformation $\mathcal{T}^j$ with elements

$$\mathcal{T}^j_{mK}=(-1)^{K+m+j}\sqrt{2K+1}\begin{pmatrix} j & K & j \\ m & 0 & -m\end{pmatrix}, \quad (2.108)$$

where K is an integer between 0 and $2j$. We can use this transformation to define the moment distribution n_K^j as [11, 12, 61]

$$n_K^j = \sum_{m=-j}^{j} N_m^j \mathcal{T}_{mK}^j, \tag{2.109}$$

or in terms of the two row matrices $\mathbf{n}^j$ and $\mathbf{N}^j$,

$$\left(\begin{array}{cccc} n_0 & \dots & n_{2j} \end{array} \right) = \left(\begin{array}{ccc} N_{-j} & \dots & N_j \end{array} \right) \left(\begin{array}{ccc} T_{-j,0}^j & \dots & T_{-j,2j}^j \\ \vdots & \ddots & \vdots \\ T_{j,0}^j & \dots & T_{j,2j}^j \end{array} \right). \tag{2.110}$$

The first three moments ($K = 0, 1,$ and 2) are proportional to the population, the orientation and the alignment. Using explicit expressions in [2], one can show that

$$\text{Population} = \mathcal{N}^j = \sum_{m=-j}^{j} N_m^j \tag{2.111}$$

$$\text{Orientation} = \mathcal{O}^j = \frac{1}{\sqrt{j(j+1)}} \frac{\sum_{m=-j}^{j} m N_m^j}{\sum_{m=-j}^{j} N_m^j} = \left\langle \frac{m}{\sqrt{j(j+1)}} \right\rangle \tag{2.112}$$

$$\text{Alignment} = \mathcal{A}^j = \left\langle \frac{3m^2 - j(j+1)}{\sqrt{j(j+1)\left[j(j+1) - \frac{3}{4}\right]}} \right\rangle. \tag{2.113}$$

In these definitions $\langle \dots \rangle$ indicates an average over the molecules. Population is the total number of molecules with a given j, orientation is proportional to the average m level, and alignment involves the squares of the m levels of the molecules.

By evaluating Eq. 2.109 for the first three moments, one can show that the proportionality factors are

$$\mathcal{N}^j = \sqrt{2j+1}\, n_0^j \tag{2.114}$$

$$\mathcal{O}^j = \sqrt{\frac{2j+1}{3}}\, \frac{n_1^j}{\mathcal{N}^j} \tag{2.115}$$

$$\mathcal{A}^j = \sqrt{\frac{2j+1}{5}}\, \frac{2n_2^j}{\mathcal{N}^j} \tag{2.116}$$

Since the orientation $\mathcal{O}^j$ and the alignment $\mathcal{A}^j$ depend on $n_1^j/\mathcal{N}^j$ and $n_2^j/\mathcal{N}^j$, they are properties that do not depend on the total number of molecules in the level j. We note that Zare [62] introduced an extra factor of 2 in the proportionality factor of $\mathcal{A}^j$ by defining alignment (Eq. 2.113) so that $-1 \leq \mathcal{A}^j \leq 2$ for large j.

Figure 2.3 shows some possible distributions of m levels for $j = 2$, each characterized by a different linear combination of moments.

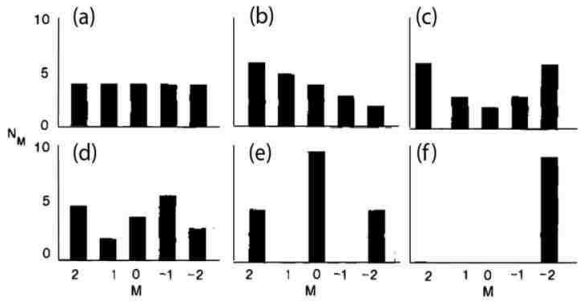

Figure 2.3: Examples of distributions of m for $j = 2$ [61]. Panel (a) shows a population uniformly distributed among the m levels. Panel (b) shows a population plus an orientation. Panel (c) shows a population plus an alignment. Panels (d), (e), and (f) show m distributions that involve linear combinations of more than two moments.

The moments can be interpreted within a semiclassical vector model, in which the angular momentum vector $\mathbf{j}$ precesses about the z axis with cone angle θ. The length of $\mathbf{j}$ is $\hbar\sqrt{j(j+1)}$, the square root of the eigenvalue of $\hat{j}^2$. The projection of $\mathbf{j}$ onto the z axis is $\hbar m$, the eigenvalue of $\hat{j}_z$. The cone angle is related to m and j by

$$\cos\theta = \frac{m}{\sqrt{j(j+1)}}. \tag{2.117}$$

Since $m/\sqrt{j(j+1)}$ already appears on the right-hand side of Eq. 2.112, one sees that orientation is the average value of $\cos\theta$ over all of the molecules with a given j. In terms of Legendre polynomials, it is the average value of $P_1(\cos\theta)$ within the level j.

For large j, in this approximation the K^{th} moment is proportional to $\langle P_K(\cos\theta)\rangle$; the m distribution can be written as a Legendre polynomial expansion of the corresponding $\cos\theta$ distribution. This interpretation follows from an approximation from Edmonds [63] that relates $3j$ coefficients to Legendre polynomials. Using the approximation leads to

$$\mathcal{T}^j_{mK} \approx \sqrt{\frac{2K+1}{2j+1}} P_K\left(\frac{m}{\sqrt{j(j+1)}}\right). \tag{2.118}$$

The approximation is best for $K \ll j$ and is exact for $K = 0$ and 1. Using this identity and Eq. 2.109, one can show that the moments are

$$n^j_K \approx \mathcal{N}^j \sqrt{\frac{2K+1}{2j+1}} \langle P_K(\cos\theta)\rangle. \tag{2.119}$$

Orientation is $\langle P_1(\cos\theta)\rangle$ and alignment is $2\langle P_2(\cos\theta)\rangle$ (because of the extra factor of 2 discussed earlier). Within this approximation, we can define similar quantities for $K > 2$ to be $\langle P_K(\cos\theta)\rangle$. By Eq. 2.119, these quantities will be proportional to the moments n^j_K by the factor $\mathcal{N}^j\sqrt{(2K+1)/(2j+1)}$.

A distribution with only a population corresponds to angular momentum vectors $\mathbf{j}$ pointed in random directions. A distribution with an orientation corresponds to a tendency for the angular momentum vectors $\mathbf{j}$ to point in one general direction. A distribution with an alignment corresponds to a tendency for the angular momentum vectors $\mathbf{j}$ to point either in some direction $\hat{r}$ or in the opposite direction $-\hat{r}$; one can then think of $\mathbf{j}$ as a two-headed arrow.

Figure 2.4 shows a comparison between several discrete quantum mechanical distributions of m levels for $j = 2$, plotted as a function of $m/\sqrt{j(j+1)}$, and the continuous semiclassical distributions, plotted as a function of $\cos\theta$. Each panel shows a distribution

$$N^j_m = \sum_K n^j_K \mathcal{T}^{j*}_{Km} \tag{2.120}$$

that is composed of only one moment K as a function of $\cos\theta$. The quantum mechanical distributions are points calculated for values of $\cos\theta = m/\sqrt{j(j+1)}$

and the Legendre polynomial approximations are lines. The agreement is fairly good for the higher moments, even though this is a low j.

Let us now consider a cell environment with an initial distribution N_m^j of molecules in m levels for a given j. Collisions will lead to the population of other levels $j'm'$. We can relate the distribution of the molecules in the final m' levels of a specific j' to N_m^j using the cross sections $\sigma(jm \to j'm')$. The relation can be given explicitly by defining a dimensionless probability matrix $\mathcal{P}^{jj'}$, with elements

$$\mathcal{P}_{mm'}^{jj'} = \frac{k_j^2}{\pi}\sigma(jm \to j'm'). \tag{2.121}$$

The probability matrix relates the two distributions such that

$$N_{m'}^{j'} = \sum_m N_m^j \mathcal{P}_{m,m'}^{jj'}, \tag{2.122}$$

or in terms of matrices

$$\mathbf{N}^{j'} = \mathbf{N}^j \mathcal{P}^{jj'}. \tag{2.123}$$

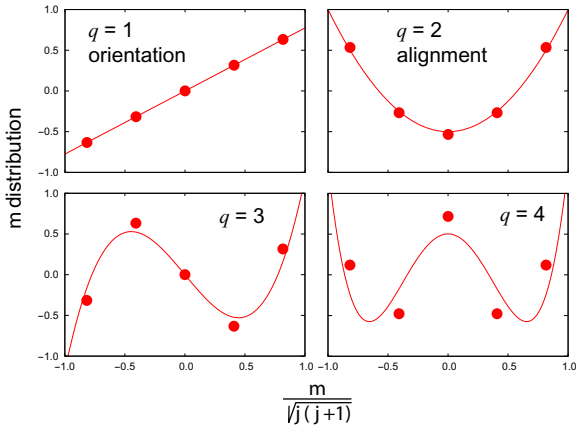

Figure 2.4: Distributions of m levels for $j = 2$ as a function of $\cos\theta$. (In this figure, q is used instead of K to denote the moment.) To obtain a physical distribution, one must add a population moment. The points were determined from Eq. 2.120 with $n_K^j = 1$ (that is, they are $\mathcal{T}_{Km}^{j*}$), while the lines were determined from Eq. 2.118; the agreement is fairly good even for $K = 4$.

We can transform this equation to the moment basis by first inserting

$$\mathcal{T}^j(\mathcal{T}^j)^\dagger = \mathbf{I}, \tag{2.124}$$

where $\mathbf{I}$ is the identity matrix, into Eq. 2.123. Then

$$\mathbf{N}^{j'} = \mathbf{N}^j \mathcal{T}^j (\mathcal{T}^j)^\dagger \mathcal{P}^{jj'}. \tag{2.125}$$

By multiplying by $\mathcal{T}^{j'}$ on the right and using Eq. 2.109, one finds

$$\mathbf{N}^{j'}\mathcal{T}^{j'} = \mathbf{N}^j \mathcal{T}^j (\mathcal{T}^j)^\dagger \mathcal{P}^{jj'} \mathcal{T}^{j'} \tag{2.126}$$

$$\mathbf{n}^{j'} = \mathbf{n}^j \left\{ (\mathcal{T}^j)^\dagger \mathcal{P}^{jj'} \mathcal{T}^{j'} \right\}. \tag{2.127}$$

The term in curly brackets in Eq. 2.127 is the transformation of the probability matrix to the moment basis:

$$\mathcal{Q}^{jj'} = (\mathcal{T}^j)^\dagger \mathcal{P}^{jj'} \mathcal{T}^{j'}. \tag{2.128}$$

The matrix $\mathcal{Q}^{jj'}$ is rectangular and of dimension $(2j+1) \times (2j'+1)$. Its elements are

$$\mathcal{Q}^{jj'}_{KK'} = \delta_{KK'} d_K(j, j') \qquad K = 0, \ldots, 2j, \quad K' = 0, \ldots, 2j' \tag{2.129}$$

so that the matrix (for $j' > j$) is

$$\mathcal{Q}^{jj'} = \left(\begin{array}{ccc|ccc} d_0 & \ldots & 0 & 0 & \ldots & 0 \\ \vdots & \ddots & \vdots & \vdots & \ddots & \vdots \\ 0 & \ldots & d_{2j} & 0 & \ldots & 0 \end{array} \right). \tag{2.130}$$

The moment distribution is a more elegant way to analyze m-changing collisions because of the diagonal form of the probability matrix in this basis; the moments are completely independent of each other.

Now we can express Eq. 2.127 as

$$\mathbf{n}^{j'} = \mathbf{n}^j \mathcal{Q}^{jj'}, \tag{2.131}$$

or

$$n^{j'}_K = \sum_{K'} n^j_{K'} Q^{jj'}_{K'K} = \delta_{KK'} n^j_{K'} d_{K'}(j, j') = n^j_K d_K(j, j'), \tag{2.132}$$

which shows that the probability $d_K(j,j') = n_K^{j'}/n_K^j$.

By using the definitions of $\mathcal{O}^j$ and $\mathcal{A}^j$ (Eqs. 2.115 and 2.116) and the fact that

$$d_0(j,j') = \frac{n_0^{j'}}{n_0^j} = \frac{\mathcal{N}^{j'}}{\sqrt{2j'+1}}\frac{\sqrt{2j+1}}{\mathcal{N}^j} = \frac{\mathcal{N}^{j'}}{\mathcal{N}^j}\sqrt{\frac{2j+1}{2j'+1}}, \tag{2.133}$$

one can determine that the fraction of orientation $= \langle P_1(\cos\theta)\rangle$ retained by the molecules in j' after many molecules have undergone collisional transitions from j is

$$\frac{\mathcal{O}^{j'}}{\mathcal{O}^j} = \frac{d_1(j,j')}{d_0(j,j')}. \tag{2.134}$$

Similarly, the fraction of alignment $= 2\langle P_2(\cos\theta)\rangle$ retained is

$$\frac{\mathcal{A}^{j'}}{\mathcal{A}^j} = \frac{d_2(j,j')}{d_0(j,j')}. \tag{2.135}$$

Moreover, by using Eqs. 2.119 and 2.133, one can show that in general

$$\frac{\langle P_K(\cos\theta)\rangle_{j'}}{\langle P_K(\cos\theta)\rangle_j} = \frac{d_K(j,j')}{d_0(j,j')}, \tag{2.136}$$

where $\langle P_K(\cos\theta)\rangle_{j'}$ is the average value of P_K over all the molecules with the rotational quantum number j'.

Using Eq. 2.130 along with a paper by Derouard [12], one can show that the $d_K(j,j')$ are related to the Grawert coefficients:

$$d_K(j,j') = \sum_{\lambda=|j-j'|}^{j+j'} (-1)^{j+j'+\lambda+K}(2\lambda+1)\begin{Bmatrix}\lambda & j & j'\\ K & j' & j\end{Bmatrix} B_\lambda(j,j') \tag{2.137}$$

$$B_\lambda(j,j') = \sum_{K=0}^{2j_<}(-1)^{j+j'+\lambda+K}(2K+1)\begin{Bmatrix}\lambda & j & j'\\ K & j' & j\end{Bmatrix} d_K(j,j'), \tag{2.138}$$

where $j_< = \min(j,j')$. The d_K and B_λ are analogous to alternative basis sets connected by an orthogonal transformation. Therefore, if one determines the Grawert coefficients, one has all the information needed to determine the fraction of a moment preserved after many collisions.

One can use Eqs. 2.138 and 2.98 to show that the $j \rightarrow j'$ cross sections are proportional to d_0,

$$\sigma(j \rightarrow j') = \frac{\pi}{k_j^2}\sqrt{\frac{2j'+1}{2j+1}}d_0(j,j'), \tag{2.139}$$

which defines the cross section for the collision transfer of population from j to j'. One can define [64] similar cross sections for the transfer of any K^{th} moment

$$\sigma_K(j \rightarrow j') = \frac{\pi}{k_j^2}\sqrt{\frac{2j'+1}{2j+1}}d_K(j,j'). \tag{2.140}$$

The rate constant $k(j \rightarrow j')$ for transitions at temperature T is the following convolution of the energy-dependent cross section (see Section 4.2.1):

$$k(j \rightarrow j') = \sqrt{\frac{1}{\pi\mu}\left(\frac{2}{kT}\right)^3}\int_0^\infty \sigma(j \rightarrow j'; E_{\text{kin}})\, E_{\text{kin}}\, e^{-E_{\text{kin}}/(kT)}\, dE_{\text{kin}}. \tag{2.141}$$

In this equation, we explicitly included the dependence of the cross section on E_{kin}, the kinetic energy of the incident particle, but usually we will suppress it. To generalize Eqs. 2.134 and 2.135 to a cell environment where the molecules have a thermal distribution of energies, one would need to evaluate the ratios

$$\frac{\int_0^\infty d_K(j \rightarrow j'; E_{\text{kin}})\, E_{\text{kin}}\, e^{-E_{\text{kin}}/kT}\, dE_{\text{kin}}}{\int_0^\infty d_0(j \rightarrow j'; E_{\text{kin}})\, E_{\text{kin}}\, e^{-E_{\text{kin}}/kT}\, dE_{\text{kin}}}. \tag{2.142}$$

Chapter 3

Potential energy surface calculations

We have calculated potential energy surfaces (PESs) for the excited states of the HeNaK and ArNaK molecules that correspond asymptotically to He ($^1S_0$) or Ar ($^1S_0$) + NaK ($A\,^1\Sigma^+$). Our calculations were performed on the Stampede supercomputer at the University of Texas using the GAMESS code [65].

In this chapter we will describe each calculation, present comparisons between the different surfaces, and describe fits of some surfaces to the long range analytic form discussed in Section 2.3.2.

3.1 Electronic structure calculations

We have calculated a total of four PESs (two for HeNaK and two for ArNaK) for the following reasons. At first, we used an MCSCF/MR-CISD method to calculate the HeNaK PES, but similar calculations for ArNaK would have required too many resources. Instead we performed what were quicker EOM-CCSD calculations, and to facilitate comparison we calculated PESs with this method for both HeNaK and ArNaK. Since the calculations took less computer time, we were able to use a larger basis set. We also performed counterpoise corrections.

By performing the counterpoise corrections, we could assess how much our potentials (and our scattering cross sections) were affected by the basis set superposition error. In addition, we have started to examine basis set convergence by performing new EOM-CCSD calculations for ArNaK with a larger basis set.

To distinguish between the PESs within the text, we will establish the following convention: The MCSCF/MR-CISD PES will be referred to as PES I: He, the EOM-CCSD PESs comparable for HeNaK and ArNaK as PES II: He and PES II: Ar, and the ArNaK PES with the larger basis as PES III: Ar.

3.1.1 Details of the calculations

First, we describe our MCSCF/MR-CISD [29, 30] calculation for the HeNaK PES [2] (PES I: He). We used a 6-311G (Pople's valence triple zeta) basis set with extra polarization functions. The basis set for He was $5s2p/3s2p$ [66]. (This notation means that five primitive s-type and two primitive p-type GTOs were contracted into three s-type basis functions and two p-type basis functions.) The basis set for Na was $13s9p3d1f/6s5p3d1f$ [66, 67] and for K it was $14s11p6d1f/8s7p4d1f$ [68]. The polarization functions are listed in Table 3.1.

Table 3.1: Gaussian type polarization basis functions used for PES I: He. Column three gives the coefficients of the normalized GTO in the contracted orbital.

Na AOs	Exponent	Coefficient	K AOs	Exponent	Coefficient
d	0.7000000	1.000000000000	d	13.3700000	0.062591844459
d	0.1750000	1.000000000000		3.4210000	0.310723063593
d	0.0437500	1.000000000000		1.0630000	0.773607911982
f	0.1500000	1.000000000000	d	0.6870000	1.000000000000
			d	0.2290000	1.000000000000
			d	0.0763333	1.000000000000
			f	1.1100000	1.000000000000

We performed an MCSCF calculation with fifteen frozen core orbitals ($1s$ for He, $1s$, $2s$, $2p_{x,y,z}$ for Na, and $1s$, $2s$, $2p_{x,y,z}$, $3s$, $3p_{x,y,z}$ for K) and two active orbitals ($3s$ for Na and $4s$ for K), for a total of 3 CSFs. Using those CSFs, we performed

an MR-CISD calculation. There were six frozen core orbitals ($1s$ for Na, and $1s$, $2s$, $2p_{x,y,z}$ for K) and eleven orbitals in the active space ($1s$ for He, $2s$, $2p_{x,y,z}$, $3s$ for Na, and $3s$, $3p_{x,y,z}$, $4s$ for K). All single and double excitations from any CSF in the active space were included, for a total of 5,673,309 CSFs of A' symmetry in the C_s symmetry of our calculations.

As we mentioned, we weren't able to perform a comparable MCSCF/MR-CISD calculation for ArNaK. Instead we performed EOM-CCSD [69] calculations (PES II: He and PES II: Ar), and we treated HeNaK and ArNaK in a parallel fashion [3]. Later we will discuss the differences between these two methods.

The basis set was obtained using the EMSL basis set library [70, 71] for a 6-311+G** basis set [67, 68, 72, 73]. This basis set differs from that used in the MCSCF/MR-CISD calculation in the following ways. As the '+' indicates, diffuse basis functions were included in the calculation. We split the f functions centered on Na [66] and K [68] in our MCSCF/MR-CISD basis set using the same factors that had been used to split the d functions. Moreover, we added one d function to He [66] with exponent 2.0 and one f function to Ar [74] with exponent 0.89. This resulted in a $5s2p1d/3s2p1d$ basis for He, a $14s11p2d1f/7s6p2d1f$ basis for Ar, a $14s10p3d3f/7s6p3d3f$ basis for Na, and a $15s12p6d3f/9s8p4d3f$ basis for K. The polarization functions are listed in Table 3.2.

For the HeNaK calculation we froze the same six core orbitals as in the MCSCF/MR-CISD calculation ($1s$ for Na and $1s$, $2s$, $2p_{x,y,z}$ for K). For the ArNaK calculation, there were eleven frozen core orbitals: $1s$ for Na, $1s$, $2s$, $2p_{x,y,z}$ for Ar, and $1s$, $2s$, $2p_{x,y,z}$ for K. The HeNaK potential was size consistent to within 10^{-10} E_h, where E_h denotes a Hartree, and the ArNaK potential was size consistent to within 10^{-9} E_h (both errors are within the noise level of the calculation). We used the counterpoise method to correct for basis set superposition error [45].

Finally, we obtained an ArNaK EOM-CCSD PES with a larger basis set (PES III: Ar). We used the cc-pCVTZ basis set (Dunning's correlation consistent core-valence triple zeta basis set) for Na [75], Feller's CVTZ basis set for K [76, 77] and an aug-cc-pCVTZ basis set for Ar (where aug means diffuse functions were included) [78, 79]. This gave an $18s12p4d2f/7s6p4d2f$ basis for Na, a

Table 3.2: Gaussian type polarization basis functions used for PES II: He and PES II: Ar. Column three gives the coefficients of the normalized GTO in the contracted orbital.

He AOs	Exponent	Coefficient	Ar AOs	Exponent	Coefficient
d	2.0000000000	1.00000000	d	1.7000000000	1.00000000
			d	0.4250000000	1.00000000
			f	0.8900000000	1.00000000
Na AOs	Exponent	Coefficient	K AOs	Exponent	Coefficient
d	0.70000000	1.000000000000	d	13.3700000	0.062591844459
d	0.1750000	1.000000000000		3.4210000	0.310723063593
d	0.0437500	1.000000000000		1.0630000	0.773607911982
f	0.6000000	1.000000000000	d	0.6870000	1.000000000000
f	0.1500000	1.000000000000	d	0.2290000	1.000000000000
f	0.0375000	1.000000000000	d	0.0763333	1.000000000000
			f	3.3300000	1.000000000000
			f	1.1100000	1.000000000000
			f	0.3700000	1.000000000000

Table 3.3: Gaussian type polarization basis functions used for PES III: Ar. Column three gives the coefficients of the normalized GTO in the contracted orbital.

Na AOs	Exponent	Coefficient	K AOs	Exponent	Coefficient
d	0.1473000	1.000000000000	d	1.75000000	1.000000000000
d	0.0623000	1.000000000000	d	0.50500000	1.000000000000
d	5.4229000	1.000000000000	d	0.10400000	1.000000000000
d	1.6074000	1.000000000000	d	0.04700000	1.000000000000
f	0.1284000	1.000000000000	f	1.20000000	1.000000000000
f	3.4291000	1.000000000000	f	0.09000000	1.000000000000
Ar AOs	Exponent	Coefficient	Ar AOs	Exponent	Coefficient
d	0.4100000	1.000000000000	d	0.1690000	1.000000000000
d	1.2540000	1.000000000000	f	0.8900000	1.000000000000
d	11.9380000	1.000000000000	f	13.6740000	1.000000000000
d	32.2140000	1.000000000000	f	0.4060000	1.000000000000

$60s25p4d2f/8s7p4d2f$ basis for K, and an $18s12p5d3f/8s7p5d3f$ basis for Ar. The polarization functions are listed in Table 3.3.

The frozen core orbitals were the same as in the other calculations. The PES was

size consistent to within 10^{-9} E_h, and we used the counterpoise method to correct for BSSE [45].

We calculated the energies as a function of the Jacobi coordinates shown in Fig. 2.2. The NaK bond length is r, and R and θ are the distance and angle of the incident particle from the center of mass of NaK. In our initial calculations the value of r was fixed at $r_0 = r_e = 7.935$ a_0, the experimental value [7] of the equilibrium internuclear separation. This value was appropriate for the rigid rotator scattering calculations that will be described in Chapter 4. For these surfaces, we included 21 values of R between 3.5 and 25.0 a_0 for HeNaK, and 21 values between 4.5 and 30 a_0 for ArNaK. For each R we typically calculated 13 angular points evenly spaced between 0° and 180° (every 15°). The MR-CISD method is not size consistent, and for this reason all relative energies for PES I: He were calculated with respect to the energy of HeNaK with a large He - NaK distance and not with respect to the sum of the energies of the fragments.

The rigid rotator potentials we obtained are shown in Fig. 3.1. Each PES is predominantly repulsive with very shallow van der Waals wells at long range. At the experimental temperature of 600 K, the average energy is $kT \approx 0.002$ E_h (440 cm^{-1}). The well depths are much smaller than the average energy; depending on the surface, the deepest wells ranged from 1.4×10^{-5} E_h to 1.8×10^{-4} E_h (3 cm^{-1} to 41 cm^{-1}).

3.1.2 Comparison between methods

Table 3.4 lists the time in processor-hours required to calculate energies at 100 geometries for each surface, including the additional time required to perform the counterpoise correction.

We performed calculations for several r with R set to a very large number (10,000 a_0) to determine the spectroscopic constants of NaK ($A\,^1\Sigma^+$); the results are tabulated in Table 3.5. In the table, r_e is the equilibrium internuclear separation, w_e quantifies the curvature of the potential at its minimum, and $w_e x_e$ quantifies the anharmonicity of the potential. For PES III: Ar, the value of $w_e x_e$ is smaller than that given by our other surfaces and the experimental data; we optimized this

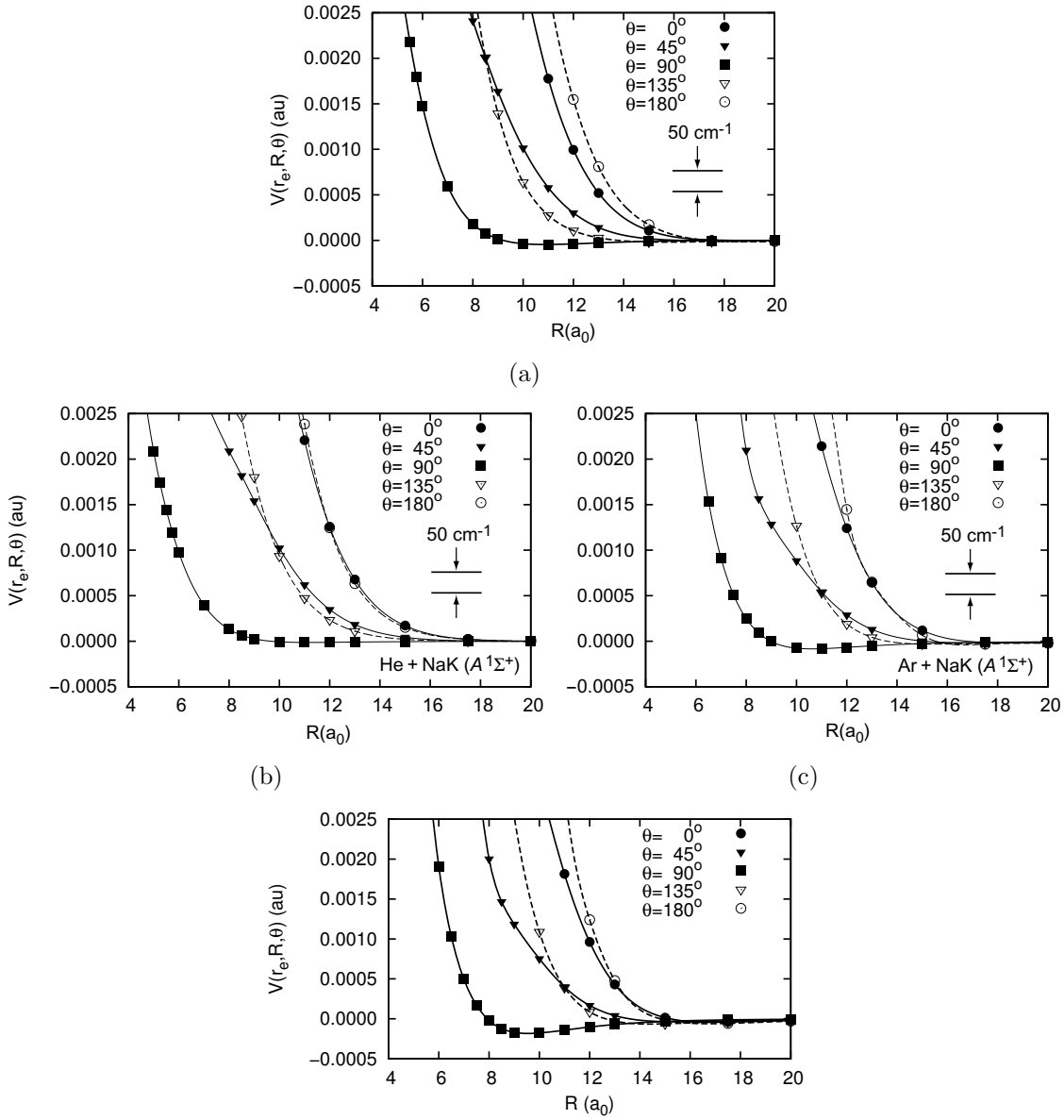

Figure 3.1: Rigid rotator PESs ($r = 7.935\ a_0$) as a function of R for fixed values of θ. Panel (a) is PES I: He, Panels (b) and (c) are PES II: He and PES II: Ar, and Panel (d) is PES III: Ar. Panel (a) reproduced from [2] with the permission of AIP publishing. Panels (b) and (c) reprinted from [3] with permission from Elsevier.

Table 3.4: Timing in processor-hours for every 100 geometries. Most calculations used 16 cpu's.

	PES I	PES II	PES III
HeNaK	2667[a]	38[a] 53[b]	N/A
ArNaK	N/A	59[a] 92[b]	243[a] 285[b]

[a]No counterpoise correction
[b]Time for the two additional surfaces needed to determine the counterpoise correction

Table 3.5: Spectroscopic constants for NaK ($A\,^1\Sigma^+$)

	$r_e\,(a_0)$	$w_e\,(\mathrm{cm}^{-1})$	$w_e x_e\,(\mathrm{cm}^{-1})$
PES I: He	7.72	93.8	0.250
PES II: He and PES II: Ar	7.95	84.0	0.266
PES III: Ar	7.87	90.1	0.140
Experiment, Ross *et al.* [7]	7.935	81.25	0.2747

basis set for smaller R where Ar interacts with NaK. The results are the same for PES II: He and PES II: Ar (as they should be), and these surfaces gave the best agreement with experiment for all three spectroscopic constants.

Figure 3.2 compares our NaK ($A\,^1\Sigma^+$) potentials with a Rydberg-Klein-Rees (RKR) potential determined from experimental data [7]. Panel (a) shows PES I, II, and III for a wide range of bond lengths. For most bond lengths, PES II agrees the best with experiment. All three potentials are similar near the equilibrium value but gradually diverge from the RKR curve as the bond stretches. The poor value of PES II: He (and PES II: Ar) near $r = 12\ a_0$ is likely due to limitations of the method used to calculate the PES; PES II and PES III were calculated using EOM-CCSD, which is a single-reference method, and that means the results may not be as accurate for higher bond lengths of NaK. We note that PES III does not have an anomalous point at $r = 12\ a_0$; it is not easy to predict where the method will fail. The single-reference nature of EOM-CCSD is part of the reason the calculations are quicker, and most of the experimental data is for low vibrational levels of NaK,

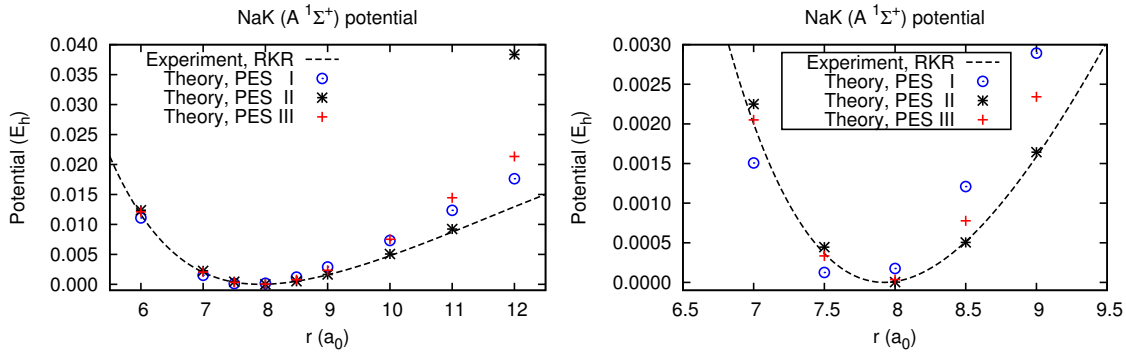

Figure 3.2: Comparison of the experimental NaK ($A\,^1\Sigma^+$) potential of Ross *et al.* [7] with the potentials obtained from our PESs. All potentials were shifted vertically so that their zeroes of energy are at their respective r_e. In Panel (a), we show the comparison for many bond lengths r. PES II agrees the best with experiment for most bond lengths but fails at $r = 12\ a_0$ because of limitations in the method used to calculate the PES. In Panel (b), we show the potential only for bond lengths near the bottom of the well, since most of the experimental data is for low vibrational levels. In this region PES II agrees the best with experiment.

for which EOM-CCSD works well. Panel (b) shows that near r_0 PES II agrees the best with experiment.

We now make some comparisons between our surfaces, noting again that at 600 K the average initial kinetic energy of He or Ar is $kT \approx 0.002\ E_h$ (440 cm^{-1}) and that the potential wells are fairly small compared to the collision energy.

First, we compare PES II: He and PES II: Ar to probe differences between Ar and He's interactions with NaK. Panel (a) of Fig. 3.3 shows that the ArNaK PES tends to have steeper repulsive walls. The ArNaK PES also has deeper wells; argon is more polarizable and the long range van der Waals attraction will be stronger between Ar and NaK. For ArNaK the deepest well is about 18 cm^{-1}, while for HeNaK it is 3 cm^{-1}; these wells are both near $\theta = 90°$ and $R = 11\ a_0$. Panels (b) and (c) of Fig. 3.3 show that in general the ArNaK potential is more asymmetric with respect to $\cos\theta = 0$ ($\theta = 90°$) than the HeNaK potential; a homonuclear diatomic molecule would have an atom-diatom potential that was exactly symmetric with

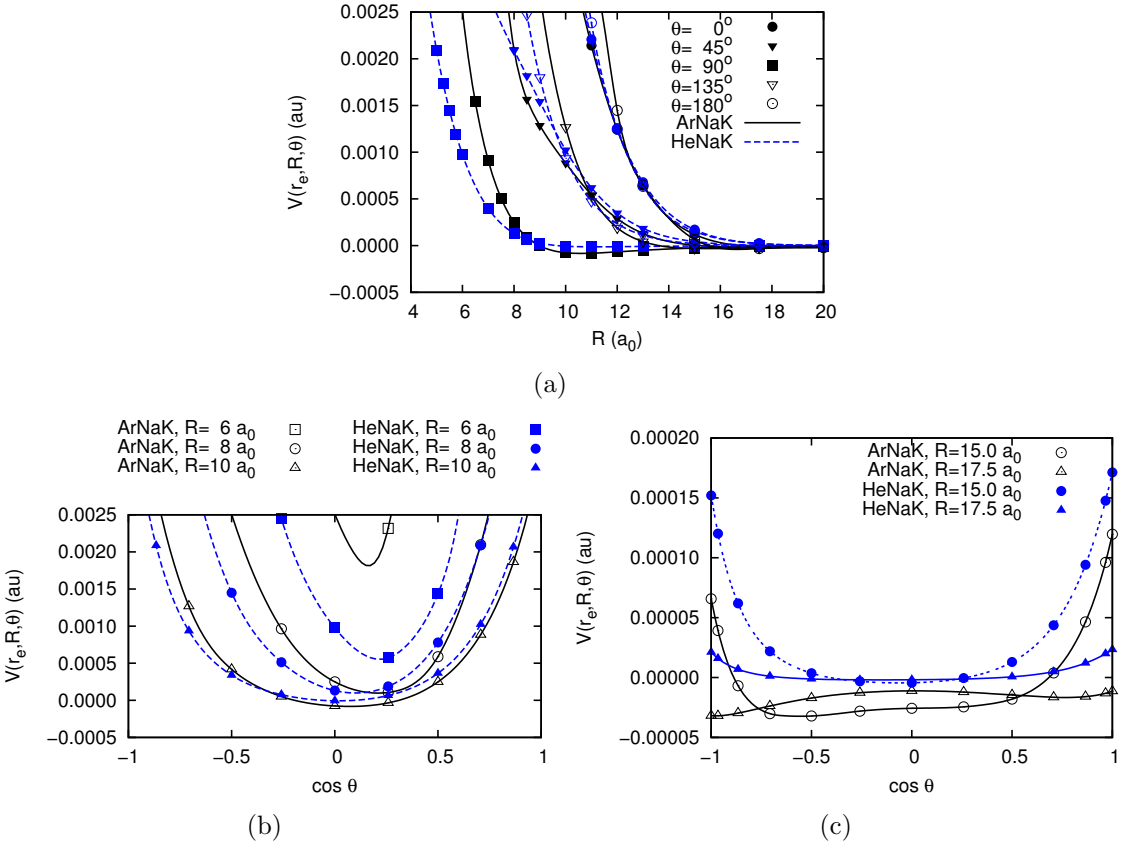

Figure 3.3: Comparison between the rigid rotator PES II: He and PES II: Ar. In Panel (a) we present the comparison for fixed angles θ as a function of R. In Panels (b) and (c) we present comparisons for fixed R as a function of $\cos\theta$.

respect to $\cos\theta = 0$. One therefore intuitively expects that He+NaK will show more of a propensity for Δj even transitions than Ar+NaK will.

Next, we make three more comparisons to assess the uncertainties in the PESs. First, we compare counterpoise corrected and uncorrected PESs. Then, we compare our HeNaK surfaces obtained with different methods and basis sets. Finally, we compare our ArNaK surfaces obtained with the same method but different basis sets, where both surfaces have been counterpoise corrected. The small differences between the surfaces due to these uncertainties can be important. Later in Chapter 4

we will see that the propensity depends very sensitively on the surface, and we will try to correlate differences in the surfaces with differences in the cross sections.

As discussed in [44], two often compensatory errors are associated with finite basis sets. These are BSSE and basis set convergence error. Correcting for BSSE tends to decrease the well depths of a PES, while using a larger basis set tends to increase them. Comparing our two counterpoise corrected ArNaK surfaces is a first step in assessing our basis set convergence error, and indeed we will see that the larger basis yields a counterpoise corrected PES with deeper wells.

In Fig. 3.4, we compare the counterpoise corrected and uncorrected PES II: He and PES II: Ar. The counterpoise correction shifted the repulsive walls to higher R and, as expected, decreased the well depths of each surface. For HeNaK, the deepest well decreased by a factor of six, from 18 cm^{-1} to 3 cm^{-1}. For ArNaK, the

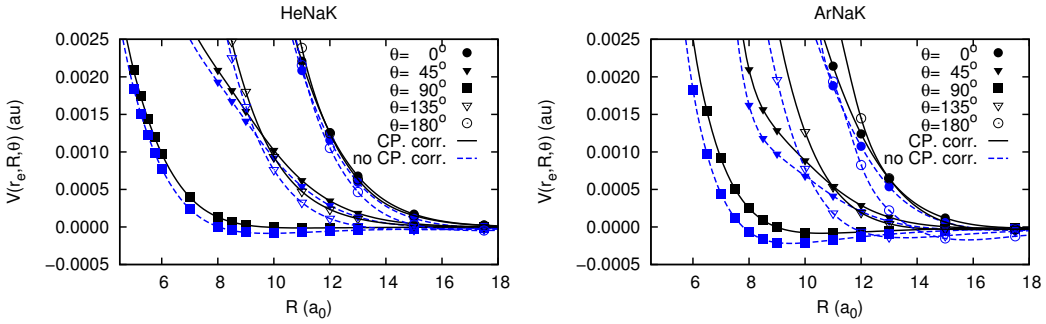

Figure 3.4: Comparison between the counterpoise corrected (solid lines) and uncorrected (dashed lines) rigid rotator PES II: He and PES II: Ar. Panel (a) shows the comparison for HeNaK and Panel (b) for ArNaK.

deepest well decreased by a factor of about two and a half, from 46 cm^{-1} to 18 cm^{-1}. Sometimes the corrections were as large as the uncorrected energies. For instance, for HeNaK for $R = 8\ a_0$, $\theta = 90°$, the uncorrected energy was about $1.3 \times 10^{-4}\ E_\mathrm{h}$ (29 cm^{-1}) and the correction was $1.26 \times 10^{-4}\ E_\mathrm{h}$ (28 cm^{-1}).

Next we comment on the differences between our HeNaK potentials (PES I: He and PES II: He). From Panel (a) of Fig. 3.5, we see that while each potential is

predominantly repulsive, the positions of the repulsive walls vary depending on the surface. PES II: He shows less repulsion and a shallower well (3 cm^{-1} vs. 10 cm^{-1}) at $\theta = 90^\circ$ and $R = 11\ a_0$, the position of PES II: He's deepest well. PES I: He had its deepest well of 11 cm^{-1} near $\theta = 105^\circ$ and $R = 11\ a_0$.

The difference in well depths between the two HeNaK surfaces is partly due to the fact that PES II: He was counterpoise corrected while PES I: He was not. Perhaps a better comparison of the potentials would be between the uncorrected PES II: He and PES I: He (Panel (b) of Fig. 3.5). The uncorrected PES II: He actually had a deeper well (18 cm^{-1} vs. 11 cm^{-1}) but the surfaces still show similar differences in their repulsive walls.

Panels (c)–(e) of Fig. 3.5 show that for $R \geq 10\ a_0$, PES II: He is more symmetric with respect to $\cos\theta = 0$, and we expect this system to show more of a propensity for Δj even transitions.

Finally, in Fig. 3.6 we present a comparison between the two ArNaK potentials obtained with different basis sets but the same method (PES II: Ar and PES III: Ar). PES II: Ar is more repulsive at any given R and has a shallower deepest well (18 cm^{-1} vs. 41 cm^{-1}). The deepest wells also occur near different geometries. For PES III: Ar, the deepest well occurs near $\theta = 75^\circ$ and $R = 8.50\ a_0$, as opposed to $\theta = 90^\circ$ and $R = 11\ a_0$ for PES II: Ar. In Panels (b)–(d), neither PES looks to be obviously more symmetric with respect to $\cos\theta = 0$ than the other.

3.1.3 Dependence on NaK bond length

Most of our scattering calculations were for a rigid rotator with $r = r_0$. Additional calculations are needed to handle vibrational excitation. Therefore we calculated the r-dependence of PES I: He and PES II: He and Ar by determining the potential for many values of R and θ at NaK bond lengths $r = 6$, 7, 8, 9, 10, and 11 a_0 (and also $r = 12$ and 13 a_0 for PES I: He).

Here we present the interaction energies for HeNaK and ArNaK obtained for different bond lengths r of NaK. For Figs. 3.7–3.12, we choose the zero of energy to be at large values of R, regardless of the bond length r. This convention corresponds

to the description of the coupling terms given in Section 2.4.4.

Figs. 3.7 and 3.8 show the interaction energies obtained from PES II: He and PES II: Ar side by side to facilitate comparison. In both figures, the left column shows the HeNaK surfaces and the right column shows the ArNaK surfaces. For every r, the ArNaK PES tends to have steeper repulsive walls and it also has deeper wells. For both surfaces a "shoulder" begins to appear at $r = 9\ a_0$ for $\theta = 45°$, and when $r = 11\ a_0$ this shoulder has become a secondary well.

Figs. 3.9 and 3.10 show the interaction energies for PES I: He and PES II: He. The left column shows PES I: He and the right column PES II: He. For bond lengths $r = 6 - 9\ a_0$ PES I: He is more repulsive at $\theta = 90°$ and for bond lengths $r = 10 - 11\ a_0$ it is less repsulsive. PES I: He also has a "shoulder" for $r = 11\ a_0$ and $\theta = 45°$.

Fig. 3.11 shows the interaction energies for PES I: He for the bond lengths $r = 12$ and $13\ a_0$. At larger bond lengths, the shoulder for $r = 11\ a_0$ and $\theta = 45°$ transitions to a secondary well, just as it did for PES II: He and Ar at $r = 11\ a_0$.

In Fig. 3.12 we take a closer look at the secondary wells that appeared for large bond lengths in Figs. 3.8 and 3.11; there are secondary wells for $\theta = 45°$, $60°$, and $75°$. Due to the single-reference nature of the EOM-CCSD calculation and its failing at $r = 12\ a_0$, we are wary of the results for $r = 10$ and $11\ a_0$. For this reason, it is interesting to see that the secondary wells appear in the multireference CI calculation as well, albeit for a higher bond length r.

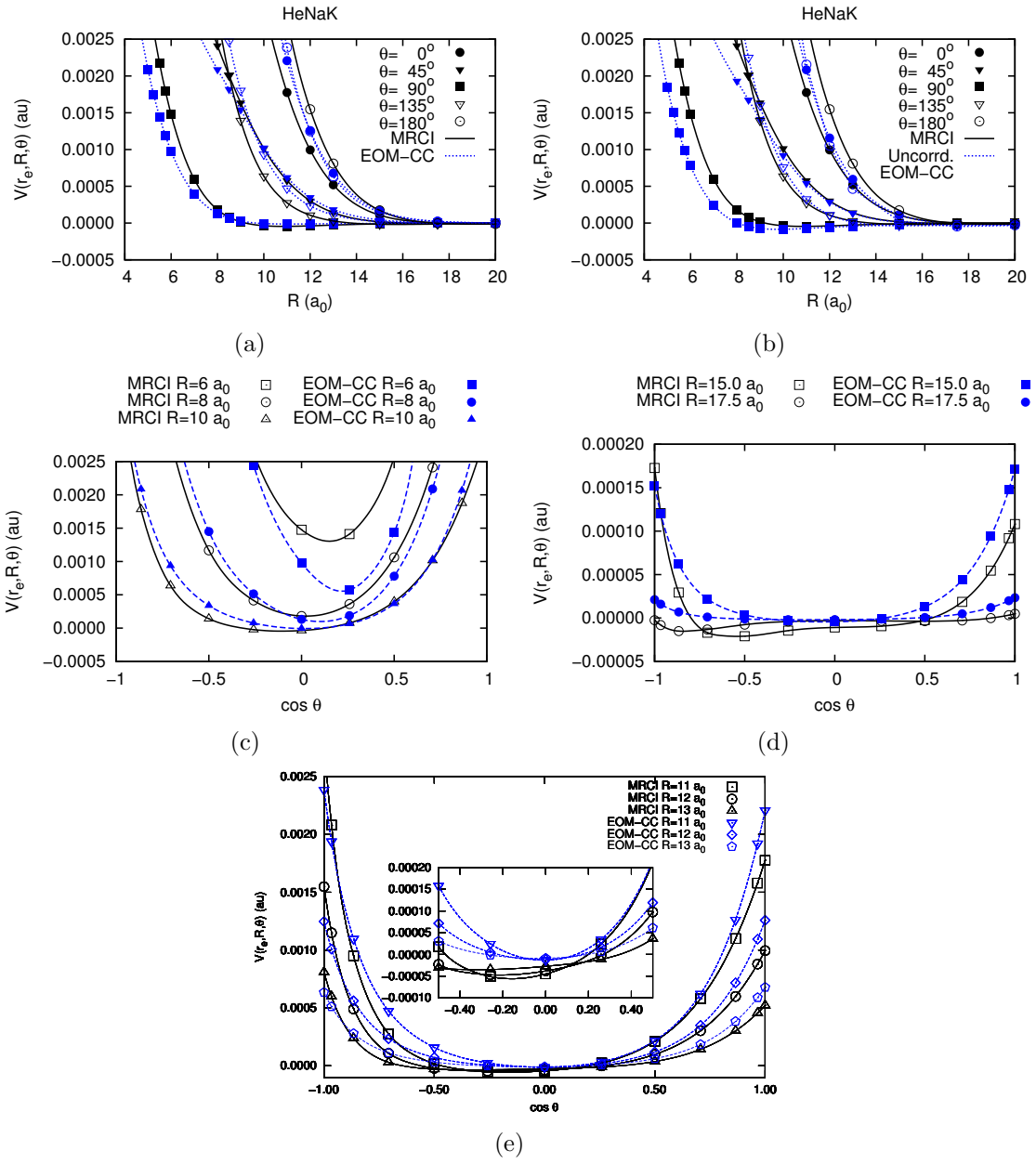

Figure 3.5: These panels compare our rigid rotator PES I: He (solid lines) and PES II: He (dashed lines). In Panels (a) and (c)–(e), we compare our PES I: He and counterpoise corrected PES II: He. In Panel (b) we compare our PES I: He and uncorrected PES II: He.

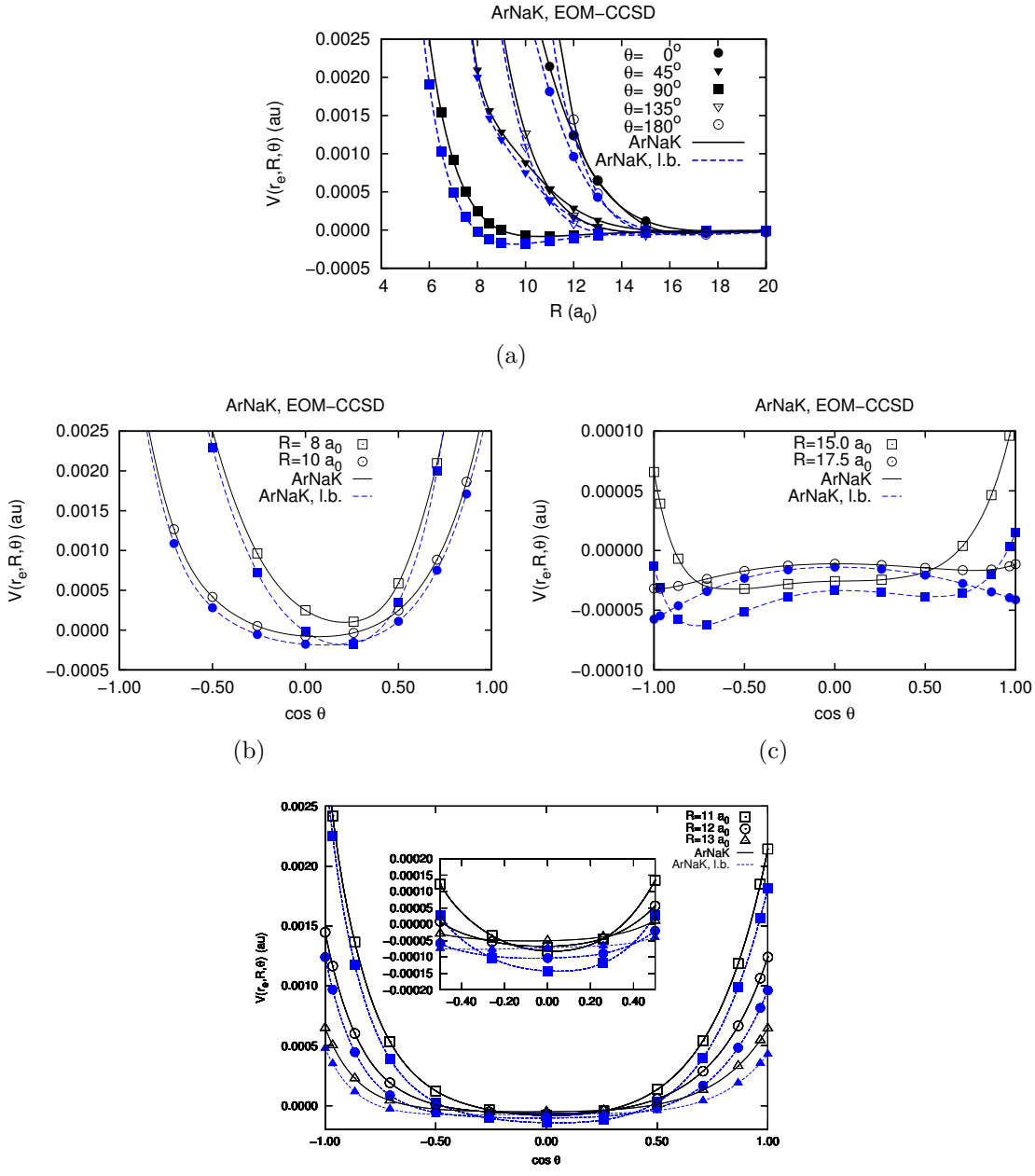

Figure 3.6: These panels compare the rigid rotator PES II: Ar and PES III: Ar. In each panel, the label 'ArNaK' corresponds to PES II: Ar and 'ArNaK, l.b.' to PES III: Ar. Panel (a) shows the PESs for fixed angles θ as a function of R. Panels (b)–(d) show the PESs for fixed R as a function of $\cos\theta$.

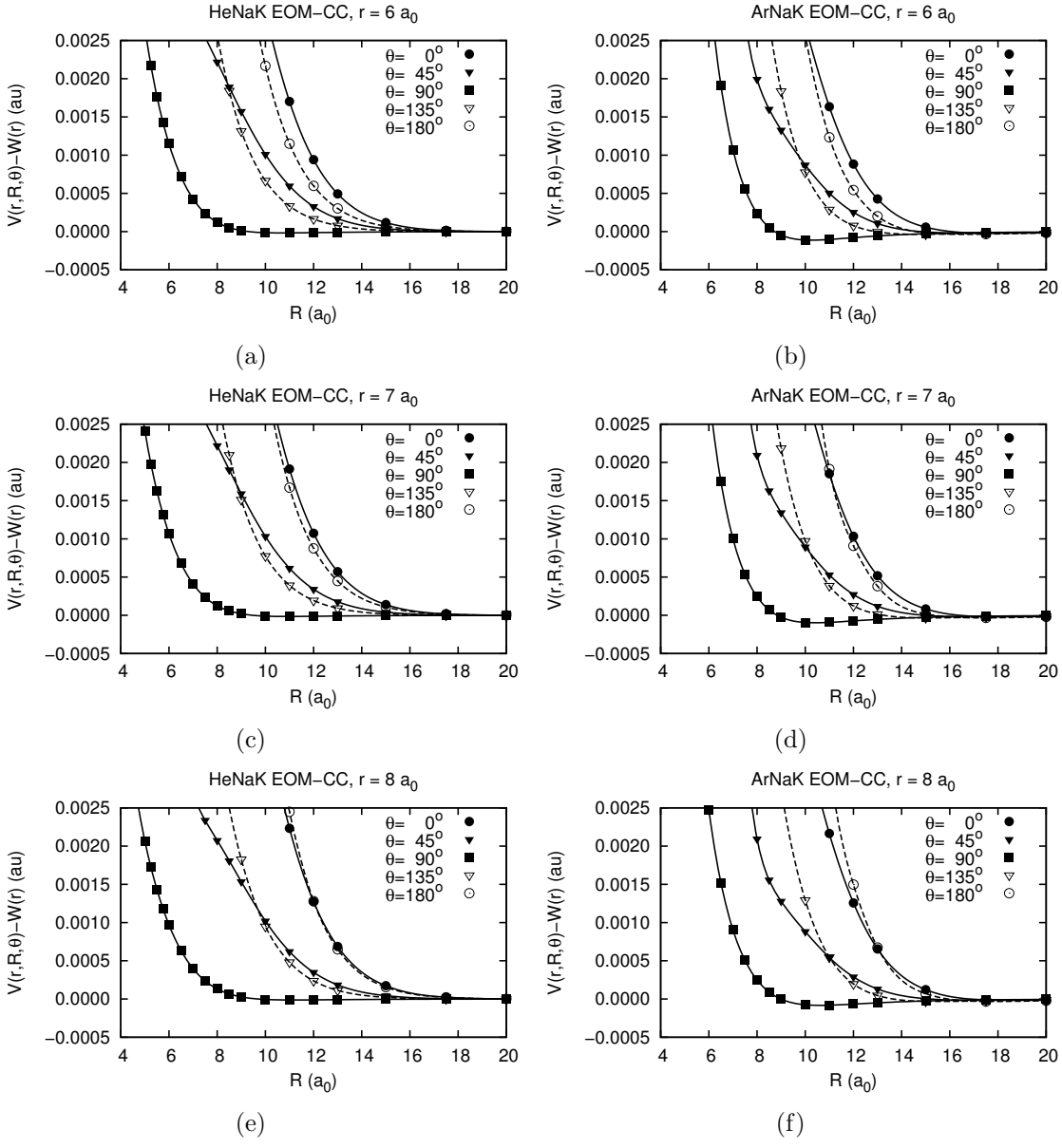

Figure 3.7: This figure shows the PES II: He and PES II: Ar interaction energies for $r = 6$ to 8 a_0, plotted as a function of R for fixed values of θ. The HeNaK and ArNaK interaction energies are shown side by side to facilitate comparison; the HeNaK interaction energies are shown in Panels (a), (c), and (e), while the ArNaK interaction energies are shown in Panels (b), (d), and (f).

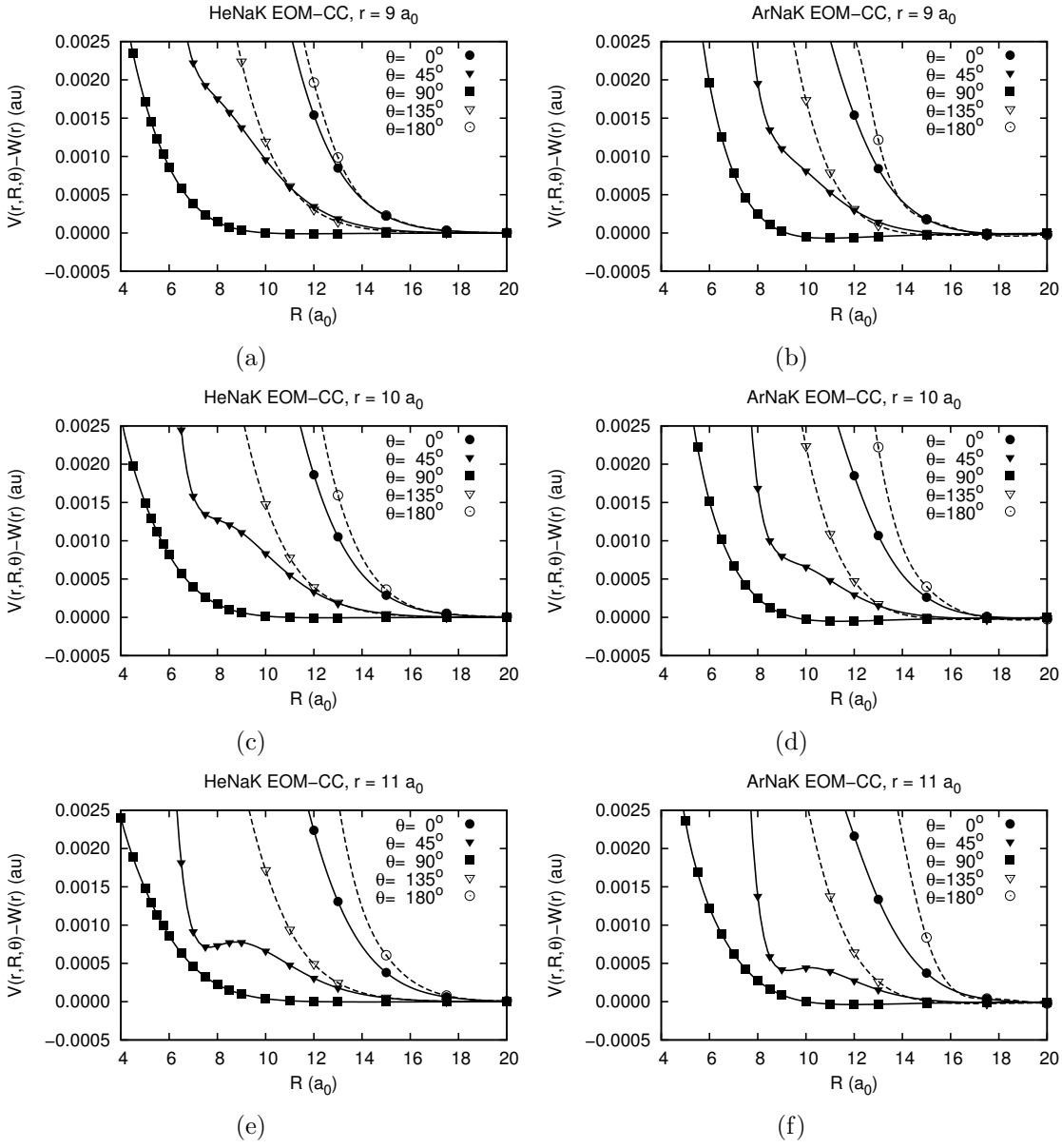

Figure 3.8: This figure shows the PES II: He and PES II: Ar interaction energies for $r = 9$ to 11 a_0, plotted as a function of R for fixed values of θ. The HeNaK interaction energies are shown in Panels (a), (c), and (e), while the ArNaK interaction energies are shown in Panels (b), (d), and (f).

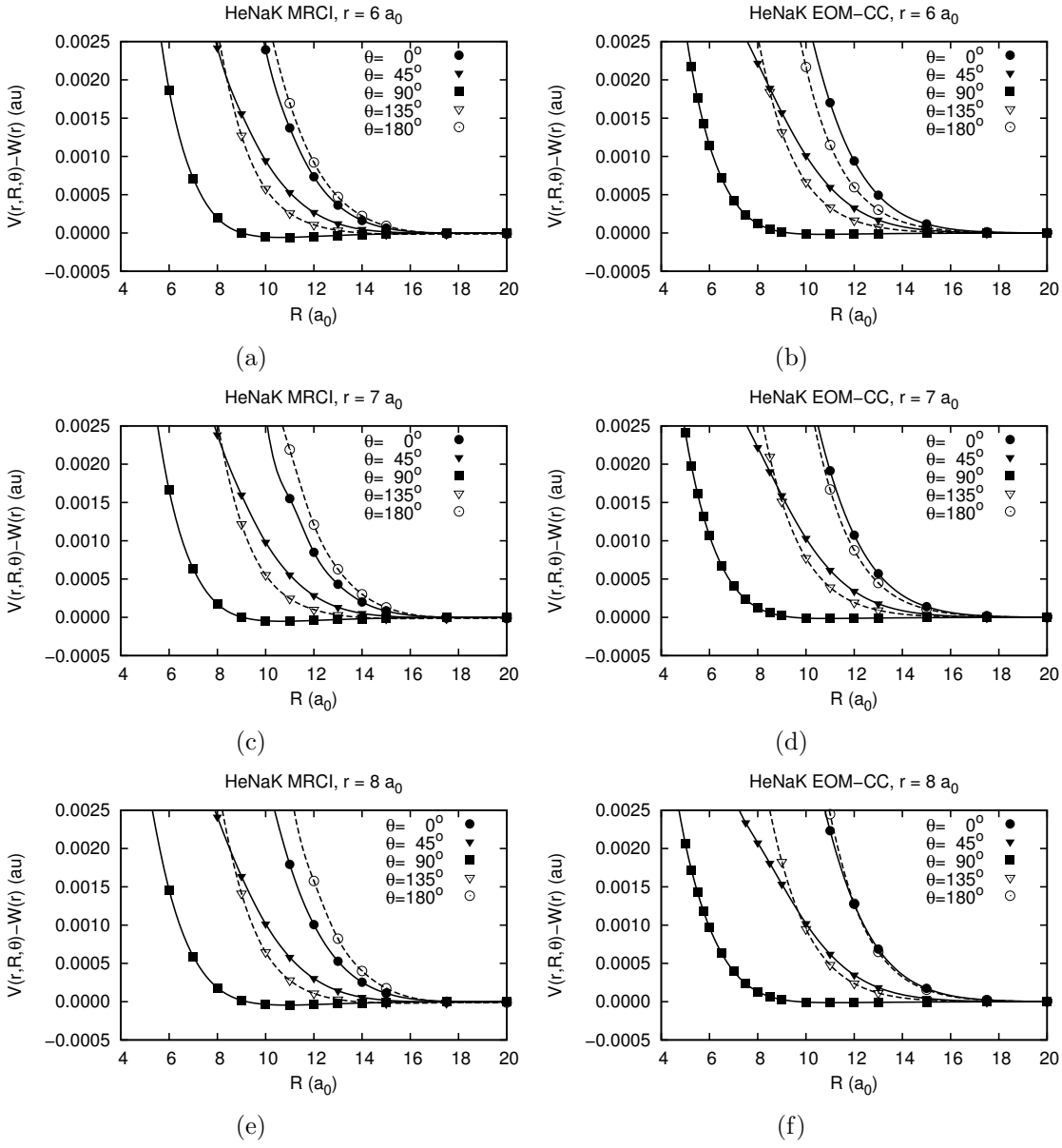

Figure 3.9: This figure shows the PES I: He and PES II: He interaction energies side by side for $r = 6$ to 8 a_0, plotted as a function of R for fixed values of θ. The PES I: He interaction energies are shown in Panels (a), (c), and (e), while the PES II: He interaction energies are shown in Panels (b), (d), and (f).

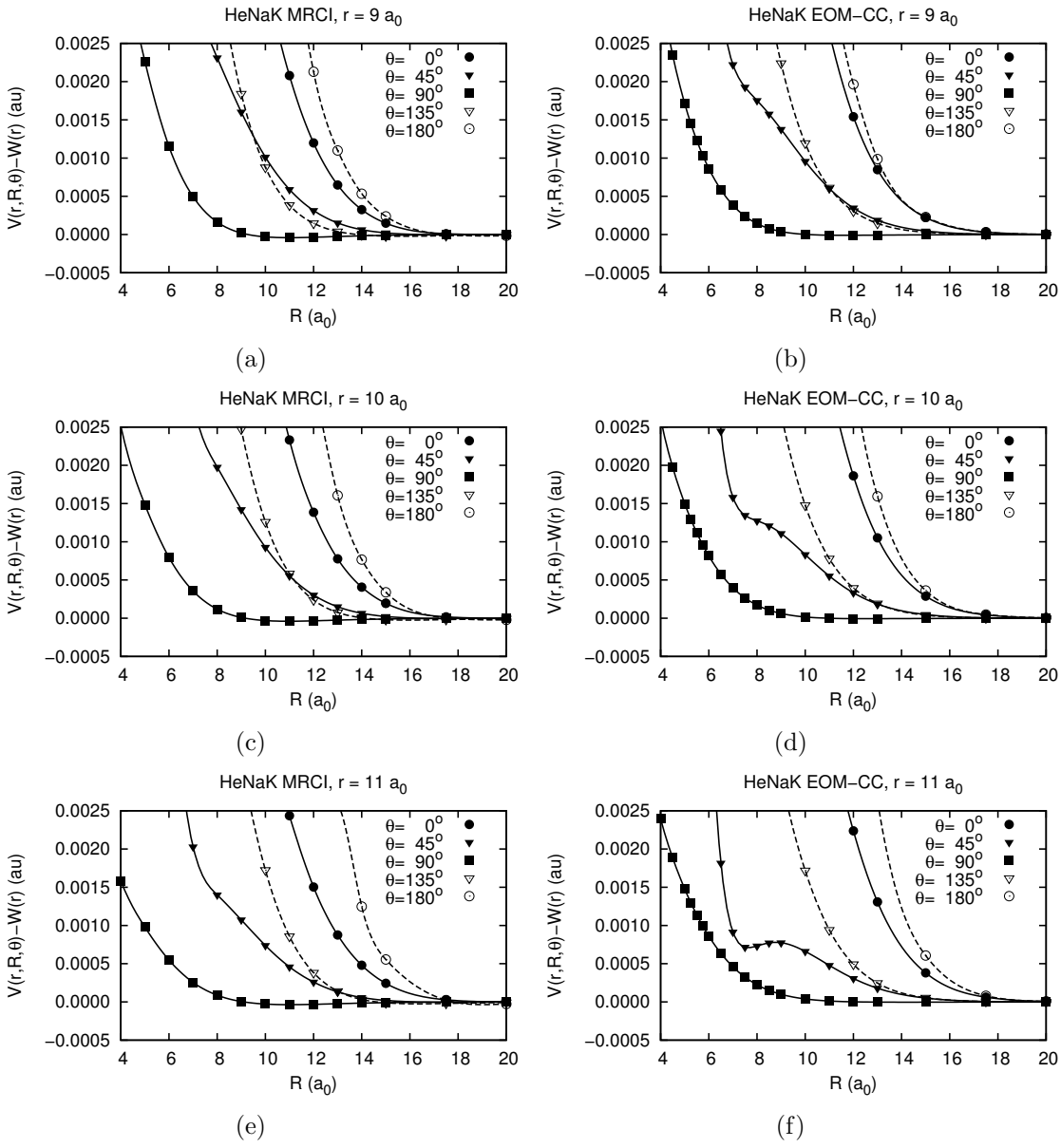

Figure 3.10: This figure shows the PES I: He and PES II: He interaction energies for $r = 9$ to 11 a_0, plotted as a function of R for fixed values of θ. The PES I: He interaction energies are shown in Panels (a), (c), and (e), while the PES II: He interaction energies are shown in Panels (b), (d), and (f).

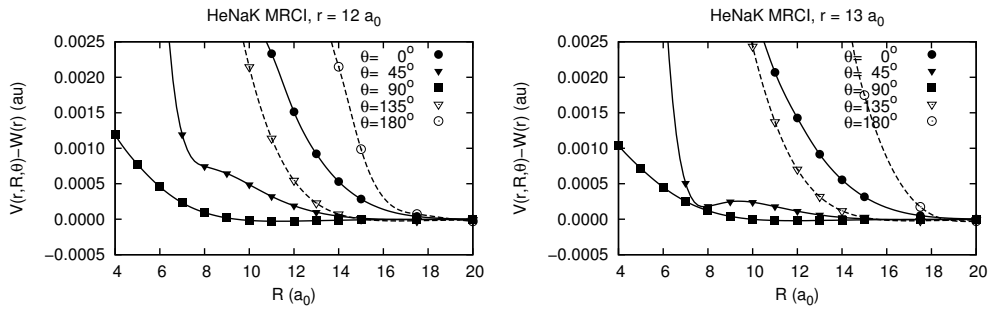

(a) (b)

Figure 3.11: This figure shows the PES I: He interaction energies for $r = 12$ and 13 a_0, plotted as a function of R for fixed values of θ.

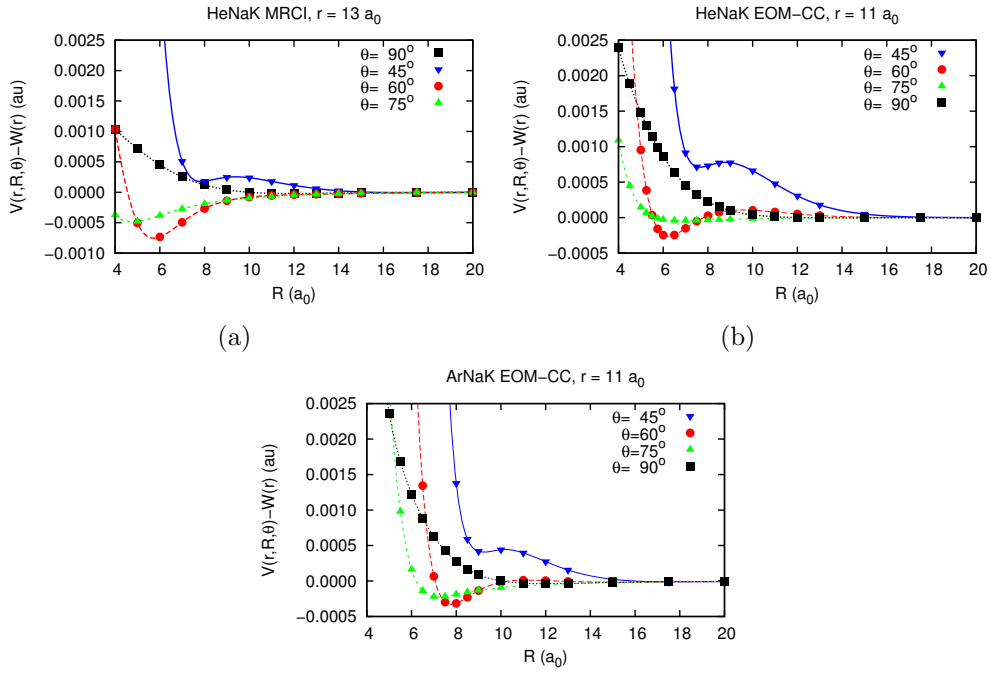

(a) (b)

(c)

Figure 3.12: In this figure, the HeNaK and ArNaK interaction energies are plotted as a function of R for fixed r and selected angles θ. Panel (a) shows the PES I: He interaction energies, Panel (b) shows the PES II: He interaction energies, and Panel (c) shows the PES II: Ar interaction energies. For each surface there are secondary wells for $\theta = 45°$, 60°, and 75°.

3.1.4 Conclusions

We have calculated four different PESs, two of which we have examined with and without the counterpoise correction. With each PES we can calculate scattering observables and compare them with experimental data. The differences in observables obtained with each PES can help us correlate features of the PES with the relative propensity for Δj even transitions.

One may wish to know which PESs we consider our "best". If one is interested in comparing HeNaK and ArNaK, then PES II: He and Ar are best; they were calculated in a parallel fashion. Outside of that comparison, we now discuss the accuracy of our PESs.

For ArNaK we expect PES III: Ar to be better because it has a larger basis set. For HeNaK we used similar basis sets but two different methods, so it is harder to say. Correcting for BSSE is considered to be important, but EOM-CCSD fails for higher bond lengths of NaK. Therefore one might expect PES II: He to be the better PES for low vibrational levels of NaK and for PES I: He to be better for higher vibrational levels of NaK.

We have shown how our results for the NaK ($A\,^1\Sigma^+$) potential compare with the high precision spectroscopic constants and RKR potential. PES II: He and Ar compare best for bond lengths between $r = 6$ and 11 a_0. PES I: He is best, however, if one is interested in bond lengths of 12 a_0 and higher.

In Section 4.2 we will compare scattering observables obtained from the different rigid rotator PESs. We will find that PES II: He and PES III: Ar agree the best with the available experiments.

3.2 Legendre expansion of the potential

For the scattering calculations one must expand the interaction energy

$$\tilde{V}(R, r, \theta) = V(R, r, \theta) - W(r) \tag{3.1}$$

in terms of Legendre polynomials (see Eqs. 2.87 and 2.107). The method used in previous work [1] had some disadvantages, so for the present work we developed an

alternative procedure.

Originally [1] the angular dependence of $\tilde{V}(R, r, \theta)$ for fixed R and r was fit using a polynomial function of $x = \cos\theta$. The fit in terms of $x^0, x^2, \ldots, x^n$ could easily be transformed into a sum of Legendre polynomials $P_0(x), P_1(x), \ldots, P_n(x)$. If there are n angular points, one can find an n-term Legendre expansion that matches every point exactly. There may be, however, unphysical oscillations between points, especially when the potential becomes highly repulsive at some angles. This situation often arose at $\theta = 0°$ or $180°$ when the distance between Na or K and the noble gas became very small.

To avoid this type of problem, we interpolated the angular dependence $\tilde{V}(R, r, \theta)$ for fixed R and r using a taut spline routine [80], which is designed to eliminate ringing (that is, extraneous inflection points) between calculated points. Then to determine the Legendre components we evaluated the standard expression for $\tilde{v}_n(R, r)$ with numerical integration:

$$\tilde{v}_n(R, r) = \frac{2n+1}{2} \int_0^\pi P_n(\cos\theta) \tilde{V}(R, r, \theta) \sin\theta \, d\theta. \tag{3.2}$$

We used Simpson's rule for the numerical integration and integrated over $\cos\theta$. We found that a step size of 10^{-4} was sufficiently small.

The angular dependence $\tilde{V}(R, r, \theta)$ for fixed R and r can be very strong if one includes highly repulsive points and will then require a large number of Legendre components. These repulsive points, however, can be well above the collision energy. We avoided this problem by replacing the calculated energy $E_{\text{calc}} = \tilde{V}(R, r, \theta)$ with the modified energy E_{mod} whenever E_{calc} was greater than a prescribed threshold, using the following formula:

$$E_{\text{mod}} = \begin{cases} E_{\text{calc}} & \text{if } E_{\text{calc}} \le E_0 \\ E_0 \left[1 + \beta \tan^{-1} \left(\dfrac{E_{\text{calc}}/E_0 - 1}{\beta} \right) \right] & \text{if } E_{\text{calc}} > E_0 \end{cases} \tag{3.3}$$

Figure 3.13 shows a plot of E_{mod}/E_0 as a function of E_{calc}/E_0 for several β.

The function defined in Eq. 3.3 and its first and second derivatives are continuous at E_0, so the modified energies join the unmodified energies very smoothly. For large

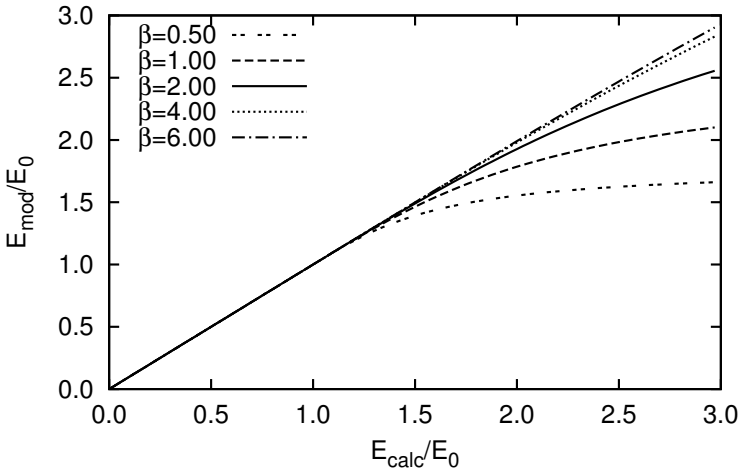

Figure 3.13: Modified energies plotted as E_{mod}/E_0 versus E_{calc}/E_0 for several β.

E_{calc}, E_{mod} approaches the limit $E_0(1 + \beta\pi/2)$. We typically chose $E_0 = 0.004\ E_{\mathrm{h}}$ and $\beta = 2$. For these values, the potential is not changed in any region of physical interest for calculations with $E \leq 0.002\ E_{\mathrm{h}}$. In Chapter 4, we will report some energy-dependent calculations and for some of the higher energies we changed E_0 and β; we will indicate whenever this was the case.

Since we typically only calculated 13 angles for each pair of r and R, we can only reliably obtain 13 Legendre components (that is what we would be able to obtain from an exact polynomial fit to all the calculated points). We will discuss convergence of the scattering results with respect to the number of Legendre components in Chapter 4; typically we included components up to $n = 10$ and $n = 15$ and found there was no appreciable difference between the results. We also found that we could reproduce the essential features of the cross sections for He+NaK and Ar+NaK by only including up to $n = 2$ (Section 4.1).

After determining the expansion coefficients $\tilde{v}_n(R, r)$ at several values of R (for fixed r), we again used the taut spline routine to interpolate as a function of R. For HeNaK, we tabulated $\tilde{v}_n(R, r)$ at intervals of 0.25 a_0 for points between $R = 3.5$ and 10 a_0 and 0.50 a_0 for points between $R = 10$ and 25 a_0. For ArNaK, we tabulated the expansion coefficients at intervals of 0.25 a_0 between all points.

Figure 3.14 shows several of the splined Legendre components $v_n(R, r_e)$ for the different rigid rotator PESs. They are plotted as a function of R and all look a bit different from one another.

In Fig. 3.15, we compare the Legendre components of the rigid rotator PES II: He and PES II: Ar. The size of $v_1(R, r_e)$ at a given R is different, and we have found that for HeNaK small changes in $v_1(R, r_e)$ can make a significant difference in the cross sections for transitions with $\Delta j = \pm 1$ [2]. The $v_1(R, r_e)$ component of ArNaK is larger than the $v_1(R, r_e)$ component of HeNaK for $R > 13\ a_0$.

For a homonuclear diatomic molecule, the atom-diatom potential will only have even Legendre components. The relative sizes of the even and odd Legendre components may help one to predict the relative cross sections for rotationally inelastic transitions for odd and even values of Δj [10]; this idea will be discussed more in Chapter 4. In Panel (a) of Fig. 3.15, $v_0(R, r_e)$ is generally larger than $v_1(R, r_e)$ for HeNaK, while for ArNaK $v_1(R, r_e) > v_0(R, r_e)$ for $R \approx 14\ a_0$. For $R > 13\ a_0$, $v_1(R, r_e)$ is a greater fraction of $v_2(R, r_e)$ for ArNaK than for HeNaK.

Next in Figs. 3.16 and 3.17, we compare the counterpoise corrected and uncorrected rigid rotator PES II: He and PES II: Ar. For HeNaK, the correction pushes $v_1(R, r_e)$ and $v_2(R, r_e)$ apart and has little effect on the higher Legendre components. For ArNaK, the correction has a bigger effect, but still pushes $v_1(R, r_e)$ and $v_2(R, r_e)$ apart. The correction causes $v_1(R, r_e)$ and $v_0(R, r_e)$ to intersect at a larger R (and makes them more similar) and it eliminates the intersection between $v_1(R, r_e)$ and $v_2(R, r_e)$ near $R = 13\ a_0$.

In Fig. 3.18, we compare our HeNaK rigid rotator PESs; the odd Legendre components show the most differences. Finally, in Fig. 3.19, we compare our ArNaK rigid rotator surfaces. Unlike the HeNaK surfaces, here the even Legendre components show the most differences; the odd components tend to look the same.

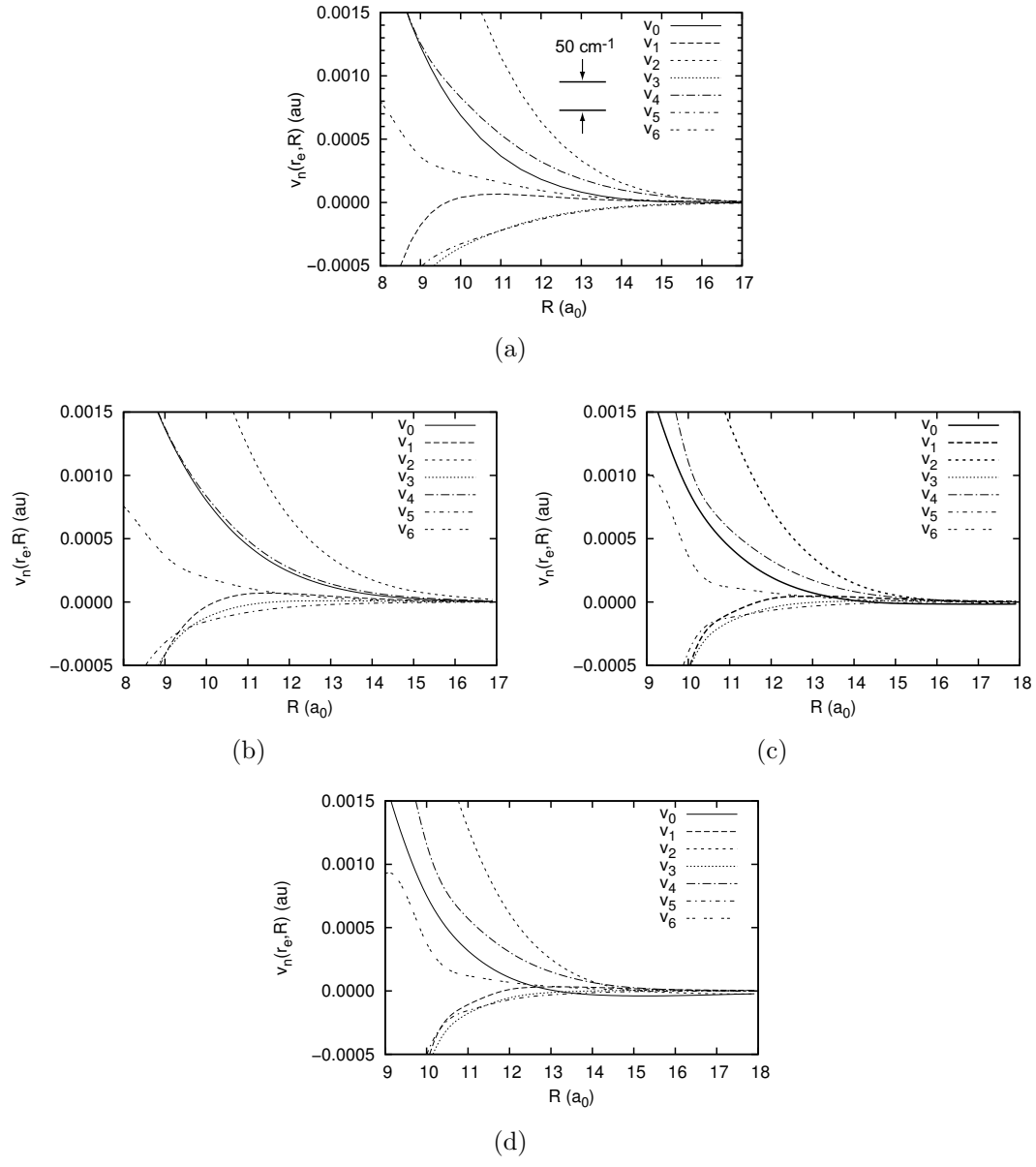

Figure 3.14: Legendre components of our rigid rotator PESs as a function of R. Panel (a) corresponds to PES I: He, Panel (b) to PES II: He, Panel (c) to PES II: Ar, and Panel (d) to PES III: Ar. Note the horizontal scale is different in Panels (a) and (b) than in Panels (c) and (d). Panel (a) reproduced from [2] with the permission of AIP publishing.

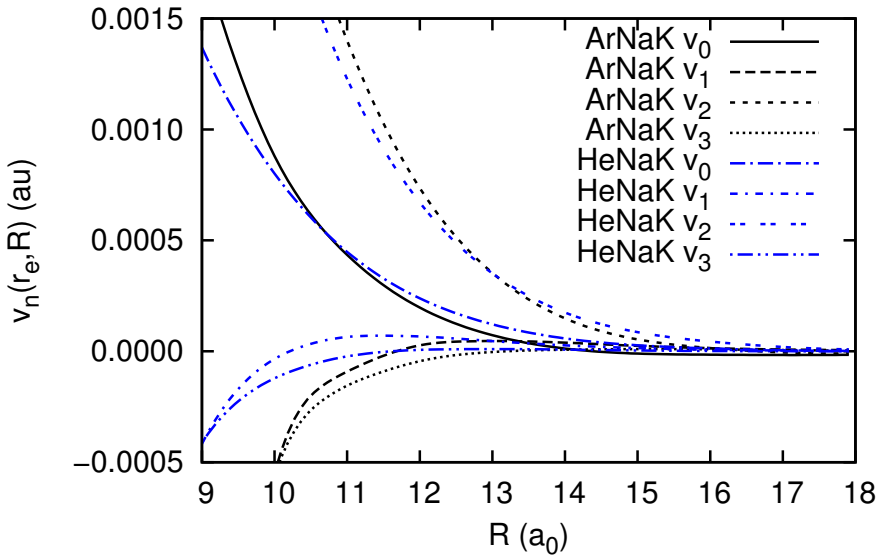

(a)

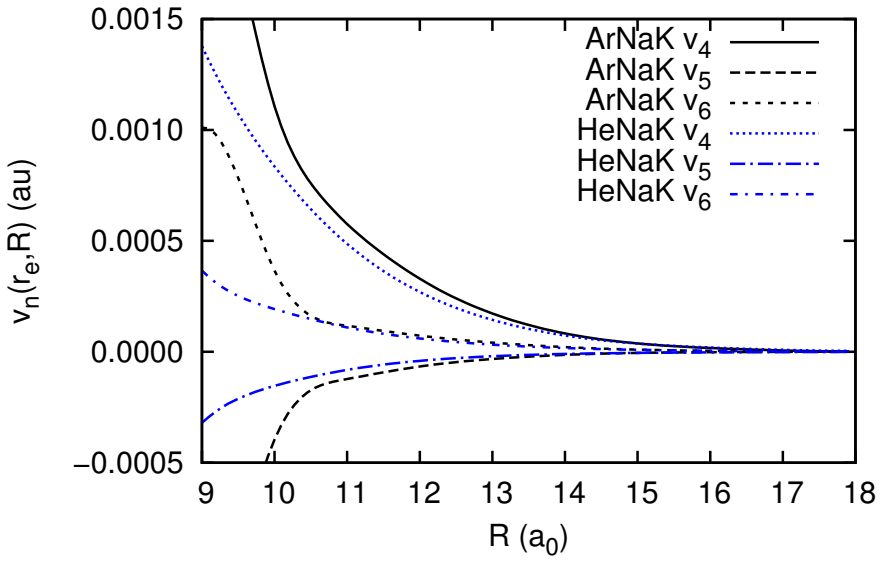

(b)

Figure 3.15: Comparison between the Legendre components of the rigid rotator PES II: He and PES II: Ar. The $v_1(R, r_e)$ component of the ArNaK PES is larger for $R > 13\ a_0$, and unlike for the HeNaK PES $v_1(R, r_e) > v_0(R, r_e)$ for $R > 14\ a_0$. Moreover, the ratio $v_1(R, r_e)/v_2(R, r_e)$ is generally greater for ArNaK than for HeNaK. The relative sizes of the Legendre components may help one to predict the relative propensity for Δj even transitions [10].

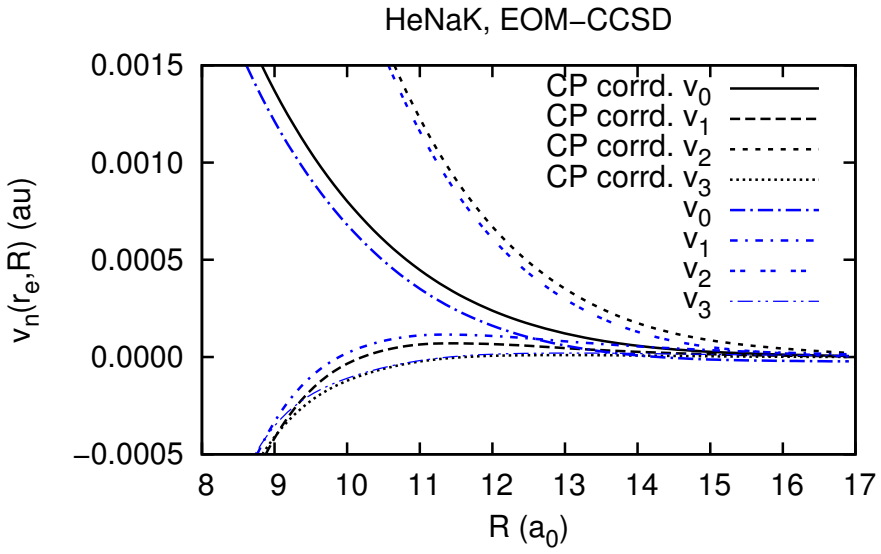

(a)

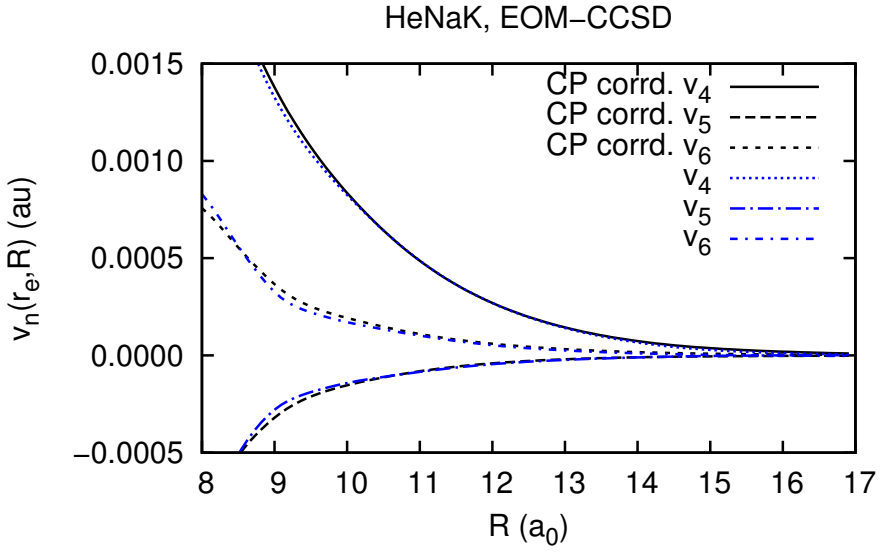

(b)

Figure 3.16: Comparison between the Legendre components of the counterpoise corrected and uncorrected rigid rotator PES II: He. The label 'CP corrd. v_n' means the n^{th} Legendre component of the counterpoise corrected PES, while the label 'v_n' means the n^{th} Legendre component of the uncorrected PES. The correction pushes $v_1(R, r_e)$ and $v_2(R, r_e)$ apart and has little effect on the higher Legendre components.

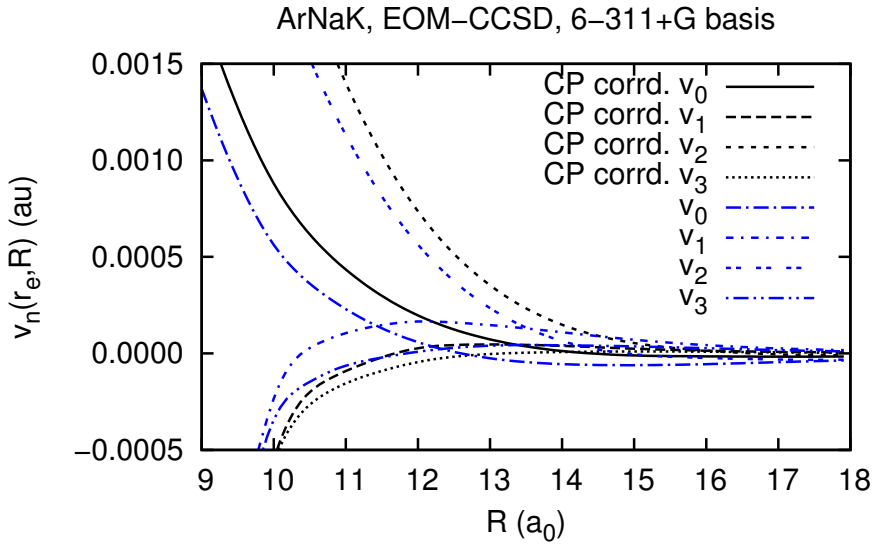

(a)

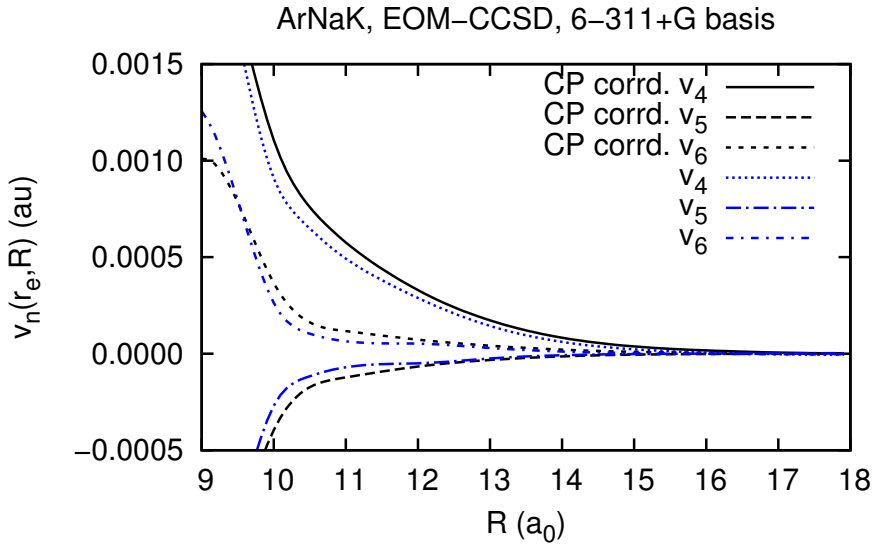

(b)

Figure 3.17: Comparison between the Legendre components of the counterpoise corrected and uncorrected rigid rotator PES II: Ar. The label 'CP corrd. v_n' means the n^{th} Legendre component of the counterpoise corrected PES, while the label 'v_n' means the n^{th} Legendre component of the uncorrected PES. The correction has a bigger effect for ArNaK than it did for HeNaK; it dramatically changes the relative sizes (and intersections) of $v_0(R, r_e)$, $v_1(R, r_e)$, and $v_2(R, r_e)$.

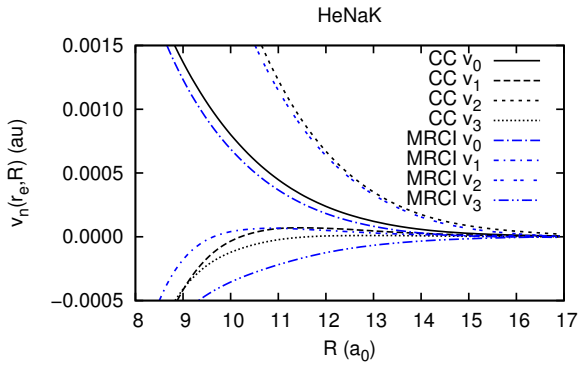

(a)

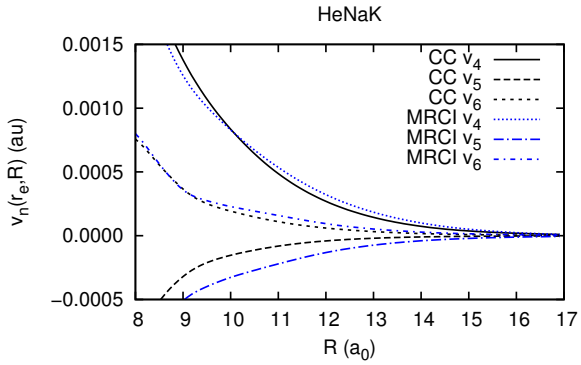

(b)

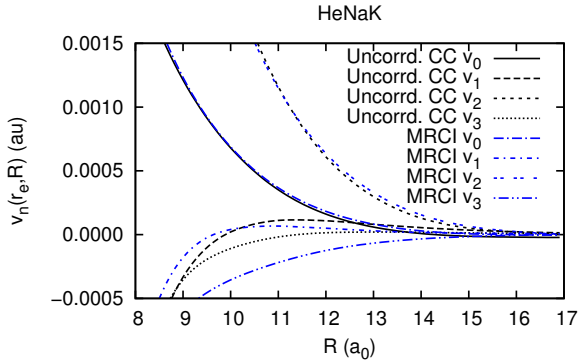

(c)

Figure 3.18: Panels (a) and (b) compare the Legendre components of the rigid rotator PES I: He and counterpoise corrected PES II: He, labeled 'MRCI' and 'CC', respectively (CC stands for Coupled-Cluster). Panel (c) shows a similar comparison but for the uncorrected PES II: He. The odd Legendre components are the most different.

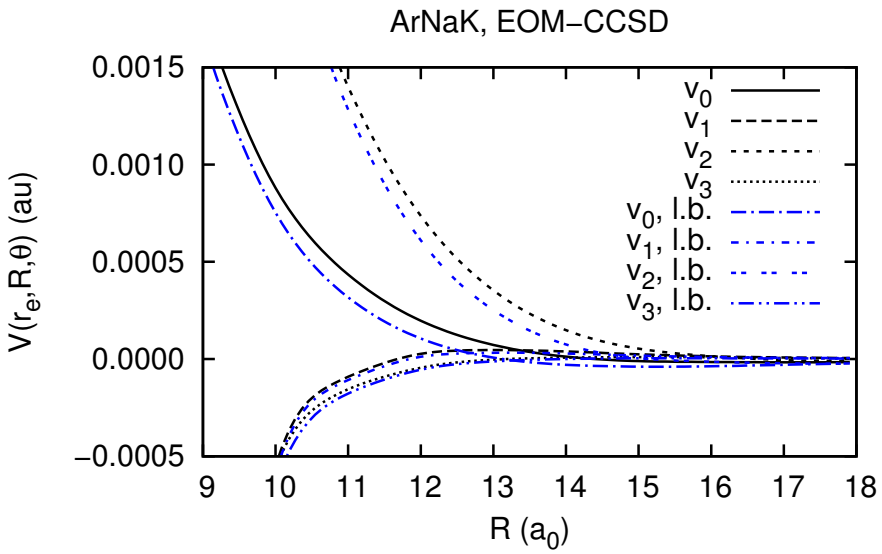

(a)

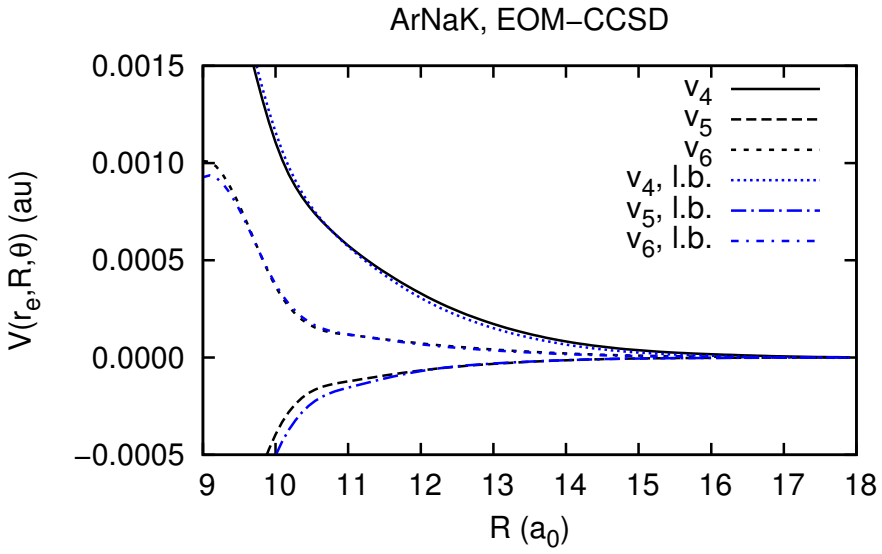

(b)

Figure 3.19: Panels (a) and (b) compare the Legendre components of the rigid rotator PES II: Ar and PES III: Ar. The label 'v_n' corresponds to PES II: Ar, while the label 'v_n, l.b.' corresponds to PES III: Ar (l.b. stands for larger basis). The even Legendre components show the most differences between the two PESs, and the odd Legendre components are fairly similar.

3.3 Fits to the long range part of the potential

When R is very large, the interaction energy between He or Ar and NaK is difficult to calculate with conventional electronic structure methods because the Gaussian exponential form of the basis functions limits the accuracy of the electronic wave functions far from each nucleus. Long range potential theory provides the correct form of the potential in this limit. If there is an intermediate range of R where the potential is reliable, and the long range form is also appropriate, then one can fit the calculated potential to an analytic function that can be extended to the limit $R \to \infty$.

There are two reasons we wanted to obtain interaction energies for large values of R. First, one can more effectively investigate convergence of scattering observables with respect to the range of integration, as will be discussed in Chapter 4. Moreover, the extended PES is necessary for low energy scattering calculations where one must integrate to very large R.

We fit PES II: He and PES II: Ar to the first three terms (R^{-6}, R^{-7}, R^{-8}) of Pack's analytic form for the long range potential (Eq. 2.42) by noting that $R^6\tilde{V}(R,r,\theta)$ is a polynomial function of $1/R$:

$$R^6\tilde{V}(R,r,\theta) = C_6(r,\cos\theta) + C_7(r,\cos\theta)/R + C_8(r,\cos\theta)/R^2 \tag{3.4}$$

where the angular dependence of C_6, C_7, and C_8 is given by

$$\begin{aligned} C_6(r,\cos\theta) &= C_6^{(0)}(r)P_0(\cos\theta) + C_6^{(2)}(r)P_2(\cos\theta) \\ C_7(r,\cos\theta) &= C_7^{(1)}(r)P_1(\cos\theta) + C_7^{(3)}(r)P_3(\cos\theta) \\ C_8(r,\cos\theta) &= C_8^{(0)}(r)P_0(\cos\theta) + C_8^{(2)}(r)P_2(\cos\theta) + C_8^{(4)}(r)P_4(\cos\theta). \end{aligned} \tag{3.5}$$

In this section we describe our fits. Although we have included enough polarization functions in the GAMESS calculations to expect C_6, C_7, and C_8 to play a role in the long range potential, we do not claim to know these coefficients to experimental accuracy because of uncertainties in the PESs.

We used a code [81] based on the Levenberg-Marquardt algorithm to perform these fits. For each bond length r, we performed a separate fit by adjusting seven

parameters ($C_6^{(0)}$, $C_6^{(2)}$, $C_7^{(1)}$, $C_7^{(3)}$, $C_8^{(0)}$, $C_8^{(2)}$, and $C_8^{(4)}$) to fit $R^6\tilde{V}(R,r,\theta)$ at 39 pairs of points R, θ. For HeNaK and 6 $a_0 \leq r \leq 10$ a_0, we fit the calculated points at 13 values of θ for $R = 30$, 32.5, and 35 a_0. For $r = 11$ a_0, we fit the calculated points for $R = 35$, 37.5, and 40 a_0. For all bond lengths of the ArNaK surface, we fit the calculated points for $R = 25$, 27.5, and 30 a_0.

Figure 3.20 shows the fits for $r = 8$ a_0. For this reduced plot, the vertical axis is R^6 times the interaction energy, and the horizontal axis is $1/R$. Figure 3.21 shows the fits in a conventional plot of the potential versus the perturber distance R.

Using the calculated points and the long range analytic form, we can evaluate the Legendre components $\tilde{v}_n(R,r)$ at all values of R. To ensure a smooth join, we first performed a spline of all the calculated points plus additional points evaluated using the analytc formula for selected values of R. Figure 3.22 shows the splines for HeNaK for $r = 8$ and 11 a_0 and for ArNaK for $r = 8$ a_0. For HeNaK, the analytic points included were for $R = 37.5$ to 50 a_0 in steps of 2.5 a_0 for 6 $a_0 \leq r \leq 10$ a_0 and for $R = 42.5$ to 52.5 a_0 in steps of 2.5 a_0 for $r = 11$ a_0. For ArNaK, the analytic points included were for $R = 30$ to 30.9 a_0 in steps of 0.1 a_0 and from $R = 32.5$ to 42.5 a_0 in steps of 2.5 a_0 for all bond lengths.

When we evaluated $\tilde{v}_n(R,r)$, we switched over from the spline to the analytic form at different values of R. Then, we performed small scattering calculations to check whether the results were sensitive to the value of R. We found that for HeNaK, joining to the spline with an analyic fit at $R = 35$ a_0 showed little difference from a join at 37.5 or 40 a_0. For ArNaK, joining to the spline with an analytic fit at $R = 30$ a_0 showed little difference from a join at 35 or 40 a_0.

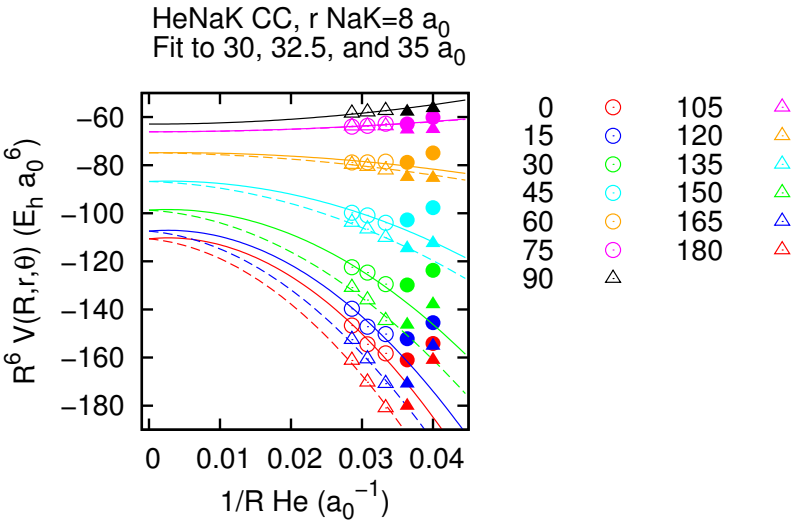

(a)

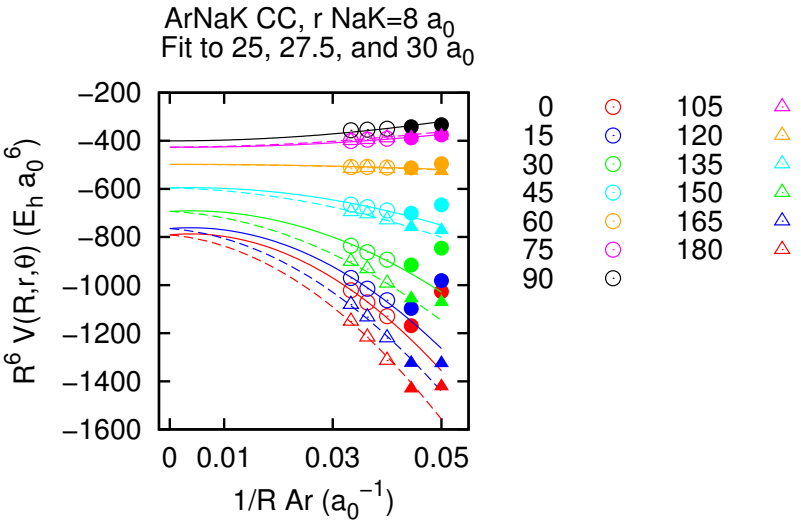

(b)

Figure 3.20: Fits to the long range interaction energies for $r = 8\ a_0$ for PES II: He (Panel (a)) and PES II: Ar (Panel (b)). The rms deviations of the fits were 0.98496 and 5.3351 $E_\mathrm{h} a_0^6$, respectively. The fit is a solid line for $\theta \leq 90°$ and a dashed line for $\theta > 90°$. The calculated values are shown as points; the solid points (for $R = 20.0$ and 22.5 a_0 for ArNaK and $R = 25.0$ and 27.5 a_0 for HeNaK) were not included in the fit and are included to demonstrate that we were in the long range region of the potential. In the plot, $\tilde{V}(R, r, \theta)$ is labeled '$V(R, r, \theta)$'.

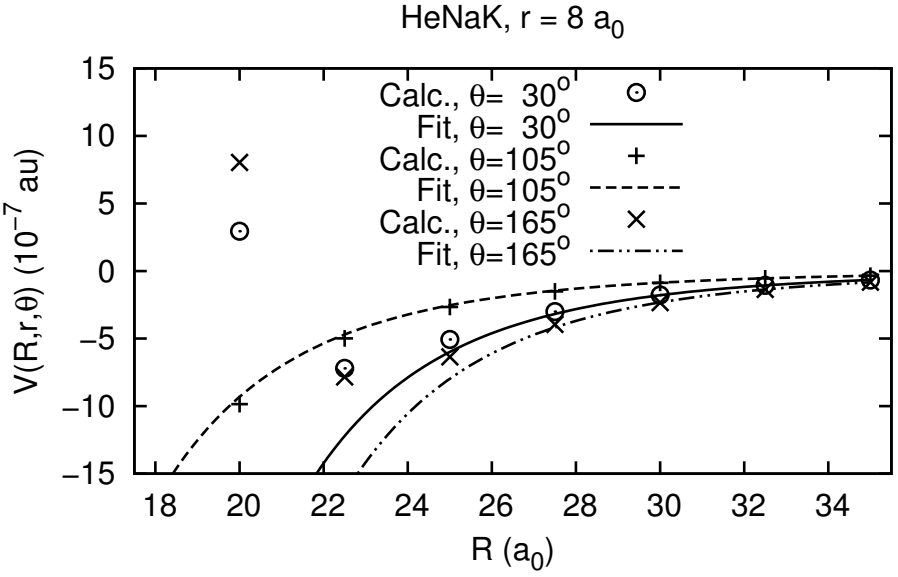

(a)

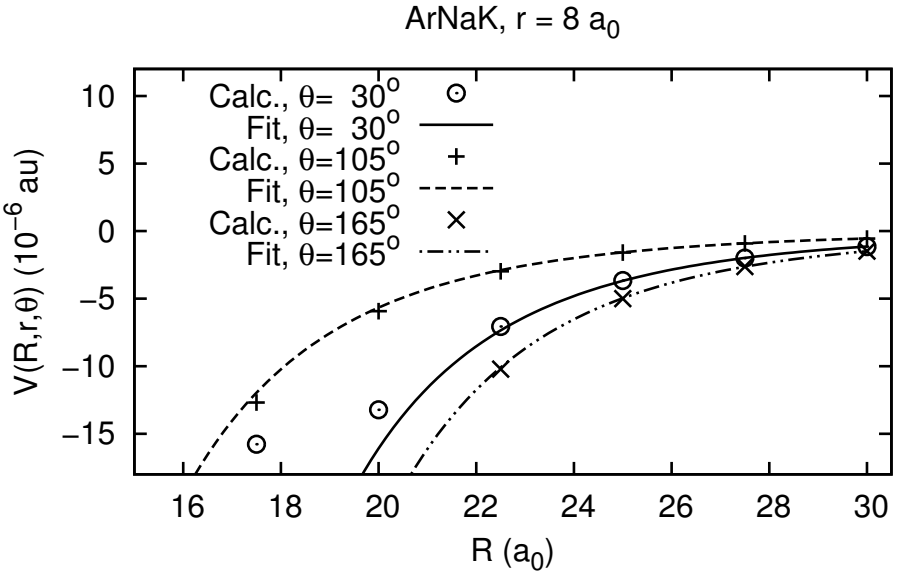

(b)

Figure 3.21: The analytic fits to the potential (lines) are shown for some angles against the calculated interaction energies for PES II: He (Panel (a)) and PES II: Ar (Panel (b)) for $r = 8\ a_0$. We note that each panel has a different vertical scale. In the plot, $\tilde{V}(R, r, \theta)$ is labeled '$V(R, r, \theta)$'.

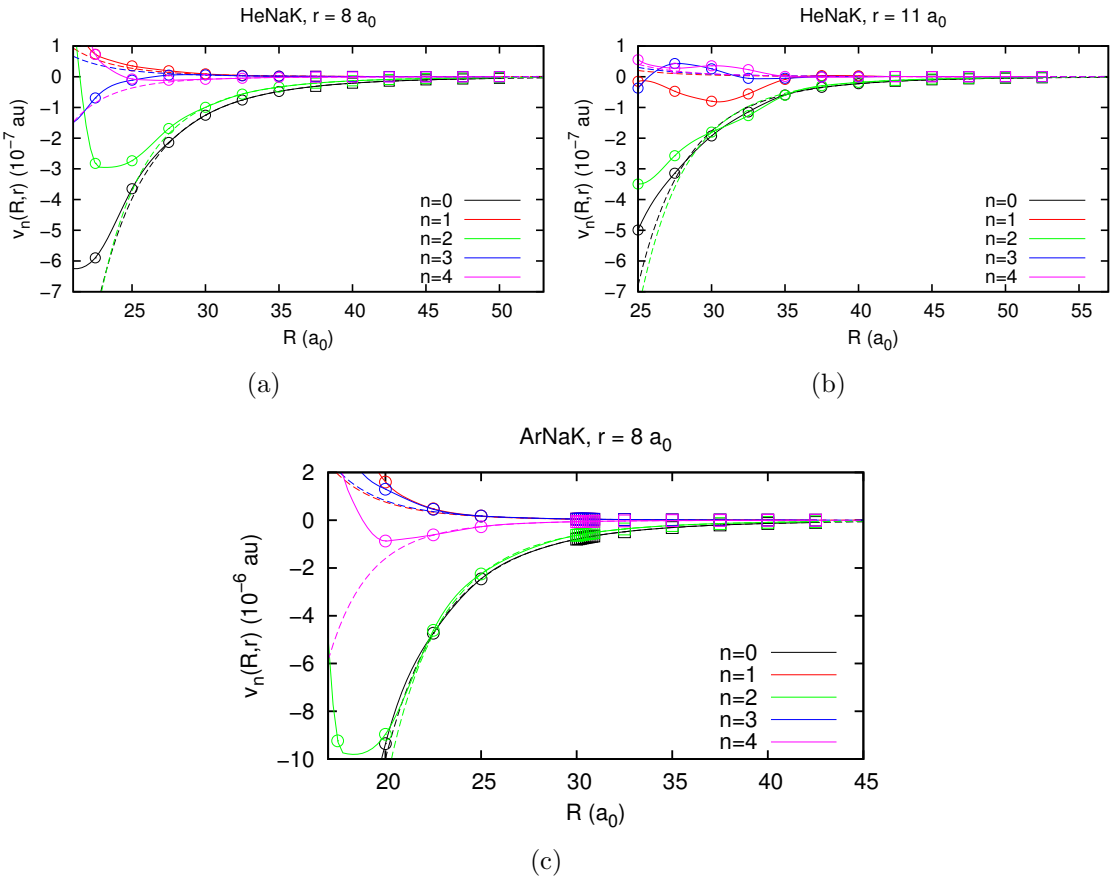

Figure 3.22: Splined calculated (circles) and analytic (squares) Legendre components for PES II: He and PES II: Ar for selected r. The spline is shown as a solid line and the analytic fit as a dotted line. Note the vertical scale changes between HeNaK and ArNaK. Panel (a) shows the spline for HeNaK, $r = 8\,a_0$. Panel (b) shows the spline for HeNaK, $r = 11\,a_0$. Panel (c) shows the spline for ArNaK, $r = 8\,a_0$.

Chapter 4

Coupled channel scattering calculations

We have performed coupled channel scattering calculations for He ($^1S_0$) or Ar ($^1S_0$) and NaK ($A\,^1\Sigma^+$) using the rigid rotator formalism developed by Arthurs and Dalgarno [17]; the bond length of NaK was fixed at the experimental value [7] for the equilibrium internuclear separation, $r_e = 7.935\ a_0$. The calculations involved solving a set of coupled differential equations (Eq. 2.90) and were performed using a code developed by Prof. Hickman [82]. The code is based on the log-derivative method [83] and features adaptive step size selection. All of the calculations were performed on the Stampede supercomputer at the University of Texas.

In this chapter we first describe the details of the numerical calculations to solve the coupled channel equations. Then we discuss our rigid rotator results for the average collision energy and compare them with experimental data from the experimental group at Lehigh [4–6]. The data are collected in an environment with a Maxwellian distribution of energies and for different initial vibrational levels. For this reason, we present additional theoretical results for the energy dependence of the rigid rotator cross sections, and for the dependence on initial v of vibrationally elastic, rotationally inelastic cross sections and fractions of orientation retained. Using these results, we estimate how energy and vibrational dependences affect our

comparison with experiment. Our calculations reproduce one of the key features of the data, the propensity for Δj even transitions, and in the last section of this chapter we explore the role played by different features of the PES in determining the propensity.

4.1 Details of the numerical calculations

Many details of the calculations were carefully considered to balance the desire for numerical accuracy with the constraints of available resources. We considered the number of channels, the integration grid and number of partial waves, and the number of terms in the Legendre expansion of the PES included in the calculation. We will discuss our considerations, focusing on the results we compare with experiment, and limiting the discussion to those results involving PES II: He and PES II: Ar (we came to the same conclusions with the other PESs).

Number of channels

The general expression (Eq. 2.90) for the coupled channel expansion must be truncated to a finite number of channels for any specific calculation. For a given total angular momentum J, the channels are labeled by j and l; one typically includes all channels that can be constructed from the target rotational levels j between $j_{\min}$ and $j_{\max}$. We normally took $j_{\min} = 0$, so $j_{\max}$ is the crucial parameter. Since the orbital angular momentum l is an integer between $|J - j|$ and $J + j$, for every $J > j_{\max}$ the number of possible l is the same and the number of channels can be determined from $j_{\max}$ alone. One can show that for $J > j_{\max}$, the number of channels N_{chan} is

$$N_{\text{chan}} = (j_{\max} + 1)^2, \tag{4.1}$$

and that for $J \leq j_{\max}$ there are less. The channels can be divided into two uncoupled sets because of conservation of the parity symmetry $p = (-1)^{J+j+l}$, corresponding to the change of sign of all coordinates. This uncoupling allows one to perform two separate calculations, each with about half the number of channels. For $J > j_{\max}$

and $p = +1$ there are $(j_{\max}+1)(j_{\max}+2)/2$ channels, while for $p = -1$ there are $j_{\max}(j_{\max}+1)/2$.

The rotational energy levels of NaK ($A\,^1\Sigma^+$) are shown in Fig. 4.1. For a total energy of 0.002 E_h (440 cm^{-1}), any level up to about $j = 80$ is accessible. Channels which are energy inaccessible (closed) at large R can also contribute to the scattering, and accurate results for successively higher initial j's require successively more channels.

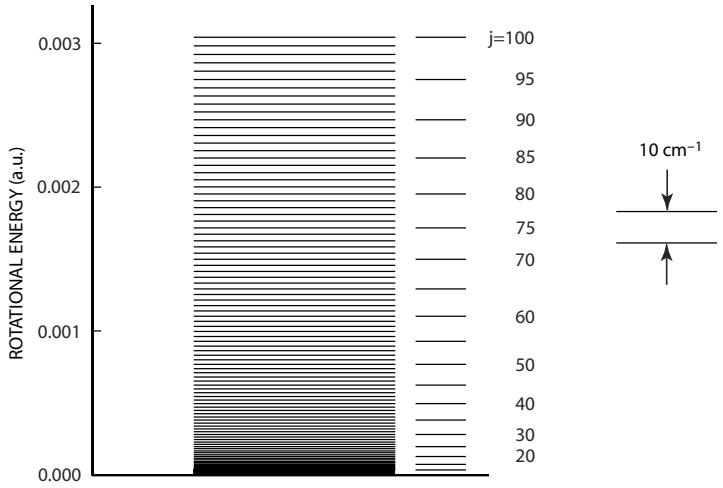

Figure 4.1: Rotational energy levels of NaK ($A\,^1\Sigma^+$), where $E_j = Bj(j+1)$ was calculated with the experimental rotational constant $B = 3.013 \times 10^{-7}$ E_h (0.066 cm^{-1}) [7]. For the collision energy of 0.002 E_h (440 cm^{-1}), any level up to about $j = 80$ is energy accessible. Reproduced from [2] with the permission of AIP publishing.

Computational resources limit the number of channels that can be included in these large scale calculations; the number of processor-hours required scales as $N_\mathrm{chan}^3 \approx j_\mathrm{max}^6$, so computational work goes up very rapidly with j_max. Fortunately, one does not always need to include all of the energy accessible channels. This is true for our calculations. Most of our results converge with respect to the number of channels for $j_\mathrm{max} = 50$ or 60.

In Figs. 4.2 and 4.3, we show cross sections for transitions from $j = 14$ and 30 for different j_max. For each increase in j_max, the cross sections decrease by a smaller

percentage. We find that the Ar+NaK results for $j = 14$ and $j = 30$ are similar enough for $j_{\max} = 50$ and 60 that a calculation for $j_{\max} = 70$ is not warranted. (We recently performed a calculation for $j_{\max} = 70$, however, to assure ourselves that the Ar+NaK orientation results for high j were converging; we will discuss orientation results a little later on.) For He+NaK, for similar reasons, we determine that $j_{\max} = 50$ is sufficient for $j = 14$. For $j = 30$, on the other hand, the results for some values of Δj ($-6 \leq \Delta j \leq +10$) are more different than in the other cases; this is because for $j_{\max} = 40$, values near $j = 40$ are less reliable. Nonetheless, judging from the trends in the other three cases, it is likely that the He+NaK results would be quite similar with those for $j_{\max} = 60$.

For $j = 14$, the cross sections for He+NaK decrease by less than 5.0% between $j_{\max} = 40$ and 50 and by less than 3.6% for Ar+NaK between $j_{\max} = 60$ and 70. For $j = 30$, the cross sections show a little more of a difference, which is to be expected since one must include channels up to a $j_{\max}$ that is larger than the initial j by some amount. For He+NaK, the odd cross sections are as much as 25% different, while the even cross sections differ by less than 12%. For Ar+NaK, the cross sections are all less than 4.5% different.

In Fig. 4.4 we show results for the fraction of orientation retained for different values of $j_{\max}$. There is very little difference in the He+NaK values for $j_{\max} = 40$ and 50; the percent differences are all within about 1% for the transitions of interest. For Ar+NaK, the values are also quite similar for $j_{\max} = 60$ and 70, and they differ by less than 3%.

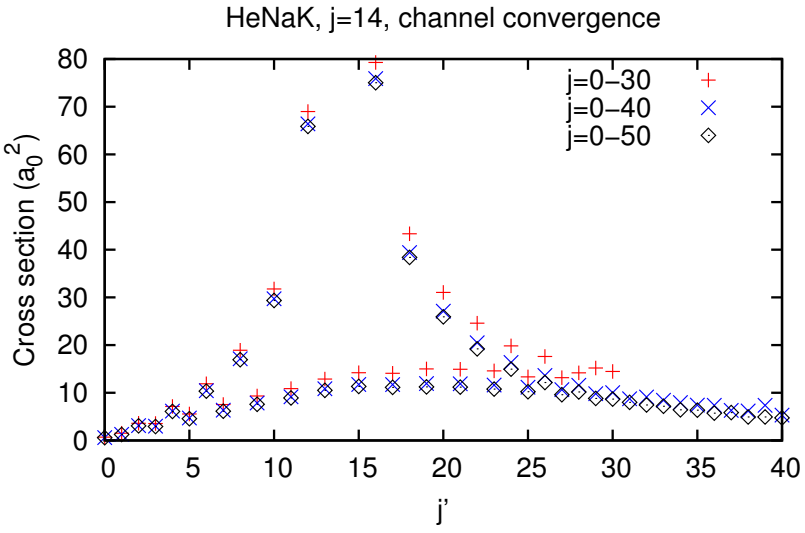

(a)

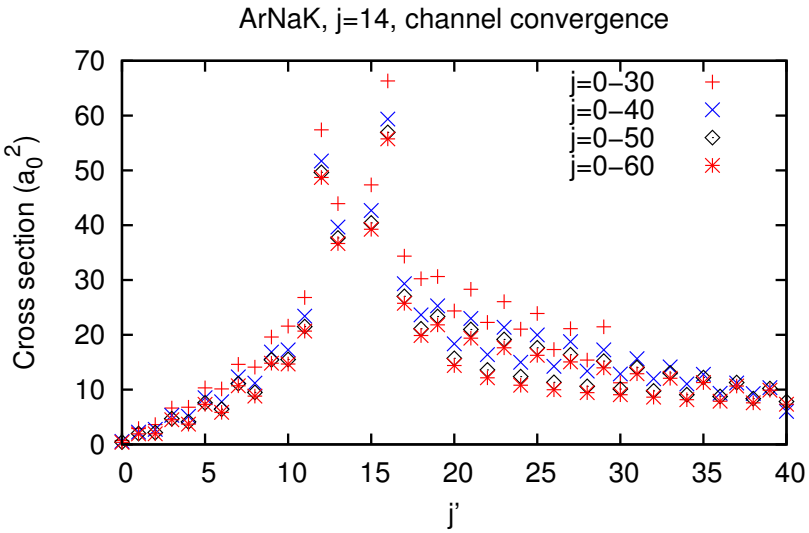

(b)

Figure 4.2: Cross sections for transitions from $j = 14$ to j' obtained using PES II: He (Panel (a)) and PES II: Ar (Panel (b)). The label '$j = 0 - 30$' means that $j_{\max} = 30$. To obtain the same level of convergence for the cross sections, we needed $j_{\max} = 50$ for He+NaK and $j_{\max} = 60$ for Ar+NaK. The other parameters were fixed; the number of Legendre components $n_{\max}+1$ was 11, the tolerance was 10^{-3}, there were 128 and 448 partial waves for He+NaK and Ar+NaK, and we integrated from 3.5 a_0 to 25 a_0 for He+NaK and from 4.5 a_0 to 30 a_0 for Ar+NaK.

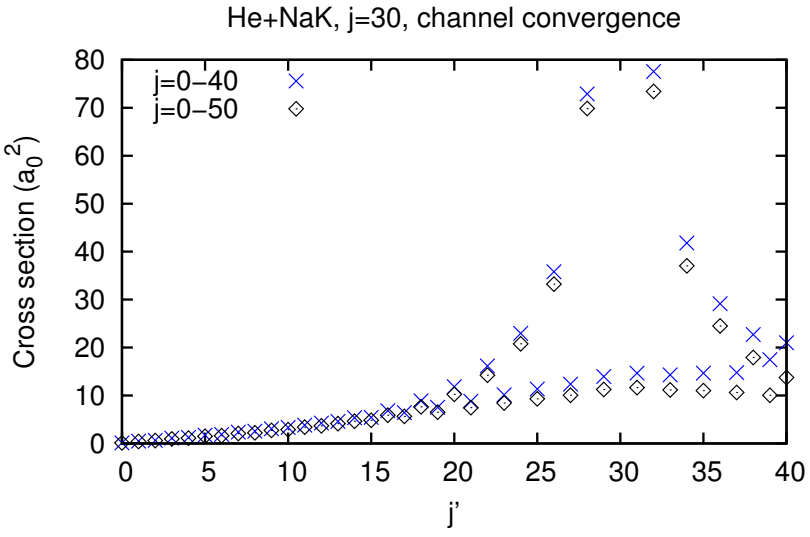

(a)

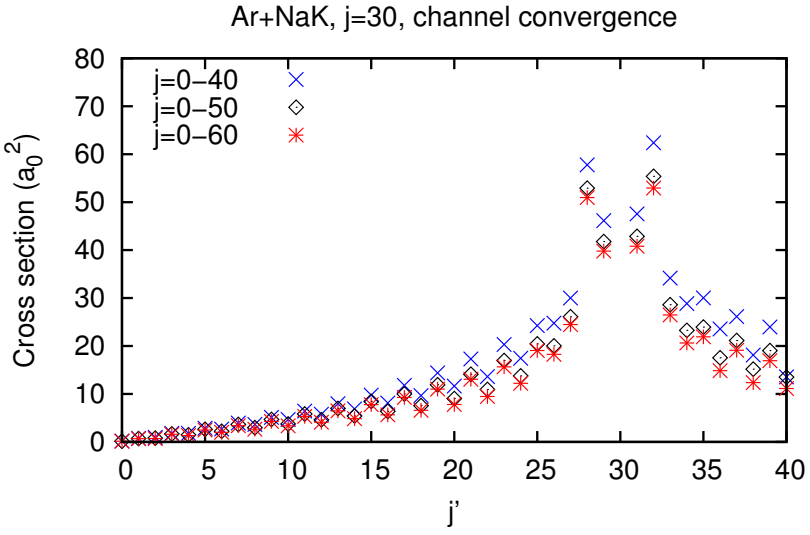

(b)

Figure 4.3: Cross sections for transitions from $j = 30$ to j' obtained using PES II: He are shown in Panel (a) and using PES II: Ar in Panel (b). The label '$j = 0-40$' means that $j_{\max} = 40$. He+NaK and Ar+NaK do not show the same level of convergence; some transitions are less converged for He+NaK. The other parameters were fixed; the number of Legendre components $n_{\max}+1$ was 11, the tolerance was 10^{-3}, there were 128 and 448 partial waves for He+NaK and Ar+NaK, and we integrated from 3.5 a_0 to 25 a_0 for He+NaK and from 4.5 a_0 to 30 a_0 for Ar+NaK.

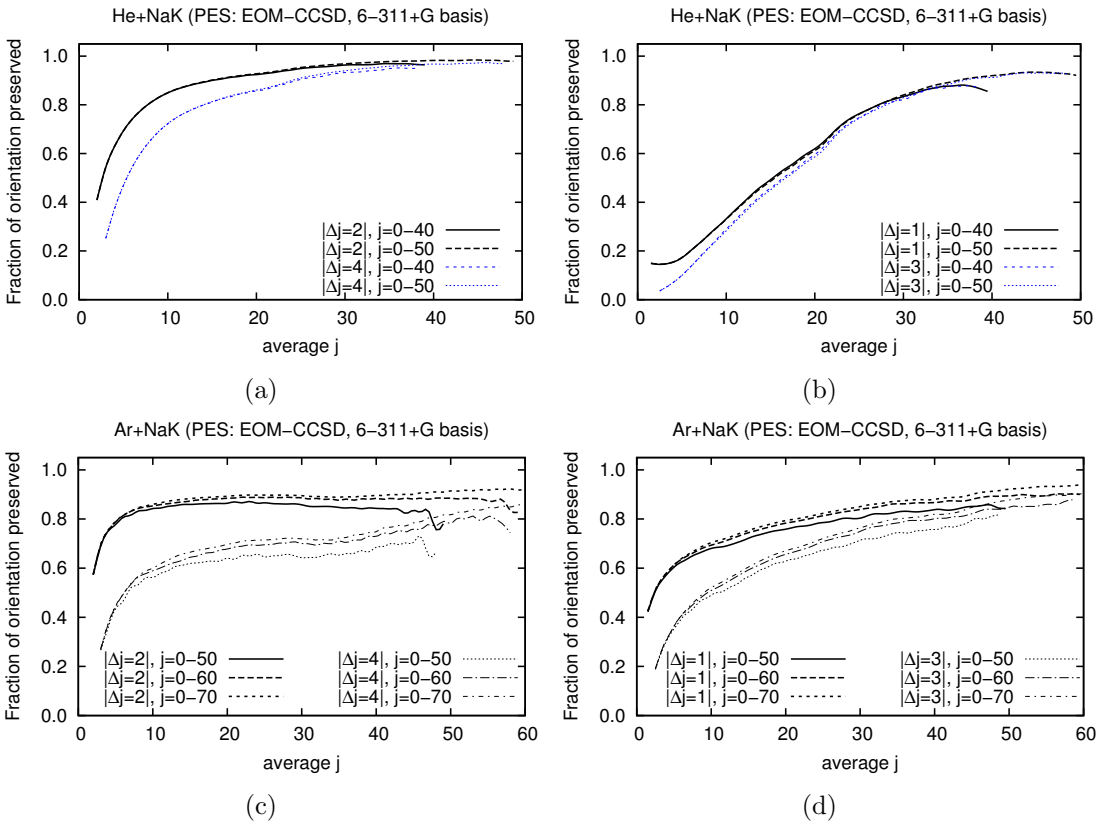

Figure 4.4: Fractions of orientation preserved are plotted for different values of $|\Delta j|$ as a function of average $j = (j + j')/2$. The results corresponding to PES II: He are shown in Panels (a) and (b) and to PES II: Ar in Panels (c) and (d). Even values of $|\Delta j|$ are shown in Panels (a) and (c), while odd values are shown in Panels (b) and (d). Each curve for a given $|\Delta j|$ corresponds to a calculation with a different number of channels; 'j=0-40' means that $j_{\max} = 40$. We note that when the average j is close to $j_{\max}$, the results are not reliable since $j_{\max}$ must be larger than the initial j by some amount, and oscillations in results in these cases are artifacts. Artifacts appear in Panels (b)–(d), where the curves for $j_{\max} = 40$ show unphysical oscillations near average $j = 40$. Another artifact appears in Panel (c), where the curve for $j_{\max} = 50$ oscillates for values of average j near 50. The other parameters are listed in the caption of Fig. 4.2. The He+NaK results are very similar, and are less than 1% different for the transitions of interest. The Ar+NaK results are also very similar; they are less than 3% different.

Integration parameters and number of partial waves

An appropriate integration grid must be used to ensure accurate numerical solutions to the coupled equations. The starting point of the integration (R_{min}) is chosen automatically by considering an approximate WKB solution to the diagonal equations and requiring that this solution be several orders of magnitude smaller at R_{min} than at the classical turning point for each channel. For $R \geq R_{\mathrm{min}}$, an adaptive step size algorithm selects the step size based on a tolerance parameter selected by the user. This algorithm allows the code to adjust the step size to the local rate of variation of the solutions. Finally, the integration is terminated at some R_{max} that must be larger than the range of the electronic potential. The user must choose a lowest possible R_{min}, which we will refer to as R^0_{min}, R_{max}, and the tolerance parameter.

We chose R^0_{min} to be 3.5 a_0 for He+NaK and 4.5 a_0 for Ar+NaK. At these R the electronic potentials are highly repulsive for all angles and the Legendre component $v_0(r_{\mathrm{e}}, R)$ has a value of about 0.013 E_{h} (2800 cm^{-1}) for both systems, which is over six times the collision energy of 0.002 E_{h} (440 cm^{-1}). In addition to the electronic potential, the effective potential also includes the repulsive centrifugal term in Eq. 2.90, and the classical turning point for channels with $l > 0$ will occur at larger R than for those with $l = 0$. Therefore our R^0_{min} are sufficient for all channels.

The value of R_{max} depends on the maximum partial wave J_{max} that must be included in the calculation. Roughly speaking, J_{max} can be related to the impact parameter b of the collision by $J = bk_j$, where k_j is related to the initial kinetic energy E_{kin} by $E_{\mathrm{kin}} = \hbar^2 k_j^2/(2\mu)$. (This relation follows from $\mathbf{J} \approx \mathbf{l} = \mathbf{r}\times\mathbf{p} = \mathbf{r}\times\hbar\mathbf{k}$.) For large values of J, the physical picture is that the trajectory of the incident particle is approximately a straight line that passes the center of the potential at a distance b. At sufficiently large b, the interaction potential will be negligible, so the corresponding J will not contribute strongly to the scattering. For each J, one determines a partial cross section $\sigma^J(j \rightarrow j')$, and the sum of these partial cross

sections is the total cross section:

$$\sigma(j \to j') = \sum_{J=0}^{\infty} \sigma^J(j \to j'). \tag{4.2}$$

One must try to choose a sufficiently large $J_{\max}$ so that partial waves with $J > J_{\max}$ make a negligible contribution to the scattering. Then one can approximate the cross sections as

$$\sigma(j \to j') \approx \sum_{J=0}^{J_{\max}} \sigma^J(j \to j'). \tag{4.3}$$

The previous arguments imply that $J_{\max}$ is related to the range of the interaction potential. Once $J_{\max}$ is set, it follows that the upper limit of integration $R_{\max}$ should be at least b in order to include the regions where the interaction potential is most likely to modify the trajectory.

Figure 4.5 shows several calculations that illustrate the relation between $J_{\max}$ and $R_{\max}$. For selected transitions of He+NaK and Ar+NaK, the panels show $(k_j^2/\pi)\sigma^J(j \to j')$ as a function of J on a log-log plot for several different values of $R_{\max}$. The curves for a given $R_{\max}$ tend to be well behaved up to a certain J and then to fall off precipitously. This fall off starts roughly at the value of J where the corresponding impact parameter b is larger than $R_{\max}$. In other words, after the fall off, the integration is not carried out far enough to include the most important region of the interaction, so the partial cross section decreases dramatically.

We compared the cross sections and fractions of orientation preserved for the values of $R_{\max}$ and $J_{\max}$ used to obtain the different curves in Fig. 4.5. For He+NaK, integrating to 25 a_0 and including partial waves up to $J = 127$ is sufficient. The cross sections of interest differ only slightly in the fourth significant figure between $R_{\max} = 25$ and 30 a_0 and the fractions of orientation preserved are identical to four significant figures. Between $R_{\max} = 30$ and 40 a_0 only the elastic cross sections differ in the fourth significant figure. The Ar+NaK results show small differences in the fourth significant figure between $R_{\max} = 30$ and 40, except for transitions with $|\Delta j| = 2$, for which the results differ in their third significant figures.

The straight line labelled "fit" in each panel of Fig. 4.5 indicates that the partial cross sections for large values of J (each calculated using a sufficiently large $R_{\max}$)

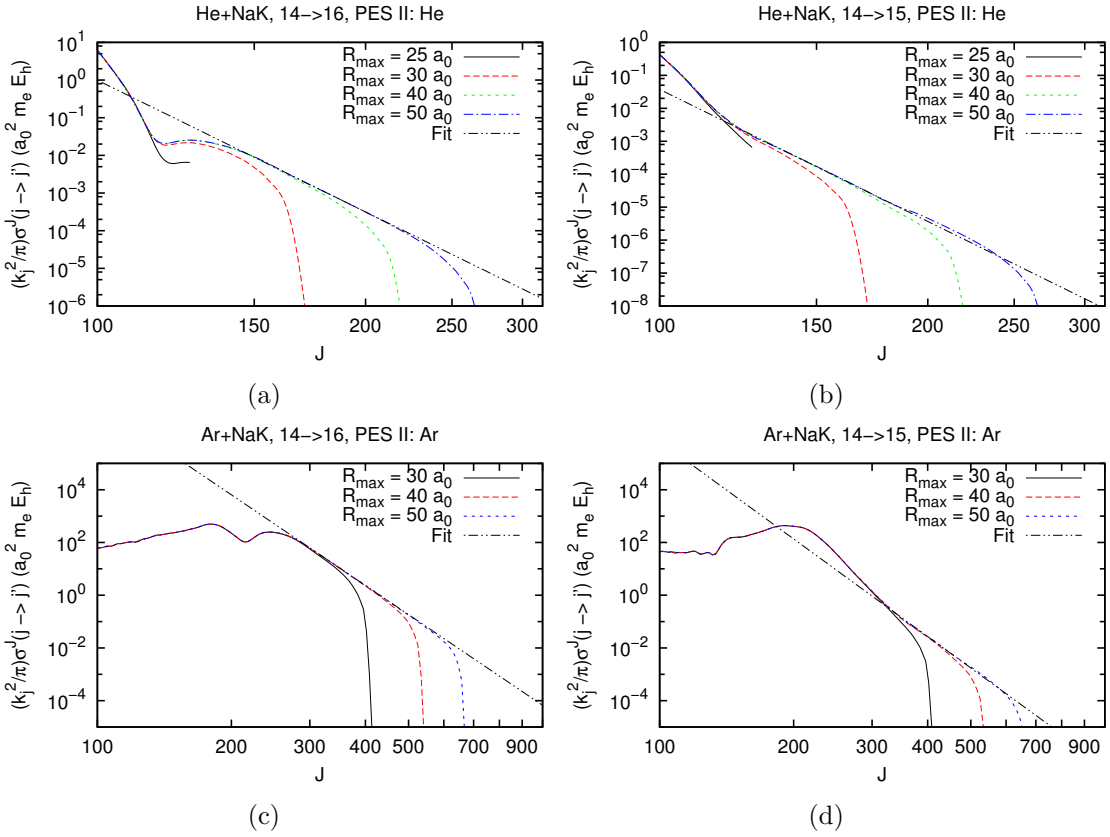

Figure 4.5: Log-log plot of $(k_j^2/\pi)\sigma^J(j \to j')$ in units of $a_0^2 m_e E_\mathrm{h}$ for $p = +1$ obtained using PES II: He (Panels (a) and (b)) and PES II: Ar (Panels (c) and (d)). Panels (a) and (c) show partial cross sections for $j = 14 \to 16$, while Panels (b) and (d) show results for $j = 14 \to 15$. Within each panel, each curve corresponds to a different upper limit of integration. For a given upper limit of integration, the partial cross sections roughly fall off at the J for which the impact parameter $b \approx J/k_j$ is larger than the upper limit of integration. Increasing the upper limit of integration allows for more accurate results for the same J. The fits, labeled "fit", were performed for regions where the partial cross sections display a power law dependence. For these calculations, the number of Legendre components was $n_\mathrm{max} + 1 = 11$, the tolerance was 10^{-3}, and $j_\mathrm{max} = 50$. For He+NaK, we used $J_\mathrm{max} = 127$, 175, 223, and 271 for the upper limits of 25, 30, 40, and 50 a_0, respectively. For Ar+NaK, we used $J_\mathrm{max} = 447$, 543, and 672 for the upper limits of 30, 40, and 50 a_0.

would follow a power law behavior:

$$\sigma^J(j \to j') \approx AJ^{-c}. \tag{4.4}$$

Each calculation for a fixed $R_{\max}$ follows the fit up to a point, and then falls sharply when J becomes too large for that value of $R_{\max}$. One can use the power law determined by the fitted curve to estimate the cross sections in the limit of summing all the partial cross sections to infinity (and in the limit of infinite $R_{\max}$):

$$\begin{aligned}
\sigma(j \to j') &= \sum_{J=0}^{\infty} \sigma^J(j \to j') && (4.5)\\
&\approx \sum_{J=0}^{J_{\max}} \sigma^J(j \to j') + A \int_{J_{\max}+1}^{\infty} J^{-c} dJ && (4.6)\\
&= \sum_{J=0}^{J_{\max}} \sigma^J(j \to j') + \frac{A}{c-1}(J_{\max}+1)^{1-c}, \quad c > 1. && (4.7)
\end{aligned}$$

We determined the power law dependence of selected partial cross sections by performing linear fits of $\log_{10} \sigma^J(j \to j')$ as a function of $\log_{10} J$. We performed these fits for each parity for transitions from $j = 14$ to 15–18 and from $j = 30$ to 31–34. We fit to the curve corresponding to $R_{\max} = 50\ a_0$ in the region where the curves appeared to follow the same straight line. Our values for c ranged from 7 to 24; in Panels (a)–(d), c was 11.6, 13.3, 11.4, and 12.3, respectively. For He+NaK, the correction was so small that the effect on the cross sections was negligible. For instance, for $14 \to 16$ and $30 \to 32$, the difference was on the order of $10^{-4}\%$. (We obtained these results by adding the correction to the cross sections for $J_{\max} = 223$ and $R_{\max} = 40\ a_0$; we have already shown the cross sections for $R_{\max} = 25\ a_0$, $J_{\max} = 127$ and $R_{\max} = 40\ a_0$, $J_{\max} = 223$ are almost identical to four significant figures.) For Ar+NaK, the only non-negligible differences were for the transitions $14 \to 16$, shown in Panel (c) of Fig. 4.5, and $30 \to 32$. For those transitions, integrating from $J = 448$ to ∞ and using the cross section for $R_{\text{int}} = 30\ a_0$ gave about a 2% difference for the transition from $j = 14$ to 16 and about a half of a percent difference for $j = 30$ to 32. Of course, we must be wary of the fact

that the partial cross sections for $R_{\max} = 30\ a_0$ were falling steeply near $J = 447$, as Panel (c) of Fig. 4.5 shows, and $\sigma(14 \rightarrow 16)$ might be a little smaller than it would be if $R_{\max}$ were higher. To estimate this additional contribution, we fixed $J_{\max} = 447$ and integrated to $R_{\max} = 30$ and 40 a_0 (with $j_{\max} = 30$). For the transition $j = 14 \rightarrow 16$, the cross sections changed by about 1%. Even with this correction, we estimate that integrating to $R_{\max} \rightarrow \infty$ and including $J_{\max} \rightarrow \infty$ would yield cross sections that were about 2% different from those obtained with $R_{\max} = 30\ a_0$ and $J_{\max} = 447$ for Ar+NaK for $j = 14 \rightarrow 16$. We expect the result for $j = 30 \rightarrow 32$ to also be unaffected by this change, and for the cross sections to remain within about 0.5% different.

We also investigated the effect of separately fixing $J_{\max}$ or $R_{\max}$ on the cross sections for $j = 14$ and on the fractions of orientation preserved; we performed these tests for $j_{\max} = 30$ and expect similar results for higher $j_{\max}$. For He+NaK, fixing $J_{\max} = 127$ and integrating to 25 a_0 and to 40 a_0 made no noticable difference in the results, with small changes in the fourth significant figures. Likewise, fixing $R_{\max}$ at 25 a_0 and setting $J_{\max} = 128$ or 159 gave results that were virtually identical to their fourth significant figures. For Ar+NaK, fixing $J_{\max} = 447$ and integrating to 30 a_0 and 40 a_0 also made no noticeable difference, except for $|\Delta j| = 2$ for which there were differences in the third significant figure; we have already discussed the effect on the $|\Delta j| = 2$ cross sections. For $J_{\max} = 447$ and $R_{\max} = 30\ a_0$, the partial cross sections near $J_{\max}$ were quite small and decreased as a power of ten for each increase by one in J; we expect the results to be well converged with respect to J.

Finally, we performed calculations with different tolerances for the adaptive step size selection. The code determines the step size for integration by taking a certain step, ΔR, and a step of half that size, $\Delta R/2$. The tolerance is a measure of the desired accuracy of the solution, and the next step size will be larger if the previous step led to "too accurate" of a solution. On the other hand, if the solutions for ΔR and $\Delta R/2$ are not accurate enough, then the code will take a step size of $\Delta R/4$, and so on, until the desired accuracy is achieved.

We must compromise between accuracy and computer time constraints. For instance, we have found that for He+NaK using a tolerance of 10^{-2} increases the

calculation time by about 50 percent compared to a tolerance of 10^{-1}, and for Ar+NaK it increases the time by about a factor of three. We generally chose the largest tolerance that would give four significant figures of accuracy.

We have compared results for tolerances of 10^{-3}, 10^{-2}, and 10^{-1}, with $j_{\max} = 50$ and $n_{\max} = 10$. For He+NaK, we integrated from 3.5 to 25 a_0 and included partial waves up to $J_{\max} = 127$. For Ar+NaK, we integrated from 4.5 to 30 a_0 and included up to $J_{\max} = 447$. For He+NaK, the cross sections for $j = 14$ and 30 are identical to within the fourth significant figure for 10^{-3} and 10^{-2}, and are also identical except for small changes in the fourth significant figures of the elastic cross sections between 10^{-2} and 10^{-1}. The fractions of orientation retained for $j = 30$ are identical to within four significant figures for all tolerances. For Ar+NaK, the cross sections for $j = 14$ and 30 are identical to within four significant figures for 10^{-3} and 10^{-2}, and differ in the third and fourth significant figures between 10^{-2} and 10^{-1}. In the latter case, the percent differences were all less than a percent, but we note that there are unphysical oscillations in some of the partial cross sections for a tolerance of 10^{-1}. The fractions of orientation retained are identical to the fourth significant figure between all three tolerances.

Legendre expansion of the PES

We considered the number of terms needed in the Legendre expansion of the potential (Eq. 2.87). We have compared results for an 11- and 16-term expansion; we calculated $V(R, r, \theta)$ at thirteen values of θ for each R and therefore can't expect to determine accurately many more than that number of components. For these comparisons we let $j_{\max}$ be 50 and fixed the other parameters at what we will use for our final values. We do not expect the results to change much with $j_{\max}$. For He+NaK, the results differ slightly in the fourth significant figure; the cross sections of interest ($j = 14$ and 30) are less than 0.7% different, while the fractions of orientation retained for $j = 30$ are less than 0.2% different. For Ar+NaK, the relevant cross sections differ in their third and fourth significant figures and are also less than 0.7% different. The fractions of orientation retained for transitions from $j = 30$ are

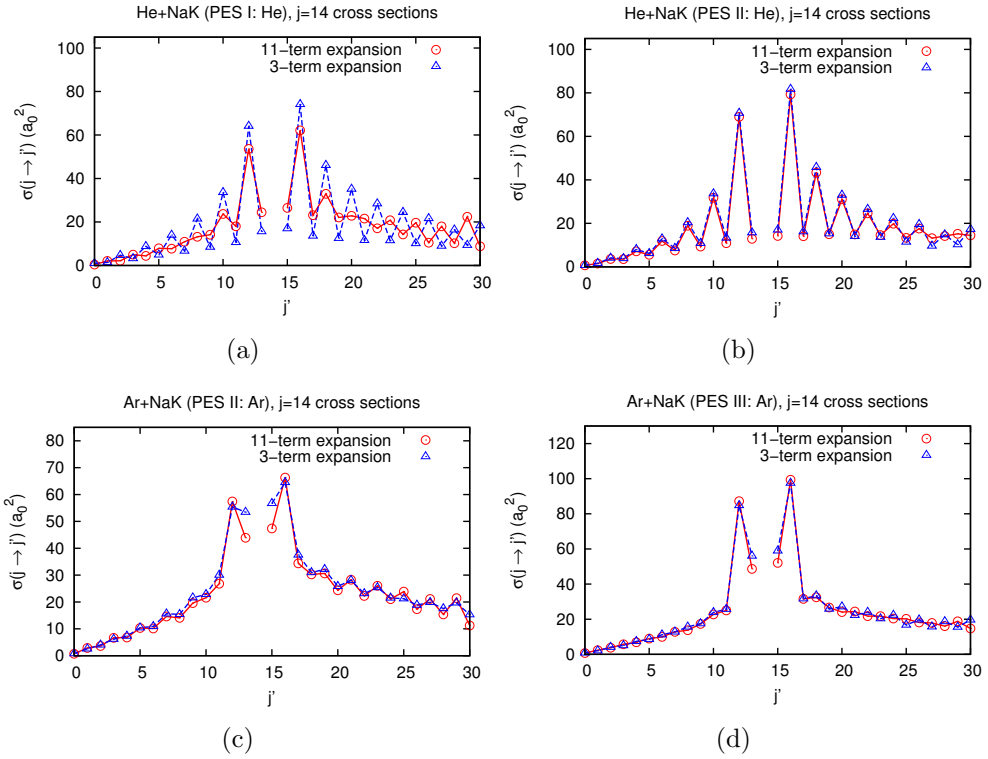

Figure 4.6: Cross sections in units of a_0^2 for transitions from $j = 14$ to j' for $n_{\max} = 10$ (labelled "11-term expansion") and $n_{\max} = 2$. In Panels (b) and (c), we show results for PES II: He and PES II: Ar. (We have also included results for PES I: He and PES III: Ar in Panels (a) and (d) to refer to in a later section.) For both He+NaK and Ar+NaK, the cross sections for $n_{\max} = 2$ reproduce the essential features of the results we obtained for $n_{\max} = 10$. For these calculations, the other parameters were fixed; these cross sections were obtained for $j_{\max} = 30$, a tolerance of 10^{-3}, 128 and 448 partial waves for He+NaK and Ar+NaK, and upper limits of integration of 25 a_0 for He+NaK and 30 a_0 for Ar+NaK.

less than 1.4% different.

We have also identified the minimum number of terms in the Legendre expansion needed to reproduce the essential features of the results. In Figs. 4.6 and 4.7, we show that $n_{\max} = 2$ is sufficient for both the cross sections and the fractions of orientation retained. The computer time does not change significantly with $n_{\max}$, so for our final results we use the better converged values for $n_{\max} = 10$. This result is

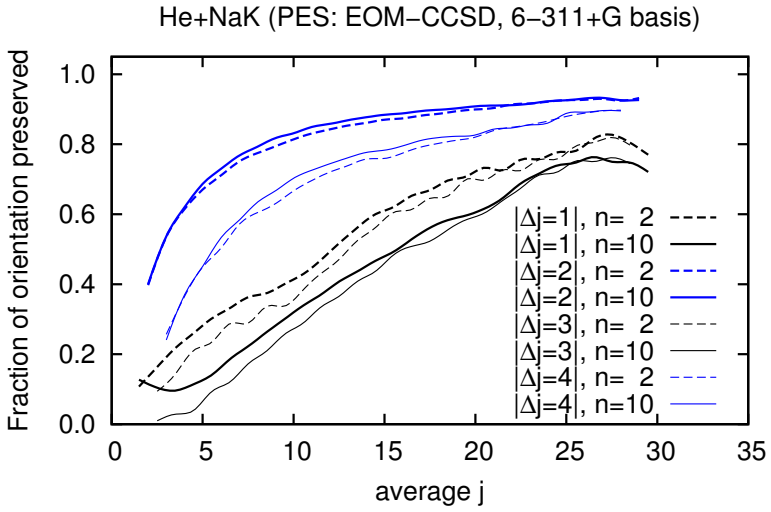

(a)

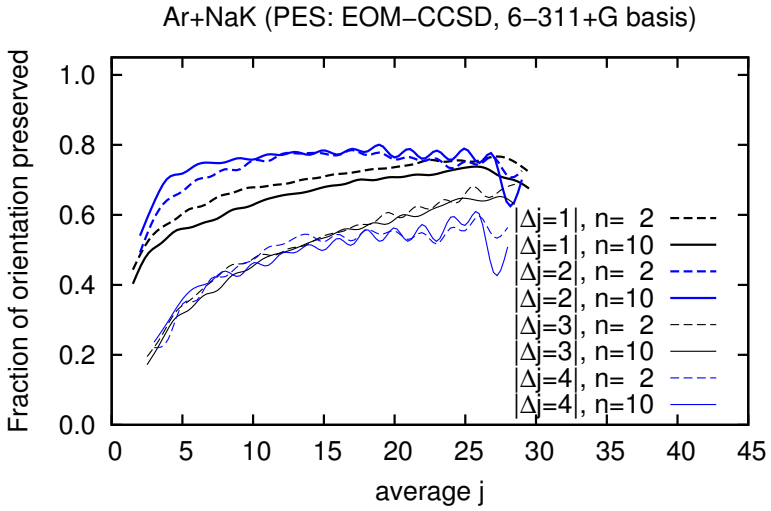

(b)

Figure 4.7: Fraction of orientation retained for fixed $|\Delta j|$ as a function of average j for $n_{\max} = 10$ and $n_{\max} = 2$. Panels (a) and (b) show results for PES II: He and PES II: Ar. For both He+NaK and Ar+NaK, the general trends are reproduced for $n_{\max} = 2$, but more Legendre components are needed for converged values. The results shown here were obtained for $j_{\max} = 30$, and so the results for average j near 30 are artifacts. We also used a tolerance of 10^{-3}, 128 and 448 partial waves for He+NaK and Ar+NaK, and upper limits of integration of 25 a_0 for He+NaK and 30 a_0 for Ar+NaK.

useful, however, in Section 4.4 when we investigate the dependence of the propensity on the PES.

Summary

The most significant of the (small) uncertainties discussed in this section are associated with the number of channels included in the calculation. For a given $j_{\max}$, these uncertainties are the smallest when the initial j is much less than $j_{\max}$ and then increase with j. We compared $j_{\max} = 40$ and 50 for He+NaK and $j_{\max} = 60$ and 70 for Ar+NaK, both sets at $E = 0.002\ E_{\mathrm{h}}$. The cross sections for $j = 14$ for each pair of calculations were within 5.0% for He+NaK and within 3.6% for Ar+NaK. For $j = 30$, the corresponding changes were 25% for He+NaK and 4.5% for Ar+NaK. The fractions of orientation retained for transitions from $j = 30$ were within 1% for He+NaK and within 3% for Ar+NaK.

The partial wave sum was truncated at $J_{\max} = 127$ for He+NaK at $E = 0.002\ E_{\mathrm{h}}$, and the integration was carried out from at least $R^0_{\min} = 3.5\ a_0$ to $R_{\max} = 25\ a_0$. For Ar+NaK, these values were $J_{\max} = 447$, $R^0_{\min} = 4.5\ a_0$, and $R_{\max} = 30\ a_0$. Using an analytic fit to the large-J behavior of the partial wave cross sections, we confirmed that the effect of truncating the sums at $J_{\max}$ was very small. There was one exception and this was for Ar+NaK for transitions with $|\Delta j| = 2$, where the cross sections increase by about 2.0% for $j = 14$ and by about 0.5% for $j = 30$. For both systems, we used a tolerance of 10^{-3}, which gave results that were identical to four significant figures with the results for a tolerance of 10^{-2}.

For most calculations we used an 11-term Legendre expansion of the potential. Comparison with the 16-term expansion showed small differences in the fourth significant figures for He+NaK and in the third and fourth significant figures for Ar+NaK. Remarkably, additional tests showed that three terms ($n = 0, 1, 2$) were enough to reproduce the essential features of the results.

4.2 Comparison with experimental results

In this section we will compare our results with available experimental data provided by the group of Prof. Huennekens [4–6].

4.2.1 Cross sections and rate constants

The experiments were conducted at a temperature of 600 K and, assuming thermal equilibrium, the cell environment contains a Maxwellian distribution of energies; cross sections for several different energies contribute to the data collected. That is why the experiments actually determine rate constants $k_{i\to f}(T)$, which are defined as the thermal average of the product of the relative velocity and the cross section:

$$k_{i\to f}(T) = \sqrt{\frac{2}{\pi}\left(\frac{\mu}{kT}\right)^3}\int_0^\infty \mathsf{v}\sigma_{i\to f}(\mathsf{v})\,\mathsf{v}^2 e^{-\mu\mathsf{v}^2/(2kT)}\,d\mathsf{v}. \tag{4.8}$$

We can express the rate constants in terms of energy by using the relationship between the relative velocity and the kinetic energy of the incident particle, $E_{\rm kin} = \mu\mathsf{v}^2/2$. By using this relation, one can express Eq. 4.8 as

$$k_{i\to f}(T) = \sqrt{\frac{1}{\pi\mu}\left(\frac{2}{kT}\right)^3}\int_0^\infty \sigma_{i\to f}(E_{\rm kin})\,E_{\rm kin}\,e^{-E_{\rm kin}/(kT)}\,dE_{\rm kin}. \tag{4.9}$$

If the cross section is independent of energy, say $\sigma^0_{i\to f}$, then one can greatly simplify Eq. 4.9:

$$\begin{aligned} k_{i\to f}(T) &= \sqrt{\frac{1}{\pi\mu}\left(\frac{2}{kT}\right)^3}\,\sigma^0_{i\to f}\int_0^\infty E_{\rm kin}\,e^{-E_{\rm kin}/(kT)}\,dE_{\rm kin} &(4.10)\\ &= \sigma^0_{i\to f}\bar{\mathsf{v}}, &(4.11)\end{aligned}$$

where $\bar{\mathsf{v}}$ is the average thermal velocity, $\sqrt{8kT/\pi\mu}$. Our calculations reported in Section 4.3.1 show that the cross sections depend weakly on energy, so in this section we will use Eq. 4.11 to compare our cross sections with experimental rate constants. Large energies require an enormous amount of resources, so we have made some estimates of the rate constants one would obtain by using Eq. 4.9 based on possible extrapolations to larger energies; these results will be presented in Section 4.3.1.

4.2.2 Rates for initial levels $(v, j) = (0, 14)$, $(1, 26)$, and $(0, 30)$

In Figs. 4.8–4.10, we present a comparison between the experimental [6] and theoretical rate constants for initial levels $(v, j) = (0, 14)$, (1,26), (0,30). The experimental error bars shown are for the absolute rate constants, and there is less uncertainty in the relative rates. An iterative procedure was used [6] to correct the experimental rate constants for so-called multiple collision effects, which may arise at higher densities when there is a contribution to the $j \to j'$ rate from a two-step process through an intermediate level. The iterative procedure is not exact, but it provides an upper limit for the error due to neglect of multiple collision effects. Thus we determined the experimental error bars as follows: the upper bound is the rate constant that was not corrected for multiple collision effects plus its uncertainty, while the lower bound is the rate constant estimated by correcting for multiple collision effects.

Panels (a) and (b) of Figs. 4.8–4.10 compare results for He+NaK, where the theoretical results were obtained using PES I: He and PES II: He, respectively. For $j = 14$ and 26, there is better agreement with absolute rate constants for PES II: He, while for $j = 30$ there is better agreement for PES I: He. We note, however, that the data for He+NaK for $(v, j) = (0, 30)$ was based on a smaller set of observations than for the other levels. The experiments indicate that the propensity for Δj even transitions persists to high $|\Delta j|$, and we reproduce that behavior with PES II: He. With PES I: He an inverse propensity (that is, a tendency for Δj odd rates to be larger than those for Δj even) appears for higher $|\Delta j|$. We will say more about this inverse propensity in Section 4.4. Meanwhile, Panels (c) and (d) of Figs. 4.8–4.10 compare results for Ar+NaK for PES II: Ar and PES III: Ar, respectively. In all cases, we obtain the best agreement for PES III: Ar. The experiments observed a propensity for Δj even transitions that persists to about $|\Delta j| = 6$, after which there is no propensity. We predict the development of an inverse propensity at higher $|\Delta j|$ that is much more pronounced for PES II: Ar. This is another reason that the results for PES III: Ar agree better with experiment.

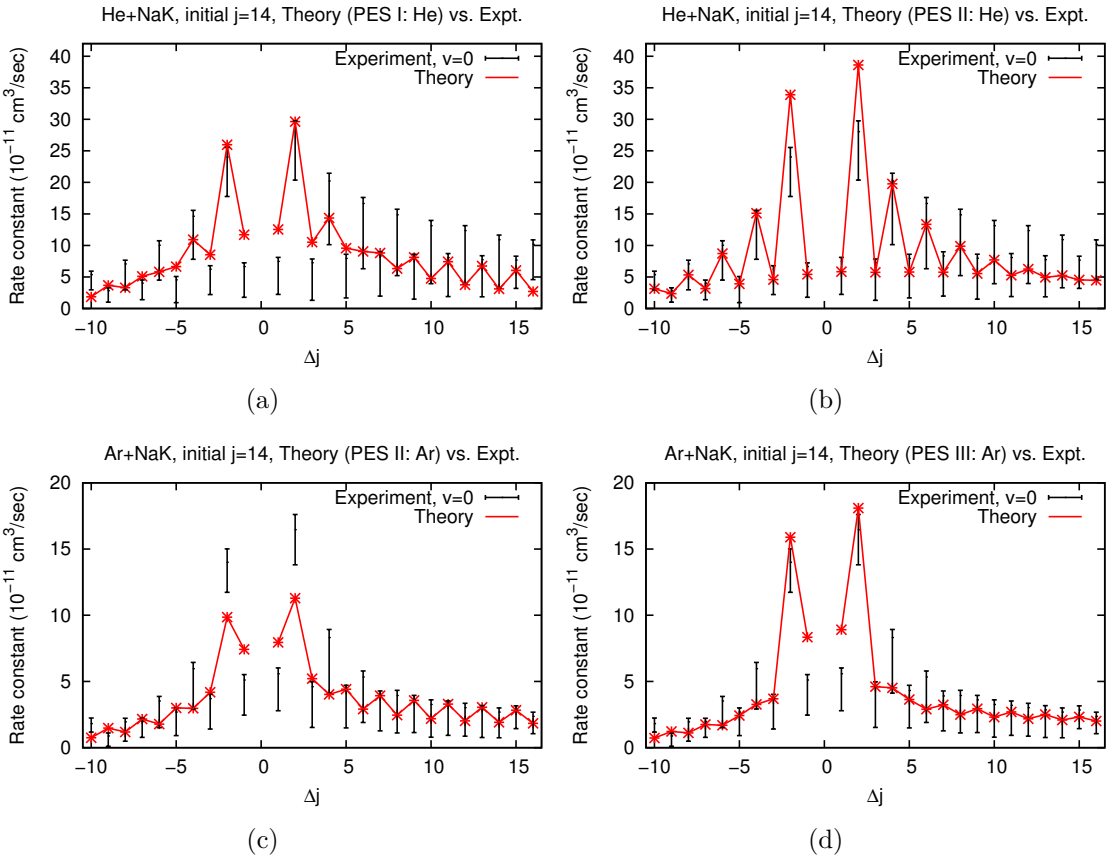

Figure 4.8: Panels (a) and (b) compare approximate theoretical rate constants for He+NaK for PES I: He and PES II: He, respectively, with experimental values for $j = 14$ and $v = 0$ [6]. Panels (c) and (d) show similar comparisons for Ar+NaK for PES II: Ar and PES III: Ar. For He+NaK, the results for PES II: He agree the best with experiment, while for Ar+NaK the results for PES III: Ar agree the best.

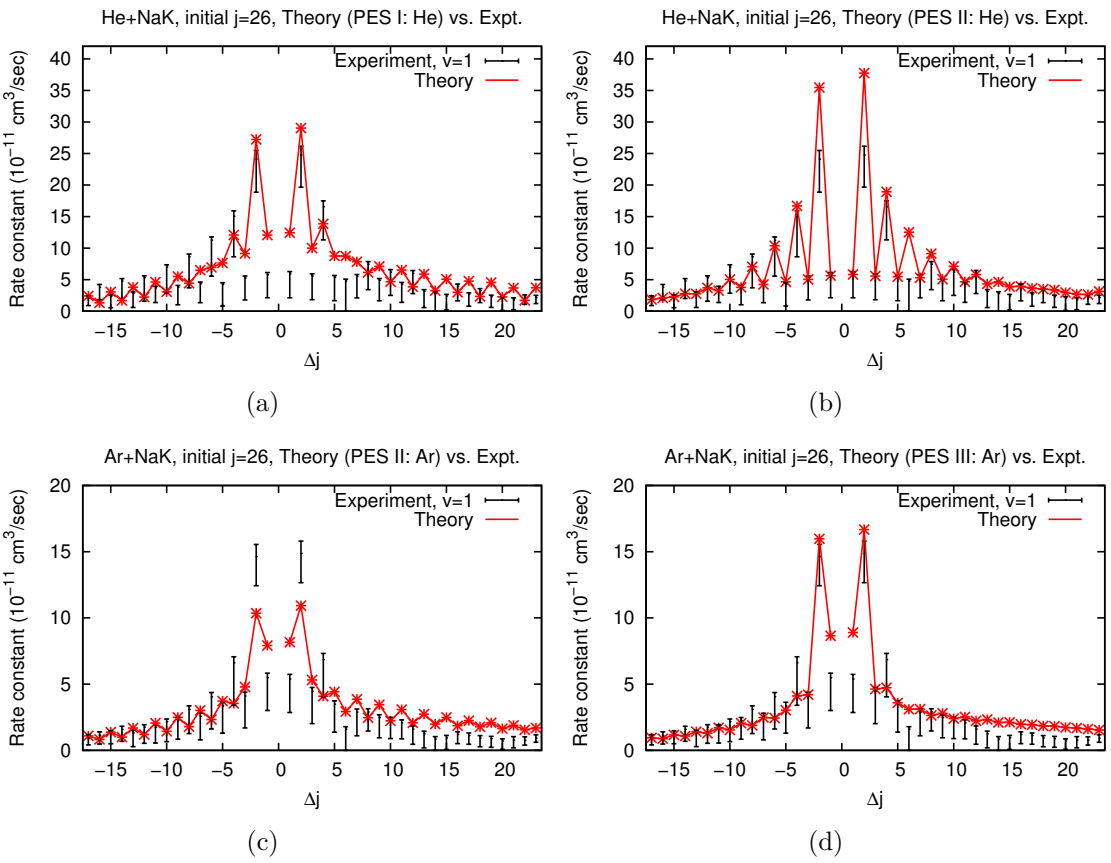

Figure 4.9: Panels (a) and (b) compare approximate theoretical rate constants for He+NaK for PES I: He and PES II: He, respectively, with experimental values for $j = 26$ and $v = 1$ [6]. Panels (c) and (d) show similar comparisons for Ar+NaK for PES II: Ar and PES III: Ar. Our calculations are for $v = 0$, but we have found that the cross sections depend weakly on the vibrational level [2]. The experimental results for $\Delta j = 6$ and $\Delta j = 12$–19 were affected by spin-orbit coupling with the $b\,^3\Pi$ electronic state; since our calculations neglect fine structure effects, we do not predict such effects. Ignoring these transitions, for He+NaK the results for PES II: He agree the best with experiment, while for Ar+NaK the results for PES III: Ar agree the best; this is also what we found for $j = 14$.

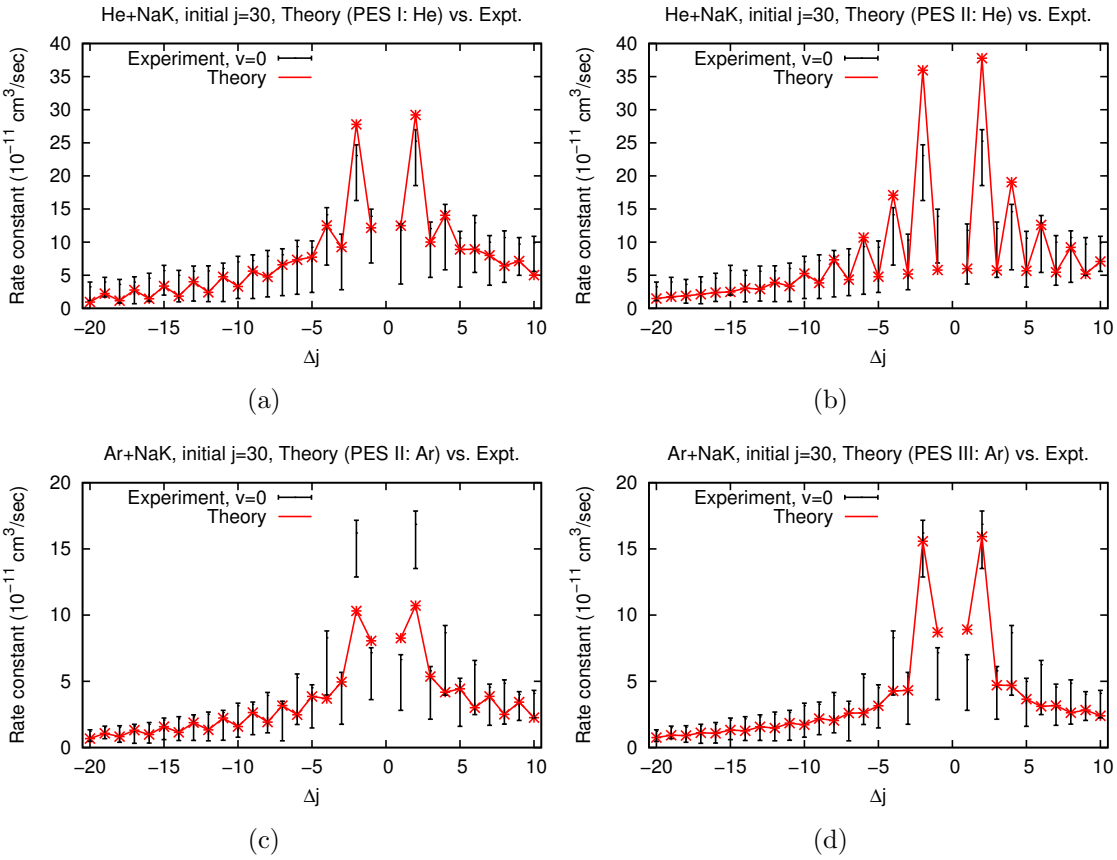

Figure 4.10: Panels (a) and (b) compare approximate theoretical rate constants for He+NaK for PES I: He and PES II: He, respectively, with experimental values for $j = 30$ and $v = 0$ [6]. Panels (c) and (d) show similar comparisons for Ar+NaK for PES II: Ar and PES III: Ar. For He+NaK, the results for PES I: He agree the best with experiment, in contrast with $j = 14$ and 26; we note that the experimental results for He+NaK for $(v, j) = (0, 30)$ are based on a smaller number of observations. For Ar+NaK, the results for PES III: Ar agree the best, just as they did for $j = 14$ and 26.

4.2.3 Relative cross sections

In Fig. 4.11 we present our cross sections as a function of average $j = (j + j')/2$ for fixed Δj. For both systems and for each PES, we predict that there is a difference between $\sigma(j \to j+\Delta j)$ and $\sigma(j \to j-\Delta j)$ that is more pronounced for lower average j. Moreover, we predict a qualitatively different behavior for He+NaK between the odd and even Δj transitions, as shown in Panels (a) and (b) of Fig. 4.11.

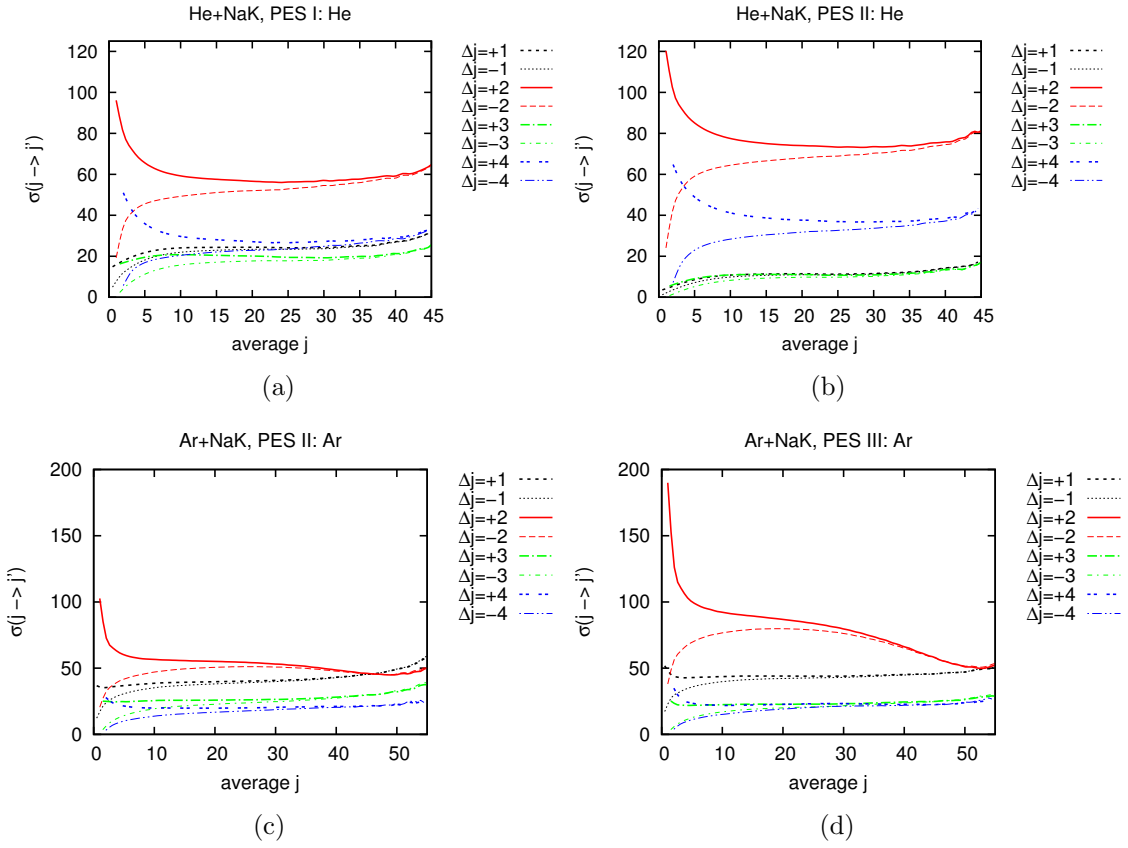

Figure 4.11: Cross sections in units of a_0^2 as a function of average j for fixed Δj are shown for He+NaK in Panels (a) and (b) and for Ar+NaK in Panels (c) and (d). Each panel corresponds to a different PES. We predict that the difference between $\sigma(j \to j+\Delta j)$ and $\sigma(j \to j-\Delta j)$ is more pronounced at lower average j, and that for He+NaK the odd and even transitions show qualitatively different behaviors.

We can compare these results with experiment. The cross sections (Eq. 2.95) can be rewritten in terms of two factors. The first depends only on the initial j. The second is symmetric under the interchange of j and j' and thus depends only on the average j (or for short, $\bar{j}$) and $|\Delta j|$. We can therefore express the cross sections as

$$\sigma(j \to j') = \frac{\pi}{(2j+1)k_j^2} \sum_J \sum_{l,l'} (2J+1) \left| T^J_{jl,j'l'} \right|^2 = \frac{\pi}{(2j+1)k_j^2} f(\bar{j}, |\Delta j|). \quad (4.12)$$

One can show that

$$\sigma(j \to j + \Delta j) - \sigma(j \to j - \Delta j) \approx \frac{\pi}{k_j^2} \frac{\partial f}{\partial \bar{j}} (\bar{j}, |\Delta j|) \frac{\Delta j}{2j+1}. \quad (4.13)$$

Therefore, the more pronounced difference $\sigma(j \to j + \Delta j) - \sigma(j \to j - \Delta j)$ that we predict at lower average j could be related to the slope of $f(\bar{j}, |\Delta j|)$, the factor $(2j+1)^{-1}$, or both.

In Fig. 4.12 we show experimental and theoretical values for $f(\bar{j}, |\Delta j|)$ for both He+NaK and Ar+NaK; this comparison is a way to look at the trends predicted by all four experimental data sets. Panels (a) and (b) show the results for He+NaK. For both PESs, we predict that the slope of f is approximately constant, and so does experiment within the error bars (with the possible exception of $|\Delta j| = 2$). Thus experiment and theory both predict differences in $\sigma(j \to j + \Delta j)$ and $\sigma(j \to j - \Delta j)$ that increase as $\bar{j}$ decreases, and these differences are primarily due to the factor $1/(2j+1)$ in Eq. 4.13. We obtain better agreement for the slope of f for odd $|\Delta j|$ transitions with PES II: He and for even $|\Delta j|$ with PES I: He. Additionally, the values of f we predict for PES II: He for different $|\Delta j|$ are in the same order as the experimental data for each average j. Meanwhile, in Panels (c) and (d) of Fig. 4.12 we show results for Ar+NaK. Our results indicate that the slope of f is constant when $|\Delta j| \neq 2$, and this is consistent with experimental error bars. For $|\Delta j| = 2$, we predict that the slope of f is not constant; there's a change around $\bar{j} = 30$. The experimental error bars could be consistent with that; they do not appear to lie along one line. Therefore for $|\Delta j| = 2$ the differences between $\sigma(j \to j + \Delta j)$ and $\sigma(j \to j - \Delta j)$ are related to both the factor of $1/(2j+1)$ in Eq. 4.13 and to the change in the slope of $f(\bar{j}, |\Delta j|)$ near $\bar{j} \approx 35$. The agreement is better for

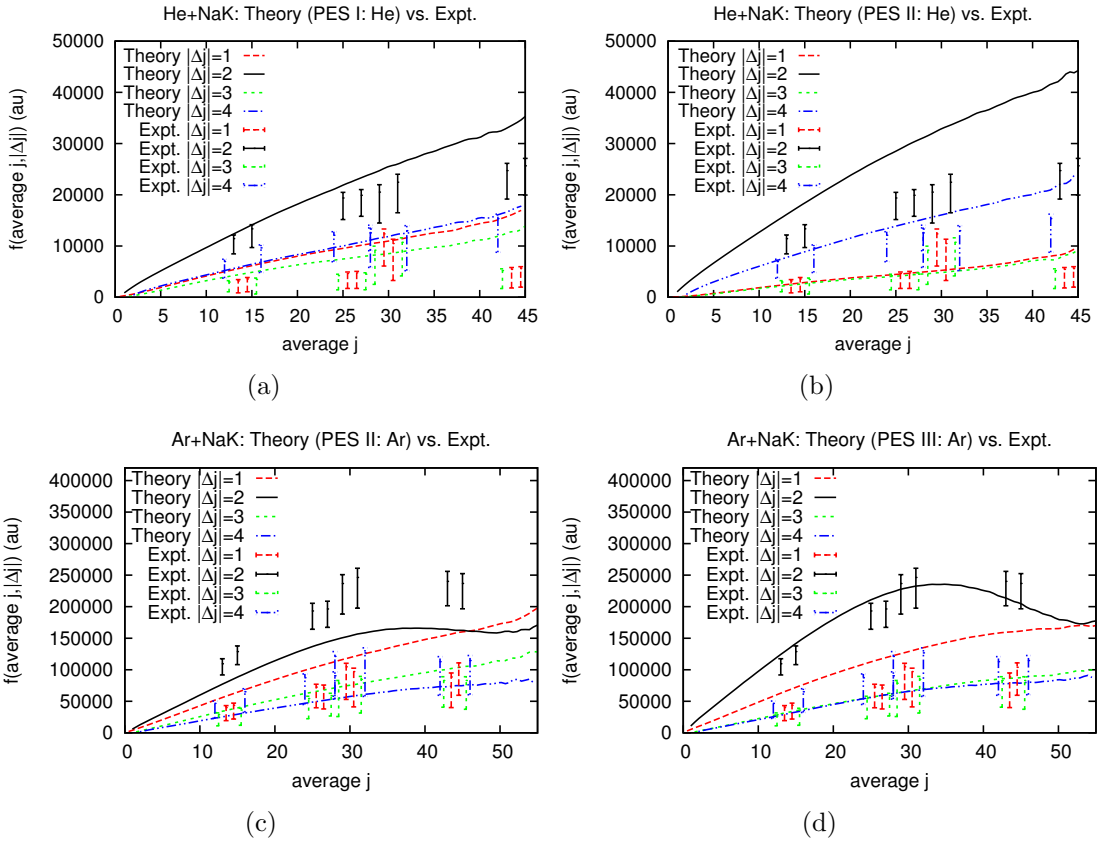

Figure 4.12: Comparison between theoretical and experimental $f(\bar{j}, |\Delta j|)$ for He+NaK and Ar+NaK for each PES. The lines show the theoretical values and the vertical bars show the experimental values. We extracted approximate values of f from experiment by converting rate constants [6] to cross sections with Eq. 4.11 and multiplying them by $(2j+1)k_j^2/\pi$. The experimental data was for $(v,j) = (0,14)$, $(0,30)$, $(1,26)$, and $(2,44)$; we have found there is little dependence on v for the cross sections [2] and will discuss this more in Section 4.3.2. We note once more that the experimental data for He+NaK for $(0,30)$ is based on a smaller set of observations.

PES III: Ar than PES II: Ar, with more points lying within experimental error bars for $|\Delta j| = 2$ and 3. It is difficult to say whether we predict a different ordering of the curves than the experiments do because of the way the error bars overlap.

4.2.4 Quenching rates

Some of our results have provided input for the experimental analysis [6]. The analysis involves rate equations with unknown quenching rates, and the primary contribution to the quenching rate for a given j is rotationally inelastic collisions. Figure 4.13 shows that we predict that $\sum_{j \neq j'} \sigma(j \rightarrow j')$ is fairly constant with respect to j. This prediction was incorporated in the experimental analysis [6], and different possible values for a constant quenching rate were determined using different methods. In Fig. 4.13, we have plotted the lowest and highest experimental quenching cross sections, connected them with an error bar, and compared them with our results for $\sum_{j \neq j'} \sigma(j \rightarrow j')$. Our quenching cross sections are always higher than the experimental values, regardless of the PES, but they are closer for Ar+NaK.

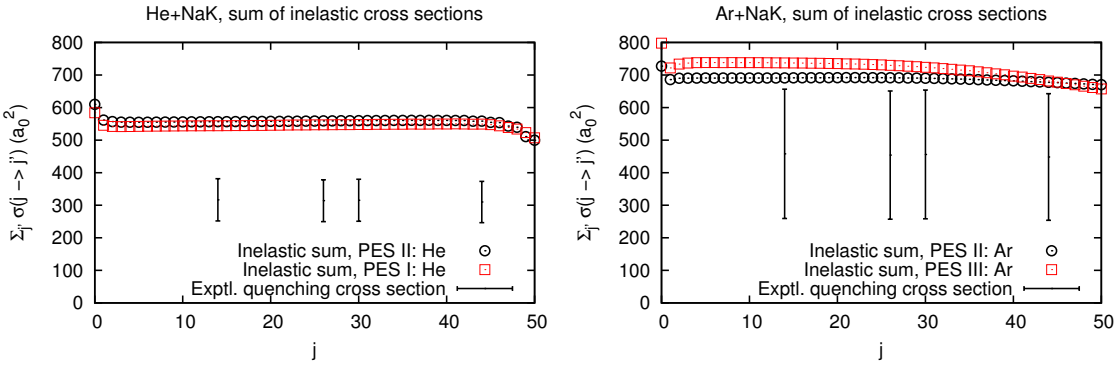

(a) (b)

Figure 4.13: Comparison of quenching cross sections as a function of j. We converted the experimental rate constants [6] to approximate cross sections using Eq. 4.11. By using different methods, the experimentalists obtained different constant values for the quenching rates. We plotted their lowest and highest constant values, connected them with an error bar, and compared with our results for $\sum_{j \neq j'} \sigma(j \rightarrow j')$. In all cases, our quenching cross sections are higher than the data points, although the difference is smaller for Ar+NaK.

4.2.5 Transfer of moments

In addition to cross sections, we have also compared fractions of orientation retained with experimental values for transitions from $j = 30$ [4, 5]. The comparison is not perfect; the data are for $v = 16$ while our calculations are for $v = 0$. In Section 4.3.2 we will discuss what we estimate to be the vibrational dependence of the transfer of orientation. Moreover, we mentioned in Section 2.5 that to evaluate the fraction of orientation preserved in a cell environment (that is, to generalize Eq. 2.134) where the molecules have a thermal distribution of energies, one would need to evaluate the ratios

$$\frac{\int_0^\infty d_1(j \to j'; E_{\rm kin})\, E_{\rm kin}\, e^{-E_{\rm kin}/kT}\, dE_{\rm kin}}{\int_0^\infty d_0(j \to j'; E_{\rm kin})\, E_{\rm kin}\, e^{-E_{\rm kin}/kT}\, dE_{\rm kin}}. \tag{4.14}$$

We have not yet done this, and our approximation $d_1(j, j')/d_0(j, j')$ will be more accurate if $\sigma_0(j \to j')$ and $\sigma_1(j \to j')$ do not depend strongly on the energy; so far, we have found this is true for $\sigma_0(j \to j')$.

In Fig. 4.14 we compare theoretical and experimental [4, 5] fractions of orientation retained for transitions from $j = 30$ as a function of Δj. The He+NaK results are shown in Panel (a), and the Ar+NaK results are shown in Panel (b). In both cases, the results do not indicate much sensitivity to the PES. For He+NaK, we are within error bars for Δj odd transitions and for $|\Delta j| = +4$, but we are outside of the error bars for $\Delta j = \pm 2$ and -4. However, the experimental data point at $\Delta j = -4$ looks like an outlier. For Ar+NaK, we predict a greater fraction of orientation is preserved than the data suggests. For instance, for $\Delta j = -4$, we predict a fraction that is about 0.7, while the lower bound for the data is about 0.3, which means experiment and theory are around 80 percent different for $\Delta j = -4$. Nonetheless, both theory and experiment predict that less orientation is preserved for Ar+NaK than for He+NaK.

The fraction of orientation retained is symmetric in j and j', so one can plot the results in terms of the average $j = (j + j')/2$ and the absolute value of Δj. In Panels (a) and (b) of Fig. 4.15 we present such plots for He+NaK for each PES,

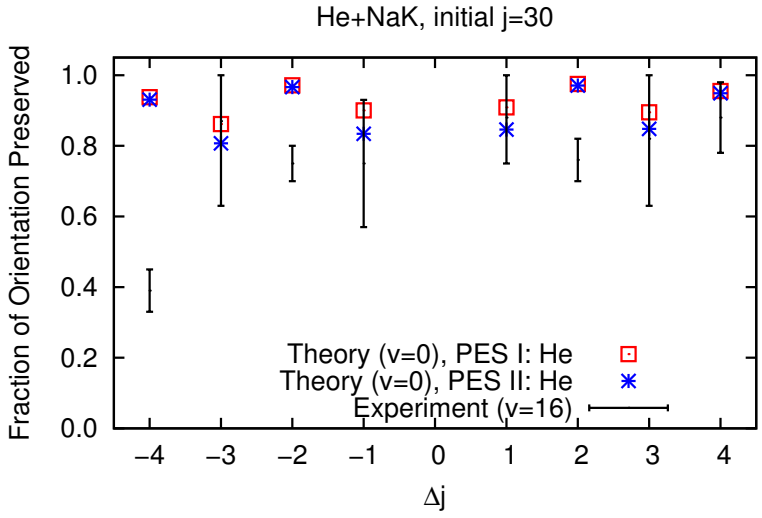

(a)

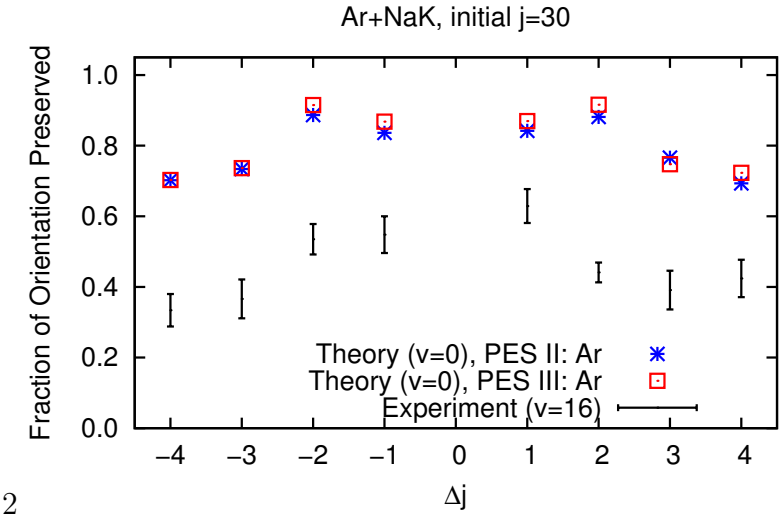

2

(b)

Figure 4.14: Comparison between theory and experiment of the fraction of orientation retained after many collisions for He+NaK, Panel (a), and for Ar+NaK, Panel (b), as a function of Δj for $j = 30$. The experimental data [4, 5] is shown as a black vertical bar, and in each panel there are theoretical results for two different PESs. Panel (a) shows that for He+NaK the theoretical results are within error bars for Δj odd transitions and for $\Delta j = +4$, and that the data for $\Delta j = -4$ looks like an outlier. Panel (b) shows that for Ar+NaK we predict a greater fraction of orientation is preserved for all transitions.

and in Panels (c) and (d) we present them for Ar+NaK. In every case, we predict that it's easier for the projectiles to destroy orientation when the rotational energy of the molecules is low (low average j). As the molecules rotate with more energy, though, it becomes more difficult to destroy orientation and a greater fraction is preserved. With additional data, we could confirm this prediction. For He+NaK we

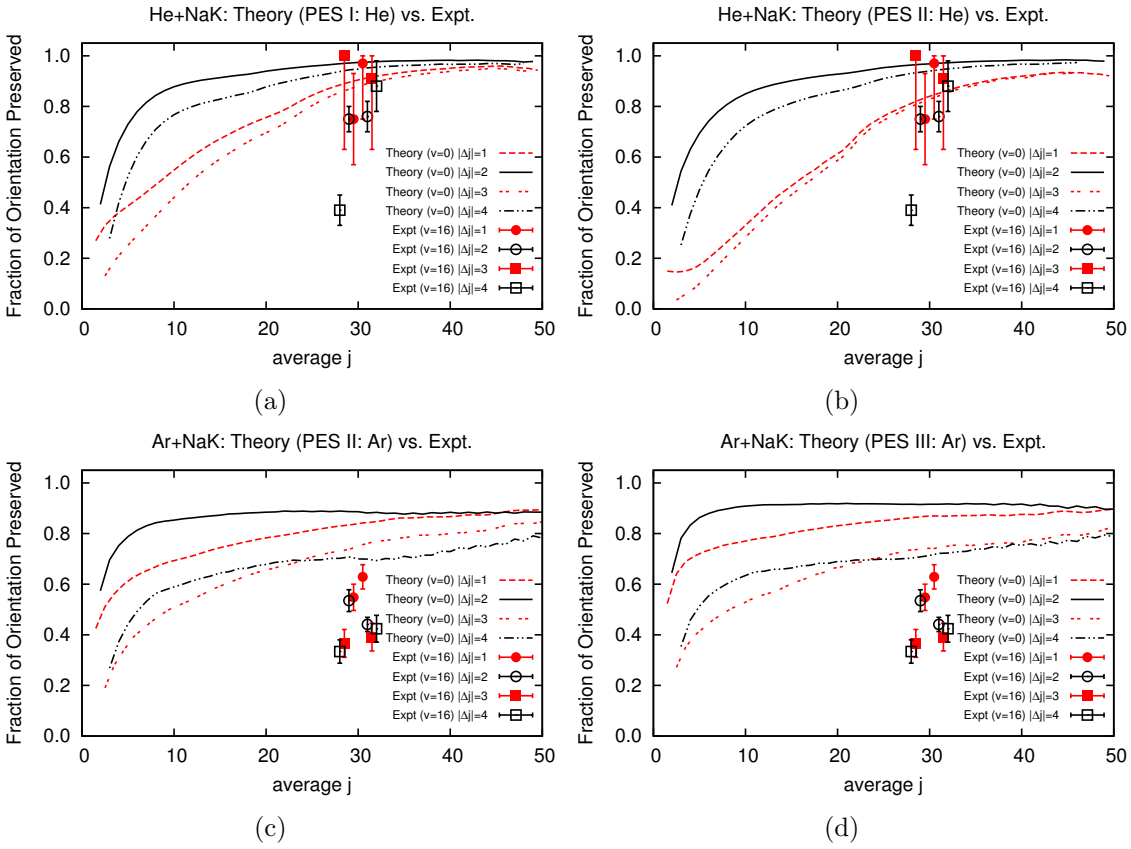

Figure 4.15: Comparison between theory and experiment [4, 5] for the fraction of orientation retained after many collisions as a function of the average j for He+NaK and Ar+NaK. Panel (a) shows the result for PES I: He, Panel (b) for PES II: He, Panel (c) for PES II: Ar, and Panel (d) for PES III: Ar. There is more of a difference between the results for the two He+NaK PESs than the results for the two Ar+NaK PESs, and we predict different trends for He+NaK than for Ar+NaK.

predict that as the average j decreases, there will be an enhanced difference between

fractions of orientation preserved for odd and even $|\Delta j|$. Moreover, we predict that this difference is more pronounced for PES II: He than PES I: He. At present, however, experimental data is needed for comparison in this region. For Ar+NaK, we don't predict the same difference between odd and even $|\Delta j|$. Instead, we see a switchover point between average $j = 20$ and 30 where the fraction of orientation retained becomes higher for $|\Delta j| = 3$ than for $|\Delta j| = 4$, and another switchover point for PES II: Ar between average $j = 40$ and 50 where the fraction becomes higher for $|\Delta j| = 1$ than $|\Delta j| = 2$; additional data are needed to confirm these predictions. Each Ar+NaK PES shows very similar results, with small changes in the average j at which the switchovers occur.

Finally, we show that the trends in the orientation results are distinct from the trends in the population results, which we should expect since the orientation in a level (v, j) is independent of the population in that level. In Fig. 4.16, we present our values for the population moment, $d_0(j, j')$, as a function of the average j. In Panel (a) we show that for PES I: He, $d_0(j, j')$ is fairly similar for $|\Delta j| = 1$, 2, and 3, in contrast with the difference between fractions of orientation preserved for odd and even $|\Delta j|$ shown in Panel (a) of Fig. 4.15. In Panel (c) of Fig. 4.16, there is a different ordering of the $d_0(j, j')$ with respect to $|\Delta j|$ than the ordering of the fractions of orientation retained (Panel (c) of Fig. 4.15), and there is no switchover point between $|\Delta j| = 3$ and 4 in the results for $d_0(j, j')$. These examples are sufficient to show that trends in the population moments do not determine the trends in the fractions of orientation preserved.

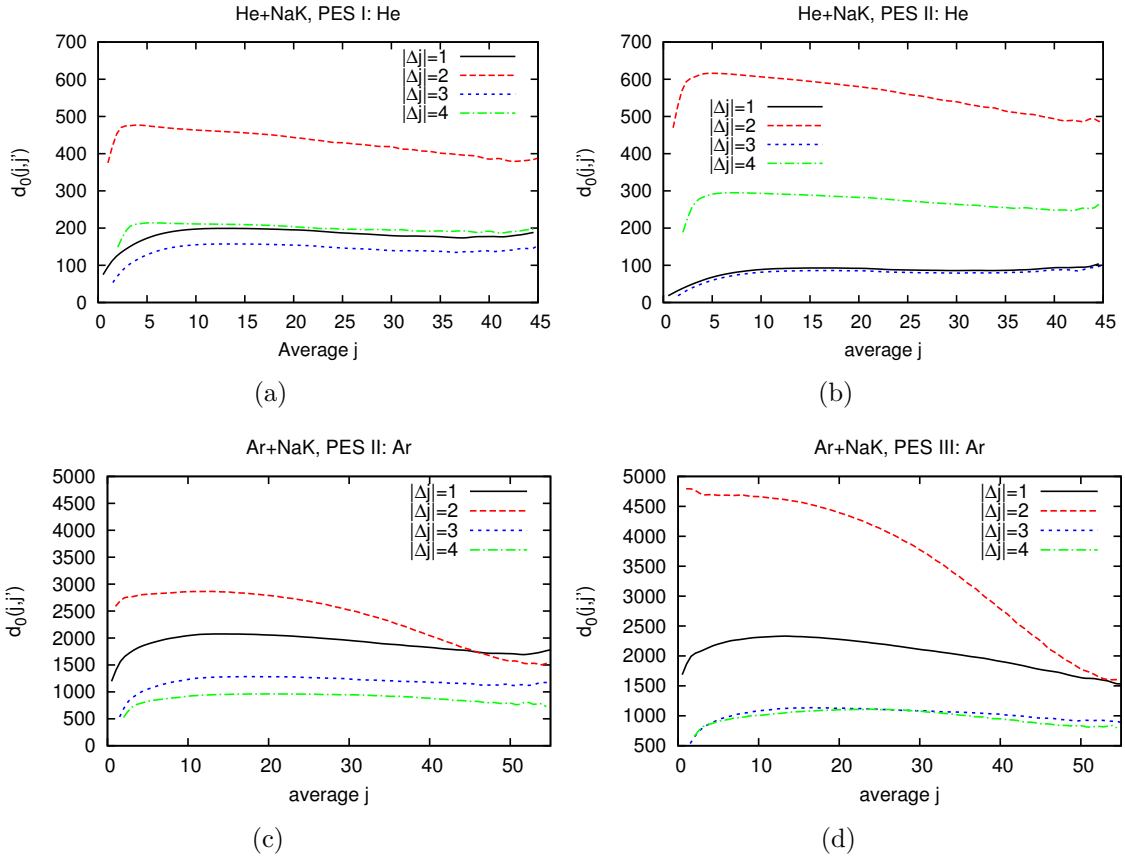

Figure 4.16: The population moment $d_0(j, j')$ for fixed $|\Delta j|$ as a function of average j is shown for PES I: He in Panel (a), for PES II: He in Panel (b), for PES II: Ar in Panel (c), and for PES III: Ar in Panel (d). As expected, the trends in $d_0(j, j')$ are different from the trends in the fraction of orientation retained, $d_1(j, j')/d_0(j, j')$.

4.3 Additional theoretical results

4.3.1 Energy dependence of the cross sections

In this section we present calculations of the energy dependence of the $j \to j'$ cross sections and use them to estimate the rate constants one would obtain with the exact expression, Eq. 4.9. We also examine the dependence of the quenching cross sections (introduced in Section 4.2.4) on energy. The results we present are for PES II: He and PES II: Ar.

The calculations for other energies were similar to those described in Section 4.1 for $E = 0.002\ E_\mathrm{h}$, except for the following points. First, we determined a different upper limit of integration, R_max, and highest partial wave, J_max, for each total energy E; their values are listed in Table 4.1. We selected each R_max by positing that the potential $V(R, r_\mathrm{e}, \theta)$ is negligible when it is a certain fraction of the collision energy. For simplicity, we examined the ratio between the zeroth Legendre component of the PES, $v_0(R)$, which is the angle-averaged potential, and the total energy. Specifically, for energies lower than $0.002\ E_\mathrm{h}$, we chose R_max by requiring that $v_0(R_\mathrm{max})/E$ be the same value as it is for $E = 0.002\ E_\mathrm{h}$ and $R_\mathrm{max} = 30\ a_0$. For the He+NaK calculations with $E > 0.002\ E_\mathrm{h}$, we let $R_\mathrm{max} = 30\ a_0$, which is more than sufficient by the same argument. Then for each total energy we determined J_max from $J_\mathrm{max} \approx R_\mathrm{max} k_j$. Second, for the He+NaK calculations with $E = 0.004$ and $0.008\ E_\mathrm{h}$, we changed the value of E_0 at which the electronic energies were modified (Eq. 3.3) from $0.004\ E_\mathrm{h}$ to $0.010\ E_\mathrm{h}$ and kept $\beta = 2$. With this new E_0, we reproduced results for $E = 0.001\ E_\mathrm{h}$ that we had obtained using $E_0 = 0.004\ E_\mathrm{h}$ to within 1.5%.

Rotationally inelastic cross sections

Figure 4.17 presents the calculated cross sections for He+NaK and Ar+NaK for several initial kinetic energies and for initial $j = 14$. Both systems show a dependence on the energy, especially for lower initial kinetic energies, while the propensity does not change significantly. To determine rate constants using the exact expression, Eq. 4.9, one must convolute the cross sections with the distribution $E_\mathrm{kin}^j e^{-E_\mathrm{kin}^j/kT}$ for

Table 4.1: Parameters used in the calculation of cross sections for PES II: He and PES II: Ar for different total energies. Every calculation involved $j_{\max} = 50$, a tolerance of 10^{-3}, and an eleven-term Legendre expansion of the PES. We performed high energy calculations for He+NaK only, since the Ar+NaK calculations require more resources.

	He+NaK			Ar+NaK		
Total energy (E_h)	$R^0_{\min}$ (a_0)	$R_{\max}$ (a_0)	$J_{\max}$	$R^0_{\min}$ (a_0)	$R_{\max}$ (a_0)	$J_{\max}$
0.0080^a	3.5	30	319	N/A	N/A	N/A
0.0040^a	3.5	30	239	N/A	N/A	N/A
0.0025^b	3.5	30	175	4.5	30	447
0.0015^b	3.5	32	143	4.5	32	367
0.0010^b	3.5	34	127	4.5	34	319
0.0005^b	3.5	38	111	4.5	38	255

$^a E_0 = 0.010\ E_h$ and $\beta = 2$
$^b E_0 = 0.004\ E_h$ and $\beta = 2$

$T = 600\,K$; the distribution (scaled by an arbitrary constant) is shown as a solid black line in Fig. 4.17. Since we calculated the He+NaK cross sections for a broader range of energies, the He+NaK rate constants we predict will be less uncertain than the Ar+NaK rate constants.

The cross sections (given earlier as Eq. 2.95) can be written as

$$\sigma(j \to j') = \frac{\pi}{k_j^2(2j+1)} \sum_J \sum_{l,l'} (2J+1) \left| T^J_{jl,j'l'} \right|^2 . \tag{4.15}$$

The energy dependence of the cross sections at low energies is often determined largely by the $1/k_j^2$ factor. If this is the case, then the product of $E^j_{\text{kin}} = \frac{1}{2}\mu k_j^2$ and $\sigma(j \to j')$ should be approximately a straight line. Indeed, Fig. 4.18 shows that the values of $E^j_{\text{kin}}\sigma(j \to j')$ for $j = 14$ do show an approximate linear behavior. The points in Fig. 4.18 are the calculated $E^j_{\text{kin}}\sigma(j \to j')$, and the lines are linear fits to the calculated points for each transition. The results of the fits are listed in Table 4.2.

We estimated rate constants $k_{i\to f}(T)$ by using the linear fits to extrapolate $E^j_{\text{kin}}\sigma(j \to j')$ to infinity and substituting the extrapolation into Eq. 4.9. The

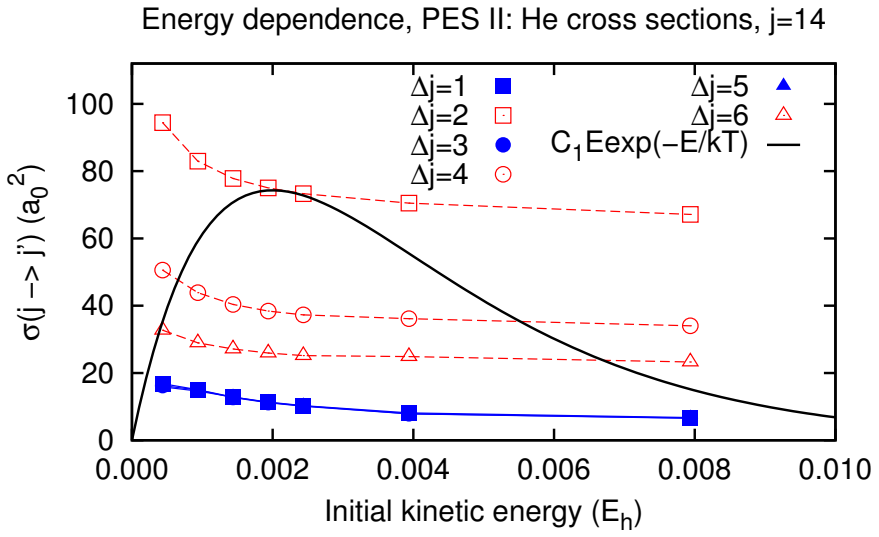

(a)

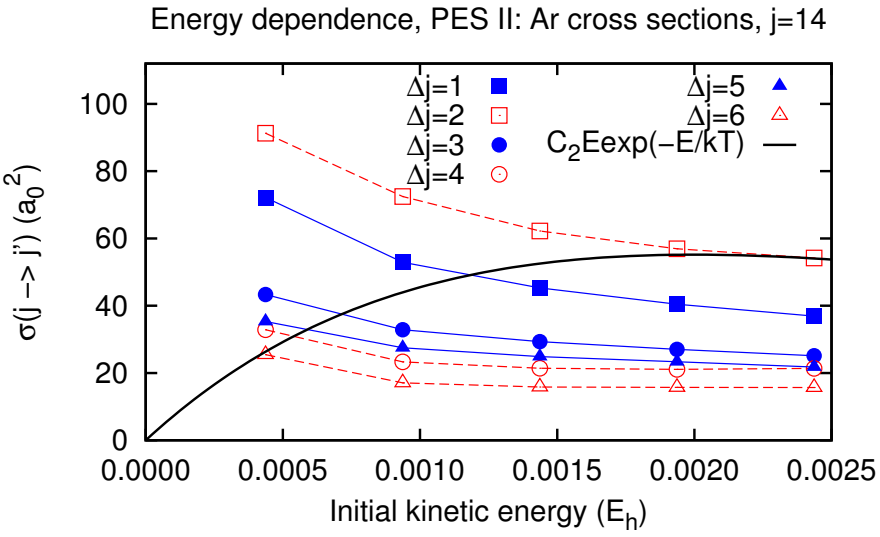

(b)

Figure 4.17: Energy dependence of $j = 14$ cross sections for fixed Δj. Panel (a) shows the cross sections for PES II: He, while Panel (b) shows them for PES II: Ar. Both panels show the distribution $E^j_{\rm kin} e^{-E_{\rm kin}/kT}$ for $T = 600\,K$ (multiplied by an arbitrary constant) as a solid curve labelled "C_1Eexp(-E/kT)" in Panel (a) and "C_2Eexp(-E/kT)" in Panel (b). The distribution is negligible for $E^j_{\rm kin} \approx 0.015\ E_{\rm h}$, and one can see that there are a broader set of He+NaK calculations than Ar+NaK calculations; the rates we estimate for He+NaK will be less uncertain than for Ar+NaK.

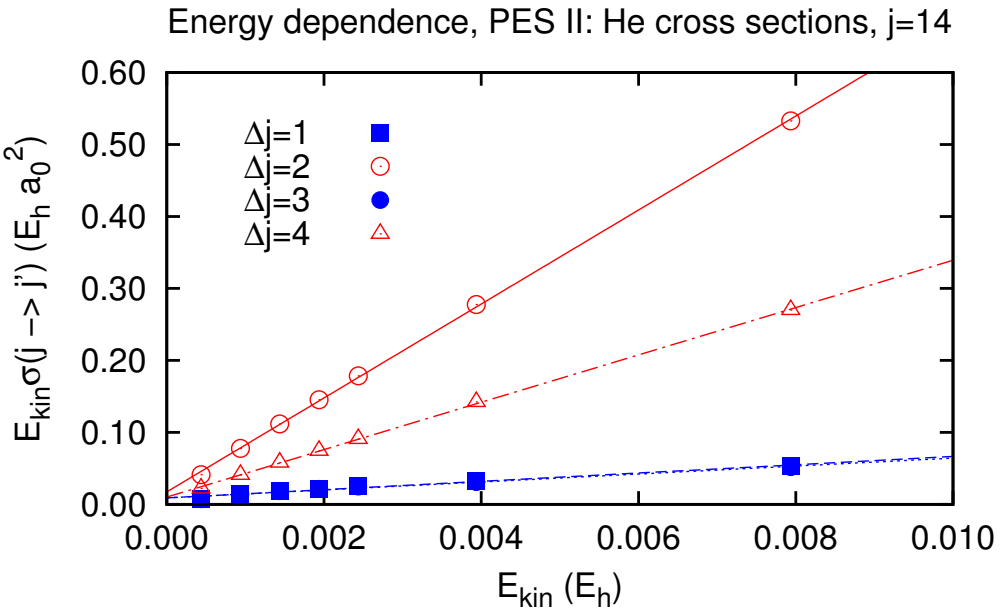

(a)

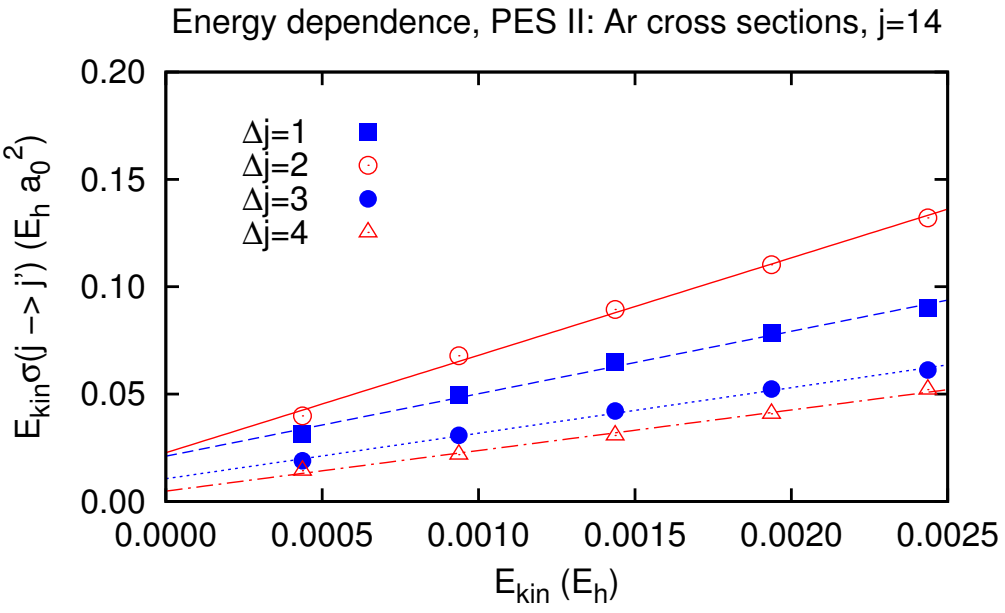

(b)

Figure 4.18: Calculated values of $E^j_{\text{kin}}\sigma(j \to j')$ for $j = 14$ and fixed Δj, along with the linear fits to the calculated points. Panel (a) shows results for PES II: He, while Panel (b) shows results for PES II: Ar.

Table 4.2: Linear fits to $E^j_{\rm kin}\sigma(j \to j')$ for $j = 14$ and fixed Δj, where $E^j_{\rm kin}\sigma(j \to j')$ is in units of $E_{\rm h}a_0^2$. The fits presented here are shown as lines in Fig. 4.18.

	He+NaK		Ar+NaK	
Δj	$E^j_{\rm kin}\sigma = a_1 E^j_{\rm kin} + a_0$	rms	$E^j_{\rm kin}\sigma = a_1 E^j_{\rm kin} + a_0$	rms
1	$5.77126E^j_{\rm kin} + 0.00890$	0.00236	$29.0913E^j_{\rm kin} + 0.02107$	0.00234
2	$65.2729E^j_{\rm kin} + 0.01733$	0.00306	$45.3744E^j_{\rm kin} + 0.02271$	0.00244
3	$5.53389E^j_{\rm kin} + 0.00895$	0.00246	$21.2114E^j_{\rm kin} + 0.01060$	0.00112
4	$32.9050E^j_{\rm kin} + 0.01022$	0.00176	$18.9025E^j_{\rm kin} + 0.00482$	0.00134

expression for the rate constant, with $E^j_{\rm kin}\sigma(j \to j') = a_1 E^j_{\rm kin} + a_0$, is

$$k_{i\to f}(T) \approx \bar{\mathsf{v}} \left(a_1 + \frac{a_0}{kT} \right). \tag{4.16}$$

In the column of Table 4.3 labelled "Eq. 4.16", we present the rate constants we estimated by using Eq. 4.16 and the values of a_0 and a_1 determined by the linear fits shown in Fig. 4.18. We also present the rate constants shown in Section 4.2.2 that we estimated by using $k_{i\to f}(T) \approx \bar{\mathsf{v}}\sigma^0_{i\to f}$ in the column labelled "$\bar{\mathsf{v}}\sigma^0_{i\to f}$." For He+NaK, the rate constants estimated from the linear fit to $E^j_{\rm kin}\sigma(j \to j')$ were less than 8.2% different from those estimated from $\bar{\mathsf{v}}\sigma^0_{i\to f}$, while for Ar+NaK the rate constants were less than 9.5% different.

Table 4.3: Rate constants in units of 10^{-11} cm^3/sec for $j = 14$ and fixed Δj that we estimated from the approximate formula $k_{i\to f}(T) = \bar{\mathsf{v}}\sigma^0_{i\to f}$, as well as the rate constants we estimated from Eq. 4.16 for the lines shown in Fig. 4.18.

	He+NaK		Ar+NaK	
Δj	$\bar{\mathsf{v}}\sigma^0_{i\to f}$	Eq. 4.16	$\bar{\mathsf{v}}\sigma^0_{i\to f}$	Eq. 4.16
1	5.831	5.261	7.951	8.023
2	38.61	38.05	11.29	11.49
3	5.739	5.151	5.211	5.367
4	19.76	19.57	4.025	4.315

Of course, for kinetic energies greater than those for which we've performed calculations, the values of $E^j_{\rm kin}\sigma(j \to j')$ may not lie on the same straight line as the calculated values (approximately) do. To test the sensitivity of the rate constants to higher energy points, we used the following method, which is illustrated by Figs. 4.19 and 4.20. We first generated three possible values of $\sigma(j \to j')$ for $E^j_{\rm kin} = 0.016\ E_{\rm h}$, shown as open squares labelled "Dummy points" in Figs. 4.19 and 4.20, which we will call A, B, and C. We chose $E^j_{\rm kin} = 0.016\ E_{\rm h}$ because the distribution $E^j_{\rm kin} e^{-E^j_{\rm kin}/kT}$ for $T = 600\,K$ is very small there, as can be seen from the solid curves labelled either "$C_1 E e^{-E/kT}$" or "$C_2 E e^{-E/kT}$". We generated A by using the linear fit to the calculated $E^j_{\rm kin}\sigma(j \to j')$, shown as a solid curve labelled "Linear fit to $E\sigma$," to extrapolate to $E^j_{\rm kin} = 0.016\ E_{\rm h}$. Then we let $B = 2A$ and $C = A/2$.

With either A, B, or C and the calculated points, we determined possible extrapolations of $E^j_{\rm kin}\sigma(j \to j')$, which are shown as dotted curves labelled "Extrapolations." The dotted lines begin when the kinetic energy is $\tilde{E}^j_{\rm kin}$, the highest initial kinetic energy for which we have performed a calculation. For $j = 14$, $\tilde{E}^j_{\rm kin} = 0.0079\ E_{\rm h}$ for He+NaK and $0.0024\ E_{\rm h}$ for Ar+NaK, so the extrapolations are more extreme for Ar+NaK. The extrapolations were determined by requiring that for $E^j_{\rm kin} > \tilde{E}^j_{\rm kin}$, $E^j_{\rm kin}\sigma(j \to j')$ lie along the line connecting $\tilde{E}^j_{\rm kin}\sigma(j \to j')$ to either $E_{\rm kin}A$, $E_{\rm kin}B$, or $E_{\rm kin}C$; let these lines be of the form $E^j_{\rm kin}\sigma(j \to j') = b_1 E^j_{\rm kin} + b_0$. Thus we estimated rate constants by using a piecewise functional form for $E^j_{\rm kin}\sigma(j \to j')$ given by

$$E^j_{\rm kin}\sigma(j \to j') = \begin{cases} a_1 E^j_{\rm kin} + a_0 & \text{for } 0 \le E^j_{\rm kin} \le \tilde{E}^j_{\rm kin} \\ b_1(E^j_{\rm kin} - \tilde{E}^j_{\rm kin}) + a_1 \tilde{E}^j_{\rm kin} + a_0 & \text{for } E^j_{\rm kin} > \tilde{E}^j_{\rm kin} \end{cases} , \quad (4.17)$$

where $E^j_{\rm kin}\sigma(j \to j') = a_1 E^j_{\rm kin} + a_0$ is the linear fit to the calculated points, and where $b_0 = (a_1 - b_1)\tilde{E}^j_{\rm kin} + a_0$ by continuity arguments.

We determined the formula for the corresponding rate constants by inserting Eq. 4.17 into Eq. 4.9 and evaluating the integral analytically to obtain

$$k_{i\to f}(T) \approx \bar{\mathrm{v}} \left(\frac{a_0}{kT} + a_1 + (b_1 - a_1) e^{-\tilde{E}^j_{\rm kin}/kT} \right) . \quad (4.18)$$

In Table 4.4, we present the rate constants that we have determined for $j = 14$. The rate constants estimated with Eq. 4.18 for the calculated cross sections and either 'B' or 'C' varied from those estimated from the linear fit to the calculated $E^j_{\rm kin}\sigma(j \to j')$ by less than 3.3% for He+NaK and 26.4% for Ar+NaK. The Ar+NaK rate constants that we estimate are more sensitive to higher energy points because $\tilde{E}^j_{\rm kin}$ is smaller for Ar+NaK than for He+NaK.

In Fig. 4.21 we present the range of rates that we have estimated with the extrapolations as a solid vertical bar. For clarity, the bar is displaced and lies slightly to the right of the appropriate Δj. The rates we estimated by using $\bar{\mathrm{v}}\sigma^0_{i\to f}$ are shown as points, and the experimental error bars are shown as dotted vertical lines. For He+NaK, our uncertainty is small, and so the rates will likely not change by much when one accounts for the energy dependence. We note that for odd Δj the range of rates we estimated from the extrapolations does not overlap with the

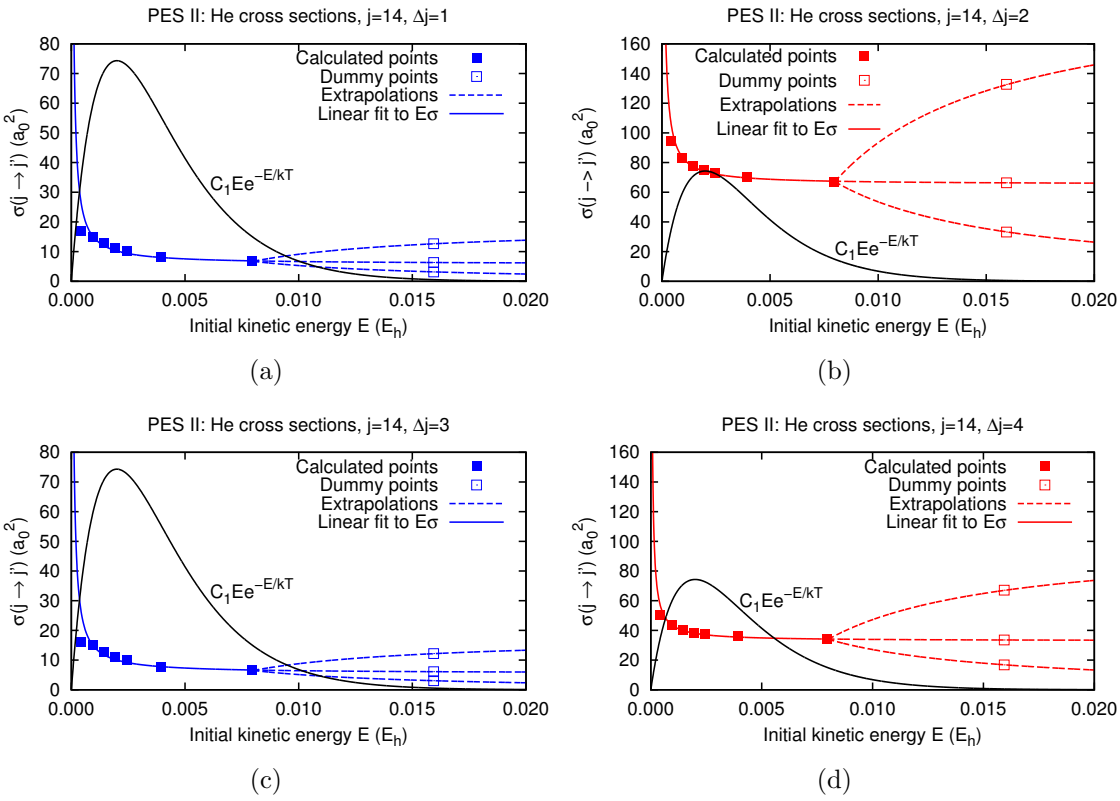

Figure 4.19: Plots of $\sigma(j \to j')$ as a function of $E^j_{\rm kin}$ for PES II: He and $j = 14$. Each panel shows a different Δj. The vertical scale for Δj odd transitions is half that for Δj even transitions, since the Δj odd cross sections are smaller. The calculated cross sections are shown as solid squares, while the generated (non-calculated) points A, B, and C at $E^j_{\rm kin} = 0.016\ E_{\rm h}$ are shown as open squares. The generated point A is the middle open square, and was obtained by using the linear fit to $E^j_{\rm kin}\sigma(j \to j')$ (shown as the solid curve labelled "Linear fit to $E\sigma$") to extrapolate to $E^j_{\rm kin} = 0.016\ E_{\rm h}$. The other two points are $B = 2A$ and $C = A/2$. We estimated rate constants by extrapolating the cross sections as follows. For initial kinetic energies from zero to the highest value for which we've performed a calculation, we let the cross sections follow the curve labelled "Linear fit to $E\sigma$." (We note that for the Δj odd transitions the solid curve deviates more significantly from the calculated point of lowest energy than it does for the even transitions.) Then for higher energies we let the cross sections follow one of the dotted curves labelled "Extrapolations." We used the different extrapolations to estimate the sensitivity of the rate constants to high energy points.

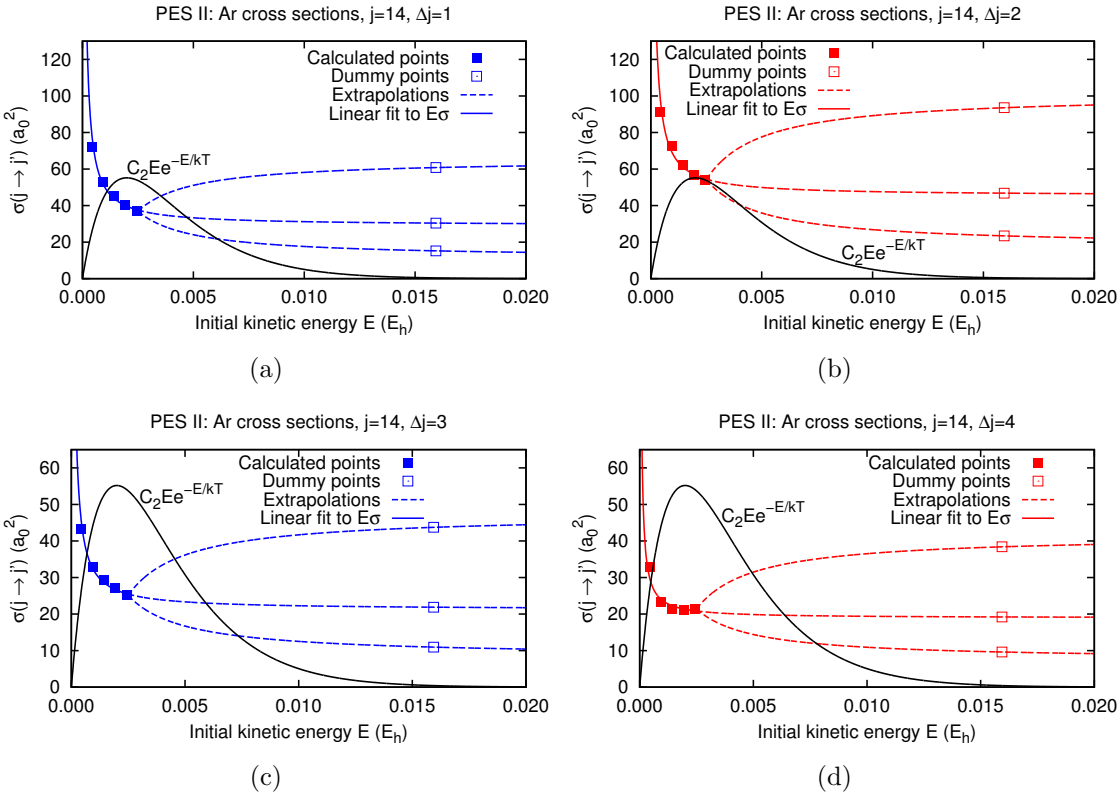

Figure 4.20: Same as Fig. 4.20 but for PES II: Ar. The vertical scale for transitions with $\Delta j = 3$ and 4 transitions is half that for transitions with $\Delta j = 1$ and 2. The extrapolations are more extreme than they were for He+NaK, since the He+NaK calculations cover a broader range of energies.

rates we estimated from $\bar{\mathrm{v}}\sigma^0_{i\to f}$, probably because the fit labelled "Linear fit to $E\sigma$" in Fig. 4.19 deviates significantly from the calculated point of lowest energy. For Ar+NaK, our uncertainty in the rate constants is greater and our range of rates overlaps with experimental error bars for $\Delta j = 2$, 3, and 4; the experimentally observed propensity for $\Delta j = 4$ in the rate constants could be a result of collisions for $E > 0.0025\ E_\mathrm{h}$.

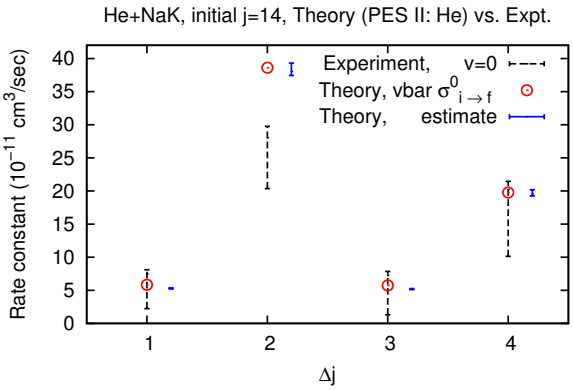

(a)

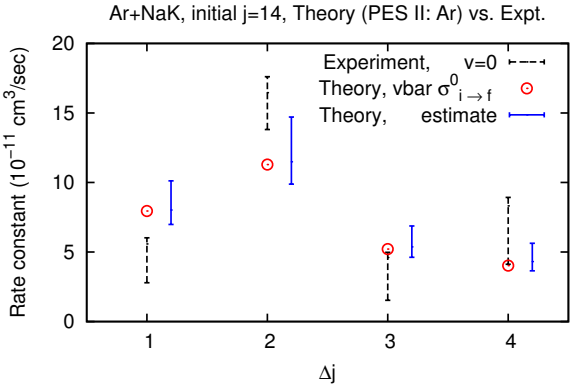

(b)

Figure 4.21: Comparison between our estimated rate constants and experimental error bars for $j = 14$ as a function of Δj. Panel (a) shows the comparison for PES II: He, while Panel (b) shows it for PES II: Ar. The range of rates that we estimated by using different extrapolations of the energy dependent cross sections is shown as a solid vertical bar. The bars are displaced to the right by $\Delta j = 0.2$ for clarity. The rate constants we estimated from $k_{i\to f}(T) \approx \bar{v}\sigma^0_{i\to f}$ are shown as points, and the experimental error bars are shown as dotted vertical lines. For He+NaK, our estimated uncertainty in the rate constants that we predict is very small. For He+NaK for the odd Δj, the uncertainty estimated from the extrapolations does not overlap with the points, which is likely due to the deviation of the fit from the calculated point of lowest initial kinetic energy in Fig. 4.19. For Ar+NaK, the uncertainty in the rates is larger, and this leads to agreement with experiment for $\Delta j = 2$ through 4. One can see that for Ar+NaK our estimated rates for $\Delta j = 3$ and 4 overlap; it's possible that the propensity for $\Delta j = 4$ observed experimentally is present in our results as well.

Table 4.4: Rate constants in units of 10^{-11} cm^3/sec estimated from the fits shown in Figs. 4.19 and 4.20. The initial j is 14.

He+NaK

Δj	$\bar{v}\sigma^0_{i\to f}$	Eq. 4.16	Eq. 4.18 with value C	Eq. 4.18 with value B
1	5.831	5.261	5.381	5.202
2	38.61	38.05	39.31	37.43
3	5.739	5.151	5.267	5.095
4	19.76	19.57	20.20	19.25

Ar+NaK

Δj	$\bar{v}\sigma^0_{i\to f}$	Eq. 4.16	Eq. 4.18 with value C	Eq. 4.18 with value B
1	7.951	8.023	10.12	6.985
2	11.29	11.49	14.71	9.880
3	5.211	5.367	6.875	4.619
4	4.025	4.315	5.629	3.649

Quenching cross sections

We examined quenching cross sections (sums of inelastic cross sections) as a function of total energy. We had predicted in Section 4.2.4 that the quenching cross sections were approximately constant with respect to j. Figure 4.22 shows $\sum_{j' \neq j} \sigma(j \rightarrow j')$ as a function of the total energy. Since the initial kinetic energies are similar to the total energies ($E^j_{\mathrm{kin}} = E - 3.013 \times 10^{-7} j(j+1)\ E_{\mathrm{h}}$), we expect that the results would show the same trends if plotted against initial kinetic energy; we used the total energy to avoid performing many calculations for slightly different initial kinetic energies. For He+NaK, the results are approximately constant with respect to j for each total energy, except for the two lowest total energies, $E = 1 \times 10^{-4}$ and $5 \times 10^{-4}\ E_{\mathrm{h}}$. For those two energies, the channels are closed when $j \geq 18$ and 41, respectively. The quenching cross sections are approximately constant with respect to j until j is near the value for which the channels become closed. At that point, the cross sections drop precipitously. This behavior will likely not affect the quenching rates very much at $T = 600\,K$, since $E^j_{\mathrm{kin}} e^{-E^j_{\mathrm{kin}}/kT}$ emphasizes higher energies, and we expect the quenching rates to be fairly constant with respect to j, as we predicted in Section 4.2.4. For Ar+NaK, results near the average collision energy are approximately constant with respect to j, but for lower energies the dependence on j is somewhat stronger. Without higher energy points, it is difficult to say whether the quenching rates for Ar+NaK would be approximately constant with respect to j.

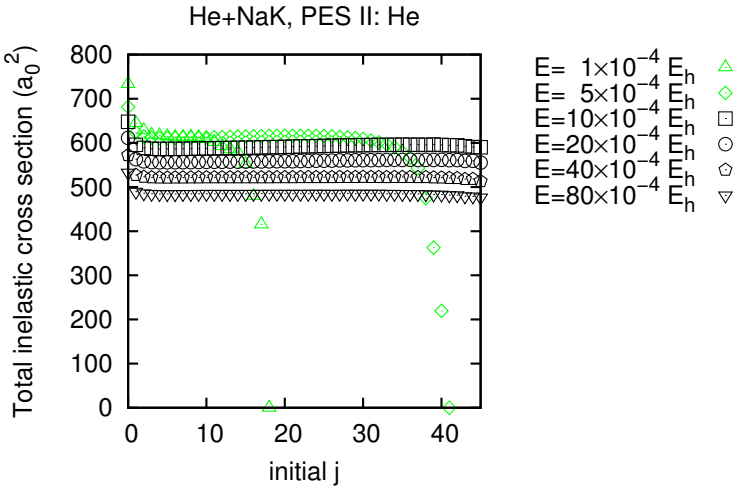

(a)

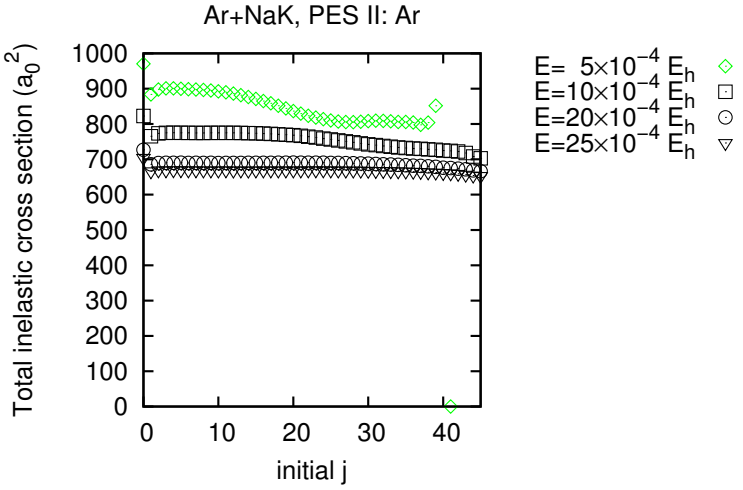

(b)

Figure 4.22: Energy dependence of quenching cross sections, $\sum_{j \neq j'} \sigma(j \rightarrow j')$, for He+NaK (Panel (a)) and Ar+NaK (Panel (b)) as a function of the initial j. For the energies 1×10^{-4} and 5×10^{-4} E_h, channels are energy inaccessible for $j \geq 18$ and 41, respectively. For He+NaK, The quenching cross sections for those values of E drop precipitously before reaching a value of zero. Aside from the precipitous drops, the quenching cross sections are fairly constant with j. We expect the quenching rate constant to be constant with j, as we predicted in Section 4.2.4. For Ar+NaK, the lower energy curves show more of a dependence on the energy, and we do not have calculations for $E = 0.004$ and 0.008 E_h like we did for He+NaK.

4.3.2 Vibrational effects

We have estimated how the results for vibrationally elastic transitions ($vj \rightarrow vj'$) depend on v. This section presents the approximations made to obtain these estimates and then compares the results with experimental data. We note that our collaborator, Prof. Forrey from Penn State Berks, is in the process of estimating the vibrational dependence by making different approximations than those used here.

Simplified coupling terms

In Section 2.4.4, we showed that in order to incorporate the vibration of the molecule in the scattering calculation, one must include vibrational wave functions in the expansion of the target wave function. When one does this, the number of channels (and hence the computational effort required) becomes much larger than for the rigid rotator, because there are rotational levels for every vibrational level included. In order to perform a tractable calculation, we made the approximation of including only one vibrational wave function for the target state. A separate calculation can then be performed for each initial vibrational level; the physical assumption is that the collision does not change the vibrational level. There is some justification for this approach in the experimental data [6]; for small values of v, the vibrationally inelastic rate constants are about an order of magnitude smaller than the vibrationally elastic rate constants for both He+NaK and Ar+NaK.

The coupled equations including vibrational excitation were given in Eq. 2.105. In the limit that the sum over vibrational levels has only a single term, these equations have the same form as the rigid rotator equations (Eq. 2.90); the coupling terms are the Legendre components of the interaction potential averaged over the appropriate wave functions:

$$\mathcal{V}_n^{vjvj'}(R) = \int \chi_{vj}(r)\tilde{V}_n(R,r)\chi_{vj'}(r)\,dr. \tag{4.19}$$

We make the further approximation that the vibrational-rotational wave functions χ_{vj} (which are solutions to Eq. 2.103) are independent of j. The coupling terms are then much simpler to evaluate, and one can also show that they reduce to the rigid

rotator limit. If we consider $v = 0$ and replace the squared ground vibrational wave function by a δ-function centered at the equilibrium internuclear separation $r_{\rm e}$, we have

$$\begin{aligned} \mathcal{V}_n^{0j0j'}(R) &\approx \int \chi_0(r)\tilde{V}_n(R,r)\chi_0(r)\,dr & (4.20)\\ &= \int \tilde{V}_n(R,r)\delta(r-r_{\rm e})\,dr & (4.21)\\ &= V_n(R,r_{\rm e}). & (4.22) \end{aligned}$$

The final expression, $V_n(R, r_{\rm e})$, is the same as the rigid rotator coupling term, Eq. 2.87, confirming that our approximations lead to a sensible expression in the $v = 0$ limit.

The computational details of the vibrational averaging of the Legendre components are as follows. We determined the Legendre components, $\tilde{V}_n(R, r)$, for the six bond lengths $r = 6, 7, 8, 9, 10$, and 11 a_0 by using the procedure described in Section 3.2. Then, for each n and R, we used a least squares fitting routine [84] to fit $\tilde{V}_n(R, r)$ to a fifth degree polynomial in r. This fit provides the derivatives [85] of $\tilde{V}_n(R, r)$, which can be used to expand each component in a Taylor series about $r_{\rm e}$:

$$\tilde{V}_n(R,r) = \tilde{V}_n(R,r)\Big|_{r_{\rm e}} + \frac{\partial \tilde{V}_n(R,r)}{\partial r}\bigg|_{r_{\rm e}} (r-r_{\rm e}) + \frac{1}{2!}\,\frac{\partial \tilde{V}_n(R,r)^2}{\partial^2 r}\bigg|_{r_{\rm e}} (r-r_{\rm e})^2 + \ldots . \quad (4.23)$$

Now one can express the vibrational average in terms of the average values of powers of $(r - r_{\rm e})$:

$$\begin{aligned} \int \chi_v^*(r)\tilde{V}_n(R,r)\chi_v(r)\,dr = \tilde{V}_n(R,r)\Big|_{r_{\rm e}} &+ \frac{\partial \tilde{V}_n(R,r)}{\partial r}\bigg|_{r_{\rm e}} \int \chi_v^*(r)(r-r_{\rm e})\chi_v(r)\,dr \\ &+ \frac{1}{2!}\,\frac{\partial \tilde{V}_n(R,r)^2}{\partial^2 r}\bigg|_{r_{\rm e}} \int \chi_v^*(r)(r-r_{\rm e})^2\chi_v(r)\,dr + \ldots . \quad (4.24) \end{aligned}$$

For each v, we evaluated Eq. 4.24 by using the first six terms of the Taylor expansion given by Eq. 4.23. We calculated the average values of $(r - r_{\rm e})^n$ numerically with Morse wave functions [86] for $j = 0$ constructed by using the experimental value for $r_{\rm e}$ [7], and the $w_{\rm e}$ and $w_{\rm e}x_{\rm e}$ for NaK ($A\,^1\Sigma^+$) determined from PES II.

We calculated vibrationally averaged Legendre components for vibrational levels up to $v = 16$. We have verified that the Morse vibrational wave functions for $v = 16$ do not contain significant contributions from bond lengths $r < 6\ a_0$ or $r > 11\ a_0$, as can be seen in Panel (a) of Fig. 4.23. Moreover, Panel (b) shows that the corresponding Morse potential does not deviate significantly from our calculated potential for NaK ($A\,^1\Sigma^+$) in the energy range of interest.

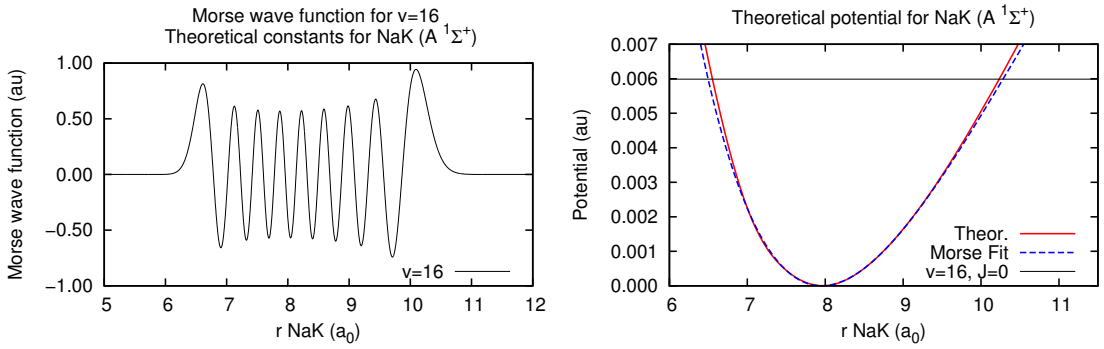

(a) (b)

Figure 4.23: Panel (a) shows that the Morse vibrational wave function for $v = 16$ is negligible outside of the range of bond lengths ($6 \leq r \leq 11\ a_0$) included in our PESs. Thus we can safely average Legendre components using Morse wave functions for levels up to $v = 16$. Panel (b) shows that the corresponding Morse potential does not deviate significantly from the NaK ($A\,^1\Sigma^+$) potential calculated from PES II in the relevant energy range. The black horizontal line labelled "$v = 16$, $J = 0$" corresponds to the energy for $v = 16$ and $j = 0$ calculated from $E_{\rm vib} = w_{\rm e}(v + 1/2) - w_{\rm e}x_{\rm e}(v + 1/2)^2$.

Figs. 4.24 and 4.25 show the first three vibrationally averaged Legendre components for different values of v for PES II: He and PES II: Ar, respectively. (In Section 4.1, we showed that for the rigid rotator a three-term Legendre expansion of the PES was sufficient to reproduce the essential features of the results of an eleven-term expansion.) Within each figure, Panel (a) shows Legendre components for the rigid rotator and for $v = 0$, 1, and 2; they are all very similar. Panel (b) shows components for $v = 7$ and Panel (c) shows components for $v = 16$. As v increases, the $n = 0$ component becomes more repulsive (perhaps because NaK seems "bigger"

when it is in a higher vibrational level), and the separation between the $n = 1$ and $n = 2$ components increases within the range of R shown. For some values of R, the magnitude of the $n = 1$ component decreases with an increase in v; that is, the averaged potential becomes less asymmetric with respect to inversion symmetry in these regions. One might therefore expect an enhancement in the propensity for Δj even transitions as v increases, if these regions of the potential contribute strongly to the scattering.

Vibrationally elastic cross sections $\sigma(vj \to vj')$

Figure 4.26 shows cross sections for the rigid rotator and for $v = 0$. They are virtually identical, confirming Eq. 4.22, and supporting the comparisons we made between our rigid rotator results and experimental [6] rate constants for $v = 0$ in Figs. 4.8, 4.10, and 4.12. We also compared our rigid rotator results with experiment [6] for $v = 1$ and 2 in Figs. 4.9 and 4.12; Figure 4.27 shows that our cross sections for the rigid rotator and for $v = 2$ are very similar.

Figure 4.28 presents a comparison between cross sections for the rigid rotator and for $v = 16$. There is more of a difference than there was for $v = 0$ and 2. For instance, He+NaK cross sections shown in Panel (a) are 80% different ($\approx 2\ a_0^2$) for $0 \to 1$ and 61% different ($\approx 5\ a_0^2$) for $14 \to 15$. Additionally, for $v = 16$ there is a propensity for Δj even transitions for large Δj that was not present in the rigid rotator results. Nonetheless, the cross sections still show the same essential features, and the changes appear relatively minor in the figure. Panel (b) shows that the differences between cross sections for the rigid rotator and for $v = 16$ are more pronounced for Ar+NaK than they were for He+NaK, but that these differences do not radically alter the results. The biggest change is that the inverse propensity (for Δj odd) present in rigid rotator results for high Δj is absent for $v = 16$; instead the propensity for Δj even persists to high Δj.

Figure 4.29 shows cross sections for $j = 14$ and fixed $\Delta j \leq 4$ as a function of v. The points on the left-hand side of the vertical bar are for the rigid rotator. Panel (a) shows results for PES II: He, while Panel (b) shows results for PES II: Ar.

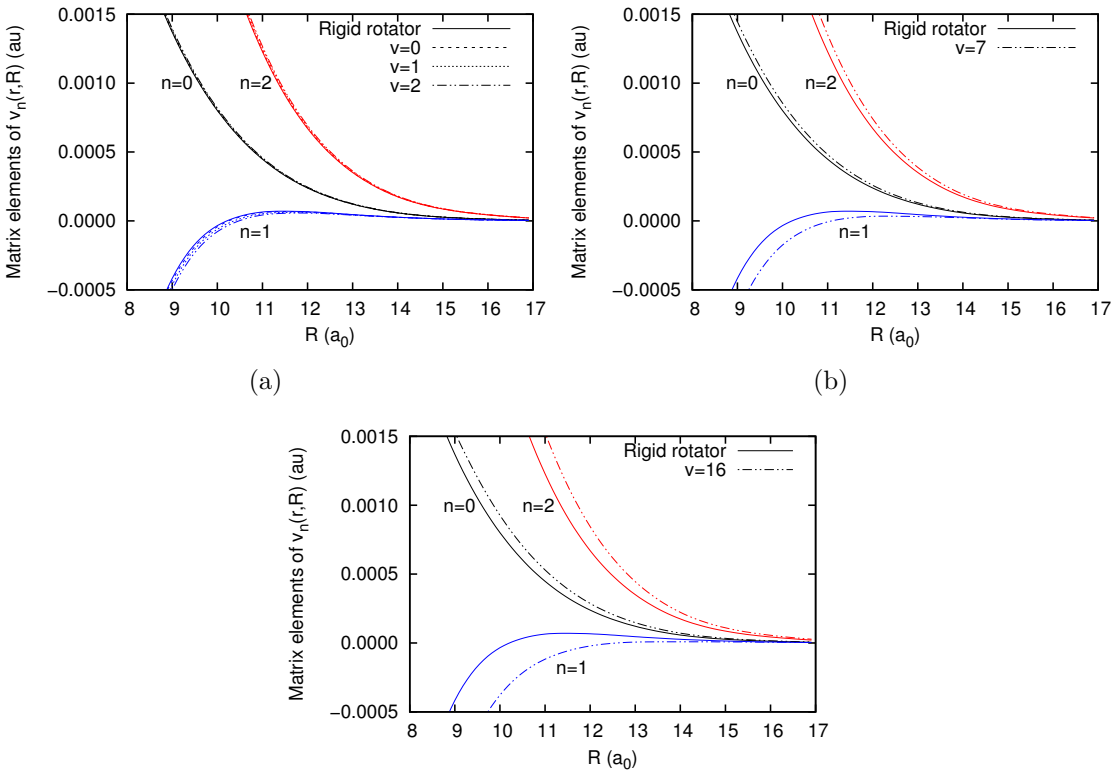

Figure 4.24: Comparison between the PES II: He Legendre components used in the rigid rotator calculation and vibrationally averaged Legendre components for different values of v. Within each panel, there are three sets of curves labeled '$n = 0$', '$n = 1$', and '$n = 2$'; these are the first three Legendre components. For each such set of curves, the Legendre components are shown as a solid line and labelled "Rigid rotator", while the vibrationally averaged Legendre components each have their own line type and are labelled by v. Panel (a) shows the comparison for averaged components obtained for $v = 0$, 1, and 2. The separation between the $n = 1$ and 2 components increases as v increases. There is hardly an effect on the Legendre components, but the odd Legendre components are affected a bit more than the even components. Panel (b) shows the comparison for $v = 7$, and Panel (c) for $v = 16$; the $n = 1$ component is most affected. The overall trend is that as v increases, the separation of the $n = 1$ and $n = 2$ components increases. For some values of R, the magnitude of the $n = 1$ component decreases with an increase in v; such a decrease indicates the averaged potential is less asymmetric with respect to inversion symmetry in these regions.

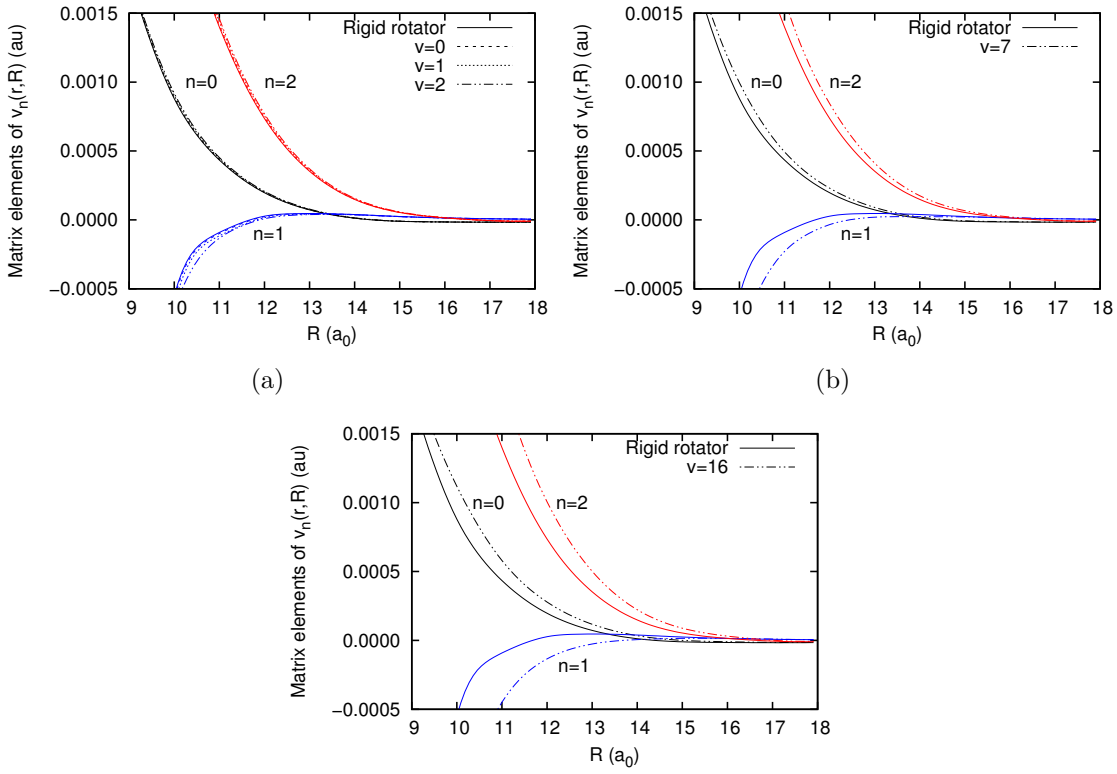

(a) (b) (c)

Figure 4.25: Same as in Fig. 4.24 except for PES II: Ar. The results are very similar to the He+NaK results.

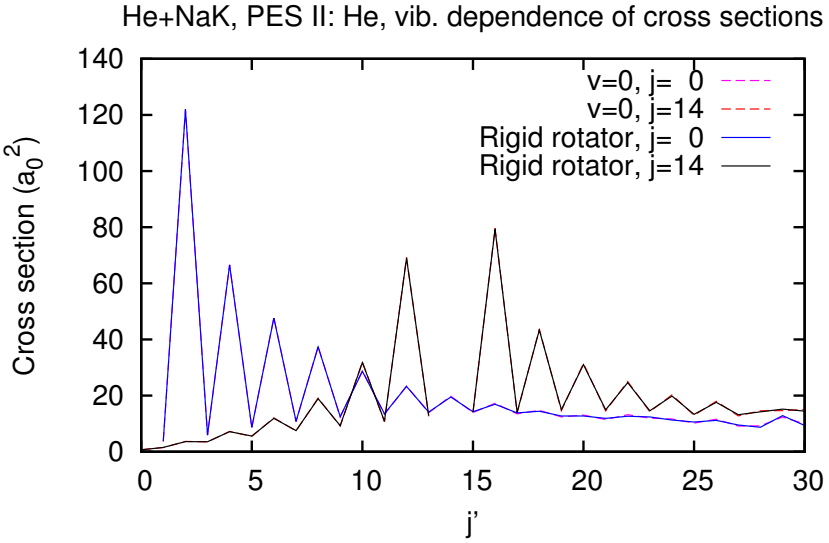

(a)

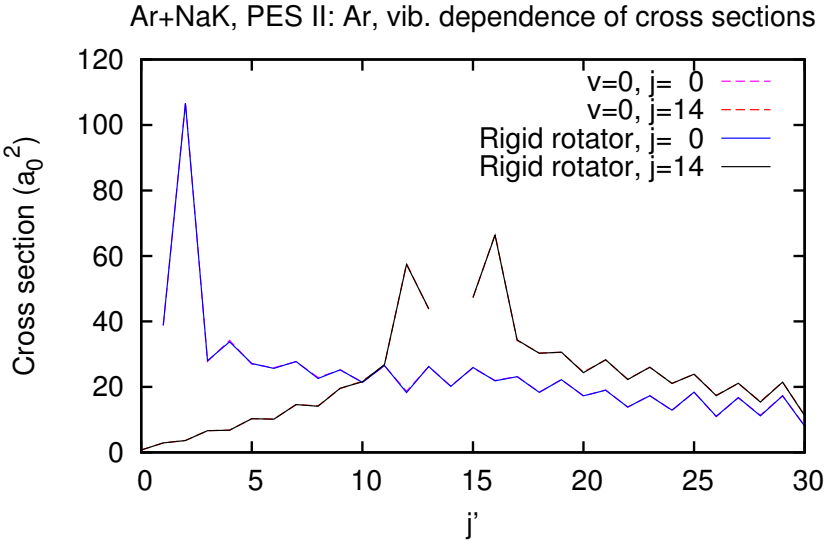

(b)

Figure 4.26: Comparison between cross sections for the rigid rotator and for $v = 0$, both obtained for $j_{\max} = 30$. Panel (a) shows results for PES II: He, while Panel (b) shows results for PES II: Ar. In both cases, the cross sections are very similar, confirming Eq. 4.22 and supporting comparisons made in Sections 4.2.2 and 4.2.3 between our rigid rotator results and experimental rate constants [6] for $v = 0$.

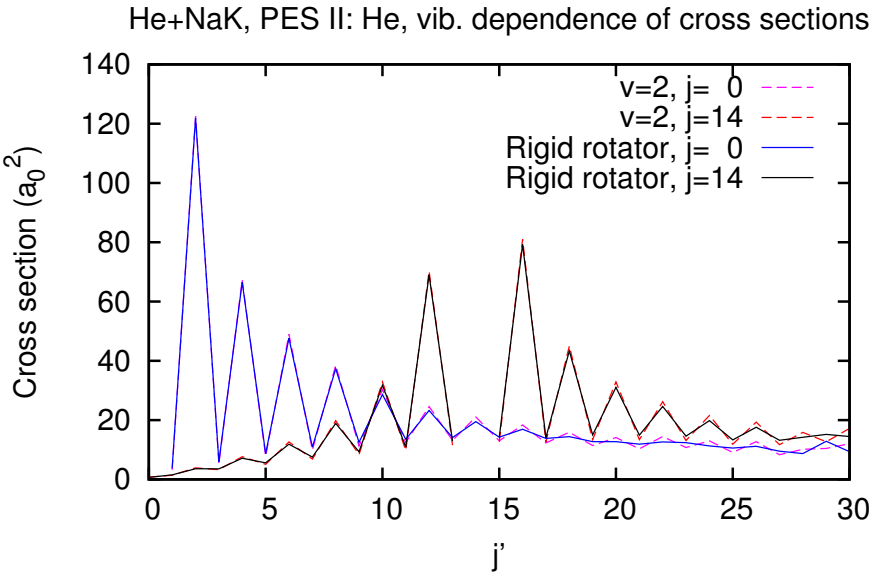

(a)

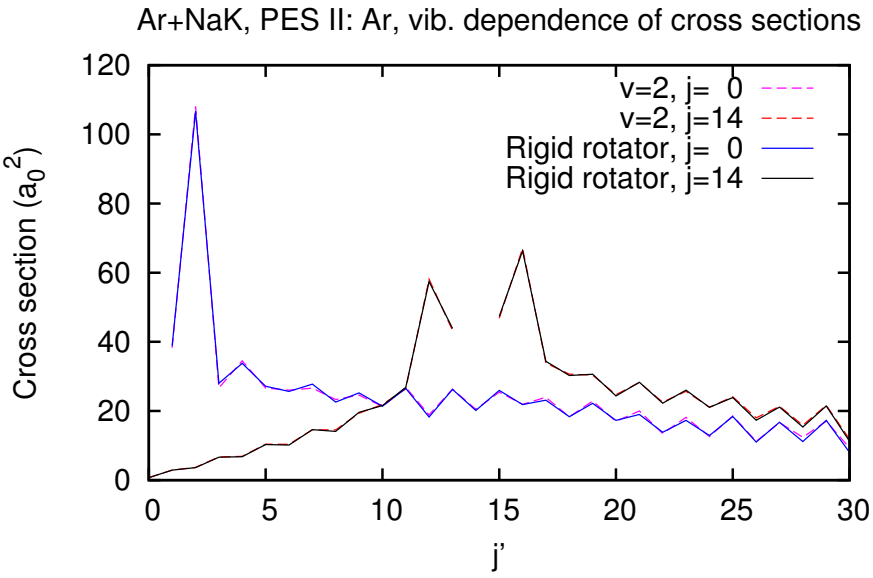

(b)

Figure 4.27: Same as Fig. 4.26 except the rigid rotator cross sections are compared with the cross sections for $v = 2$. The similarity between the cross sections supports our comparison of rigid rotator results with experimental rate constants [6] for $v = 1$ and 2 in Sections 4.2.2 and 4.2.3.

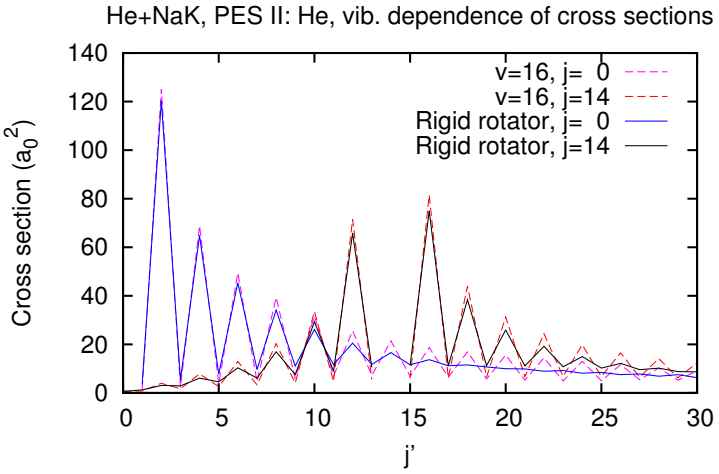

(a)

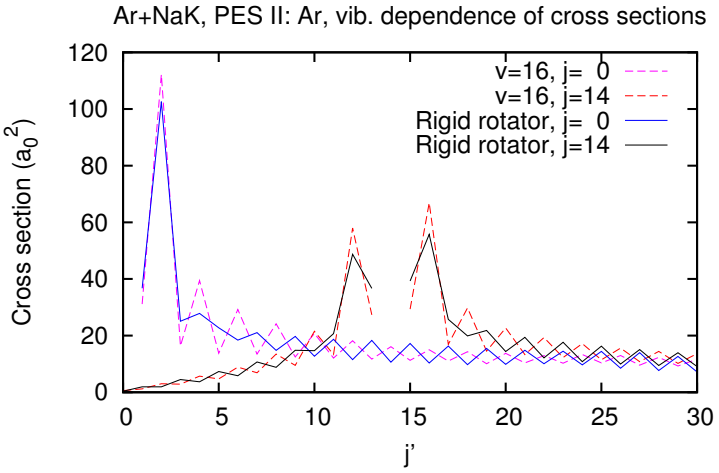

(b)

Figure 4.28: Same as Fig. 4.26 except the rigid rotator cross sections are compared with the cross sections for $v = 16$, and $j_{\max} = 50$ for He+NaK and 60 for Ar+NaK. The results for the rigid rotator and for $v = 16$ are more different than they were for $v = 0$ and 2, particularly for Ar+NaK. Nonetheless, there are no major changes in the behavior of the cross sections for He+NaK or for Ar+NaK, aside from some differences in the propensity for Δj even transitions. For He+NaK, there is a propensity for high Δj transitions for $v = 16$ where there was no propensity for the rigid rotator. For Ar+NaK, the inverse propensity seen at higher Δj for the rigid rotator is no longer seen for $v = 16$. Instead, the propensity persists to high Δj.

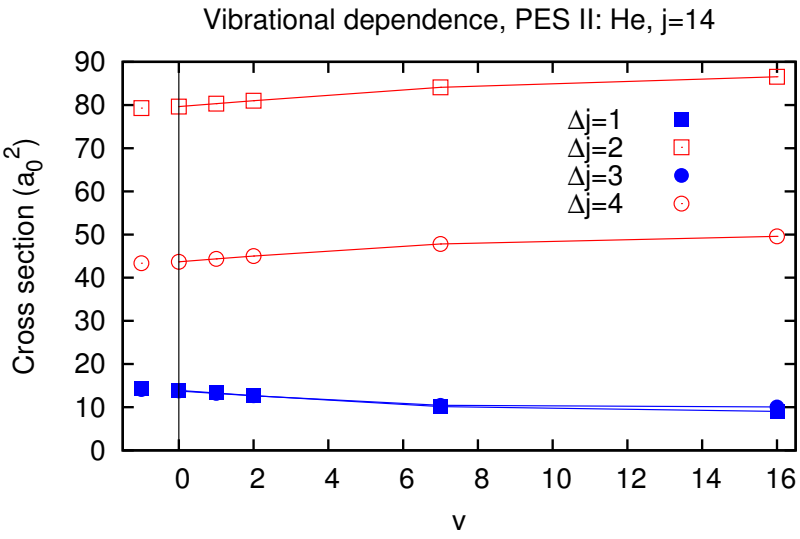

(a)

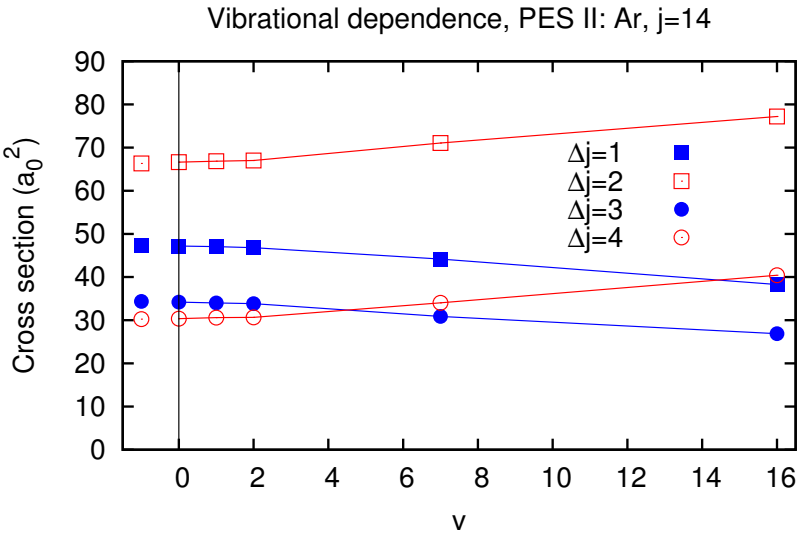

(b)

Figure 4.29: Cross sections for $j = 14$ are shown for fixed $\Delta j \leq 4$ as a function of v. The points to the left of the vertical bar are the cross sections for the rigid rotator. For He+NaK, shown in Panel (a), there is little dependence on v for these small Δj, although one can still discern an enhancement in the propensity as v increases. For Ar+NaK, there is more of a dependence, with a propensity for $\Delta j = 4$ present for higher v.

As v increases, the Δj even cross sections increase, while the Δj odd cross sections decrease; the propensity for Δj even transitions becomes stronger. This is not very noticeable in Panel (a); most of the change in the relative rates occurs for higher Δj than those shown. In Panel (b), though, it is more noticeable, since the trends cause the curves to change order, with cross sections for $\Delta j = 4$ larger than for $\Delta j = 1$ or 3 at higher v.

Figure 4.30 shows experimental rate constants [4–6] for vibrationally elastic transitions from $(v, j) = (0, 30)$ (red vertical lines) and from $(v, j) = (16, 30)$ (black vertical lines displaced horizontally by $\Delta j = +0.2$). The figure also shows our calculated rate constants for $v = 0$ (red circles) and for $v = 16$ (black squares displaced horizontally by $\Delta j = +0.2$). We reproduce the general trends of the data for $v = 0$ and 16, with the exception being that we reproduce the experimentally observed propensity for $|\Delta j| = 4$ transitions for Ar+NaK for $v = 16$ but not $v = 0$. Despite some differences, there is not a significant dependence on v in the experimental data or in our calculated rate constants for these values of Δj.

Equation 4.12 shows that the expression for the rotationally inelastic cross sections contains a factor $f(\bar{j}, |\Delta j|)$ that is symmetric under the interchange of j and j'; the values of $f(\bar{j}, |\Delta j|)$ are identical for two transitions $vj \to vj'$ and $vj' \to vj$. We wish to demonstrate that the experimental data for $v = 1$ is not very different from $v = 0$, in agreement with our predictions. One way to do this is to show that $f(\bar{j}, |\Delta j|)$ is identical for transitions $v'j \to v'j'$ and $vj' \to vj$, where v and v' are either zero or one. To this end, Fig. 4.31 shows experimental values of $f(\bar{j}, |\Delta j|)$ for pairs of transitions with the same average j and $|\Delta j|$ as vertical bars. The vertical bars for transitions with $j' < j$ are, for clarity, displaced by average $j = +0.4$ and dotted. The $f(\bar{j}, |\Delta j|)$ for $0, 14 \to 0, 30$ and $0, 30 \to 0, 14$ are shown as blue vertical bars for average $j = 22$ and $|\Delta j| = 16$. Of course, these bars overlap, and the values of $f(\bar{j}, |\Delta j|)$ are identical. The red bars for average $j = 20$ and $|\Delta j| = 12$ correspond to transitions $0, 14 \to 0, 26$ and $1, 26 \to 1, 14$; these bars also overlap, which indicates that there is not much difference between cross sections for $v = 1$ and for $v = 0$. Similarly, the black bars for average $j = 28$ and $|\Delta j| = 4$, which correspond to transitions $1, 26 \to 1, 30$ and $0, 30 \to 0, 26$, overlap. Thus we conclude that, at

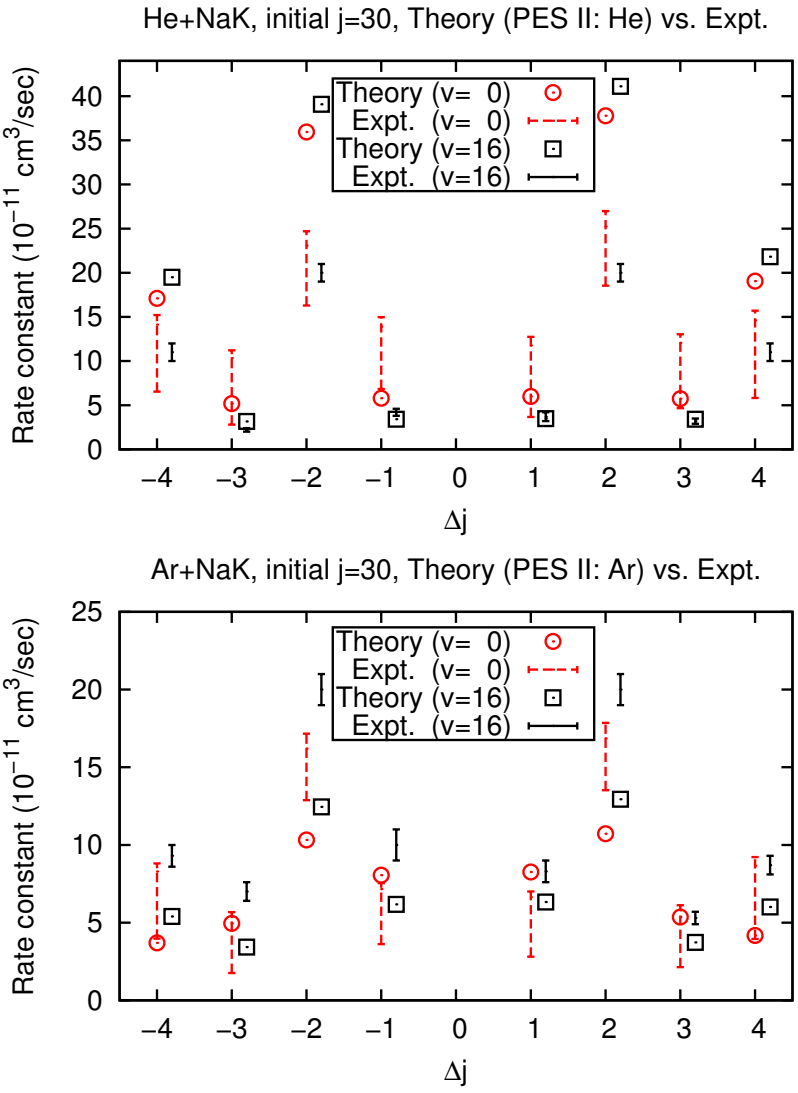

Figure 4.30: Comparison of theory with experiment [4–6] for rotationally inelastic cross sections from $(v, j) = (16, 30)$ and $(v, j) = (0, 30)$. Rate contants for $v = 0$ are red, while the rate constants for $v = 16$ are black and displaced by $\Delta j = 0.2$ (for clarity). We estimated rate constants from our cross sections by using the approximate formula $k_{i\to f}(T) \approx \bar{v}\sigma^0_{i\to f}$. Panel (a) shows the comparison for PES II: He, while Panel (b) shows the comparison for PES II: Ar. For both $v = 0$ and $v = 16$ we reproduce the general trends in the data, except that for Ar+NaK we predict a propensity for $|\Delta j| = 4$ for $v = 16$ but not $v = 0$. For these Δj, the experimental data and our calculated rate constants are fairly insensitive to v.

least for these transitions, there is not much difference between the experimental rate constants for $v = 0$ and $v = 1$, in agreement with our results. We have also plotted our calculated $f(\bar{j}, |\Delta j|)$ for $v = 0$ (they are virtually identical for $v = 1$), for comparison. The calculated values and experimental error bars do not overlap for $|\Delta j| = 4$, but there is overlap for $|\Delta j| = 12$ and 16.

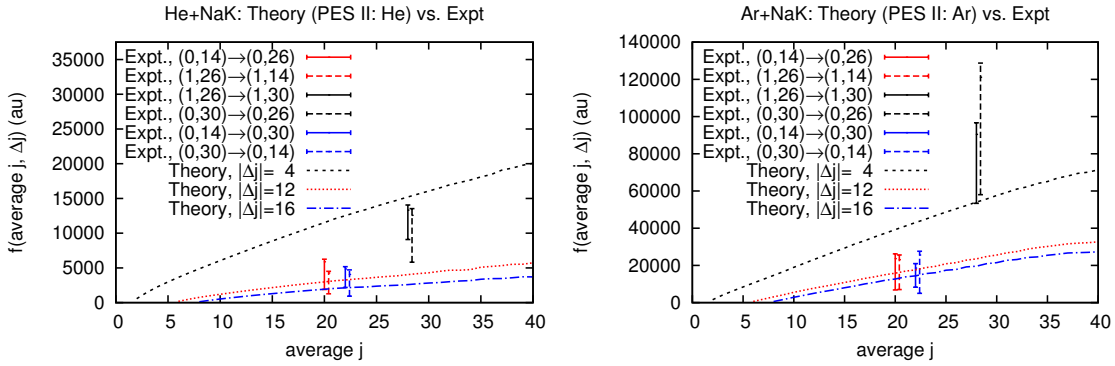

Figure 4.31: Values of $f(\bar{j}, |\Delta j|)$ as a function of average j for fixed $|\Delta j|$. Theoretical values for $v = 0$, which are virtually identical for $v = 1$, are shown as lines, while the experimental values for $v = 0$ and $v = 1$ are shown as vertical bars. Experimental data for transitions with $j' < j$ are plotted as dotted bars and displaced by average $j = 0.4$ for ease of comparison. Experimental values for $0, 30 \rightarrow 0, 14$ and $0, 14 \rightarrow 0, 30$ overlap, as they should, since $f(\bar{j}, |\Delta j|)$ is symmetric under the interchange of j and j' for a given v. The other pairs of vertical bars are for transitions $vj \rightarrow vj'$ and $v'j' \rightarrow v'j$, which will only overlap if the cross sections for v and v' are fairly similar. Since the values of $f(\bar{j}, |\Delta j|)$ do overlap for these transitions, we conclude that there is little difference between data for $v = 0$ and 1, in agreement with our calculations. We also note that theory and experiment overlap for $|\Delta j| = 12$ and 16.

Quenching cross sections

Figure 4.32 shows that for PES II: He and PES II: Ar, the quenching cross sections (which were introduced in Section 4.2.4) for the rigid rotator and for $v = 7$ are very similar. In both cases they are approximately constant with respect to j, supporting the assumption made in the experimental analysis [6] that the quenching rates are

the same constant value for $v = 0$, 1, and 2.

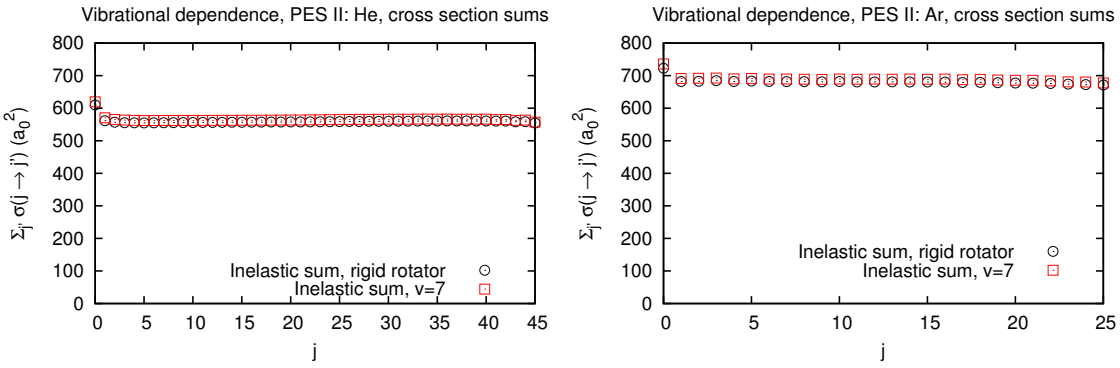

Figure 4.32: Sums of rotationally inelastic cross sections, $\sum_{j \neq j'} \sigma(j \rightarrow j')$, as a function of j for the rigid rotator calculation and for $v = 7$. Panel (a) shows this comparison for PES II: He, while Panel (b) shows it for PES II: Ar. In both cases, the quenching cross sections do not depend much on v, and are approximately constant with j. We note that in Panel (b) the range of j is smaller than in Panel (a) because for Ar+NaK we performed the calculation with $j_{\max} = 30$. This value for $j_{\max}$ was chosen simply to save computer time; the trends in the quenching cross sections are not affected by this choice.

Transfer of moments

In Fig. 4.33, we present a comparison between experiment and theory for the fractions of orientation preserved, $d_1(j, j')/d_0(j, j')$, in transitions from $j = 30$. The experimental data [4, 5] is for $v = 16$. The boxes show our $d_1(j, j')/d_0(j, j')$ for $v = 16$, while the asterisks show them for $v = 0$. Panel (a) shows results for PES II: He. We predict that the $d_1(j, j')/d_0(j, j')$ for Δj even transitions are very similar for $v = 0$ and 16, and that for Δj odd transitions they are lower for $v = 16$ than $v = 0$. The level of agreement with experiment does not change; in both cases we are within the same experimental error bars. Panel (b) shows results for PES II: Ar. While the $d_1(j, j')/d_0(j, j')$ are smaller for Δj odd transitions, we are still outside of the experimental error bars for all transitions. Theory and experiment agree that a greater fraction of orientation is preserved in collisions with He

than with Ar.

In Fig. 4.34, we present theoretical results for $d_1(j, j')/d_0(j, j')$ as a function of average j for fixed $|\Delta j|$. Panels (a) and (b) show results for He+NaK. The even $|\Delta j|$ transitions shown in Panel (b) are hardly affected, but less orientation is preserved for odd $|\Delta j|$ transitions for $v = 16$ than for the rigid rotator, as shown in Panel (a). Panels (c) and (d) show results for Ar+NaK. As with He+NaK, the even $|\Delta j|$ transitions shown in Panel (d) are very similar, but the odd $|\Delta j|$ transitions show more of a difference. In general, we predict the same trends in the orientation results; the fraction of orientation preserved increases with average j.

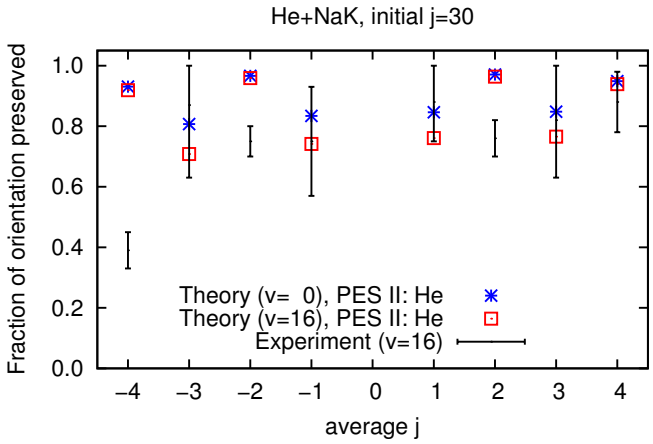

(a)

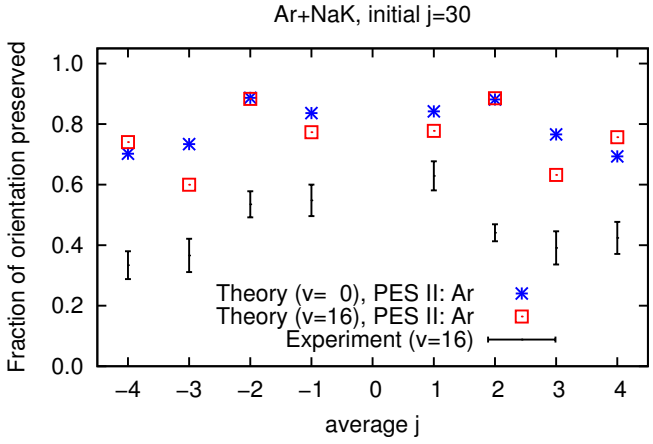

(b)

Figure 4.33: Comparison of our calculated $d_1(j,j')/d_0(j,j')$ for $v = 0$ (asterisks) and 16 (squares) with experimental data [4, 5] for $v = 16$ (vertical bars). (There is no available experimental data for $v = 0$.) The initial j is 30. Results for He+NaK are shown in Panel (a) and results for Ar+NaK are shown in Panel (b). The boxes show our $d_1(j,j')/d_0(j,j')$ for $v = 16$, while the asterisks show them for $v = 0$. For He+NaK, we predict that, for odd Δj, less orientation is preserved for $v = 16$ than for the rigid rotator. The level of agreement with experiment, however, does not change. For Ar+NaK, as with He+NaK, we predict that less orientation is preserved for odd Δj transitions for $v = 16$ than for the rigid rotator. Despite these differences, the level of agreement with experiment does not change by much, and experiment and theory agree that collisions with Ar destroy orientation more effectively than collisions with He.

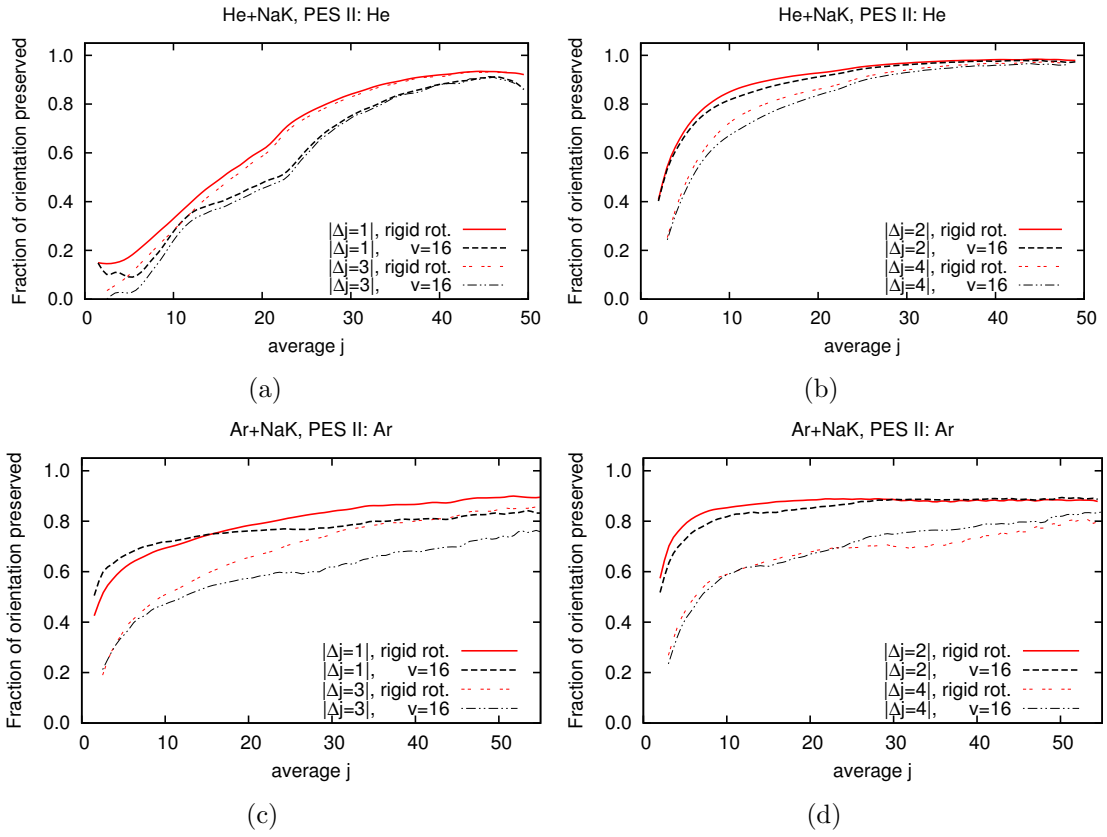

Figure 4.34: Fractions of orientation retained are shown for the rigid rotator and for $v = 16$. Panels (a) and (b) show results for PES II: He, while Panels (c) and (d) show results for PES II: Ar. For both the rigid rotator and $v = 16$, we predict that the orientation is harder to destroy as the average j increases, even though the absolute magnitude of these fractions is different.

4.4 Connection between the PES and the Δj even propensity

One of our objectives is to understand what determines the strength of the propensity for Δj even transitions exhibited by He+NaK and Ar+NaK. For an atom interacting with a homonuclear diatomic molecule, such as Na_2, there is a selection rule for Δj even transitions. Since K is the closest alkali atom to Na, one might suppose that the propensity would be related to the "almost homonuclearity" of NaK. That's part of the story, but it's not the whole story; experimental data [5, 6] show that He+NaK exhibits a stronger propensity for Δj even than Ar+NaK, so the degree of this propensity cannot be explained by properties of the molecule alone. Rather, the strength of the propensity is related to the deviation of the atom-diatom PES from symmetry under the exchange of Na and K.

In this section, we identify a region in the PES that tends to be very asymmetric. The propensity can be greatly affected if this region is in a part of the potential that contributes strongly to the scattering. Moreover, we develop a model which provides a simple way of understanding why a very asymmetric region should arise, and the predictions of the model agree well with our calculations.

4.4.1 Background

For homonuclear diatomic molecules, the strict selection rule for Δj even transitions (in the absence of nuclear spin) is a consequence of symmetry under exchange of the two atoms of the molecule. The rule derives from the parities of the wave functions of the two states connected by the transition, as well as the symmetry of the interaction that caused the transition [9].

The PES contains all the details of the interaction needed to treat a collision, including symmetry properties. Panel (a) of Fig. 4.35 depicts the geometry of an atom interacting with a homonuclear molecule, using Jacobi coordinates. The two nuclei are indistinguishible, so the PES is symmetric with respect to $\theta = 90°$ for all R. The corresponding Legendre expansion of the PES contains only even components,

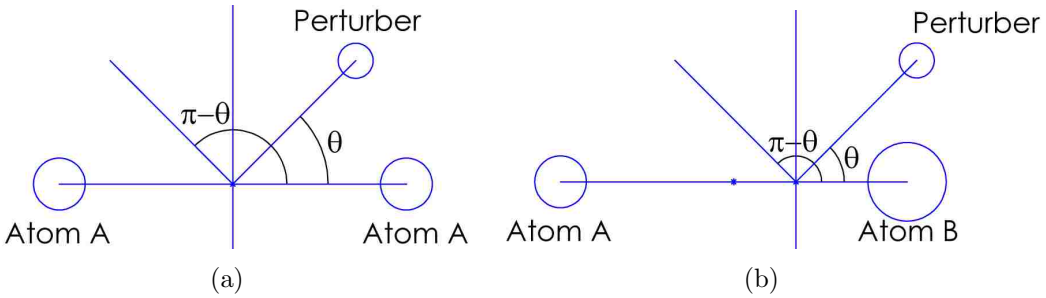

Figure 4.35: Schematic of the interaction between a generic atom (labelled "Perturber") and a diatomic molecule, using Jacobi coordinates. Panel (a) illustrates the interaction when the molecule is homonuclear. The center of mass is at the midpoint of the molecule and the PES is symmetric about $\theta = 90°$. Panel (b) illustrates the interaction when the molecule is heteronuclear. The center of mass shifts towards the heavier atom, which in this figure is Atom B. The PES is no longer symmetric about $\theta = 90°$, because atoms A and B are different.

since even and odd Legendre polynomials are symmetric and antisymmetric with respect to $\theta = 90°$:

$$P_n(\cos\theta) = (-1)^n P_n\big(\cos(\pi - \theta)\big). \tag{4.25}$$

Panel (b) of Fig. 4.35 depicts the geometry of a heteronuclear diatomic molecule interacting with an atom. The PES is no longer totally symmetric with respect to $\theta = 90°$, and the Legendre expansion includes a symmetric portion with even components and an antisymmetric portion with odd components.

The strength of the propensity for Δj even transitions should depend on the relative contributions to the scattering by the symmetric and antisymmetric portions of the PES; a semiclassical analysis by McCurdy and Miller [10] supports this conclusion. McCurdy and Miller looked at this problem using a very simple potential with a three-term Legendre expansion of the form

$$V(R,\theta) = V_0(R)\Big[1 + a_1 P_1(\cos\theta) + a_2 P_2(\cos\theta)\Big], \tag{4.26}$$

where the ratio of the $n = 1$ and $n = 2$ Legendre components is independent of R. McCurdy and Miller took $V_0(R)$ to be a Lennard-Jones potential and investigated

several cases where $a_1, a_2 > 0$. There is only one antisymmetric Legendre component in the expansion, $P_1(\cos\theta)$, and McCurdy and Miller varied its coefficient a_1 to see how the propensity was affected. First they set $a_1 = 0$ and reproduced the selection rule for Δj even transitions. Then, they let a_1 be much smaller than a_2, so that the PES was only very slightly asymmetric, and there was a very strong propensity for Δj even transitions. Next, they let a_1 be a little smaller than a_2, and there was a propensity at low Δj and an inverse propensity (for odd Δj) at high Δj. Finally, they let a_1 be larger than a_2, so that the PES was very asymmetric, and the propensities washed out.

4.4.2 Dependence of the propensity on the size of $|v_1(R)|$

Motivated by the previous considerations, we performed a quantum mechanical study to correlate features of the PES with the propensity for Δj even transitions. Our potentials are more general than the form used by McCurdy and Miller [10], Eq. 4.26. We typically expanded $V(R, \theta)$ in 11–16 Legendre components (Eq. 2.87), and the ratio of $v_1(R)$ and $v_2(R)$ depends on R, so applying their results to our situation is not straightforward. We first performed several test calculations that included only the first three terms in the Legendre expansion:

$$V(R, \theta) = v_0(R) + v_1(R)P_1(\cos\theta) + v_2(R)P_2(\cos\theta). \tag{4.27}$$

These calculations reproduced many of the essential features of our original results (see Fig. 4.6) and led us to perform further tests using only three terms.

Then we tried a series of three-term calculations in which we scaled our $v_1(R)$ by a constant factor. Panels (a) and (b) of Fig. 4.36 show the results of decreasing the asymmetry of the PES by decreasing $v_1(R)$. For both He+NaK and Ar+NaK, decreasing $v_1(R)$ led to a stronger propensity for Δj even for all Δj; Ar+NaK's slight inverse propensity (for odd Δj) turned into a regular propensity. When we let $v_1(R) = 0$, we reproduced the selection rule for Δj even transitions. Next, we increased the asymmetry in the same manner. Panels (c) and (d) of Fig. 4.36 show the resulting cross sections. For He+NaK, increasing $v_1(R)$ caused the cross sections

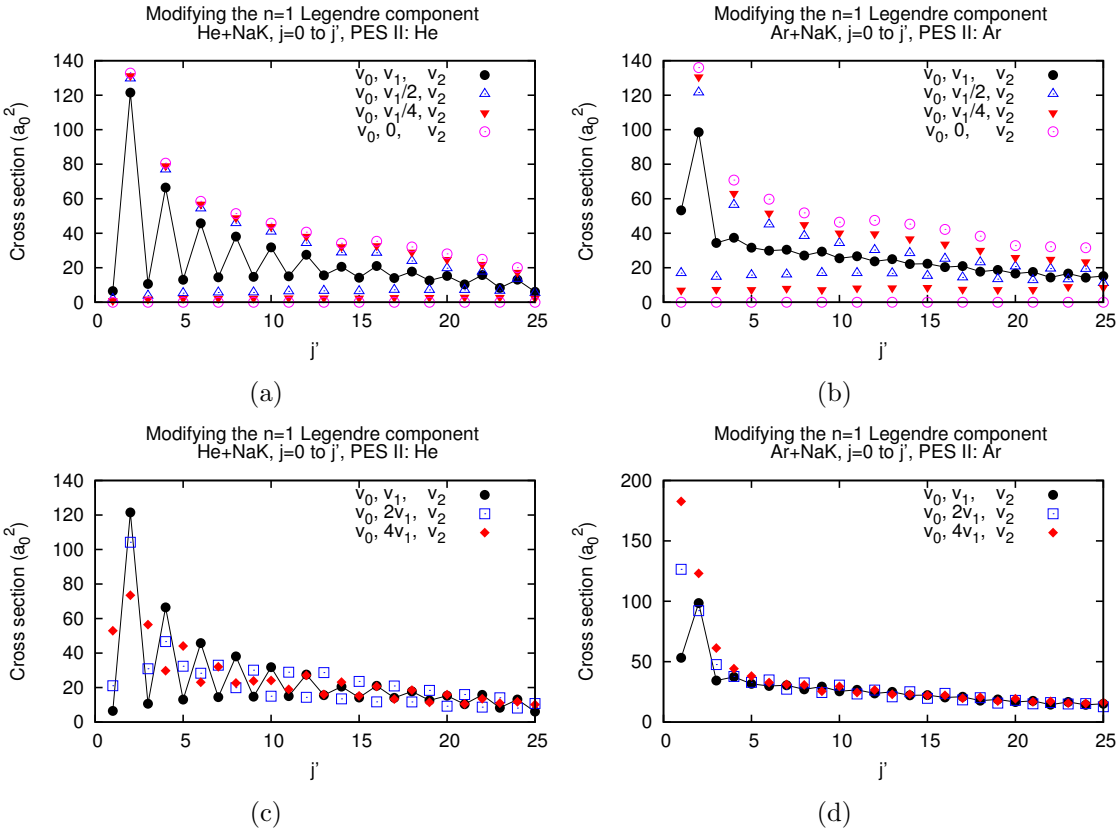

Figure 4.36: Effect of modifying the coefficient $v_1(R)$ on rotationally inelastic cross sections. The initial j is zero. The label 'v_0, v_1, v_2' corresponds to the unmodified three-term expansion of the PES. Panels (a) and (b) show the effect of decreasing the asymmetry present in PES II: He and PES II: Ar; the propensity is enhanced as $v_1(R)$ decreases, until $v_1(R)$ is zero and there is a strict selection rule for Δj even. Panels (c) and (d) show the effect of increasing $v_1(R)$. For He+NaK, the cross sections start to exhibit inverse propensities for Δj odd transitions for some values of Δj, while for Ar+NaK, increasing $v_1(R)$ washes out any propensities.

to exhibit an inverse propensity for some values of Δj, while for Ar+NaK, increasing $v_1(R)$ led to cross sections without a propensity.

These results confirm that, for our systems, the strength of the propensity is linked to the size of the antisymmetric portion of the PES. Nonetheless, we expect that the ratio $|v_1(R)|/|v_2(R)|$ plays a role, as McCurdy and Miller [10] demonstrated with their surface. Since each of our Legendre components depends on R differently, we must take a different approach to assess how the relative magnitudes of $|v_1(R)|$ and $|v_2(R)|$ affect the propensity.

4.4.3 Dependence of the propensity on the relative sizes of $|v_1(R)|$ and $|v_2(R)|$

We found it useful to identify regions of the potentials in which $|v_1(R)| > |v_2(R)|$, which we will refer to as "regions of greatest asymmetry" (RGAs). We then examined our results to assess whether the effect of these regions was sufficient to diminish the propensity for Δj even transitions.

In many cases, we were able to isolate the effect of RGAs by looking at partial cross sections $\sigma^J(j \to j')$ for certain values of J. We can roughly associate each J with an impact parameter $b \approx J/k_j$ (see Section 4.1, page 97). If b is large enough, we can take the corresponding classical trajectory to be a straight line, and the classical turning point will be equal to b. Figure 4.37 illustrates the situation. The shaded region shows a possible RGA defined by a minimum (R_1) and a maximum (R_2) value of R; a trajectory with impact parameter $b < R_2$ will pass through the RGA, but the RGA has the greatest influence on trajectories with $R_1 \leq b < R_2$, because the probability density of the partial wave is maximum near the classical turning point of the trajectory. Therefore for our calculations, as long as the RGA occurs at large enough R, we can associate a certain range of partial waves with trajectories that preferentially sample the potential in the RGA.

The shaded rectangles in Panels (a) and (b) of Fig. 4.38 highlight the RGAs of PES II: He and PES III: Ar. The RGA for HeNaK occurs at a larger R than for ArNaK. At our collision energies, however, both RGAs occur at large enough R to justify considering straight-line trajectories, so we can probe their effects.

The shaded rectangles in Panels (a) and (b) of Fig. 4.39 show the range of impact

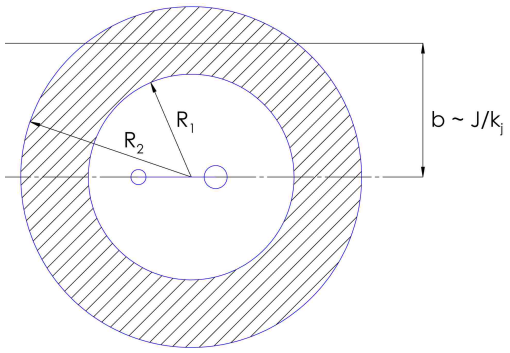

Figure 4.37: Relation between the impact parameter $b \approx J/k_j$ and the region of the potential sampled by the partial wave. For large b, the trajectory is approximately a straight line and the impact parameter is a classical turning point. The shaded area is an RGA. Trajectories with impact parameters $R_1 \leq b < R_2$ preferentially sample the RGA; those with $b < R_1$ still encounter the RGA, but it has less of an influence.

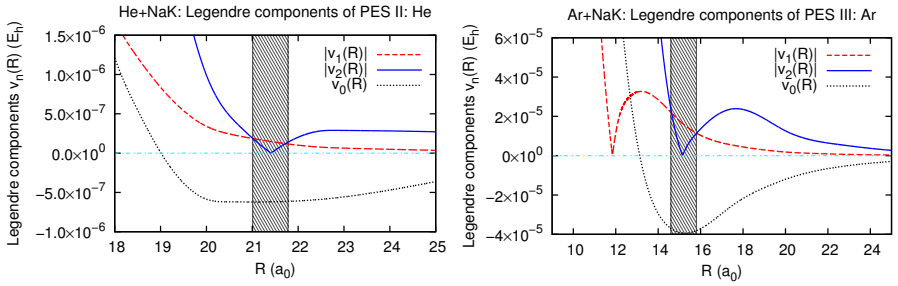

(a) (b)

Figure 4.38: The RGAs of PES II: He (left) and PES III: Ar (right), highlighted by shaded rectangles. The RGAs both occur at relatively large R, although each has a different position and thus (as we discuss in the text) a different effect.

parameters for which trajectories are most influenced by the RGA. We can assess whether these trajectories contribute significantly to the scattering cross sections by looking at the dotted curve in Panels (a) and (b); the dotted curve shows the sum of all inelastic partial cross sections for $\Delta j \leq j_{\max}$ as a function of $J/k_j \approx b$. For He+NaK, trajectories that preferentially sample the RGA do not contribute much to the inelastic cross sections, so the RGA has little effect. For Ar+NaK, however,

the RGA is in a region of the potential that influences the results more. The dashed and solid curves in Panel (b) show the Ar+NaK partial cross sections for $0 \to 1$ and $0 \to 2$; the RGA clearly diminishes the propensity for $\Delta j = 2$ transitions.

Panels (a) and (b) of Fig. 4.39 show that the total inelastic partial cross sections for large J are dominated by contributions from $0 \to 1$ and 2; the interaction is not strong enough to change Δj by much more than two. On the other hand, for small J there is strong mixing, so that the partial cross sections for each Δj are roughly the same size. For both He+NaK and Ar+NaK, trajectories that never reach the RGA have large impact parameters associated with large J, and we will now discuss how such trajectories contribute to the exhibited propensities for $\Delta j = 2$.

The solid circles in Panels (c) and (d) of Fig. 4.39 are sums of all partial cross sections for trajectories that never reach the RGA. For PES II: He, the trajectories that don't reach the RGA sample the potential where the coupling is very weak, and they contribute negligibly to the scattering cross sections. For PES III: Ar, however, trajectories that don't reach the RGA contribute much more, and the solid circles in Panel (d) show a strong propensity for $\Delta j = 2$ transitions. The squares in Panels (c) and (d) are sums of the rest of the partial cross sections (trajectories that reach the RGA). For PES II: He, the squares show a propensity for all Δj even transitions; although these trajectories reach the RGA, the RGA has a very small effect on the results. On the other hand, the RGA of PES III: Ar has a stronger influence, and the squares in Panel (d) do not show a propensity for $\Delta j = 2$. The open circles in Panels (c) and (d) are the total cross sections $\sigma(j \to j')$, obtained from summing over all the partial cross sections. For He+NaK, the total cross sections are determined from trajectories that reach the RGA; the total cross sections show a strong propensity for Δj even that persists to high Δj because the RGA is inconsequential. For Ar+NaK, the contribution from trajectories that never reach the RGA leads to a spike in the total cross sections where $\Delta j = 2$, while the cross sections for $\Delta j \neq 2$ are mostly determined from trajectories that probe the (consequential) RGA. This is why Ar+NaK doesn't show a strong propensity for higher Δj like He+NaK does.

All cross sections presented in this section were determined by using three-term

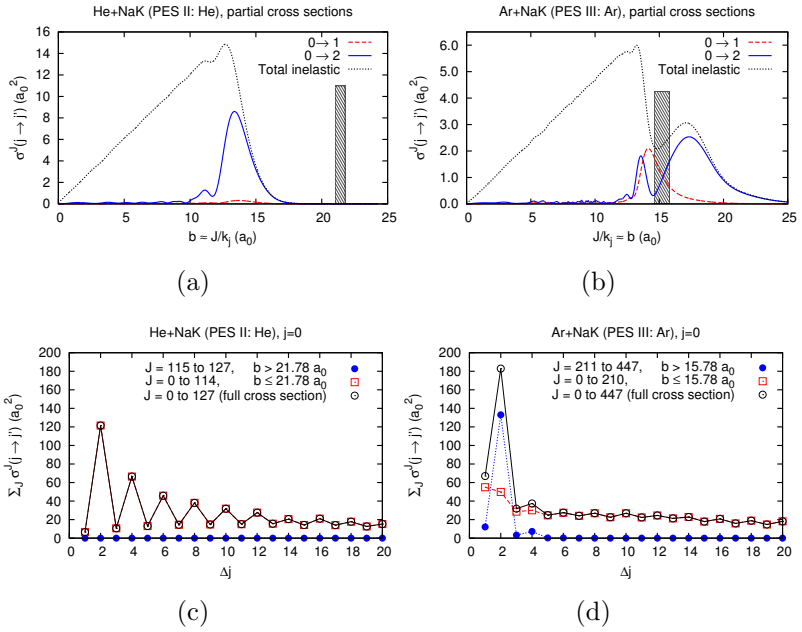

Figure 4.39: Connection between the propensity and features of the potential for PES II: He (left) and PES III: Ar (right). Panels (a) and (b) show partial cross sections as a function of impact parameter b. The dotted curve shows the total inelastic partial cross section, which is the sum of all partial cross sections for $j = 0$ to any j' in the range 1–30. The rectangle shows the range of impact parameters that preferentially sample the RGA. Based on the sizes of the inelastic partial cross sections, the ArNaK RGA has a greater influence on Ar+NaK scattering than the HeNaK RGA has on He+NaK scattering. The dashed and solid curves show partial cross sections for $j = 0$ to $j' = 1$ and 2; the effect of the ArNaK RGA is to diminish the propensity, so that there is a range of b for which there is no propensity for $\Delta j = 2$. Panels (c) and (d) show sums of partial cross sections for different ranges of J. The solid circles correspond to trajectories that don't probe the RGA and the squares to trajectories that reach the RGA. The open circles are total inelastic cross sections (partial cross sections summed over all J). For He+NaK, trajectories that probe the RGA make up most of the total cross sections, but the RGA has very little influence. Thus, there is a strong propensity for all Δj even transitions. For Ar+NaK, the total cross sections exhibit a spike at $\Delta j = 2$ because of trajectories that never reach the RGA. The other cross sections, for $\Delta j \neq 2$, are determined by trajectories that probe the RGA, and thus there is not really a strong propensity for higher Δj.

Legendre expansions of the potentials, but we have verified that the results of the eleven-term Legendre expansions look similar. The partial cross sections for trajectories that never reach the RGAs or which have classical turning points in the RGAs are almost identical for the eleven- and three-term expansions. The other partial cross sections (for smaller J) show some differences, leading to differences in the cross sections (Fig. 4.6). Nonetheless, the general trends are the same.

Each RGA in Fig. 4.38 contains a zero of $v_2(R)$. This observation is not surprising. Any point R where $v_2(R) = 0$ will satisfy $|v_1(R)| \geq |v_2(R)|$, so such a point will likely correspond to an RGA. The question then arises, what causes a zero of $v_2(R)$? We address this question by considering Fig. 4.40, which shows the potentials given by the three-term Legendre expansions of our PESs as a function of $\cos\theta$, for several fixed values of R near to or in the RGA. The potentials all have negative values in this region. For the largest R, there are two local minima near the ends of the molecule ($\cos\theta = \pm 1$). As R decreases, however, the potentials exhibit a single minimum near the middle, where $\cos\theta = 0$. In other words, there is a change in sign of the curvature of the potential in the RGA. Since $P_2(\cos\theta)$ is the only term in the three-term expansion that is quadratic in $\cos\theta$, this sign change occurs as $v_2(R)$ passes through zero. In the next section we will develop a simple model to explain why the zero occurs.

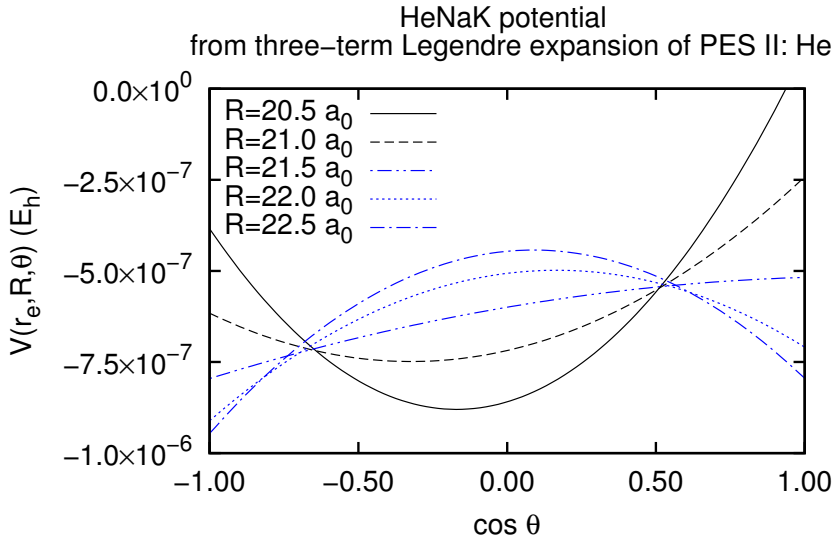

(a)

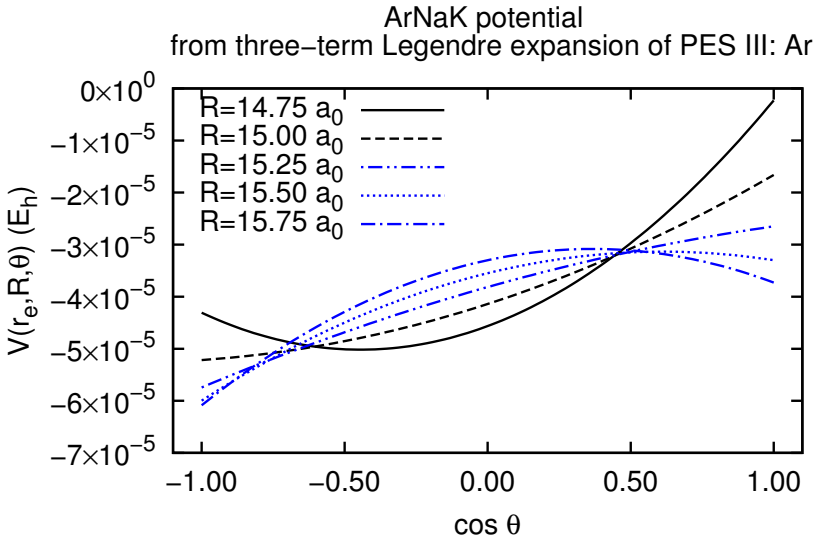

(b)

Figure 4.40: Potentials plotted as a function of $\cos\theta$ for fixed values of the atom-molecule distance R near or in an RGA; the potentials were determined from the three-term Legendre expansion of the corresponding PES. Panel (a) corresponds to PES II: He, and Panel (b) to PES III: Ar. Since $P_2(\cos\theta)$ is quadratic in $\cos\theta$, the $n = 2$ component changes sign as the ends of the molecule become less attractive than the region near the middle of the molecule.

4.4.4 Model for zeros of $v_2(R)$

We have developed a very simple model, based on the interaction of a homonuclear molecule with a distant perturber, that provides a way to estimate where a zero of $v_2(R)$ should arise. We will find that averaging the predictions of this model for He (or Ar) interacting with Na_2 and K_2 gives a back-of-the-envelope explanation for the difference in the locations of the RGAs of HeNaK and ArNaK.

Fig. 4.41 shows the geometry of an atom interacting with a homonuclear diatomic molecule. The distance from the perturber to the center of mass of the molecule is R, the bond length of the molecule is $2a$, and the distances of the perturber from each atom of the molecule are r_1 and r_2.

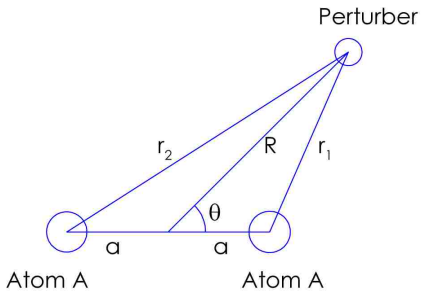

Figure 4.41: Interaction of a perturbing atom with a homonuclear diatomic molecule.

Our model assumes the three-body PES is the sum of the two-body interactions between the perturber and each atom of the homonuclear diatomic molecule:

$$V_{\rm tot}(R,\theta) = V(r_1) + V(r_2). \tag{4.28}$$

We can express r_1 and r_2 in terms of R, a, and $\cos\theta$ by using the law of cosines:

$$r_1^2 = R^2 + a^2 - 2aR\cos\theta \tag{4.29}$$

$$r_2^2 = R^2 + a^2 + 2aR\cos\theta. \tag{4.30}$$

Then, with $u = \cos\theta$, we have

$$V_{\rm tot}(R,u) = V\big(r_1(u)\big) + V\big(r_2(u)\big). \tag{4.31}$$

The premise of the model is that $v_2(R)$, the $n = 2$ Legendre component of $V_{\rm tot}(R, u)$, is zero at the R where the curvature of the PES is zero at $u = 0$. We will therefore identify $v_2(R) = 0$ with the R at which

$$\left.\frac{\partial^2 V_{\rm tot}(R,u)}{\partial u^2}\right|_{u=0} = 0. \tag{4.32}$$

This approximation is exact if $v_0(R)$ and $v_2(R)$ are the only terms, and should be reasonable if the terms for $n = 4$, 6, etc. are small.

By taking the second derivative of Eq. 4.31 with respect to u and evaluating at $u = 0$, one finds that the condition given by Eq. 4.32 is satisfied when

$$\frac{d^2V(r)}{dr^2} = \frac{1}{r}\frac{dV(r)}{dr}, \tag{4.33}$$

where, as illustrated by Fig. 4.42,

$$r = r_1(0) = r_2(0) = \sqrt{R^2 + a^2}. \tag{4.34}$$

Eq. 4.33 is an algebraic equation to determine a particular r for a known potential $V(r)$. Once r has been determined, one can solve for R by using Eq. 4.34.

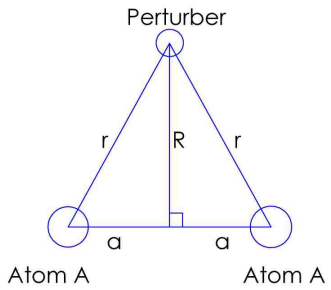

Figure 4.42: Interaction of a perturbing atom with a homonuclear diatomic molecule for $\theta = 90^\circ$ ($u = 0$).

We will show that in some cases the term on the right hand side of Eq. 4.33 is very small. Then Eq. 4.32 is satisfied when $V(r)$ has an inflection point:

$$\frac{d^2V(r)}{dr^2} \approx 0. \tag{4.35}$$

For a typical two-body potential, with an attractive well and a repulsive wall, the inflection point occurs where the long-range attractive forces start to compete with short-range forces.

Special Case: Lennard-Jones potential

Analytic results can be determined if $V(r_1)$ and $V(r_2)$ are Lennard-Jones potentials, given by

$$V(r) = 4\epsilon \left[\left(\frac{\sigma}{r}\right)^{12} - \left(\frac{\sigma}{r}\right)^{6} \right], \tag{4.36}$$

where ϵ is the well depth and σ is the position where the potential is zero.

By inserting the first and second derivatives of $V(r)$,

$$\frac{dV(r)}{dr} = 4\epsilon \left[-\frac{12\sigma^{12}}{r^{13}} + \frac{6\sigma^{6}}{r^{7}} \right] \tag{4.37}$$

$$\frac{d^2V(r)}{dr^2} = 4\epsilon \left[\frac{156\sigma^{12}}{r^{14}} - \frac{42\sigma^{6}}{r^{8}} \right], \tag{4.38}$$

into Eq. 4.33, one finds that Eq. 4.32 is satisfied where

$$r \approx 1.23\sigma. \tag{4.39}$$

This is very close to the inflection point, for which

$$r \approx 1.24\sigma. \tag{4.40}$$

Generalization to our PESs

Since our model involves a homonuclear diatomic molecule, we used a simple procedure to apply the results of the model to our heteronuclear systems.

First, we approximated the two-body potentials between the perturber and either Na or K, using the eleven-term expansion of our PES, $V(R, \theta)$, for the angles $\theta = 0°$ and 180°. Panel (a) of Fig. 4.43 illustrates the idea for $\theta = 0°$; we assume that for large R, the shape of the PES is dominated by the two-body interaction between K and the perturber. The atom-atom potential depends on the interatomic distance r, rather than the distance from the center of mass R, so we expressed the potential

in terms of r. Then, we repeated this procedure for $\theta = 180°$ to approximate the potential between Na and the perturber.

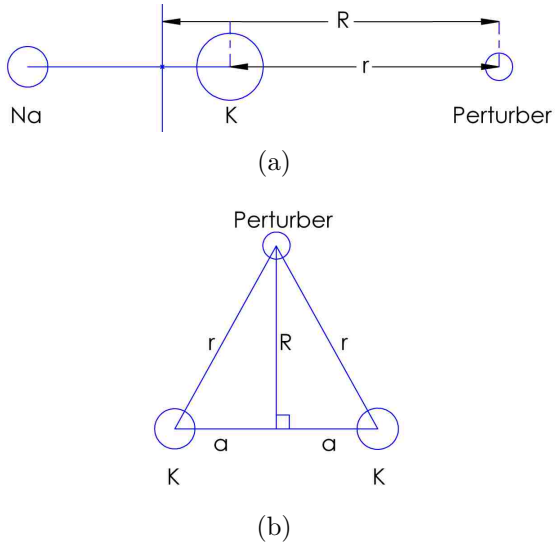

Figure 4.43: Procedure for applying our model, appropriate for an atom interacting with a homonuclear molecule, to our systems, which involve a heteronuclear molecule. Panel (a) shows the collinear geometry where the perturber is to the right of K ($\theta = 0°$). We assume that the PES for this geometry, with the perturber far away, is approximately the interatomic potential between the perturber and K. The interatomic potential would depend on the distance r between the perturber and K. Panel (b) shows the interaction between the perturber and K_2 for $u = 0$ ($\theta = 90°$).

Once we had approximated the interatomic potentials, we estimated the first and second derivatives of each potential numerically, with respect to the interatomic distance. Then we determined where Eq. 4.33 was satisfied for the interaction between the perturber and K_2 (depicted in Panel (b) of Fig. 4.43) and between the perturber and Na_2. For the perturber + K_2 system, we calculated $R = \sqrt{r^2 - a^2}$ by using the bond length $2a$ of the first excited singlet state of K_2; this state corresponds to NaK in the $A\,^1\Sigma^+$ electronic state. Correspondingly, for the perturber + Na_2 system we calculated R by using the bond length of the first excited singlet state of Na_2. Finally, we averaged our two values of R to estimate the point at which the

model predicts $v_2(R) = 0$ for He+NaK and Ar+NaK.

The estimated values for the R at which $v_2(R) = 0$ are given in Table 4.5, along with the R obtained from the calculated Legendre components. The results of the model agree well with our *ab initio* calculations, with differences not exceeding 1 a_0. We also note that Eqs. 4.33 and 4.35 gave similar results.

We have shown that for He+NaK and Ar+NaK the zero of $v_2(R)$ (and therefore the RGA of the potential) depends on the inflection points of the PES for $\theta = 0°$ and $\theta = 180°$. This part of the potential is difficult to calculate, since it requires an accurate balance of long-range and short-range forces. Therefore it is not easy to nail down the details of the propensity, and the strength of the propensity can be sensitive to seemingly small changes in the potential.

Table 4.5: Estimates and calculated values for the R where $v_2(R) = 0$ for different PESs.

	R where $v_2(R) = 0$ in a_0		
	from $V''(r) = V'(r)/r$	from $V''(r) = 0$	from *ab initio* calculations
PES II: He	21.3	21.7	21.4
PES II: Ar	15.7	15.9	16.7
PES III: Ar	14.5	14.8	15.2

Chapter 5

Semiclassical model for m-changing transitions in rotationally inelastic collisions

5.1 Introduction

We recently published a semiclassical model [3] for the change in the polar angle $\theta = \cos^{-1}\left(m/(j+\frac{1}{2})\right)$ in rotationally inelastic collisions in a cell-type experiment. This model addressed discussion in the literature [11, 12] concerning whether θ is approximately conserved in such collisions. We reported that many of our calculations for He or Ar with NaK showed that θ was nearly conserved, and we presented a simple analysis for a special case that yielded a Lorentzian-like distribution, centered at $\theta' = \theta$, for the final θ'. The polar angle distribution from our semiclassical model also led to a remarkably accurate formula for the semiclassical cross sections $\sigma_{\rm sc}(jm \to j'm')$, in which m and m' are treated as continuous variables.

In this chapter we will summarize the work presented in [3] and also present additional calculations and derivations that identify the precise mathematical approximations that lead to the semiclassical formulas. We will present additional results for analytic approximations to our expression for the polar angle distribution; in

one case, we will derive the Lorentzian-like distribution from [3] more rigorously.

5.2 Physical model for polar angle distribution

In order to discuss our semiclassical model, we must first introduce the notion of a "tipping angle distribution."

Derouard [12] has discussed a semiclassical interpretation of collisions that change j to j'. The basis of this interpretation is that transitions from a rotational state j to a state j' can be represented by vector coupling diagrams as shown in Fig. 5.1 [2]. The initial and final rotational angular momenta $\mathbf{j}$ and $\mathbf{j}'$ are coupled by the angular momentum transferred in the collision, $\mathbf{j} - \mathbf{j}'$. The lengths of $\mathbf{j}$ and $\mathbf{j}'$ are the same in all three diagrams shown in Fig. 5.1, but the angular momentum transferred in the collision depends on the final orientation of $\mathbf{j}'$. This angular momentum, λ, is

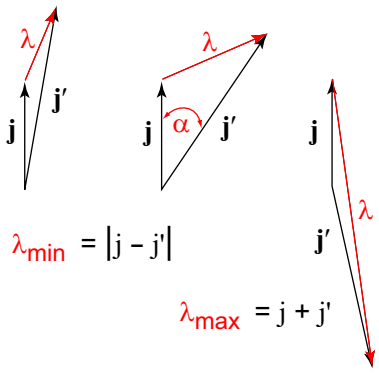

Figure 5.1: Vector coupling diagram [12] illustrating transfer of angular momentum λ in transitions from j to j'. The lengths of j and j' are the same in all three diagrams. The angular momentum transferred is related to the "tipping angle" α between $\mathbf{j}$ and $\mathbf{j}'$. Reproduced from [2] with the permission of AIP publishing.

related to the angle α between $\mathbf{j}$ and $\mathbf{j}'$, which we will refer to as the "tipping angle," by the law of cosines:

$$\lambda(\lambda+1) = j(j+1) + j'(j'+1) - 2\sqrt{j(j+1)j'(j'+1)}\cos\alpha. \tag{5.1}$$

For large j and j', one can consider α a continuous variable. The semiclassical counterpart of the Grawert coefficients (see Eq. 2.96) is the distribution of tipping angles α [12].

The tipping angle distribution $B(j, j'; \cos\alpha)$ can be expressed in terms of the $d_K(j, j')$, where the $d_K(j, j')$ are related to the transfer of moments of the distribution of m levels. By starting with Eq. 2.138,

$$B_\lambda(j, j') = \sum_{K=0}^{2j_<} (-1)^{j+j'+\lambda+K} (2K+1) \begin{Bmatrix} \lambda & j & j' \\ K & j' & j \end{Bmatrix} d_K(j, j'), \tag{5.2}$$

and replacing the $6j$ symbol by using the approximation [63]

$$P_K(\cos\alpha) \approx \lim_{j,j' \gg 1} (-1)^{j+j'+\lambda+K} \sqrt{[j][j']} \begin{Bmatrix} \lambda & j & j' \\ K & j' & j \end{Bmatrix}, \tag{5.3}$$

where $[j] = 2j + 1$, one finds that

$$B(j, j'; \cos\alpha) = \frac{1}{\sqrt{[j][j']}} \sum_{K=0}^{2j_<} (2K+1) d_K(j, j') P_K(\cos\alpha). \tag{5.4}$$

Eq. 5.4 shows that for $j, j' \gg 1$ the tipping angle distribution can be expanded in Legendre polynomials in $\cos\alpha$, with the details of the system contained in the expansion coefficients $(2K+1)d_K(j, j')$. We will use this result in our semiclassical model. By integrating both sides of Eq. 5.4 over $\sin\alpha\, d\alpha$ and invoking the relation between $d_0(j, j')$ and $\sigma(j \to j')$ given in Eq. 2.139, one can show that

$$\sigma(j \to j') = \frac{\pi(j' + \frac{1}{2})}{k_j^2} \int_0^\pi B(j, j'; \cos\alpha) \sin\alpha\, d\alpha, \tag{5.5}$$

which confirms Derouard's interpretation [12] that the semiclassical Grawert coefficients give the distribution of tipping angles.

In Fig. 5.2, we present our vector model interpretation of $jm \to j'm'$ transitions [3]. In this model, the initial rotational angular momentum vector $\mathbf{j}$ precesses about the z-axis with a cone angle of $\theta = \cos^{-1}\left(m/(j + \frac{1}{2})\right)$. A collision tips $\mathbf{j}$ by an angle α, giving rise to the final rotational angular momentum $\mathbf{j}'$, which precesses about the z-axis with a cone angle of θ'. One can determine the relationship between the

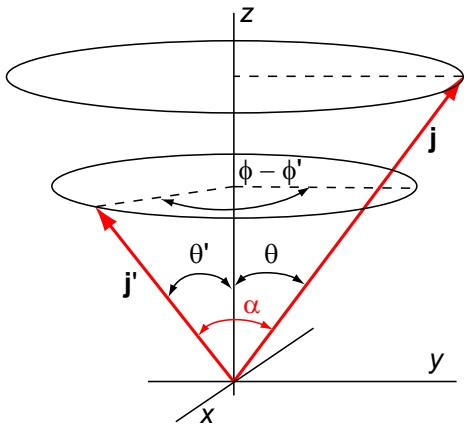

Figure 5.2: Definitions of the angles θ, θ', and α related to the initial and final angular momenta $\mathbf{j}$ and $\mathbf{j}'$. The azimuthal angles of $\mathbf{j}$ and $\mathbf{j}'$ are ϕ and ϕ', respectively. Reprinted from [3] with permission from Elsevier.

tipping angle α and the other angular variables by noting that $\cos\alpha = \hat{\mathbf{j}} \cdot \hat{\mathbf{j}}'$, or

$$\cos\alpha = \cos\theta\cos\theta' + \sin\theta\sin\theta'\cos(\phi - \phi'). \tag{5.6}$$

We are interested in the probability $\mathcal{P}_{jj'}(\theta,\theta')\sin\theta'\,d\theta'$ that an average collision changes θ to a final value in the range between θ' and $\theta' + d\theta'$. The premise of our model is that $\mathcal{P}_{jj'}(\theta,\theta')$ is the average value of $B(j,j';\cos\alpha)$ as $\mathbf{j}$ and $\mathbf{j}'$ sweep around their circular paths in the diagram. Since values of $\phi - \phi'$ between 0 and π cover the whole range of possible values of α, the expression for $\mathcal{P}_{jj'}(\theta,\theta')$ is

$$P_{jj'}(\theta,\theta') = \frac{1}{\pi}\int_0^\pi B(j,j',\cos\alpha)\,d(\phi - \phi'). \tag{5.7}$$

Following Vilenkin [87], one can evaluate the integral in Eq. 5.7 by changing the integration variable from $(\phi - \phi')$ to α. Using Eq 5.6, we obtain

$$d(\phi - \phi') = \frac{\sin\alpha\,d\alpha}{\sqrt{(\cos\alpha - \cos(\theta+\theta'))(\cos(\theta-\theta') - \cos\alpha)}}. \tag{5.8}$$

By substituting Eq. 5.8 into Eq. 5.7, one obtains an integral expression for $P_{jj'}(\theta,\theta')$ in terms of α,

$$P_{jj'}(\theta,\theta') = \frac{1}{\pi}\int_{\alpha_{\min}}^{\alpha_{\max}} \frac{B(j,j';\cos\alpha)\sin\alpha\,d\alpha}{\sqrt{(\cos\alpha - \cos(\theta+\theta'))(\cos(\theta-\theta') - \cos\alpha)}}, \tag{5.9}$$

where the condition that $0 \leq \alpha \leq \pi$ yields

$$\alpha_{\min} = |\theta - \theta'|, \quad \alpha_{\max} = \begin{cases} \theta + \theta' & \text{if } \theta + \theta' \leq \pi \\ 2\pi - (\theta + \theta') & \text{if } \theta + \theta > \pi \end{cases} . \tag{5.10}$$

The range of integration includes the values of α for which the radicand in the denominator of Eq. 5.9 is nonnegative. A further change of variable to $x = \cos\alpha$ leads to

$$\mathcal{P}_{jj'}(\theta, \theta') = \frac{1}{\pi} \int_{\cos(\theta'+\theta)}^{\cos(\theta-\theta')} \frac{B(j, j'; x)\, dx}{\sqrt{(x - \cos(\theta + \theta'))(\cos(\theta - \theta') - x)}} \tag{5.11}$$

One can evaluate Eq. 5.11 by using a special case of a result due to Vilenkin [87],

$$\frac{1}{\pi} \int_{\cos(\theta+\theta')}^{\cos(\theta'-\theta)} \frac{P_K(x)dx}{\sqrt{(x - \cos(\theta' + \theta))(\cos(\theta' - \theta) - x)}} = P_K(\cos\theta) P_K(\cos\theta'), \tag{5.12}$$

and the Legendre expansion of $B(j, j'; x)$ in x given by Eq. 5.4, to obtain a closed form expression for $\mathcal{P}_{jj'}(\theta, \theta')$,

$$\mathcal{P}_{jj'}(\theta, \theta') = \frac{1}{\sqrt{[j][j']}} \sum_{K=0}^{2j_<} (2K + 1) d_K(j, j') P_K(\cos\theta) P_K(\cos\theta'). \tag{5.13}$$

This expression has the correct limiting behavior for the limiting case $\theta = 0$. Then the tipping angle $\alpha = \theta'$; all the $P_K(\cos(0))$ are equal to one, and Eq. 5.13 reduces to Eq. 5.4, so that

$$\mathcal{P}_{jj'}(0, \theta') = B(j, j'; \cos\theta') = B(j, j'; \cos\alpha). \tag{5.14}$$

We can also show that the total cross section for changing j to j' is a constant times the integrated probability for changing θ to any θ', independent of θ. Integrating Eq. 5.13 over θ' and using the relationship between $\sigma(j \to j')$ and $d_0(j, j')$, Eq. 2.139, leads to

$$\sigma(j \to j') = \frac{\pi}{k_j^2} (j' + \tfrac{1}{2}) \int_0^\pi \mathcal{P}_{jj'}(\theta, \theta') \sin\theta'\, d\theta'. \tag{5.15}$$

Equation 5.15 is consistent with the quantum result for collisions in a cell-type experiment: when one averages over the direction of the incident particle, the sum

over m' of the cross sections for the $jm \to j'm'$ transitions is independent of the initial m.

If one treats m and m' as continuous variables, then one can transform the angular distribution $\mathcal{P}_{jj'}(\theta,\theta')\sin\theta'\,d\theta'$ into a semiclassical distribution of m' levels. The final polar angle θ' is related to m' by

$$\cos\theta' = \frac{m'}{\sqrt{j'(j'+1)}} \approx \frac{m'}{j'+\frac{1}{2}}, \tag{5.16}$$

and by taking differentials on both sides of Eq. 5.16, we have

$$d(\cos\theta') = -\sin\theta'\,d\theta' = \frac{dm'}{j'+\frac{1}{2}}. \tag{5.17}$$

The relationships given by Eqs. 5.16 and 5.17 lead to a semiclassical cross section for the change in the continuous variable m,

$$\sigma_{\rm sc}(jm \to j'm') = \frac{\pi}{k_j^2\sqrt{[j][j']}}\sum_{K=0}^{2j_<}(2K+1)d_K(j,j')P_K\left(\frac{m}{j+\frac{1}{2}}\right)P_K\left(\frac{m'}{j'+\frac{1}{2}}\right). \tag{5.18}$$

We will refer to Eqs. 5.13 and 5.18 as the "exact semiclassical" formulas.

5.3 Alternate derivation of $\mathcal{P}_{jj'}(\theta,\theta')$

Invoking the vector model provides an appealing physical interpretation of $jm \to j'm'$ transitions, but the mathematical approximations behind the results are not obvious. This section presents an alternate derivation of Eqs. 5.13 and 5.18 that clarifies the point. One can start with an alternate expression for $jm \to j'm'$ cross sections,

$$\sigma(jm \to j'm') = \frac{\pi}{k_j^2}(-1)^{m+m'+j+j'}\sum_K(-1)^{2K}(2K+1)d_K(j,j') \times \begin{pmatrix} j & K & j \\ m & 0 & -m \end{pmatrix}\begin{pmatrix} j' & K & j' \\ m' & 0 & -m' \end{pmatrix}. \tag{5.19}$$

This formula is exact and was presented in [11]; it can be derived by inverting Eq. 2.128 in Section 2.5, leading to

$$\mathcal{P}^{jj'} = \mathcal{T}^{j}\,\mathcal{Q}^{jj'}(\mathcal{T}^{j'})^{\dagger}. \tag{5.20}$$

Using Eq. 2.129 to write this equation in terms of matrix elements gives

$$\mathcal{P}^{jj'}_{mm'} = \sum_{K} \mathcal{T}^{j}_{mK} d_K(j,j') \mathcal{T}^{j'}_{Km'}. \tag{5.21}$$

By using Eqs. 2.108 and 2.121, one obtains Eq. 5.19.

We now invoke Edmonds' [63] relation between $3j$ coefficients and Legendre polynomials, which can be written

$$(-1)^{K+m+j} \begin{pmatrix} j & K & j \\ m & 0 & -m \end{pmatrix} \approx \sqrt{\frac{1}{2j+1}} P_K\left(\frac{m}{j+\frac{1}{2}}\right), \tag{5.22}$$

Using this expression allows us to replace the discrete quantum numbers m in the $3j$ coefficients by the continuous variable used in the semiclassical model and thereby obtain Eqs. 5.18 and 5.13.

This analysis clearly demonstrates that Eq. 5.22 provides the mathematical justification for the semiclassical model. As Malenda *et al.* [2] discussed, Eq. 5.22 is most accurate for $K \ll j$ and is exact for $K = 0$ and 1. Figure 2.4 showed that it works fairly well even for low j with $K \approx j$.

5.3.1 Selected results for He and Ar collisions with NaK

In Figs. 5.3 and 5.4, we present some typical angular distributions $\mathcal{P}_{jj'}(\theta,\theta')\sin\theta'\,d\theta'$ for He+NaK and Ar+NaK, respectively; we determined the $d_K(j,j')$ quantum mechanically, but classical trajectories could also be used [88]. Each panel of the figures shows a different transition $j \to j'$. Within each panel, angular distributions for several fixed initial θ are shown; each distribution has its own color. For angles not too close to $\theta = 0°$ or 180°, the θ' distributions have a peak when $\theta' = \theta$ and, for a given transition, tend to have a very similar shape and height. Based on the behavior of the $d_K(j,j')$, we were able to derive an analytic approximation to the angular

distribution that accounts for these features, which we will discuss in Section 5.4.1. The angular distribution in Eq. 5.13 satisfies

$$\mathcal{P}_{jj'}(\theta, \theta') = \mathcal{P}_{jj'}(\pi - \theta, \pi - \theta'), \tag{5.23}$$

which accounts for the obvious symmetry of the distributions for $\theta = 45^\circ$ and $\theta = 135^\circ$ in Figs. 5.3 and 5.4. For the same reason, the curves for $\theta = 90^\circ$ are symmetric about $\theta' = 90^\circ$. When $\theta = 0$, Eq. 5.14 shows that the angular distribution is the tipping angle distribution. For He+NaK, the even (right) and odd (left) Δj transitions shown in Fig. 5.3 have probability distributions with a strikingly different character. For Ar+NaK, the difference between the probability distributions for the even and odd Δj transitions shown in Fig. 5.4 is not as striking as it was for He+NaK. We also note that the distributions broaden as the average j decreases for both systems.

Figures 5.5 and 5.6 show a comparison of quantum mechanical distributions of m' levels (points) with the corresponding exact semiclassical distributions (lines) for He+NaK and Ar+NaK, respectively. In these figures, the average j is about 30. In Figs. 5.7 and 5.8, we show another comparison for an average j of about 5. The agreement is quite good, even for low initial j's, which reflects the accuracy of Eq. 5.22. In Fig. 5.7, He+NaK showed large secondary peaks for the Δj odd transitions (left side); the nature of these peaks is not yet known. They are not present for the same transitions for Ar+NaK, as Fig. 5.8 shows.

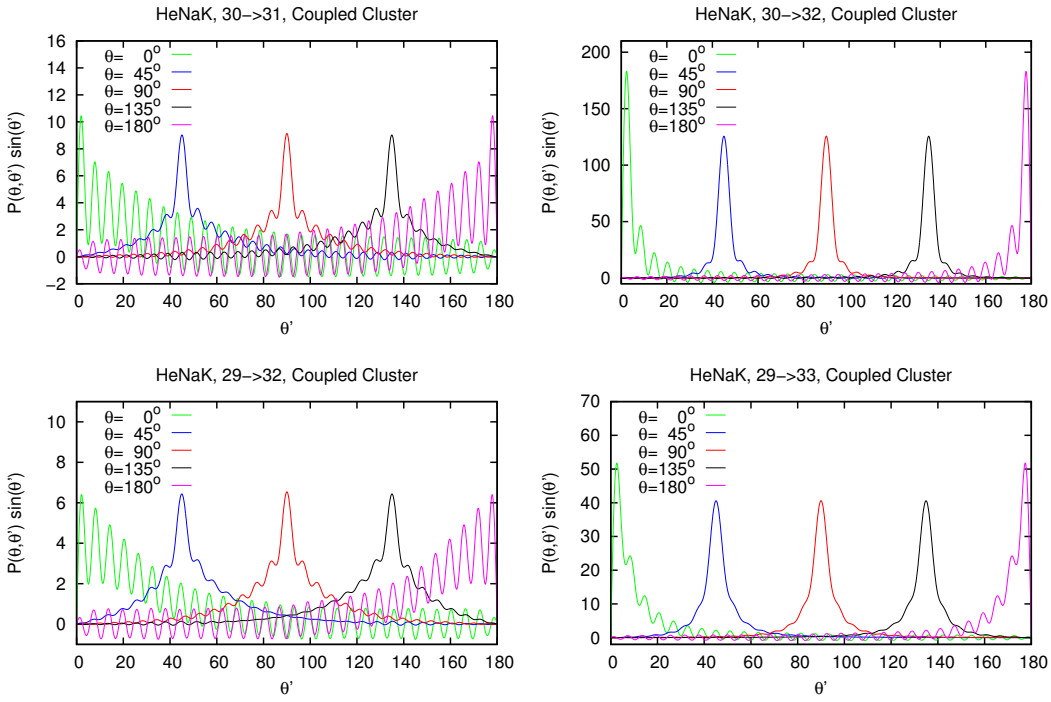

Figure 5.3: Angular distributions for PES II: He. Each panel corresponds to a different transition, and within each panel, distributions of different color correspond to different initial θ. The odd Δj distributions (left) have a different character than the distributions for even Δj (right). Distributions with θ not too close to 0^o or 180^o have a peak where $\theta' = \theta$, and they tend to have the same shape and height for a given transition.

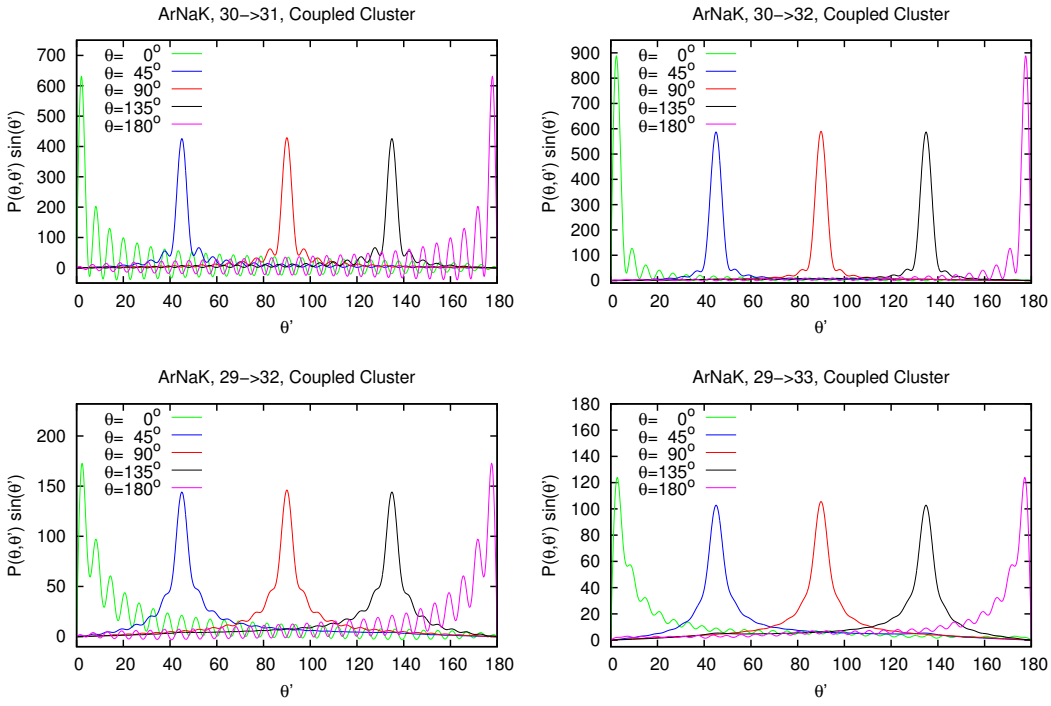

Figure 5.4: Same as Fig. 5.3, but for PES II: Ar. The distributions for odd and even Δj are more similar for Ar+NaK than they are for He+NaK.

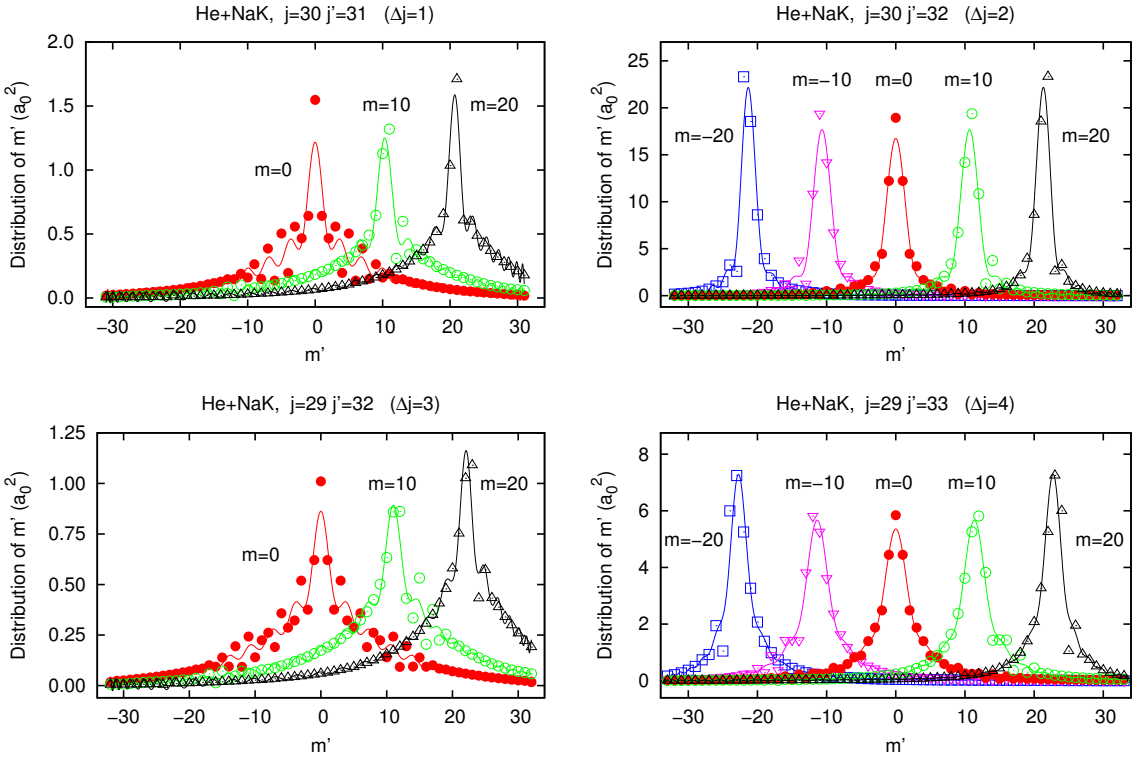

Figure 5.5: Quantum mechanical distributions of m' levels for PES II: He are shown as points, while semiclassical distributions are shown as lines. Each panel shows results for a different transition, and within each panel there are several distributions labelled by their initial m. In all cases, the quantum mechanical and semiclassical results agree very well.

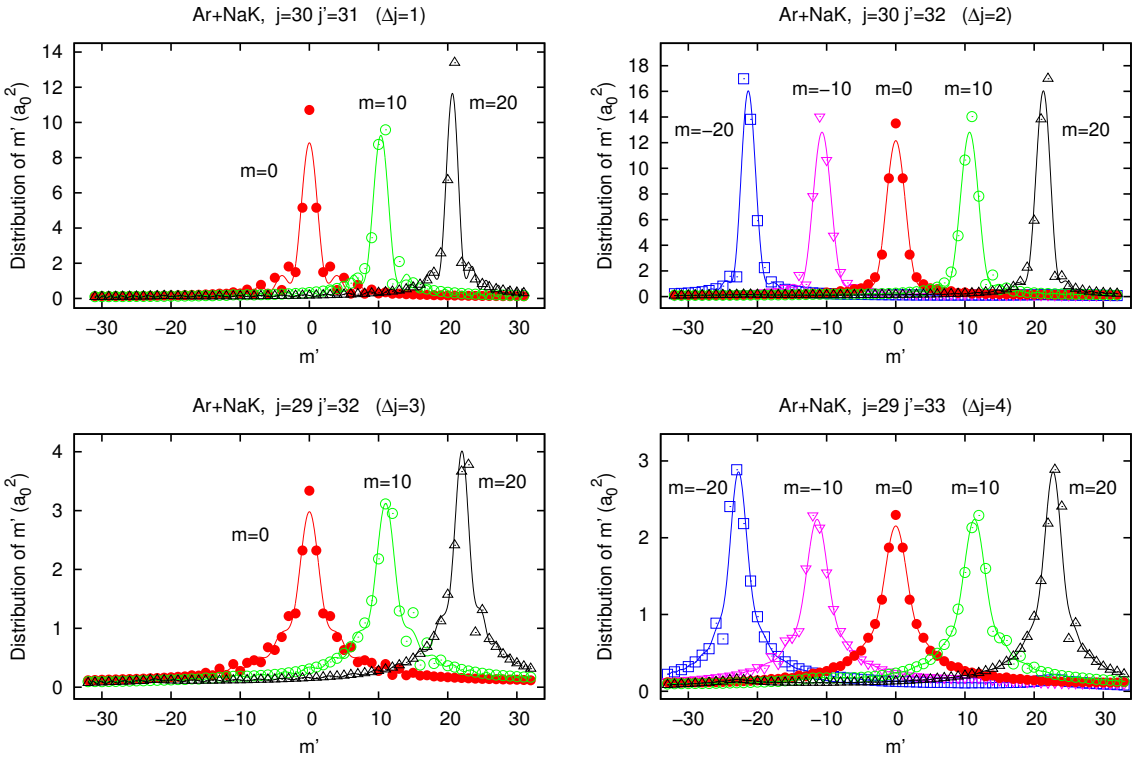

Figure 5.6: Same as Fig. 5.5 but for PES II: Ar. Figure in lower right hand corner reprinted from [3] with permission from Elsevier.

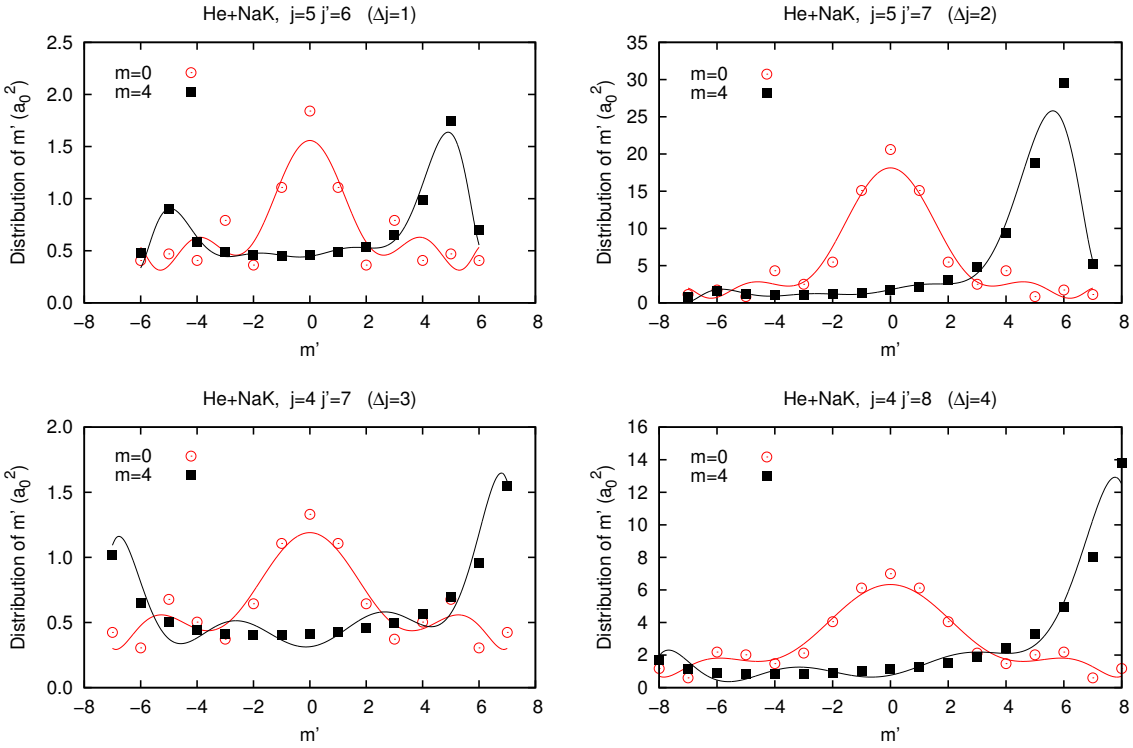

Figure 5.7: Quantum mechanical distributions of m' levels for PES II: He are shown as points and semiclassical distributions as lines. The average j is around 5, and one can see that for each m the semiclassical approximation agrees quite well, even for these low j. The primary peaks of the distributions are for values of m' near where $\theta' = \theta$, and there are large secondary peaks for the Δj odd transitions shown on the left hand side of the figure.

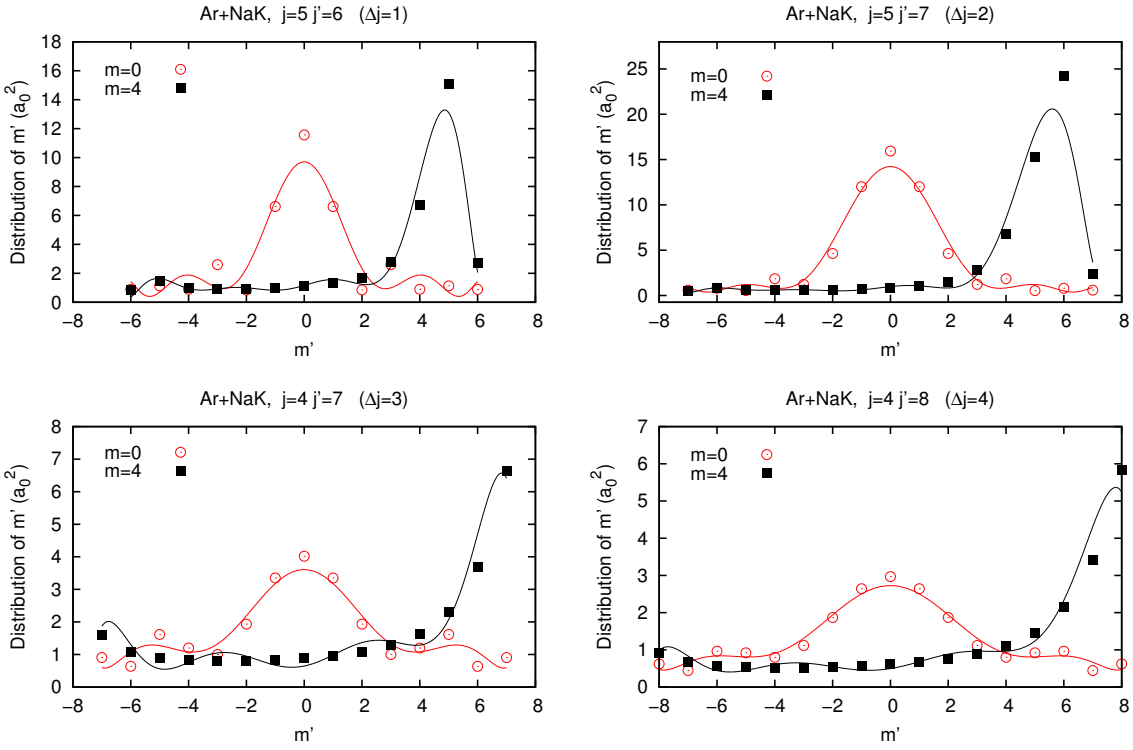

Figure 5.8: Same as Fig. 5.7 but for PES II: Ar. Unlike for He+NaK, there are no large secondary peaks for the Δj odd transitions shown on the left hand side of the figure.

5.4 Analytic results for special cases and comparison with calculations

We have identified two special cases that admit analytic approximations to the distribution of final polar angles θ' (Eq. 5.13). These cases correspond to particular functional forms of $d_K(j, j')$. If $d_K(j, j')$ has an exponential dependence on K, then one can derive a near-Lorentzian angular distribution that is peaked at $\theta' = \theta$ when θ is not too close to 0° or 180°. Several transitions for He+NaK and Ar+NaK can be described by this model. The other special case corresponds to a strong attractive interaction between the molecule and its perturber. This case leads to a near-random distribution of the direction of the final $\mathbf{j}'$, or equivalently to a distribution

of final θ' dominated by the geometrical factor $\sin\theta'$. We present a model system that illustrates this behavior.

5.4.1 Lorentzian polar angle distribution

This section considers the special case that the $d_K(j,j')$ follow an exponential form:

$$d_K(j,j') = Ae^{-\beta K}. \tag{5.24}$$

If we substitute Eq. 5.24 into Eq. 5.13 and extend the upper limit of the sum over K to infinity, then we obtain a closed form expression. Changing the upper limit should be justified as long as the exponential decay constant β is large enough to make $\exp(-\beta K)$ very small for $K > 2j_<$.

By following the steps in Appendix A, one finds

$$\begin{aligned}
\mathcal{P}_{jj'}(\theta,\theta')\sin\theta' &\approx \frac{A\sin\theta'}{\sqrt{[j][j']}}\sum_{K=0}^{\infty}(2K+1)e^{-\beta K}P_K(\cos\theta)P_K(\cos\theta') \\
&= \frac{A}{\sqrt{[j][j']}}\frac{e^{\beta/2}\sinh\beta\sin\theta'}{4\left(\sinh^2\left(\frac{\beta}{2}\right)+\sin^2\left(\frac{\theta-\theta'}{2}\right)\right)^{3/2}} \\
&\quad\times\ {}_2F_1\left(\tfrac{3}{2},\tfrac{1}{2};1;\frac{-\sin\theta\sin\theta'}{\sinh^2\left(\frac{\beta}{2}\right)+\sin^2\left(\frac{\theta-\theta'}{2}\right)}\right),
\end{aligned} \tag{5.25}$$

where ${}_2F_1\left(\cdots\right)$ is a Gauss hypergeometric function and $[n] = 2n+1$. We will show below that for typical values of β, the shape of this function depends primarily on θ/β and θ'/β. Figure 5.9 illustrates this behavior. Except for θ/β and θ'/β less than about one, the distribution is peaked near $\theta' = \theta$.

Now we consider the limiting behavior of Eq. 5.25 for angles θ and θ' not too close to 0° or 180°. For our systems the argument of the hypergeometric function in Eq. 5.25 is then typically a real, negative number with a large magnitude. In that case the asymptotic behavior is

$${}_2F_1(\tfrac{3}{2},\tfrac{1}{2};1;-|x|) \overset{|x|\gg 1}{\approx} \frac{2}{\pi}\left(\frac{1}{1+|x|}\right)^{1/2} \approx \frac{2}{\pi}|x|^{-1/2}, \tag{5.26}$$

where the first form of the asymptotic limit follows from the linear transformation formulas in Abramowitz and Stegun [54] (see §15.3.8); we have confirmed the accu-

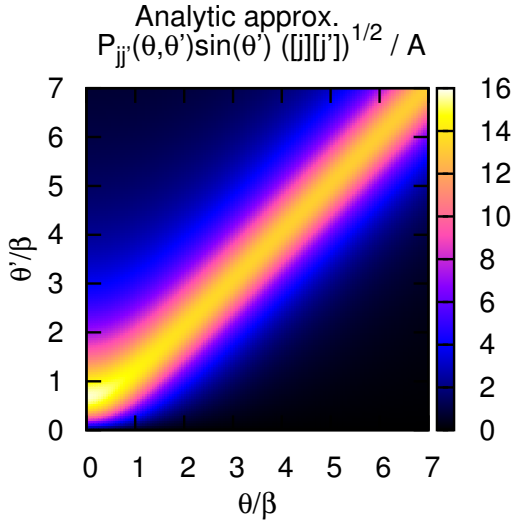

(a)

Figure 5.9: False color plot of Eq. 5.25 (without the factor $A/\sqrt{[j][j']}$) for $\beta = 0.05$. For $\theta = 0$, the function is proportional to the analytic approximation to the tipping angle distribution, with a peak value at $\theta'/\beta = \sqrt{2}/2$ (which we will discuss in a later section). As θ increases, the distribution becomes narrowly peaked at $\theta' = \theta$.

racy of Eq. 5.26 by numerical calculation. By using Eq. 5.26 and assuming β and $\theta' - \theta$ are small, we reduced Eq. 5.25 to the following near-Lorentzian form:

$$\mathcal{P}_{jj'}(\theta,\theta')\sin\theta' \approx \left(\frac{\sin\theta'}{\sin\theta}\right)^{1/2} e^{\beta/2}\frac{2A}{\sqrt{[j][j']}}\left\{\frac{1}{\pi}\frac{\beta}{(\theta'-\theta)^2+\beta^2}\right\} \quad (5.27)$$

$$\approx \left(\frac{\sin\theta'}{\sin\theta}\right)^{1/2}\frac{e^{\beta/2}}{\beta}\frac{2A}{\sqrt{[j][j']}}\left\{\frac{1}{\pi}\frac{1}{\left(\frac{\theta'}{\beta}-\frac{\theta}{\beta}\right)^2+1}\right\} \quad (5.28)$$

The factor in curly brackets in Eq. 5.27 is a Lorentzian centered at $\theta' = \theta$ with a full width half maximum of 2β. This result provides justification *a posteriori* for assuming $(\theta' - \theta) \ll 1$. In addition, $\beta \ll 1$ is well satisfied for the systems we have investigated.

For He+NaK, the $d_K(j, j')$ for many of the even Δj transitions can be fit to a single exponential. A representative example is shown in Fig. 5.10, where the

$d_K(j, j')$ are plotted on a semi-log scale. The plus signs in Fig. 5.10 show the $d_K(j, j')$ for He+NaK for $j = 29$ to $j' = 33$, and the solid line is an exponential fit to the $d_K(29, 33)$. The exponential fits the points fairly well. In other cases, He+NaK transitions with odd Δj were often well approximated by a sum of two exponentials, and for Ar+NaK, the $d_K(j, j')$ were best fit by a sum of two exponentials for all values of Δj. In this situation, Eqs. 5.25 and 5.27 are easily generalized to a sum of terms. The circles in Fig. 5.10 show the $d_K(j, j')$ for Ar+NaK for $j = 28$ to $j' = 33$. For small K, the $d_K(j, j')$ rapidly decay and approximately follow a steep straight line in the plot, or a "fast" exponential. For large K, the $d_K(j, j')$ follow a different straight line in the plot with a more gradual slope, or a "slow" exponential. The dotted line in Fig. 5.10 shows the sum of a fast and a slow exponential. Physically, the exponential decay of the $d_K(j, j')$ means that one is less likely to retain higher moments of the m-distribution. As the average j decreases, we find that the $d_K(j, j')$ decay more rapidly; higher moments are less likely to be preserved for transitions with a smaller j and j'. (We note that the $d_K(j, j')$ do not always decay exponentially; Fig. 5.11 shows an unusual oscillatory structure.)

Figure 5.12 compares the Lorentzian approximations (shown as dashed curves) with the exact semiclassical θ' distributions, Eq. 5.13, (shown as solid curves) for the fits to the $d_K(j, j')$ shown in Fig. 5.10. Results are shown for $\theta = 90°$, but they are similar for other angles not too close to $\theta = 0$ or $180°$. The panel on the left shows the single Lorentzian corresponding to the one-exponential fit to $d_K(29, 33)$ for He+NaK. The Lorentzian agrees reasonably well with the exact semiclassical distribution, and the agreement improves if one includes the extra factors $\sqrt{\sin\theta'/\sin\theta}\exp(\beta/2)$ in Eq. 5.27. The panel on the right shows the sum of the two Lorentzians corresponding to the two-exponential fit to $d_K(28, 33)$ for Ar+NaK, which also agrees well with the exact semiclassical distribution. As with He+NaK, the agreement improves upon inclusion of the extra factors in Eq. 5.27. Also shown in the panel on the right are the separate Lorentzian terms as dotted lines. The narrow Lorentzian is most important at small values of $\theta' - \theta$ and arises from the slow exponential that dominates the large-K behavior of the $d_K(28, 33)$ shown in Fig. 5.10. Conversely, the much broader Lorentzian that dominates the angular

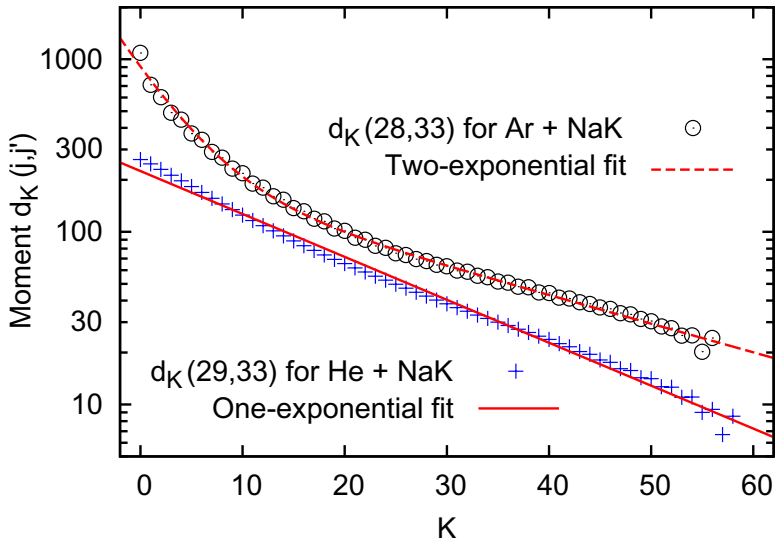

Figure 5.10: Values of $d_K(j, j')$ for fixed transitions $j \to j'$ as a function of K. For PES II: He, the $d_K(j, j')$ for the transition $29 \to 33$ are shown as blue plus signs. The corresponding one-exponential fit is shown as a solid red line. For PES II: Ar, the $d_K(j, j')$ for $28 \to 33$ are shown as black circles, along with the two-exponential fit shown as a dotted red line. The $d_K(j, j')$ for most transitions were best fit by a sum of two exponentials, except for even transitions for He+NaK, which were often best fit by a single exponential. Reprinted from [3] with permission from Elsevier.

distribution for large $\theta' - \theta$ comes from the rapid decay of $d_K(28, 33)$ at small K.

The analytic approximations may provide valuable qualitative understanding of the shape of the polar angle distribution, but a one- or two-exponential fit will not always accurately represent the behavior of the $d_K(j, j')$, as the example in Fig. 5.11 shows. For quantitative results, the exact semiclassical formula Eq. 5.13 is more accurate.

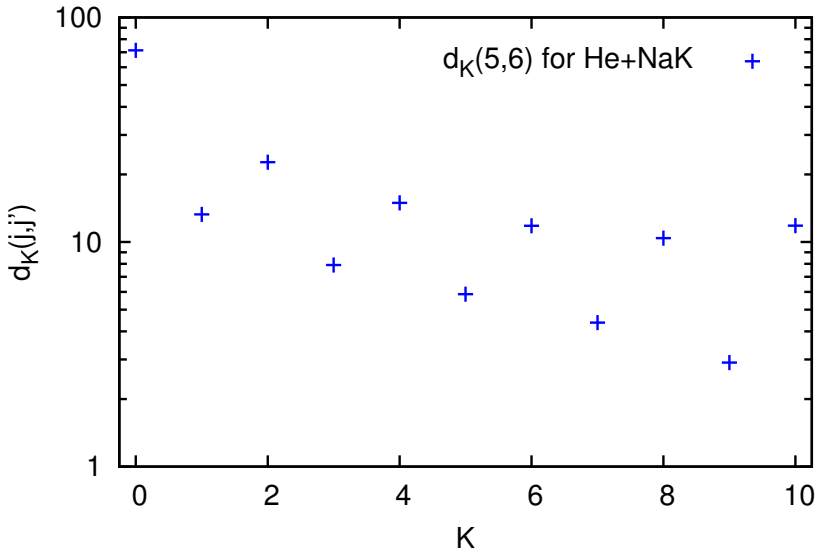

Figure 5.11: Values of $d_K(j, j')$ for PES II: He for the transition $j = 5$ to $j' = 6$ shown on a semi-log scale. For this transition, the $d_K(j, j')$ do not decrease exponentially in K. Instead, there is a propensity to retain even moments of the m distribution after many collisions. The even terms are typically about twice as large as the odd terms.

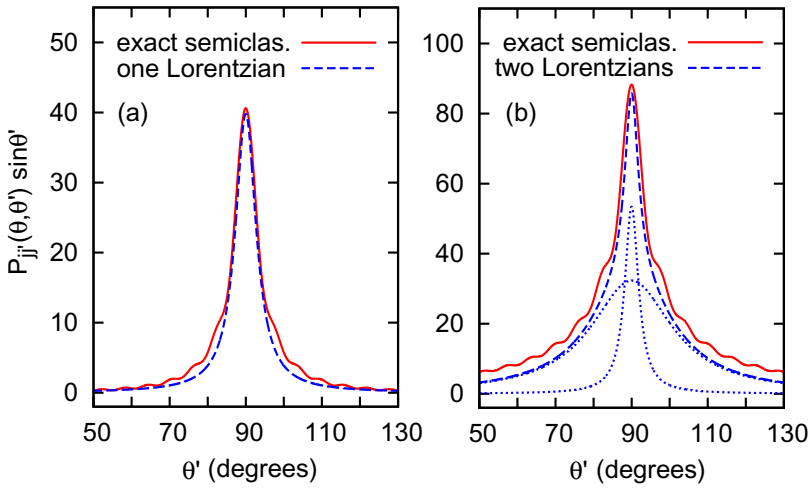

Figure 5.12: Comparison of exact semiclassical distributions, Eq. 5.13, (solid curves) with the Lorentzian approximations to them (dashed curves) for $\theta = 90°$. Each Lorentzian was determined from Eq. 5.27 without the factor $\sqrt{\sin\theta'/\sin\theta}\exp(\beta/2)$. The figure on the left is for PES II: He, and the Lorentzian approximation was determined by using the exponential fit to the $d_K(29, 33)$ shown in Fig. 5.10. The figure on the right is for PES II: Ar, and the dashed curve is the sum of the two Lorentzians (each shown as a dotted curve) corresponding to the two-exponential fit to the $d_K(28, 33)$ shown in Fig. 5.10. In both cases, the Lorentzian approximations agree fairly well with the exact semiclassical distributions, and using the full approximation given by Eq. 5.27 leads to better agreement. Reprinted from [3] with permission from Elsevier.

5.4.2 Random orientation of final j'

If $d_K = d_0\delta_{K0}$, another special case arises, which can be regarded as the $\beta \to \infty$ limit of $d_K(j,j') = Ae^{-\beta K}$. In this special case, the only moment of the m' distribution retained after many collisions is the population, so all m' levels are equally populated, and

$$\sigma(jm \to j'm') = \frac{\sigma(j \to j')}{(2j'+1)}. \tag{5.29}$$

One can confirm Eq. 5.29 by inserting $d_K = d_0\delta_{K0}$ into Eq. 5.19 and using the identity [89]

$$\begin{pmatrix} j & 0 & j \\ m & 0 & -m \end{pmatrix} = (-1)^{2j} \begin{pmatrix} j & j & 0 \\ m & -m & 0 \end{pmatrix} = (-1)^{2j} \frac{(-1)^{j-m}}{\sqrt{2j+1}}, \tag{5.30}$$

as well as the relationship between $\sigma(j \to j')$ and $d_0(j,j')$ given by Eq. 2.139. The semiclassical and quantum mechanical m' distributions are identical in this case, since Eq. 5.22 is exact for $K = 0$:

$$\sigma(jm \to j'm') = \sigma_{\mathrm{sc}}(jm \to j'm'). \tag{5.31}$$

Therefore the angular distribution is

$$\mathcal{P}_{jj'}(\theta,\theta')\sin\theta' = \frac{d_0(j,j')\sin\theta'}{\sqrt{(2j+1)(2j'+1)}} = \frac{k_j^2}{\pi}\frac{\sigma(j \to j')}{2j'+1}\sin\theta', \tag{5.32}$$

which one can confirm from Eq. 5.13 by noting that $P_0(\cdots) = 1$. In this case, the final $\mathbf{j}'$ is equally likely to be oriented in any direction, and the angular distribution is dominated by the geometrical factor $\sin\theta'$.

We were able to realize the special case $d_K = d_0\delta_{K0}$ by choosing a model potential with very deep wells (on the order of 0.16 E_{h}, or about 4.4 eV). To determine the model potential, we started with an analytic fit to a PES for LiCN provided by Essers *et al.* [90]. We started with this fit to ensure that the angular dependence and curvature of the wells in our model potential would be reasonable. We emphasize, however, that our model PES is not intended to be an accurate representation of LiCN. The analytic fit of Essers *et al.* approaches its asymptotic (large R) value very

slowly and would lead to a lengthy scattering calculation. To reduce the amount of computer time involved, we replaced the fit provided by Essers *et al.* with a Morse potential for each angle, with the constraint that each Morse potential have the same asymptotic (large R) value. Figure 5.13 shows the fit of Essers *et al.* (solid line) and the corresponding Morse potential (dashed line) for a fixed Jacobi angle $\theta = 0$ (see Fig. 2.2).

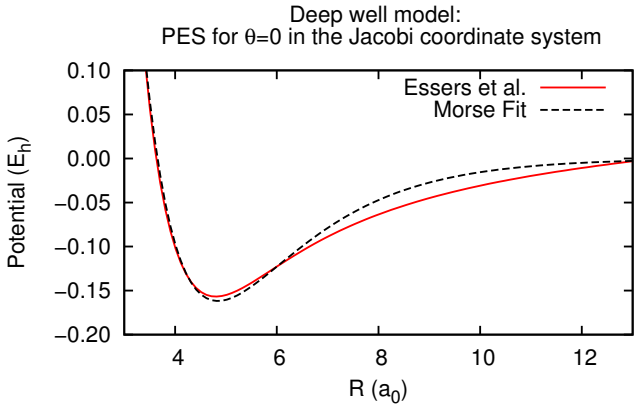

Figure 5.13: A PES with a deep well [90] and the corresponding Morse potential for the collinear geometry C-N-Li. Using Morse potentials for each angle leads to a faster scattering calculation.

Panel (a) of Fig. 5.14 shows the first five Legendre components of our model PES. They are quite different from those of PES II: He, which are shown in Panel (b) on a vertical scale that is ten times smaller than in Panel (a). The angular dependence, determined by components with $n > 0$, is somewhat different; the $n = 2$ component has a well for the model PES but not for He+NaK, and the $n = 1$ components have a different sign for some values of R. The most notable difference, however, is in the $n = 0$ component. The $n = 0$ component of the model PES has a deep well even when R is relatively small, while the $n = 0$ component of the He+NaK PES is repulsive, with a very shallow well at larger R.

We performed scattering calculations using our deep well model PES for a total energy of $E = 0.002\ E_\mathrm{h}$. The rotational energy levels were determined from $E_j = Bj(j+1)$ with the rotational constant $B = 8.655 \times 10^{-6}\ E_\mathrm{h}$ appropriate for

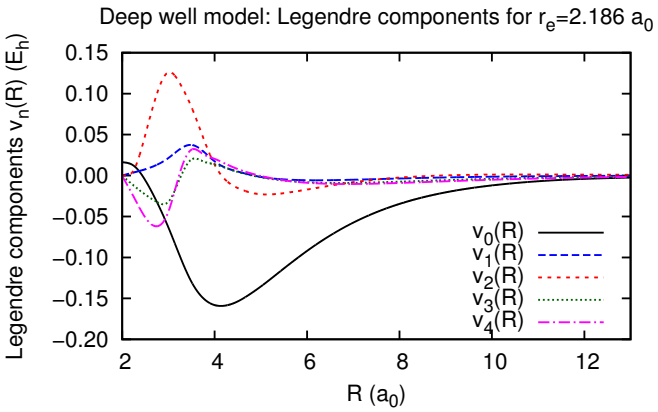

(a)

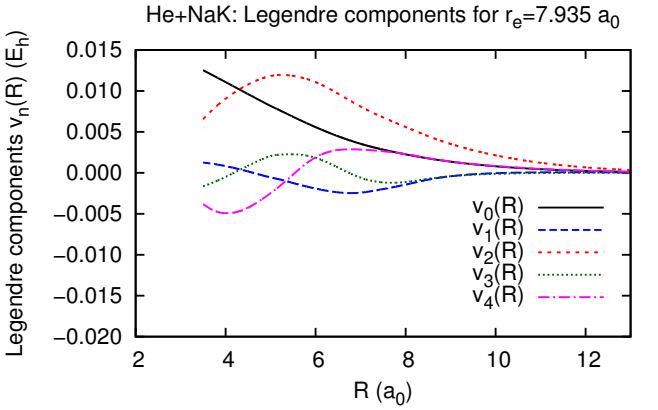

(b)

Figure 5.14: The first five Legendre components of our deep well model PES, shown in Panel (a), and of PES II: He, shown in Panel (b). The vertical scale in Panel (b) is a factor of ten smaller than the vertical scale of Panel (a). The angular dependence is different between the two PESs, since the $n = 2$ component has a well in Panel (a) but not Panel (b), and the $n = 1$ component is positive in Panel (a) and mostly negative in Panel (b). The most significant difference between the two PESs is that the $n = 0$ component of the model PES is deeply attractive even at close range, whereas the $n = 0$ component of PES II: He is mostly repulsive.

CN. Our scattering calculations were performed such that the $d_K(j, j')$ were converged with respect to the different parameters involved in the calculation.

Panel (a) of Fig. 5.15 shows $d_K(j, j')/d_0(j, j')$ for $j = 10$ and $j' = 12$. The value for $K = 1$ is about an order of magnitude smaller than for $K = 0$ and the $d_K(j, j')$ for $K \geq 5$ are negligible. These values approach the special case where $d_K(j, j') = d_0(j, j')\delta_{K0}$, as do the $d_K(j, j')$ for other transitions as well. The quantum mechanical and semiclassical m' distributions are very broad and nearly constant; an example is shown in Panel (b) of Fig. 5.15. Figure 5.16 shows that the corresponding angular distributions for different initial θ are dominated by the factor $\sin\theta'$.

The results are just what one might expect. The attractive well is very deep, so in any collision the atom and the molecule get very close together and interact strongly, randomizing the final m' levels of the molecule.

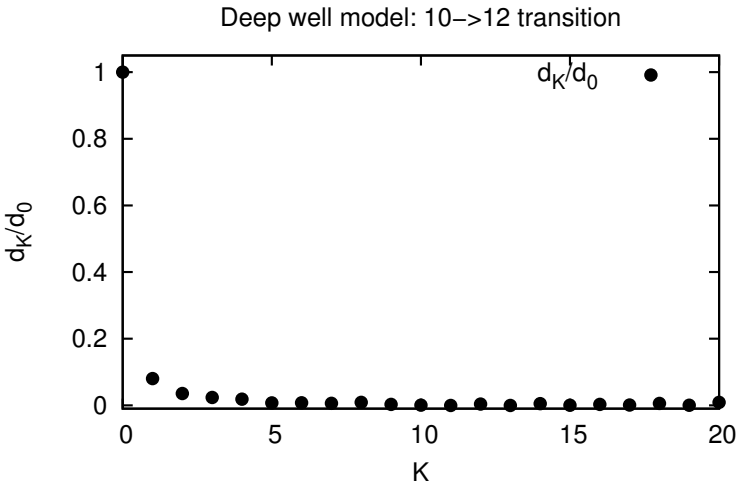

(a)

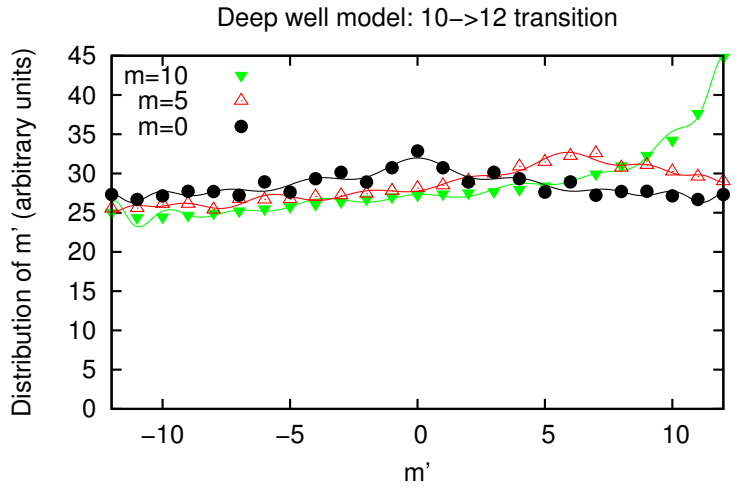

(b)

Figure 5.15: Results of the scattering calculation with the deep well model PES for the transition $j = 10$ to $j' = 12$. Panel (a) shows that $d_K(j, j')/d_0(j, j')$ is approaching the special case where $d_K(j, j') = d_0(j, j')\delta_{K0}$, with only a few small but non-negligible higher moments. Panel (b) shows the corresponding quantum mechanical (points) and semiclassical (lines) m' distributions for $m = 0$, 5 and 10. Both the quantum mechanical and semiclassical m' distributions are fairly constant with respect to m and m', with the distribution for $m = 10$ being the least constant for large m'.

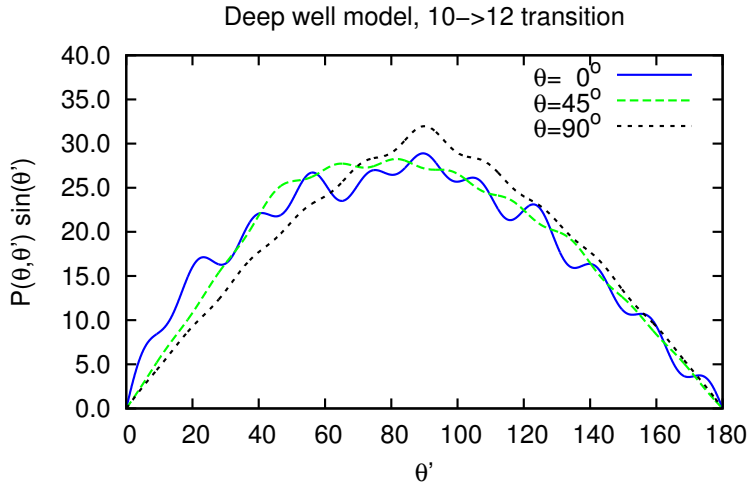

Figure 5.16: Selected angular distributions for the deep well model PES for the transition $j = 10$ to $j' = 12$. The distributions are largely determined by the geometrical factor $\sin\theta'$.

5.4.3 Tipping angle distribution (finite sum)

We have shown that the distribution of final polar angles θ' when $\theta = 0$ is the tipping angle distribution. This result is exact semiclassically, but requires evaluation of the finite sum in Eqs. 5.4 or 5.13. By assuming $d_K \approx Ae^{-\beta K}$ and using the results obtained by extending the upper limit of the sum to infinity, we obtained a simple closed form expression for the tipping angle distribution. In this section, we present additional analysis that allows us to approximate the finite sum as well.

The closed form approximation to the polar angle distribution, Eq. 5.25, can be evaluated for $\theta = 0$ by noting that ${}_2F_1(\frac{3}{2}, \frac{1}{2}; 1; 0) = 1$, which follows from §15.1.1 in A&S [54]. Then the analytic approximation to the tipping angle distribution is

$$\mathcal{P}_{jj'}(0, \theta') \sin\theta' \approx \frac{A}{\sqrt{[j][j']}} \frac{e^{\beta/2} \sinh\beta \sin\theta'}{4\left(\sinh^2(\beta/2) + \sin^2(\theta'/2)\right)^{3/2}}. \tag{5.33}$$

Alternatively, a direct evaluation of Eq. 5.33 is in Appendix B. For small θ' and β, Eq. 5.33 reduces to

$$\mathcal{P}_{jj'}(0, \theta') \sin\theta' \approx \frac{A}{\sqrt{[j][j']}} \frac{e^{\beta/2}}{\beta} \left\{ \frac{2(\theta'/\beta)}{\left[1 + (\theta'/\beta)^2\right]^{3/2}} \right\}. \tag{5.34}$$

The expression in curly brackets depends only on θ'/β and determines the shape of the distribution. The other factors depend on the transition and determine the height. The maximum of Eq. 5.34 occurs at $\theta'/\beta = \sqrt{2}/2 \approx 0.707$; thus β is a characteristic tipping angle.

We were able to determine an analytic approximation to the tipping angle distribution for the case where the $d_K(j, j')$ behave exponentially but with the upper limit of the sum $K = 2j_<$, as in Eq. 5.4, rather than infinity, as was the case for Eq. 5.34. We did this in the following way. First, we approximated the portion of the sum for which $K_0 \leq K \leq \infty$, where K_0 is an arbitrary constant. The steps are

given in Appendix C, and the resulting expression is

$$\frac{A\sin\theta'}{\sqrt{[j][j']}}\sum_{K=K_0}^{\infty}(2K+1)e^{-\beta K}P_K(\cos\theta')\approx$$
$$\frac{2A}{\sqrt{[j][j']}}\left(\frac{2}{\pi}\frac{\sin\theta'}{\beta}\right)^{1/2}\frac{e^{\beta/2}}{\beta}\mathrm{Re}\frac{\exp\left[i\left(\pi/4-\frac{3}{2}\tan^{-1}(\theta'/\beta)\right)\right]\Gamma\left(\frac{3}{2},K_0\left(\beta+i\theta'\right)\right)}{\left(1+(\theta'/\beta)^2\right)^{3/4}}, \tag{5.35}$$

where $\Gamma(a,z)$ denotes the incomplete gamma function. Then, we subtracted Eq. 5.35 from the approximation to the infinite sum, Eq. 5.34, for $K_0 = 2j_< + 1$.

Figure 5.17 shows the analytic approximation given by Eq. 5.34 for He+NaK for $j = 29$ to $j' = 33$ as a solid black curve. Figure 5.17 also shows the corresponding exact semiclassical tipping angle distribution determined by Eq. 5.4 as a blue dashed line (and it passes between the quantum mechanical points shown as solid circles). While the exact semiclassical distribution oscillates in θ'/β, the analytic approximation does not. The analytic approximation to the finite sum for He+NaK for $j = 29$ to $j' = 33$ is the curve labelled "Analytic approx., finite sum" in Fig. 5.17. The analytic approximation to the infinite sum passes between the oscillations in the analytic approximation to the finite sum; the sum to infinity averages out the oscillations. Moreover, the oscillations in both the analytic approximation to the finite sum and the exact semiclassical distribution occur at similar θ'/β. The remaining discrepancy between the analytic approximation to the finite sum and the exact semiclassical distribution is due primarily to the fact that $d_K(29,33)$ is only approximately exponential, since Eq. 5.35 is very accurate for $K_0 = 59$ (as Fig. C.1 in Appendix C demonstrates for this particular value of β).

Eq. 5.34, the infinite sum approximation to the tipping angle distribution, was derived from Eq. 5.25. Eq. 5.25 is the infinite sum approximation to Eq. 5.13, the exact semiclassical polar angle distribution. Even though Eq. 5.34 washes out the oscillations in the exact semiclassical tipping angle distribution, integrals are done over the tipping angle distribution to determine Eq. 5.13, and so the oscillations don't matter much for most angles. This is evidenced by the agreement between the approximate and exact semiclassical polar angle distributions shown in Section 5.4.1,

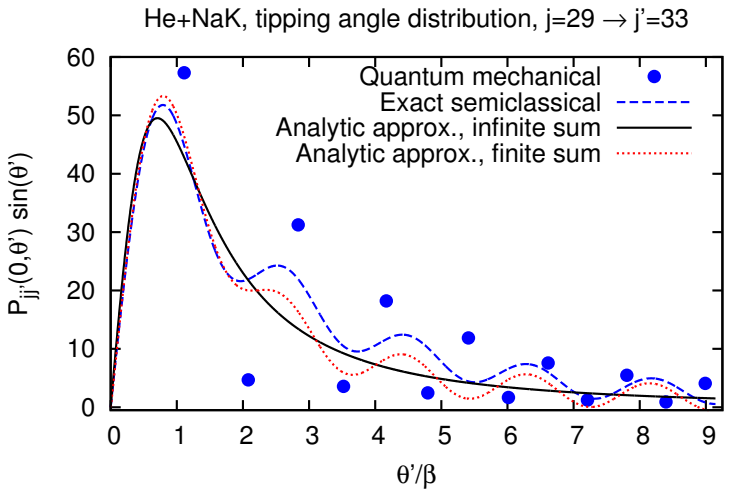

Figure 5.17: Quantum mechanical tipping angle distribution as solid circles and exact semiclassical tipping angle distribution along with two different analytic approximations to it as lines. The exact semiclassical distribution was determined from Eq. 5.4 with $\alpha = \theta'$. The solid curve labelled "Analytic approx., infinite sum" was determined from Eq. 5.34. There are no oscillations present in this curve. The dotted curve labelled "Analytic approx., finite sum" was determined by subtracting Eq. 5.35 from Eq. 5.34. The dotted curve does show oscillations, and they match up reasonably well with the oscillations in the exact semiclassical distribution; the remaining differences are mostly due to the fact that the $d_K(j, j')$ is not exactly exponential. One can see from the solid curve that summing to $K = \infty$ averages out the oscillations in the distribution.

in conjunction with the good agreement between the quantum mechanical and exact semiclassical m' distributions.

Chapter 6

Conclusions and Future Work

6.1 Conclusions

We have performed quantum mechanical scattering calculations of He and Ar collisions with NaK ($A\,^1\Sigma^+$). The work has mainly focused on the $v = 0$ vibrational state of the NaK molecule, although we have estimated cross sections for vibrationally elastic transitions for higher vibrational states. We determined HeNaK and ArNaK PESs by using *ab initio* methods as implemented by GAMESS. Then we performed coupled-channel scattering calculations for $jm \rightarrow j'm'$ cross sections and for the fractions of moments retained after collisions.

We compared our calculated $j \rightarrow j'$ cross sections with experimental data [6]. The absolute magnitudes of the rate constants agree well, and we reproduce the experimentally observed propensity for Δj even transitions. We have correlated the strength of the propensity with the position of a very asymmetric region of the PES that tends to diminish the propensity. We developed a simple model that illustrates that such an asymmetric region may arise near the point where short range forces start to compete with long range forces in the shallow wells. An accurate calculation of the potential in this region is critical because the propensity can be very sensitive to it.

We have also determined fractions of orientation retained by an ensemble of

molecules that experience collisions in a cell environment for He+NaK and Ar+NaK for $v = 0$, and we approximated them for $v = 16$. We compared our results with experimental data for $v = 16$ [4, 5]. For He+NaK, many of our calculated values for $v = 0$ and 16 are within experimental error, while for Ar+NaK we predict that more orientation is retained than the data suggest. In agreement with the experimental data, which is for high average j, we predict that collisions with Ar destroy orientation more effectively than collisions with He. We also predict that He and Ar destroy less orientation as the average j (of j and j') increases, and that for many values of the average j, collisions induced by He with $|\Delta j|$ even are more likely to preserve orientation than with $|\Delta j|$ odd. Future experiments involving transitions with average j in the range 10–20 would test these predictions.

We also developed a semiclassical model for m-changing collisions. The model leads to closed form expressions for semiclassical $jm \to j'm'$ cross sections (where m and m' are continuous variables) and for the corresponding distributions of final polar angles $\theta' = m'/\sqrt{j'(j'+1)}$. The semiclassical cross sections agree well with our calculated quantum mechanical cross sections for He+NaK and Ar+NaK, even for low j. The polar angle distributions for He+NaK and Ar+NaK are typically peaked where $\theta' = \theta$ when θ is not too close to 0 or 180°, in agreement with discussions in the literature that the polar angle θ tends to be conserved for collisions between atoms and small molecules in a cell environment.

We have identified two special cases for which the final polar angle distribution admits analytic approximations. In the first, the distribution is near-Lorentzian and peaked where $\theta' = \theta$ for most angles; the He+NaK and Ar+NaK results exhibited this behavior. In the second case, the m' levels are completely randomized by collisions, and we used a model potential with very deep wells to realize this special case.

6.2 Future Work

A collaboration with Dr. Robert Forrey at Penn State Berks is underway to calculate vibrationally inelastic rate constants using PES II: He and PES II: Ar. Once the calculations are completed, we will compare the results with available experimental data [6].

We would like to identify a system which shows a propensity for Δj even at low Δj and an inverse propensity (for Δj odd) at higher Δj. For this reason, we propose future calculations and experiments for Ne + NaK and Kr + NaK. Another idea would be to apply an external electric field to He+NaK and Ar+NaK to alter the PES and change the exhibited propensity. Comparison between experiment and theory for different electric field strengths would be a sensitive test of the accuracy of the PES.

In addition, we would like to correlate features of the $jm \to j'm'$ cross sections with regions of the PES to understand what governs the transfer of moments. Work should be done to determine if there is a fundamental significance to our empirical observation that for He+NaK and Ar+NaK the $d_K(j, j')$ are often well approximated by one- or two-exponentials in K. When we assumed $d_K(j, j') \approx Ae^{-\beta K}$, our analytical approximations to the polar angle distributions often involved $(\theta' - \theta)/\beta$, indicating this might be a characteristic quantity.

By using a model potential with a very deep well, we showed that a strong interaction can randomize the m' levels of the molecule. Experimental data is available for the strongly interacting system K + NaK ($A\,^1\Sigma^+$) [4–6], and the data show that collisions with K destroy orientation much more effectively than with He or Ar. Future work would involve performing calculations for this system to determine the extent to which the other moments are destroyed; we hypothesize that the m' levels of NaK will be completely randomized by the interaction with K.

For He+NaK and for small j, some of the polar angle distributions show a peak where $\theta' = \theta$ and an unexplained secondary peak near $\theta' = \pi - \theta$. Future experiments might verify these predictions and a model could be developed to understand this behavior.

Should additional computational resources become available, we have identified the most important uncertainties in the calculations to reduce. The cross sections are most sensitive to the PES, and one should focus resources on calculating new surfaces with larger basis sets. Of secondary importance would be determining higher energy cross sections and including more channels in the scattering calculation.

Appendix A

Here are the details of the derivation of Eq. 5.25. We would like to determine an analytic approximation to Eq. 5.13 given the following two assumptions. We assume that $d_K \approx A\exp(-\beta K)$, and that the sum in Eq. 5.13 can be extended from $K = 2j_<$ to infinity without affecting the results very much. Thus we wish to evaluate

$$\mathcal{P}_{jj'}(\theta,\theta')\sin\theta' \approx \frac{A}{\sqrt{[j][j']}} D_\beta(\theta,\theta')\sin\theta', \tag{A.1}$$

where $[n] = 2n+1$ and

$$D_\beta(\theta,\theta') = \sum_{K=0}^{\infty}(2K+1)e^{-\beta K}P_K(\cos\theta)P_K(\cos\theta'). \tag{A.2}$$

To evaluate Eq. A.1, one must determine $D_\beta(\theta,\theta')$. (We note that a simpler equation is evaluated by a similar method in Appendix B.)

Equation A.2 can be evaluated exactly given the following two identities. The first is the generating function for the product of two Legendre polynomials (Eq. 2 in [91]),

$$\sum_{K=0}^{\infty} t^K P_K(\cos\theta)P_K(\cos\theta') = \frac{1}{\sqrt{1+t^2-2t\cos(\theta-\theta')}}\,{}_2F_1\left(\tfrac{1}{2},\tfrac{1}{2};1;\frac{-4t\sin\theta\sin\theta'}{1+t^2-2t\cos(\theta-\theta')}\right), \tag{A.3}$$

where ${}_2F_1(\cdots)$ is a Gauss hypergeometric function. The second identity is the

derivative of Eq. A.3 with respect to t,

$$\sum_{K=1}^{\infty} K t^{K-1} P_K(\cos\theta) P_K(\cos\theta') = \frac{\cos(\theta-\theta')-t}{(1+t^2-2t\cos(\theta-\theta'))^{3/2}} {}_2F_1\left(\tfrac{1}{2},\tfrac{1}{2};1;\frac{-4t\sin\theta\sin\theta'}{1+t^2-2t\cos(\theta-\theta')}\right) + \frac{(t^2-1)\sin\theta\sin\theta'}{(1+t^2-2t\cos(\theta-\theta'))^{5/2}} {}_2F_1\left(\tfrac{3}{2},\tfrac{3}{2};2;\frac{-4t\sin\theta\sin\theta'}{1+t^2-2t\cos(\theta-\theta')}\right), \quad \text{(A.4)}$$

which we determined from Eq. A.3 with the identity (15.2.1 in A&S [54])

$$\frac{d}{dz} {}_2F_1\left(a,b;c;z\right) = \frac{ab}{c} {}_2F_1\left(a+1,b+1;c+1;z\right). \quad \text{(A.5)}$$

Given Eqs. A.3 and A.4, the evaluation of Eq. A.2 can proceed as follows. One starts by expressing Eq. A.2 as

$$D_\beta(\theta,\theta') = 2e^{-\beta}\sum_{K=1}^{\infty} K\left(e^{-\beta}\right)^{K-1} P_K(\cos\theta)P_K(\cos\theta') + \sum_{K=0}^{\infty}\left(e^{-\beta}\right)^{K} P_K(\cos\theta)P_K(\cos\theta'). \quad \text{(A.6)}$$

Then, by letting $t = e^{-\beta}$ and inserting Eqs. A.3 and A.4 into Eq. A.6, one finds that

$$D_\beta(\theta,\theta') = \frac{1-e^{-2\beta}}{(1+e^{-2\beta}-2e^{-\beta}\cos(\theta-\theta'))^{3/2}}\left({}_2F_1\left(\tfrac{1}{2},\tfrac{1}{2};1;z\right) + \frac{z}{2}\,{}_2F_1\left(\tfrac{3}{2},\tfrac{3}{2};2;z\right)\right), \quad \text{(A.7)}$$

where $z = -4e^{-\beta}\sin\theta\sin\theta'/(1+e^{-2\beta}-2e^{-\beta}\cos(\theta-\theta'))$. One can simplify Eq. A.7 with the identification

$${}_2F_1\left(\tfrac{3}{2},\tfrac{3}{2};2;z\right) = \frac{1}{1-z} {}_2F_1\left(\tfrac{1}{2},\tfrac{1}{2};2;z\right), \quad \text{(A.8)}$$

which follows from (15.3.3) in A&S [54],

$${}_2F_1\left(a,b;c;z\right) = (1-z)^{c-a-b} {}_2F_1\left(c-a,c-b;c;z\right). \quad \text{(A.9)}$$

Then by Eq. A.8, the factor $\left({}_2F_1\left(\frac{1}{2},\frac{1}{2};1;z\right) + \frac{z}{2}\,{}_2F_1\left(\frac{3}{2},\frac{3}{2};2;z\right)\right)$ in Eq. A.7 becomes

$${}_2F_1\left(\tfrac{1}{2},\tfrac{1}{2};1;z\right) + \frac{z}{2(1-z)}\,{}_2F_1\left(\tfrac{1}{2},\tfrac{1}{2};2;z\right) = {}_2F_1\left(\tfrac{3}{2},\tfrac{1}{2};1;z\right), \quad \text{(A.10)}$$

where the term on the right hand side follows from (15.2.16) in A&S [54],

$$c(a-(c-b)z)\,{}_2F_1\,(a,b;c;z)+(c-a)(c-b)z\,{}_2F_1\,(a,b;c+1;z) \\ = ac(1-z)\,{}_2F_1\,(a+1,b;c;z)\,. \quad \text{(A.11)}$$

Thus one can reduce Eq. A.7 to an expression that depends on only one hypergeometric function:

$$D_\beta(\theta,\theta') = \frac{(1-e^{-2\beta})}{(1+e^{-2\beta}-2e^{-\beta}\cos(\theta-\theta'))^{3/2}}\,{}_2F_1\left(\tfrac{3}{2},\tfrac{1}{2};1;\frac{-4e^{-\beta}\sin\theta\sin\theta'}{1+e^{-2\beta}-2e^{-\beta}\cos(\theta-\theta')}\right) \quad \text{(A.12)}$$

Equation A.12 can be cast into a more illuminating form by using the trigonometric identities (4.5.1, 4.5.2, 4.5.16, and 4.3.10 in A&S [54])

$$\left(e^{x}-e^{-x}\right) = 2\sinh x \quad \text{(A.13)}$$

$$\left(e^{x}+e^{-x}\right) = 2\cosh x \quad \text{(A.14)}$$

$$\cosh x - 1 = 2\sinh^2(x/2) \quad \text{(A.15)}$$

$$1-\cos x = 2\sin^2(x/2), \quad \text{(A.16)}$$

where x is real, and after some manipulations one finds that

$$D_\beta(\theta,\theta') = \frac{1}{4}\frac{e^{\beta/2}\sinh\beta}{\left(\sinh^2(\frac{\beta}{2})+\sin^2(\frac{\theta-\theta'}{2})\right)^{3/2}}\,{}_2F_1\left(\tfrac{3}{2},\tfrac{1}{2};1;\frac{-\sin\theta\sin\theta'}{\sinh^2(\frac{\beta}{2})+\sin^2(\frac{\theta-\theta'}{2})}\right). \quad \text{(A.17)}$$

Finally, by inserting Eq. A.17 into Eq. A.1, one arrives at Eq. 5.25.

Appendix B

Here are the details of the derivation of Eq. 5.33. We would like to determine an analytic approximation to Eq. 5.4, with $\alpha = \theta'$, given the following two assumptions. We assume that $d_K \approx A\exp(-\beta K)$, and that the sum in Eq. 5.4 can be extended from $K = 2j_<$ to infinity without affecting the results very much. Thus we wish to evaluate

$$\mathcal{P}_{jj'}(0,\theta')\sin\theta' \approx \frac{A}{\sqrt{[j][j']}} D_\beta(0,\theta')\sin\theta', \tag{B.1}$$

where $[n] = 2n+1$ and

$$D_\beta(0,\theta') = \sum_{K=0}^{\infty}(2K+1)e^{-\beta K}P_K(\cos\theta'). \tag{B.2}$$

Equation B.2 can be evaluated exactly given the generating function for the Legendre polynomial (18.12.11 in [92]) and its derivative with respect to t:

$$\sum_{n=0}^{\infty} P_n(x)t^n = \frac{1}{\sqrt{1-2xt+t^2}} \tag{B.3}$$

$$\sum_{n=1}^{\infty} nP_n(x)t^{n-1} = \frac{x-t}{(1-2xt+t^2)^{3/2}}. \tag{B.4}$$

One starts by expressing Eq. B.2 as

$$D_\beta(0,\theta') = 2\sum_{K=1}^{\infty} K(e^{-\beta})^K P_K(\cos\theta') + \sum_{K=0}^{\infty}(e^{-\beta})^K P_K(\cos\theta') \tag{B.5}$$

$$= 2e^{-\beta}\sum_{K=1}^{\infty} K(e^{-\beta})^{(K-1)} P_K(\cos\theta') + \sum_{K=0}^{\infty}(e^{-\beta})^K P_K(\cos\theta'). \tag{B.6}$$

Then, by letting $t = e^{-\beta}$ and inserting Eqs. B.3 and B.4 into Eq. B.6, one finds that

$$D_\beta(0,\theta') = 2e^{-\beta}\left(\frac{\cos\theta' - e^{-\beta}}{(1-2\cos\theta' e^{-\beta}+e^{-2\beta})^{3/2}}\right)+\frac{1}{\sqrt{1-2\cos\theta' e^{-\beta}+e^{-2\beta}}} \quad \text{(B.7)}$$

$$= \frac{1-e^{-2\beta}}{(1-2\cos\theta' e^{-\beta}+e^{-2\beta})^{3/2}} \quad \text{(B.8)}$$

One can simplify Eq. B.8 by rewriting part of the denominator as follows:

$$1-2\cos\theta' e^{-\beta}+e^{-2\beta} = e^{-\beta}\left[\left(e^{\beta}-2+e^{-\beta}\right)+2(1-\cos\theta')\right] \quad \text{(B.9)}$$

$$= e^{-\beta}\left[\left(e^{\beta/2}-e^{-\beta/2}\right)^2+4\sin^2(\theta'/2)\right] \quad \text{(B.10)}$$

$$= 4e^{-\beta}\left[\sinh^2(\beta/2)+\sin^2(\theta'/2)\right], \quad \text{(B.11)}$$

where we have used the identity $1-\cos\theta' = 2\sin^2(\theta'/2)$. Similarly, we can rewrite the numerator of Eq. B.8 as

$$1-e^{-2\beta} = e^{-\beta}\left(e^{\beta}-e^{-\beta}\right) = 2e^{-\beta}\sinh\beta. \quad \text{(B.12)}$$

By inserting Eqs. B.11 and B.12 into Eq. B.8 and rearranging terms, one finds that

$$D_\beta(0,\theta') = \frac{e^{\beta/2}\sinh\beta}{4\left[\sinh^2(\beta/2)+\sin^2(\theta'/2)\right]^{3/2}}. \quad \text{(B.13)}$$

Finally, by inserting Eq. B.13 into Eq. B.1, one arrives at Eq. 5.33. This completes the derivation.

We note that by using the following approximations, valid for $\theta' \ll 1$ and $\beta \ll 1$, we can determine Eq. 5.34 from Eq. 5.33:

$$\sinh\beta \approx \beta \qquad \sinh(\beta/2) \approx \beta/2 \qquad \sin\theta' \approx \theta'. \quad \text{(B.14)}$$

This leads to

$$D_\beta(0,\theta')\sin\theta' \approx \frac{e^{\beta/2}\theta'\beta}{4\left[(\beta/2)^2+(\theta'/2)^2\right]^{3/2}} = \frac{e^{\beta/2}}{\beta}\frac{2(\theta'/\beta)}{\left[1+(\theta'/\beta)^2\right]^{3/2}}. \quad \text{(B.15)}$$

Eq. 5.34 follows from inserting Eq. B.15 into Eq. B.1.

Appendix C

Here are the details of the derivation of Eq. 5.35. We would like to determine an analytic approximation for the portion of Eq. A.2 for which $K \geq K_0$, where K_0 is an arbitrary nonnegative integer. Thus we wish to evaluate

$$\mathcal{T}_\beta(K_0, \theta') = \sin\theta' \sum_{K=K_0}^{\infty} (2K+1) e^{-\beta K} P_K(\cos\theta'). \tag{C.1}$$

There is a factor of $A/\sqrt{[j][j']}$ which we have omitted in Eq. C.1 for clarity; we will multiply our final result for $\mathcal{T}_\beta(K_0, \theta')$ by this factor to determine Eq. 5.35.

We can evaluate Eq. C.1 approximately by noting that for large K, the Legendre polynomial behaves approximately as (8.10.7 in A&S [54])

$$P_K(\cos\theta') = \frac{\Gamma(K+1)}{\Gamma(K+\frac{3}{2})} \left(\frac{2}{\pi \sin\theta'}\right)^{1/2} \cos\left((K+\tfrac{1}{2})\theta' - \pi/4\right) + O(K^{-1}). \tag{C.2}$$

By inserting Eq. C.2 into Eq. C.1 and using

$$\frac{\Gamma(K+1)}{\Gamma(K+\frac{3}{2})} = \frac{2}{\sqrt{\pi}} \prod_{j=1}^{K} \frac{j}{j+\frac{1}{2}} \approx \frac{1}{\sqrt{K+1}}, \tag{C.3}$$

which follows from the asymptotic formula (6.1.39) in [54], along with

$$\frac{2K+1}{\sqrt{K+1}} = \frac{2(K+\frac{1}{2})}{\sqrt{(K+\frac{1}{2})+\frac{1}{2}}} \approx 2\sqrt{K+\tfrac{1}{2}}, \tag{C.4}$$

one finds that

$$\mathcal{T}_\beta(K_0,\theta') = 2\sqrt{\frac{2\sin\theta'}{\pi}}\sum_{K=K_0}^{\infty}\sqrt{K+\tfrac{1}{2}}\,e^{-\beta K}\cos\big((K+\tfrac{1}{2})\theta'-\pi/4\big) \quad \text{(C.5)}$$

$$= 2\sqrt{\frac{2\sin\theta'}{\pi}}e^{\beta/2}\sum_{K=K_0}^{\infty}\sqrt{K+\tfrac{1}{2}}e^{-\beta(K+1/2)}\cos\big((K+\tfrac{1}{2})\theta'-\pi/4\big) \quad \text{(C.6)}$$

This sum may be interpreted as the numerical evaluation of an integral over x using finite steps. Each interval from $x = K$ to $x = K + 1$ is multiplied by the functional value at the center of each step, $x = K + 1/2$. (See the extended midpoint rule, Eq. 4.1.19 in [93], and note the step size $h = 1$.) Therefore we take

$$\mathcal{T}_\beta(K_0,\theta') = 2\sqrt{\frac{2\sin\theta'}{\pi}}\,e^{\beta/2}\int_{K_0}^{\infty}\sqrt{x}\,e^{-\beta x}\cos(\theta' x-\pi/4)\,dx \quad \text{(C.7)}$$

For later use it will be convenient to change the variable of integration to $y = \beta x$. Then we have

$$\mathcal{T}_\beta(K_0,\theta') = 2\sqrt{\frac{2}{\pi}\frac{\sin\theta'}{\beta}}\,\frac{e^{\beta/2}}{\beta}\int_{\beta K_0}^{\infty}\sqrt{y}\,e^{-y}\cos\left(\frac{\theta'}{\beta}y-\pi/4\right)\,dy \quad \text{(C.8)}$$

$$= 2\sqrt{\frac{2}{\pi}\frac{\sin\theta'}{\beta}}\,\frac{e^{\beta/2}}{\beta}\int_{\beta K_0}^{\infty}\sqrt{y}\,e^{-y}\left(\frac{\sin\left(\frac{\theta'}{\beta}y\right)}{\sqrt{2}}+\frac{\cos\left(\frac{\theta'}{\beta}y\right)}{\sqrt{2}}\right)\,dy \quad \text{(C.9)}$$

This integral can be evaluated by using 3.944.2 and 3.944.4 of G&R [94]:

$$\int_u^{\infty} x^{\mu-1}e^{-\beta x}\sin(\delta x)\,dx =$$

$$\frac{i}{2}(\beta+i\delta)^{-\mu}\Gamma(\mu,(\beta+i\delta)u)-\frac{i}{2}(\beta-i\delta)^{-\mu}\Gamma(\mu,(\beta-i\delta)u) \quad \text{(C.10)}$$

$$\int_u^{\infty} x^{\mu-1}e^{-\beta x}\cos(\delta x)\,dx =$$

$$\frac{1}{2}(\beta+i\delta)^{-\mu}\Gamma(\mu,(\beta+i\delta)u)+\frac{1}{2}(\beta-i\delta)^{-\mu}\Gamma(\mu,(\beta-i\delta)u), \quad \text{(C.11)}$$

which are valid for $\mathrm{Re}\,\beta > |\mathrm{Im}\,\delta|$, and where $\Gamma(a,z)$ denotes the upper incomplete gamma function. We emphasize that the β in Eqs. C.10 and C.11 is not the same β as in $d_K(j,j') \approx A\exp(-\beta K)$.

By using Eqs. C.10 and C.11 to evaluate the integral in Eq. C.9, we find

$$\mathcal{T}_\beta(K_0,\theta') = \frac{2}{\sqrt{2}}\sqrt{\frac{2}{\pi}\frac{\sin\theta'}{\beta}}\,\frac{e^{\beta/2}}{\beta}\left[\frac{1+i}{2}\left(1+i\frac{\theta'}{\beta}\right)^{-3/2}\Gamma\left(\tfrac{3}{2},\left(1+i\frac{\theta'}{\beta}\right)\beta K_0\right)\right.$$
$$\left.+\frac{1-i}{2}\left(1-i\frac{\theta'}{\beta}\right)^{-3/2}\Gamma\left(\tfrac{3}{2},\left(1-i\frac{\theta'}{\beta}\right)\beta K_0\right)\right]. \quad \text{(C.12)}$$

By using $\Gamma(\frac{3}{2},z^*) = (\Gamma(\frac{3}{2},z))^*$, we find that the term in square brackets in Eq. C.12 is the sum of a complex number and its complex conjugate. Since $\mathrm{Re}(z) = (z+z^*)/2$, one can express Eq. C.12 as

$$\mathcal{T}_\beta(K_0,\theta') = \frac{2}{\sqrt{2}}\sqrt{\frac{2}{\pi}\frac{\sin\theta'}{\beta}}\,\frac{e^{\beta/2}}{\beta}\mathrm{Re}\left[\frac{(1+i)\,\Gamma\left(\frac{3}{2},\left(1+i\frac{\theta'}{\beta}\right)\beta K_0\right)}{\left(1+i\frac{\theta'}{\beta}\right)^{3/2}}\right]. \quad \text{(C.13)}$$

Then, by noting that $\sqrt{2}\,e^{i\pi/4} = (1+i)$, one can rewrite Eq. C.13 as

$$\mathcal{T}_\beta(K_0,\theta') = 2\sqrt{\frac{2}{\pi}\frac{\sin\theta'}{\beta}}\,\frac{e^{\beta/2}}{\beta}\mathrm{Re}\left[\frac{e^{i\pi/4}\Gamma\left(\frac{3}{2},\left(1+i\frac{\theta'}{\beta}\right)\beta K_0\right)}{\left(1+i\frac{\theta'}{\beta}\right)^{3/2}}\right]. \quad \text{(C.14)}$$

Part of the denominator of Eq. C.14 can be written as

$$\left(1+i\frac{\theta'}{\beta}\right)^{3/2} = \left(1+\left(\frac{\theta'}{\beta}\right)^2\right)^{3/4}\exp\left(i\left(\tfrac{3}{2}\tan^{-1}\left(\frac{\theta'}{\beta}\right)\right)\right), \quad \text{(C.15)}$$

which one can show by utilizing the relationships

$$\left(e^{ix}\right)^b = (\cos x + i\sin x)^b \quad \text{(C.16)}$$
$$\cos(\tan^{-1}(a)) = \frac{1}{\sqrt{a^2+1}} \quad \text{(C.17)}$$
$$\sin(\tan^{-1}(a)) = \frac{a}{\sqrt{a^2+1}} \quad \text{(C.18)}$$

Finally, by inserting Eq. C.15 into Eq. C.14, one finds that

$$\mathcal{T}_\beta^{\text{approx}}(K_0,\theta') = 2\sqrt{\frac{2}{\pi}\frac{\sin\theta'}{\beta}}\frac{e^{\beta/2}}{\beta}\text{Re}\frac{\exp\left[i\left(\pi/4-\frac{3}{2}\tan^{-1}(\theta'/\beta)\right)\right]\Gamma\left(\frac{3}{2},K_0\left(\beta+i\theta'\right)\right)}{\left(1+(\theta'/\beta)^2\right)^{3/4}} \tag{C.19}$$

By multiplying Eq. C.19 by $A/\sqrt{[j][j']}$, we arrive at Eq. 5.35, which completes the derivation. When $K_0 = 0$, the incomplete gamma function $\Gamma(a,0)$ reduces to the gamma function $\Gamma(a)$. By using this fact and noting that

$$\Gamma\left(\tfrac{3}{2}\right) = \frac{\sqrt{\pi}}{2}, \tag{C.20}$$

one finds that

$$\mathcal{T}_\beta^{\text{approx}}(0,\theta') = \frac{e^{\beta/2}}{\beta}\sqrt{\frac{2\sin\theta'}{\beta}}\,\frac{\cos\left(\pi/4-\frac{3}{2}\tan^{-1}(\theta'/\beta)\right)}{\left(1+(\theta'/\beta)^2\right)^{3/4}}. \tag{C.21}$$

Now we consider the accuracy of Eq. C.19, which approximates the sum of terms in Eq. C.1 from $K = K_0$ to ∞. We already know, from Eq. B.15, the exact sum for the case $K_0 = 0$. Therefore the exact sum from $K = 0$ to ∞ should be approximately equal to the explicit sum of the first K_0 terms, plus the approximate sum of all the rest. We can write this condition as follows:

$$\begin{aligned}\frac{2(\theta'/\beta)}{\left[1+(\theta'/\beta)^2\right]^{3/2}} &\approx \beta e^{-\beta/2}\sin\theta'\sum_{K=0}^{K_0-1}(2K+1)e^{-\beta K}P_K(\cos\theta') \\ &+ 2\sqrt{\frac{2}{\pi}\frac{\sin\theta'}{\beta}}\text{Re}\frac{\exp\left[i\left(\pi/4-\frac{3}{2}\tan^{-1}(\theta'/\beta)\right)\right]\Gamma\left(\frac{3}{2},K_0\left(\beta+i\theta'\right)\right)}{\left(1+(\theta'/\beta)^2\right)^{3/4}}\end{aligned} \tag{C.22}$$

We have scaled the terms in Eq. C.22 by dropping the factor $e^{\beta/2}/\beta$ from Eqs. B.15 and C.19 and multiplying the discrete sum above by $\beta e^{-\beta/2}$. The sum in Eq. C.22 should be understood to be zero if $K_0 = 0$. We can assess the accuracy of Eq. C.19 by evaluating the right hand side of Eq. C.22 for different values of K_0 and comparing with the exact result on the left hand side. The comparison is shown in Fig. C.1 for $\beta = 0.057$. We plot several distributions as a function of θ/β, because the left hand side of Eq. C.22 depends only on θ'/β, as does the right hand side for $K_0 = 0$

(assuming $\sin\theta' \approx \theta'$). Figure C.1 shows that the approximation is reasonable even for $K_0 = 0$ and gets progressively better as K_0 increases. The agreement is quite good for $K_0 = 10$ and nearly exact for $K_0 = 20$.

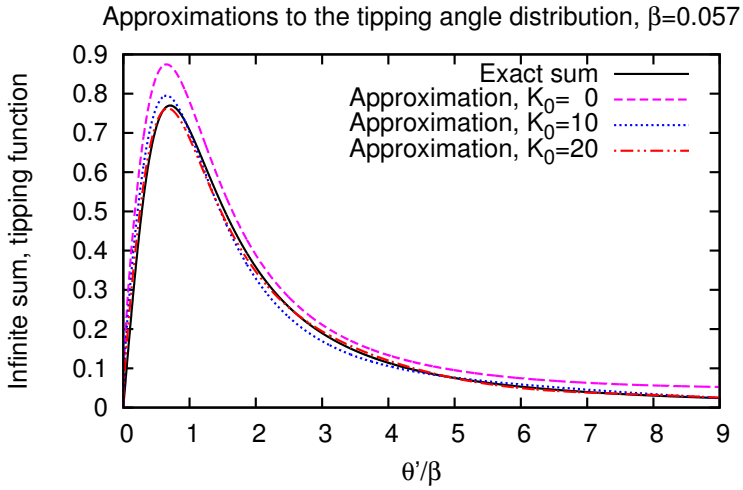

Figure C.1: Comparison of the exact infinite sum for the tipping function (the left hand side of Eq. C.22) with approximations based on using several different values of K_0 to evaluate the right hand side of Eq. C.22.

Bibliography

[1] R. F. Malenda, Ph.D. thesis, Lehigh University, 2012.

[2] R. F. Malenda, T. J. Price, J. Stevens, S. L. Uppalapati, A. Fragale, P. M. Weiser, A. Kuczala, D. Talbi, and A. P. Hickman, "Theoretical Calculations of Rotationally Inelastic Collisions of He with NaK ($A\,^1\Sigma^+$): Transfer of Population, Orientation, and Alignment", J. Chem. Phys. **142**, 224301 (12 pages) (2015).

[3] T. J. Price, A. C. Towne, D. Talbi, and A. P. Hickman, "Semiclassical Model for the Distribution of Final Polar Angles and m' States in Rotationally Inelastic Collisions", Chem. Phys. Lett. **645**, 180–186 (2016).

[4] C. M. Wolfe, S. Ashman, J. Bai, B. Beser, E. H. Ahmed, A. M. Lyyra, and J. Huennekens, "Collisional transfer of population and orientation in NaK", J. Chem. Phys. **134**, 174301 (2011).

[5] J. A. Jones, Ph.D. thesis, Lehigh University, 2015.

[6] K. M. Richter, Ph.D. thesis, Lehigh University, 2016.

[7] A. Ross, R. Clements, and R. Barrow, "The $A(2)\,^1\Sigma^+$ State of NaK", J. Mol. Spectrosc. **127**, 546–548 (1988).

[8] S. Magnier, M. Aubert-Frecon, and P. Millie, "Potential Energies, Permanent and Transition Dipole Moments for Numerous Electronic Excited States of NaK", J. Mol. Spect. **200**, 96–103 (2000).

[9] G. Herzberg, in *Molecular Spectra and Molecular Structure*, 2nd ed. (Van Nostrand Reinhold Company, New York, 1950), Vol. I. Spectra of Diatomic Molecules, pp. 131–132.

[10] C. W. McCurdy and W. H. Miller, "Interference effects in rotational state distributions: propensity and inverse propensity", J. Chem. Phys. **67**, 463 (1977).

[11] M. H. Alexander and S. L. Davis, "M dependence in rotationally inelastic collisions in cell experiments: Implications of an irreducible tensor expansion for molecules in $^1\Sigma$ electronic states", J. Chem. Phys. **78**, 6754–6762 (1983).

[12] J. Derouard, "Reorientation, polarization, and scaling laws in rotational transfer experiments", Chem. Phys. **84**, 181–192 (1984).

[13] K. Richter, T. Price, J. Jones, C. Faust, A. P. Hickman, J. Huennekens, R. F. Malenda, A. J. Ross, and P. Crozet, Rotationally inelastic collisions of He and Ar with NaK: Theory and Experiment, 2014, poster presented at the 2014 DAMOP Meeting.

[14] W. Demtroder, in *Laser Spectroscopy: Experimental Techniques*, fourth ed. (Springer, Berlin, Germany, 2008), Vol. 2, pp. 230–231.

[15] W. Demtroder, in *Laser Spectroscopy: Experimental Techniques*, fourth ed. (Springer, Berlin, Germany, 2008), Vol. 2, pp. 58–69.

[16] W. Demtroder, in *Laser Spectroscopy: Experimental Techniques*, fourth ed. (Springer, Berlin, Germany, 2008), Vol. 2, pp. 247–250.

[17] A. M. Arthurs and A. Dalgarno, "Theory of scattering by a rigid rotator", Proc. Roy. Soc. (London) Series A, Mathematical and Physical Sciences **256**, 540–551 (1960).

[18] M. Born and J. R. Oppenheimer, "On the Quantum Theory of Molecules", Ann. Physik **84**, 458 (1927), translated by S. M. Blinder in 1998, http://www.chm.bris.ac.uk/pt/manby/papers/bornop.pdf.

[19] M. Born, Goett. Nachr. Math. Phys. Kl. **6**, 1 (1951).

[20] M. Born and K. Huang, in *Dynamical Theory of Crystal Lattices* (Oxford at the Clarendon Press, Oxford, 1954), pp. 406–407.

[21] T. Jecko, "On the mathematical treatment of the Born-Oppenheimer approximation", J. Math. Phys. **55**, 053504 (26 pages) (2014).

[22] C. A. Mead and D. G. Truhlar, "Conditions for the definition of a strictly diabatic electronic basis for molecular systems", J. Chem. Phys. **77**, 6090–6098 (1982).

[23] M. A. Morrison, T. L. Estle, and N. F. Lane, in *Quantum States of Atoms, Molecules, and Solids* (Prentice Hall, Inc., Englewood Cliffs, New Jersey, 1976), pp. 267–272.

[24] D. G. Federov, S. Koseki, M. W. Schmidt, and M. S. Gordon, "Spin-orbit coupling in molecules: chemistry beyond the adiabatic approximation", Int. Rev. Phys. Chem. **22**, 551–592 (2003).

[25] John A. Pople, "Nobel Lecture: Quantum chemical models", Rev. Mod. Phys. **71**, 1267–1274 (1999).

[26] A. Szabo and N. Ostlund, *Modern Quantum Chemistry: Introduction to Advanced Electronic Structure Theory*, revised ed. (McGraw-Hill, Inc., New York, 1989).

[27] W. J. Hehre, L. Radom, P. V. R. Schleyer, and J. A. Pople, *Ab initio Molecular Orbital Theory* (John Wiley & Sons , Inc., New York, 1986).

[28] D. A. McQuarrie, *Quantum Chemistry* (University Science Books, Mill Valley, CA, 1983).

[29] P. G. Szalay, T. Muller, G. Gidofalvi, H. Lischka, and R. Shepard, "Multiconfiguration self-consistent field and multireference configuration interaction methods and applications", Chem. Rev. **112**, 108–181 (2012).

[30] M. W. Schmidt and M. S. Gordon, "The construction and interpretation of MCSCF wavefunctions", Ann. Rev. Phys. Chem. **49**, 233–266 (1998).

[31] J. F. Stanton and R. J. Bartlett, "The equation of motion coupled-cluster method. A systematic biorthogonal approach to molecular excitation energies, transition probabilities, and excited state properties", J. Chem. Phys. **98**, 7029–7039 (1993).

[32] K. Kowalski and P. Piecuch, "New coupled-cluster methods with singles, doubles, and noniterative triples for high accuracy calculations of excited electronic states", J. Chem. Phys. **120**, 1715–1738 (2004).

[33] W. J. Hehre, R. Ditchfield, and J. A. Pople, "Self-consistent molecular orbital methods. XII. Further extensions of Gaussian-type basis sets for use in molecular orbital studies of organic molecules", J. Chem. Phys. **56**, 2257–2261 (1972).

[34] J. D. Dill and J. A. Pople, "Self-consistent molecular orbital methods. XV. Extended Gaussian-type basis sets for lithium, beryllium, and boron", J. Chem. Phys. **62**, 2921–2923 (1975).

[35] M. M. Francl, W. J. Pietro, W. J. Hehre, J. S. Binkley, M. S. Gordon, D. J. DeFrees, and J. A. Pople, "Self-consistent molecular orbital methods. XXIII. A polarization-type basis set for second-row elements", J. Chem. Phys. **77**, 3654–3665 (1982).

[36] V. A. Rassolov, J. A. Pople, M. A. Ratner, and T. L. Windus, "6-31G* basis set for atoms K through Zn", J. Chem. Phys. **109**, 1223–1229 (1998).

[37] P. C. Hariharan and J. A. Pople, "The influence of polarization functions on molecular orbital hydrogenation energies", Theoret. Chimica Acta **28**, 213–222 (1973).

[38] J. K. L. MacDonald, "Successive Approximations by the Rayleigh-Ritz Variation Method", Phys. Rev. **43**, 830–833 (1933).

[39] A. J. Stone, in *The Theory of Intermolecular Forces* (Oxford University Press, New York, 1996), Vol. International Series of Monographs on Chemistry, 32, p. 69.

[40] C. C. J. Roothaan, "New developments in molecular orbital theory", Rev. Mod. Phys. **23**, 69–89 (1951).

[41] E. Apra and K. Kowalski, "Implementation of high-order multireference coupled-cluster methods on Intel many integrated core architecture", J. Chem. Theory Comput. **12**, 1129–1138 (2016).

[42] M. Nooijen, O. Demel, D. Datta, L. Kong, K. R. Shamasundar, V. Lotrich, L. M. Huntington, and F. Neese, "Communication: Multireference equation of motion coupled cluster: A transform and diagonalize approach to electronic structure", J. Chem. Phys. **140**, 081102 (5 pages) (2014).

[43] C. D. Sherrill, Counterpoise Correction and Basis Set Superposition Error, http://vergil.chemistry.gatech.edu/notes/cp.pdf, accessed: 07/14/2016.

[44] B. Brauer, M. K. Kesharwani, and J. M. L. Martin, "Some observations on counterpoise corrections for explicitly correlated calculations on noncovalent interactions", J. Chem. Theory Comput. **10**, 3791–3799 (2014).

[45] S. F. Boys and F. Bernardi, "The calculation of small molecular interactions by the difference of separate total energies. Some procedures with reduced errors.", Molec. Phys. **19**, 553–566 (1970).

[46] R. T Pack, "van der Waals coefficients through C_8 for atom-linear molecule interactions. I. CO_2-noble gas systems", J. Chem. Phys. **64**, 1659 (1976).

[47] I. G. Kaplan, in *Intermolecular Interactions: Physical Picture, Computational Methods and Model Potentials* (John Wiley & Sons, Ltd., West Sussex, England, 2006), pp. 11–13 and 319–323.

[48] E. Merzbacher, in *Quantum Mechanics* (John Wiley & Sons, Inc., New York, 1998), Vol. 3, p. 283.

[49] D. J. Griffiths, in *Introduction to Quantum Mechanics*, 2nd ed. (Pearson Education, Inc., Upper Saddle River, NJ, 2005), pp. 394–420.

[50] A. Das and A. C. Melissinos, in *Quantum Mechanics: A Modern Introduction* (Gordon and Breach Science Publishers, New York, New York, 1988), pp. 477–560.

[51] E. Merzbacher, in *Quantum Mechanics* (John Wiley & Sons, Inc., New York, 1998), Vol. 3, pp. 278–315 and 517–535.

[52] A. Messiah, in *Quantum Mechanics* (John Wiley & Sons, Inc., New York, 1962), Vol. 2, pp. 801–875.

[53] J. C. Light, in *Atom-Molecule Collision Theory*, edited by R. B. Bernstein (Plenum Press, New York, New York, 1979), Vol. 2, Chap. 6, pp. 239–259.

[54] M. Abramowitz and I. A. Stegun, *Handbook of Mathematical Functions with Formulas, Graphs, and Mathematical Tables* (Dover Publications, Inc., New York, 1965).

[55] J. M. Hutson, "An Introduction to the Dynamics of Van der Waals Molecules", Advances in Molecular Vibrations and Collision Dynamics 1A **1**, J. M. Hutson (1990), https://community.dur.ac.uk/j.m.hutson/VdWdynamics-90.pdf.

[56] D. Secrest, in *Atom-Molecule Collision Theory*, edited by R. B. Bernstein (Plenum Press, New York, New York, 1979), Vol. 2, Chap. 8, pp. 265–301.

[57] I. C. Percival and M. J. Seaton, "The partial wave theory of electron-hydrogen atom collisions", Proc. Camb. Phil. Soc. **53**, 654–662 (1957).

[58] G. Grawert, "Zur Theorie der Stobe angeregte Alkaliatome mit Edelgasatomen [On the theory of the scattering of excited alkali atoms by inert gas atoms]", Z. Phys. **225**, 283–292 (1969).

[59] W. Eastes and D. Secrest, "Calculation of rotational and vibrational transitions for the collision of an atom with a rotating vibrating diatomic oscillator", J. Chem. Phys. **56**, 640–649 (1972).

[60] W. A. Lester, Jr. and J. Schaefer, "Coupled channel study of rotational excitation of H_2 by Li^+ collisions", J. Chem. Phys. **59**, 3676–3686 (1973).

[61] C. H. Greene and R. N. Zare, "Photofragment orientation and alignment", Ann. Rev. Phys. Chem. **33**, 119–150 (1982).

[62] R. N. Zare, in *Angular momentum: Understanding spatial aspects in chemistry and physics* (Wiley, New York, 1988).

[63] A. R. Edmonds, *Angular momentum in quantum mechanics* (Princeton University Press, Princeton, NJ, 1957).

[64] M. D. Rowe and A. J. McCaffery, "Transfer of state multipoles in excited $A\,^1\Sigma_u^+$ $^7Li_2$ following rotationally inelastic collisions with He: Experiment and theory", Chem. Phys. **43**, 35–54 (1979).

[65] M. W. Schmidt, K. K. Baldridge, J. A. Boatz, S. T. Elbert, M. S. Gordon, J. H. Jensen, S. Koseki, N. Matsunaga, K. A. Nguyen, S. Su, T. L. Windus, M. Dupuis, and J. A. Montgomery, Jr., "General atomic and molecular electronic structure system", J. Comp. Chem. **14**, 1347–1363 (1993).

[66] M. J. Frisch, J. A. Pople, and J. S. Binkley, "Self-consistent molecular orbital methods 25. Supplementary functions for Gaussian basis sets.", J. Chem. Phys. **80**, 3265–3269 (1984).

[67] A. D. McLean and G. S. Chandler, "Contracted Gaussian basis sets for molecular calculations. I. Second row atoms, Z=11–18", J. Chem. Phys. **72**, 5639–5648 (1980).

[68] J. Blaudeau, M. P. McGrath, L. A. Curtiss, and L. Radom, "Extension of Gaussian-2 (G2) theory to molecules containing third-row atoms K and Ca", J. Chem. Phys. **107**, 5016–5021 (1997).

[69] K. Kowalski and P. Piecuch, "New coupled-cluster methods with singles, doubles, and noniterative triples for high accuracy calculations of excited electronic states", J. Chem. Phys. **120**, 1715–1738 (2004).

[70] D. Feller, "The role of databases in support of computational chemistry calculations", J. Comp. Chem. **17**, 1571–1586 (1996).

[71] K. L. Schuchardt, B. T. Didier, T. Elsethagen, L. Sun, V. Gurumoorthi, J. Chase, J. Li, and T. L. Windus, "Basis set exchange: A community database for computational sciences", J. Chem. Inf. Model. **47**, 1045–1052 (2007).

[72] R. Krishnan, J. S. Binkley, R. Seeger, and J. A. Pople, "Self-consistent molecular orbital methods. XX. A basis set for correlated wave functions", J. Chem. Phys. **72**, 650–654 (1980).

[73] P. M. W. Gill, B. G. Johnson, and J. A. Pople, "The performance of the Becke-Lee-Yang-Parr (B-LYP) density functional theory with various basis sets", Chem. Phys. Lett. **197**, 499–505 (1992).

[74] D. E. Woon and T. H. Dunning, Jr., "Gaussian basis sets for use in correlated molecular calculations. III. The atoms aluminum through argon", J. Chem. Phys. **98**, 1358 (1993).

[75] B. P. Prascher, D. E. Woon, K. A. Peterson, T. H. Dunning, Jr., and A. K. Wilson, "Gaussian basis sets for use in correlated molecular calculations. VII. Valence, core-valence, and scalar relativistic basis sets for Li, Be, Na, and Mg", Theor. Chem. Acc. **128**, 69–82 (2011).

[76] A. Schafer, H. Horn, and R. Ahlrichs, "Fully optimized contracted Gaussian basis sets for atoms Li to Kr", J. Chem. Phys. **97**, 2571 (1992).

[77] D. Feller, E. D. Glendening, D. E. Woon, and M. W. Feyereisen, "An extended basis set *ab initio* study of alkali metal cation–water clusters", J. Chem. Phys. **103**, 3526 (1995).

[78] D. E. Woon and T. H. Dunning, Jr., "Gaussian basis sets for use in correlated molecular calculations. III. The atoms aluminum through argon", J. Chem. Phys. **98**, 1358 (1993).

[79] K. A. Peterson and T. H. Dunning, Jr., "Accurate correlation consistent basis sets for molecular core-valence correlation effects: The second row atoms Al-Ar, and the first row atoms B-Ne revisited", J. Chem. Phys. **117**, 10548 (2002).

[80] C. de Boor, *A Practical Guide to Splines*, revised ed. (Springer, New York, 2001), codes available at: http://pages.cs.wisc.edu/ deboor/pgs/.

[81] J. More, B. Garbow, and K. Hillstrom, http://netlib.org/minpack/, source code, Accessed 10/10/2016.

[82] A. P. Hickman, D. L. Huestis, and R. P. Saxon, "Calculations of inelastic collisions of excited states of Xe with He and Ar", J. Chem. Phys. **98**, 5419–5430 (1993).

[83] B. R. Johnson, "The multichannel log–derivative method for scattering calculations", J. Comp. Phys. **13**, 445–449 (1973).

[84] L. F. Shapine, S. M. Davenport, and R. E. Huddleston, http://www.netlib.org/slatec/src/dpolft, source code, Accessed 12/05/2016.

[85] L. F. Shapine and S. M. Davenport, http://www.netlib.org/slatec/src/dp1vlu, source code, Accessed 12/05/2016.

[86] A. Lopez-Piñeiro, M. L. Sanchez, and B. Moreno, "MORSEMATEL: a rapid and efficient code to calculate vibration-rotational matrix elements for r-dependent operators of two Morse oscillators", Comput. Phys. Commun. **70**, 355–361 (1992).

[87] N. J. Vilenkin, in *Special Functions and the Theory of Group Representations*, Vol. 22 of *Translations of Mathematical Monographs* (American Mathematical Society, Providence, RI, 1968), pp. 133–134, translated from the Russian by V. N. Singh.

[88] F. J. Aoiz, M. Brouard, C. J. Eyles, J. Klos, and M. P. de Miranda, "The collisional depolarization of $^{2S+1}\Sigma$ radicals by closed shell atoms: Theory and application to OH ($A\,^2\Sigma^+$) + Ar", J. Chem. Phys. **130**, 044305 (2009).

[89] A. Messiah, in *Quantum Mechanics* (North-Holland Publishing Company, Amsterdam, 1962), Vol. II, pp. 1056–1058.

[90] R. Essers, J. Tennyson, and P. E. S. Wormer, "An SCF potential energy surface for lithium cyanide", Chem. Phys. Lett. **89**, 223–227 (1982).

[91] W. Zudilin, "A generating function of the squares of Legendre polynomials", Bull. Austral. Math. Soc. **89**, 125–131 (2014), https://arxiv.org/pdf/1210.2493.pdf.

[92] NIST: Digital Library of Mathematical Functions, http://dlmf.nist.gov/18.12, accessed 01/05/2017.

[93] W. H. Press, S. A. Teukolsky, W. T. Vetterling, and B. P. Flannery, in *Numerical Recipes: The Art of Scientific Computing*, 3rd ed. (Cambridge University Press, New York, NY, 2007), p. 161.

[94] I. S. Gradshteyn and I. M. Ryzhik, in *Table of Integrals, Series, and Products*, 5th ed. (Academic Press, inc., San Diego, CA, 1994), p. 524, edited by Alan Jeffrey and translated from the Russian by Scripta Technica, Inc.

Vita

For her undergraduate studies, Teri Price attended Tulane University with support from scholarships including a Tulane University Presidential Scholarship and a National Merit Finalist Scholarship. She received a Bachelor of Science degree in Physics and Mathematics from Tulane in 2012 and was awarded the Elsie Field DuPre Memorial Prize in Physics. She then attended Lehigh University for her graduate studies, where she joined Professor A. Peet Hickman's research group in the summer of 2013. While at Lehigh, Teri received a GAANN fellowship. In August of 2017, Teri will work as a Post-Doctoral Research Associate in the Department of Physics at Purdue University, carrying out research in molecular physics under the guidance of Professor Chris Greene.